UNIVERSITÀ DEGLI STUDI DI MILANO

Scuola di Dottorato in Scienze e Tecnologie Chimiche
Dipartimento di Chimica
XXVII Ciclo Dottorato in Chimica Industriale

Photocatalytic activity assessment of micro-sized TiO_2 used as powders and as starting material for porcelain gres tiles production

(Settori Scientifico Disciplinari: ING-IND/25; CHIM/04)

Sara Gatto
(Matricola R09615)

Tutor: Prof. Claudia L. Bianchi
Co-Tutor: Prof. Carlo Pirola

Coordinatore del Dottorato: Prof. Dominique Roberto

A.A. 2013/2014

E di tutta la seria sì numerosa e varia
di corpi e d'elementi, sol mi garbava l'aria…
…non sapevo altre formule che questa: H_2O;
E questa dissi: il bruto senz'altro mi bocciò.

"La chimica in versi", Alberto Cavaliere

Table of contents

General Abstract

1. Introduction

Nowadays, it is essential to develop and find new ways to reduce the increasing pollution deriving from anthropogenic and environmental sources. Human activities are major responsible of climate changes and ecosystems alterations, because of the increasing release of CO_2 and other harmful gases inside the atmosphere. In order to reduce the environmental impact of the human society, a great attention is now given to such processes able to reduce the pollutants concentration in both air and water systems. Advanced oxidation processes (AOPs), which involves the generation of highly reactive hydroxyl radicals ($OH^{\cdot}$), have emerged as promising air and water treatment technology for the degradation or mineralization of a wide range of pollutants.

Titanium dioxide (TiO_2) induced photocatalysis is an example of AOP processes and it has been demonstrated its efficiency in the decomposition of various organic contaminants. TiO_2 is a very well known and well-researched material due to the stability of its chemical structure, biocompatibility, physical, optical, and electrical properties. TiO_2-based photocatalysts are used for a variety of applications such as degradation of volatile organic compounds (VOCs) [1] and decomposition of nitrogen pollutants (NO_x) [2] or also organic dyes, like Methylene Blue [3].

The crystalline forms of TiO_2 are anatase, rutile and brookite. In general, TiO_2 is preferred in anatase form because of its high photocatalytic activity, non-toxicity, chemically stability; moreover, it is relatively inexpensive. For

a long time, new synthetic routes have been developed to prepare nano-TiO_2 samples in order to enhance their photocatalytic efficiency [4-6]. In fact, since many years the attention has been focused on ultrasmall semiconductive particles, because they show peculiar and enhanced properties compared to the micrometric particles ones [7]. Nano-sized TiO_2 is extremely efficient towards the photodegradation processes; in particular, photo-redox reactions are greatly enhanced thanks to the high numbers of active sites present on the extremely large surface area [8]. However, in recent years many papers published the possible health risks correlated with nano-sized materials [9,10]. The small size, shape, solubility and agglomeration degree of nano-sized materials, make them able to cross the cell boundaries or pass directly from the lungs into the blood stream and finally reach all the organs in the body [11]. On the other hand, larger particles are adsorbed by organs and cells with more difficulty.

The main question is then if it is necessary to use the nano-sized particles in an exclusive way. Kwon et al. [12] stated that nanocatalysts having small particle size, high surface area, and a high density of surface coordination unsaturated sites offer improved catalytic performance over microscale catalysts but this does not imply the impossibility a priori to use these latter in selected conditions. The use in photocatalysis of TiO_2 powders with larger-sized crystallites is a very interesting approach to reduce the possible health problems caused by nanoparticles.

2. Aims of work

The aims of this PhD work is to evaluate the photoactivity of micro-TiO_2 samples using as irradiation source both UV and LED lights. At first, commercial powdered micro- and nano-sized TiO_2 catalysts, were tested and then improved for the degradation of pollutants in both gas and aqueous phase. The ultimate purpose of the PhD work is to test the possibility of using TiO_2 for production of building materials; the photocatalytic activity of TiO_2 can be then exploited for degrading air pollutants inside domestic environments or workplaces, thus making them healthier over time. Application of photocatalysis to construction buildings began towards the end of 1980s with the production of photocatalytic glasses, which provided self-cleaning and anti-fogging properties [13]. Afterward photocatalytic cementitious materials have been patented by Mitsubishi Corp. and Italcementi SpA [14,15]. In all these construction materials, the active photocatalyst is anatase TiO_2. Although the use of photocatalytic cement is still restricted and limited, many buildings and city roads have been designed and constructed since 2000. Relevant examples are Church "Dives in Misericordia", Rome, Italy; Music and Arts City Hall, Chamberéry, France [16]. In general, the mostly used powders of commercial TiO_2 for photocatalytic applications are nanometric: this leads some advantages in terms of pollutants degradation efficiency, but many backwards too, like the difficulty to recover the catalyst or the possibility of inhalation with consequent health damage, even the high cost is not negligible. For this reasons, the optimization of the photocatalytic efficiency of micrometric compounds is desired, in order to replace definitely the nanometric catalysts. In this PhD work micro-sized TiO_2 powder was used for the preparation of

porcelain gres tiles, which are commercial manufactured products, opening a new generation of material intrinsically safer than the traditional photocatalytic products.

All samples were fully characterized investigating textural, structural, morphological and surface properties. The photoefficiency was evaluated in different ways, which can be summarized as follows:

- Assessment of the photoactivity of commercial samples, both nanometric and micrometric, in gas and aqueous phases in the presence of typical indoor and outdoor pollutants (NO_x and Volatile Organic Compounds (VOCs), textile dyes, surfactants);
- Assessment of the self-cleaning effect, evaluated by water contact angle measurements, during ultraviolet irradiation on micro-TiO_2 tiles of building materials on whose surface the oleic acid is deposited (ISO/WD 27448-1);
- Assessment of the effects of the addition of anionic or cationic ions, like fluorine, tin, rhenium or tungsten, on the catalytic surface through the impregnation method. Doping is useful to lower the titanium band gap and accordingly to increase the photocatalytic activity of the material.

3. Experimental details

3.1 Catalytic materials

a) Preparation of TiO_2 powders

Different commercially available micro- and nano-sized pigmentary-powdered TiO_2 were chosen; the catalysts were characterized and used without further treatment. In the **Table 3.1** the photocatalytic powders used in this PhD work are reported.

For each powder, the different physico-chemical characteristics are specified: XRD for the crystalline nature, BET for the surface area, XPS for the atomic composition of elements, SEM and TEM for the particles morphology, FTIR for the chemical composition of samples supported with DRS (diffuse reflectance spectra) for the characterization of the light absorption features and band-gap determinations.

Before starting the photooxidation process of pollutants, commercial TiO_2 powders were deposited in two plains of glass sample (each plain of 7.5x2.5 cm^2). TiO_2 powders (0.050 g) were first suspended in 2-propanol (50 ml) so to obtain a homogeneous suspension and then deposited by drop casting onto one side of the laminas. The solvent was simply evaporated at room temperature without any further treatment. The samples consisted in a thicker layer, obtained by overlapping three TiO_2 coatings (labelled as T, standing for triple layers, followed by the substrate abbreviation), as shown in previous works by Bianchi et al. [17,18].

Table 3.1. Main features of TiO_2-based commercial powders, used as photocatalysts, with the corresponding crystalline phase: nanometric and micrometric samples.

Powder	Crystalline phase	BET (m^2/g)	Micro/Nano	XPS OH/O_{tot}
P25 (Evonik)	75% anatase; 25% rutile	52	NANO	0.14
PC105 (Crystal)	anatase	80	NANO	0.85
1077 (Kronos)	anatase	11	MICRO	0.32
AH-R (Hundsman)	anatase	12	MICRO	0.19
AT-1 (Crystal)	anatase	12	MICRO	0.24
1001 (Kronos)	anatase	11	MIXED PHASE (micro+nano)	0.27
1002 (Kronos)	anatase	9	MIXED PHASE (micro+nano)	0.35
1071 (Kronos)	anatase	10	MIXED PHASE (micro+nano)	0.18
A-Z (Hombitam)	99% anatase	4	MICRO	0.25
AN (Hombitam)	98,5% anatase	12	MICRO	0.5
N.10 (HombiKat)	98% anatase; 2% rutile	13	MICRO	0.13

b) Preparation of vitrified tiles

Among all building materials, commercially available white tiles by GranitiFiandre SpA (sample name White Ground Active® (WGA) or Orosei Active) were chosen and used for the preparation of photocatalytic tiles. Porcelain gres tiles are manufactured under high pressure by dry-pressing of fine processed ceramic raw materials, with large proportions of quartz, feldspar, and other fluxes. The body of these materials is then fired at very

high temperatures (1200–1300°C) in kilns [19]. After impregnation with water, the tiles are subjected to temperature cycles between +5 and -5 °C, during a minimum of 100 freeze–thaw cycles, in order to verify their resistance to the frost and their durability. No evident cracks or damages were observed on the samples. The final material is thus characterized by lack of porosity, complete water-proofing, durability, hardness, wear resistance properties, and a complete frost resistance. The porcelain gres tiles were covered at the surface with a mixture of micro-TiO_2 and a commercial SiO_2-based compound prepared via ball–mill [20,21]. To achieve the desired product stability, at the end of the preparation procedure tiles were treated at high temperature (680 °C) for 80 min and then brushed to remove the powder present at the surface and not completely stuck. Temperature was precisely chosen to maintain the anatase form of the semiconductor and allow the vitrification of the tiles surface. Tiles were also prepared with the same procedure but without adding the photoactive oxide into the SiO_2-based compound for the sake of comparison (sample name White Ground (WG) or Orosei)). The surface wettability of photoactive porcelain gres tiles was evaluated by static contact angle (CA) measurements performed with an OCA20 instrument (DataPhysics Co., Germany) equipped with a CCD camera and a 500 μL-Hamilton syringe to dispense liquid droplets. [22,23].

c) Doping effect on TiO_2 powders

Micrometric TiO_2 powders were doped with cations like tungsten (W), tin (Sn) and rhenium (Re), and fluoride anions (F^-). This was done with the aim to improve the photoefficiency of the micro-sized TiO_2 catalysts, which have lower activity than the traditional nanopowders. Ren at al. [24]

demonstrated that the fluorination of TiO_2 nanocrystals gave a photocatalytic enhancement due to the higher separation efficiency of photogenerated electrons and holes. Furthermore, it has been found that the surface fluorination favors the generation of free OH radicals, which are responsible of an enhanced oxidation [25]. Regarding the doping with metal cations, in the literature is reported that Re dopant could effectively inhibit the recombination of the photoinduced electrons and holes [26]. Re can act as electron trap and promote the interfacial charge transfer processes in the composite systems, which reduces the recombination of photoinduced electron-hole pairs, thus improving the photocatalytic activity of TiO_2. Moreover, it was demonstrated that that metal particles doping can facilitate the electron excitation by creating a local electrical field, enhancing photoinduced surface redox reactions: it results in the extension of the wavelength of TiO_2 response towards the visible region [27]. The band gap energy of the doped-TiO_2 results less than that of naked TiO_2, which induces the red shift of the adsorption edge to respond to visible light. This peculiar feature gets interesting for the use of LED (Light Emission Diode) as irradiation source for the photooxidation processes, because LED emissions are located only in the visible region of light. In fact, an important aspect is the use of irradiation by visible light, through LED lamps. Several cities, like Milano, Stockholm, Los Angeles, Copenhagen, have chosen to adopt the LED emission for the outdoor illumination: Milano will substitute the 80% of urban illumination with the LED light within May 2015 (Expo start date). Advantages, connected to this emerging technology (high durability, cheapness, low energy consume), adhere very well with the

environmental safety. Thus, NO_x and VOCs photodegradation was performed with LED lamp, using micrometric doped powder.

The classical impregnation method was applied to dope the catalyst surface with fluoride anions, starting from inorganic fluoride salts (NaF, NH_4F, CaF_2 and F_2). At the end of the impregnation procedure (24 h, room temperature), powders were calcined at 400°C for 4 h and rinsed in distilled water three times.

The metal doping was performed in two different ways: it was used the same procedure of impregnation method for tin (Sn) surface doping, whereas a different surface deposition technique (decoration method) was performed for metals of tungsten (W) and rhenium (Re). Decoration of M- or MO-NPs is commonly implemented by means of ultra-sounds (US) in aqueous or organic solutions where ceramics or polymer substrate powders are dispersed [28]. In the latter case, the precursor of metal was sonicated at a costant temperature of 80°C for 3 h, with 33.0% amplitude and a 50 W cm^{-2} intensity. At the end, the solution was centrifugated many times to remove all the solvent; the final powders was washed with n-pentane and centrifugated again. The residual solvent was evaporated and the sample was finally calcined at 480°C for 40 h to completely remove the organic scents.

3.2 Testing procedure

a) Photocatalytic set-up in gas-phase

Photocatalyitc degradation of air pollutants, such as acetone, acetaldehyde, toluene (well known as VOCs) and NO_x, were conducted in

Pyrex glass cylindrical reactors having different volume depending on the type of analyzed pollutant: 5 L for VOCs and 20 L for NO_x, respectively. In the case of VOCs analysis, the gaseous mixture in the reactor was obtained by mixing hot chromatographic air (f.i. 250 °C for toluene), with relative humidity (RH) of 40%, and a fixed amount of volatilized pollutant, in order to avoid condensation. The initial concentration of VOCs in the reactor was 400 ppmv, monitored directly by micro-GC sampling. Photon sources were provided by a 500 W iron halogenide lamp (Jelosil, model HG 500) emitting in the 315–400 nm wavelength range (UV-A) at 30 Wm^{-2} or by a LED lamp, emitting into the visible region. Acetone and acetaldehyde degradation tests lasted for 2 h, whereas toluene tests for 6 h, due to the difficulty in degrading a molecule with an aromatic ring and with a complex degradation pathway [19].

For NO_x photodegradation study, a first static experimental setup was obtained used the following conditions: RH: 50%, UV light of 10 Wm^{-2} (for TiO_2 powders deposited on glass sheets) or 20 Wm^{-2} (for micro-sized TiO_2 gres tiles), with a NO_x starting value of 1000 ppb. The analytical procedure was reported by Bianchi et al. [21]. NO_x degradation by TiO_2 powders (always immobilized on a glass sheet) and photoactive tiles was conducted also in continuous conditions using a plug-flow reactor (with an effective volume of 0.025 L) built strictly following the ISO 22197-1 rule [29]. Experimental conditions were maintained as follows: RH: 40%, 20Wm^{-2}, $[NO_x]_{inlet}$=500 ppb, and 180, 32.4, 9, and 4.2 L h^{-1} total flow, respectively. A chemiluminescent analyzer (Teledyne Instruments M200E) was used to check the conversion of the pollutant in both batch and plug-flow reactor setups.

b) Photocatalytic set-up in aqueous-phase

The photocatalytic apparatus was a 1 L glass stirred reactor equipped with an iron halogenide UV lamp (500 W, Jelosil® HG500) emitting light at wavelengths of 315–400 nm and able to irradiate the reactor with a specific power of 95 Wm^{-2}, when TiO_2 powder was used as catalyst. The UV lamp was placed beside the reactor, which was cooled with water at a temperature of 30 ± 0.5°C, as reported previously by Gatto et al. [30]. TiO_2 was introduced in the reactor at the beginning of each test (0.66 g/L for surfactant degradation and 0.1 g/L for textile dyes). The variation of the surfactant (PFOA) concentration in solution was monitored by total organic carbon (TOC) analysis and ionic chromatography. The PFOA initial concentration ($[PFOA]_0$= 4 mM) was maintained lower than its critical micellar concentration (7.8 mM) in order to avoid the formation of emulsions during the kinetic tests. Samples (10 mL) of the reaction mixture were collected at different reaction times: typically at 0 min (before the start of the reaction), 30 min, 1 h, 2 h, 3 h, 4 h, 6 h and 9 h.

Textile dyes, chosen for the photodegradation tests, were Rhodamine B (RhB), Methylene Blue (MB) and Crystal Violet (CV); dyes degradation was checked every 60 min by determining the dye concentration in the water solution by a UV–vis spectrophotometer analyzer (T60 UV–vis PG LTD instruments), using water as the reference. Pure CV has an absorbance maximum at 590 nm, RhB at 555 nm and MB around 670 nm. Textile dyes degradation was also performed using photoactive tiles, covered with the micrometric 1077 powder. For this aim, a cylindrical batch reactor of 1 L volume was used for dye degradation tests in presence of ten photoactive tiles (0.03 m^2 total surface photoactive area) immersed into the liquid

solution, as reported by Bianchi et al. [31]. Refrigeration was allowed by a cooling jacket. Two different lamps directly immersed into the dye solution were used with this setup: a typical germicidal 9 W UV-C lamp (Philips TUV BL-S, model AEPL-7913 mercury vapor low pressure), with a radiant power of 1 Wm^{-2} and a 125 W UV-A lamp (Jelosil, mercury vapor low pressure), with an illuminance of 65 Wm^{-2}, in correspondence of the tiles surface. During photocatalytic tests, the TiO_2 active faces of the tiles were turned towards the UV light. After each test, the tiles were simply washed using deionized water and acetone and then left in deionized water all night long. The same dyes solution (RhB, MB, CV) were used in the present setup at a concentration of 1×10^{-5} M.

c) Self-cleaning effect

The self-cleaning capability of TiO_2 photoactive tiles was evaluated in two different ways: (1) through the measurement of the water contact angle (CA) (KRUSS GmbH) of a tile, after oleic acid deposition and UV irradiation (Jelosil, model HG 500) for 76 h and (2) through the monitoring, by a colorimeter, of the discoloration of dyes directly put on the tiles surfaces, after exposure to the sunlight (Milan – Italy, May 2012).

For water CA measurements, a test piece of porcelain gres tile of 100 ± 2mm^2 were pre-treated by ultraviolet irradiation of 20 Wm^{-2} for at least 24 hours. Then, the catalytic samples were dipped inside an oleic acid (Fluka, >80%) solution (0.5 vol%) in order to simulate a polluting condition. The presence of oleic acids on the tile surface modify its wettability. After UV irradiation it was measured the CA at an appropriate time interval, observing a continuous decrease of the CA values related to a degradation of the polluting agent. The measurement can be considered concluded when the

contact angle value of the clean photocatalytic tile is restored, as before the oleic acid deposition. For comparison, the measurement is repeated on a sample similarly polluted with oleic acid, but left in the dark for 76 hours. Furthermore, it was taken a sample of porcelain gres tile, not containing TiO_2, and it was immersed into oleic acid solution and irradiated, with the aim to evaluate the pure contribute of UV irradiation.

Dyes degradation instead was monitored by Vis-spectrometer equipped with an integrated sphere (OceanOptics, USB400-VIS-NIR-ES). 1 μL of dyes, dissolved in water, was put on the tiles surface and left under the sunlight, whose power was continuously checked from 9 am to 5 pm every day by a radiometer DeltaOhm HD2012,2. A mean power irradiation value of 7.28 W/m^2 was measured. The color analysis was performed using the CIEXYZ and CIELAB models [22].

4. Results and discussion

4.1 Characterization results

a) Powders characterization

Anatase, evidenced by XRD patterns, is the unique polymorph present for all samples, except for P25 and N.10 (by Hombikat) powders, which exhibit even the rutile phase (25 and 2%, respectively). The crystallographic reflexes (1 0 1), (2 0 0) and (2 1 1) have been employed to calculate the average crystallites size of the various titania particles. P25 and PC105, commercial nanometric powders, have comparable crystallite size centered on 25 nm, while the other samples have values between 120 and 200 nm,

confirming their micro-sized nature. These structural properties are reflected in their BET surface areas that are about 11-12 m^2/g, which are much lower compared to the nano-sized ones (**Table 3.1**). For 1001, 1002, 1071 samples Sherrer calculation was not performed, as TEM analysis reveals the presence of both micro-sized and ultrafine fractions, as it is visible in **Fig. 4.1, section d**. HR-TEM and SEM images confirmed the average crystallites sizes extrapolated by XRD analysis; moreover, it was excluded the presence of ultrafine particles in 1007, AT-1, AH-R, A-Z, AN and N.10 powders. It can be evidenced that nano-sized materials perfectly fall within the "nano" definition: in fact, both samples are characterized by average particles size of 15-30 nm (**Fig. 4.1, section a**), closely packed features and roundish contours [19]. As for what concerns the other powders (1077, AT-1, AH-R, A-Z, AN, N.10), they all exhibit well crystallized particles possessing smooth edge and average diameter size in the 120-200 nm range (see **Fig. 4.1, section b and c**), with fringes patterns belonging to the TiO_2 anatase polymorph. On the contrary, for 1001, 1002 and 1071 powders TEM images again confirm that they are composed by a mixture of both micro-sized crystallites and some ultrafine particles (**Fig. 4.1, section d**).

The surface state of the TiO_2 particles was analyzed by XPS. No significant differences can be appreciated in the Ti 2p region among all the present samples concerning the binding energies (BE) and the full width at half-maximum (FWHM) values. The peak of Ti $2p_{3/2}$ is always regular and the BE at about 458.5 ± 0.1 eV compares well with the data for Ti(IV) in TiO_2 materials [32]. The analysis of the oxygen peaks exhibits the presence of more than one component, which can be attributed to lattice oxygen in TiO_2 (529.9 eV) and to surface OH species (>531.5 eV) respectively. A

particular O_{1s} shape was observed for PC105. In this case, the OH component is very intense probably due to a particular industrial synthesis in order to enhance the photocatalytic efficiency of the sample. The hydrophilicity/hydrophobicity character of photocatalysts surface plays a crucial role in determining the adsorption step and thus the photocatalytic activity, at least in the degradation of pollutants [33]. P105 exhibits the highest concentration of OH that represent the 85% of the oxygen at the surface, as it shown in **Fig. 4.2**. It is noteworthy that the micro-sized samples, with the exception of N.10 (by HombiKat) sample, present a higher atomic concentration of OH groups in comparison with P25, pointing out the higher hydrophilic character of their surface (see **Table 3.1,** fifth column).

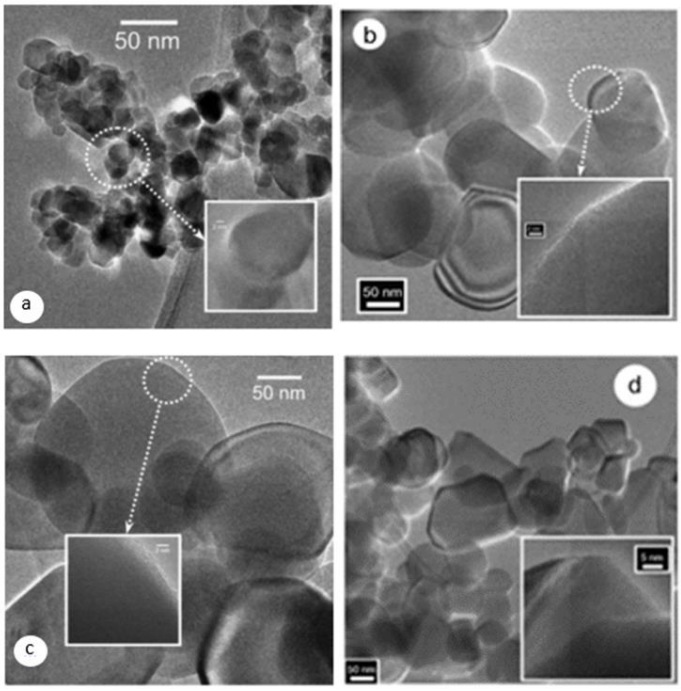

Fig. 4.1. TEM images of the various TiO_2 powders. Section a: P25; section b: 1077; section c: AH-R; section d: 1071.

FTIR spectra in the ν(OH) spectral range of the samples in air revealed two complex absorption bands, respectively located in the 3000–3450 cm^{-1} range and at $\nu \geq 3600$ cm^{-1}. Based on the spectral behavior and of our previous data [19], the former envelope can be ascribed to the stretching mode of all H-bonded OH groups present at the surface of the various solids, whereas the latter corresponds to the stretching mode of all Ti–OH species free from hydrogen bonding interactions [34]. It is well-known that surface hydroxyl radicals play a fundamental role in the photocatalytic processes [35]. In particular, photo-generated holes react with water molecules adsorbed on TiO_2 surface, leading to the formation of $OH^{\cdot}$:

$$TiO_2 + h\nu \rightarrow h^+ + e^- \quad \textbf{(3.1)}$$

$$h^+ + H_2O \rightarrow OH^{\cdot} + H^+ \quad \textbf{(3.2)}$$

The pigmentary TiO_2 powders showed appreciable amounts of OH groups and this validate their rather good performances in the photocatalyitc degradation, as reported in our previous study [19].

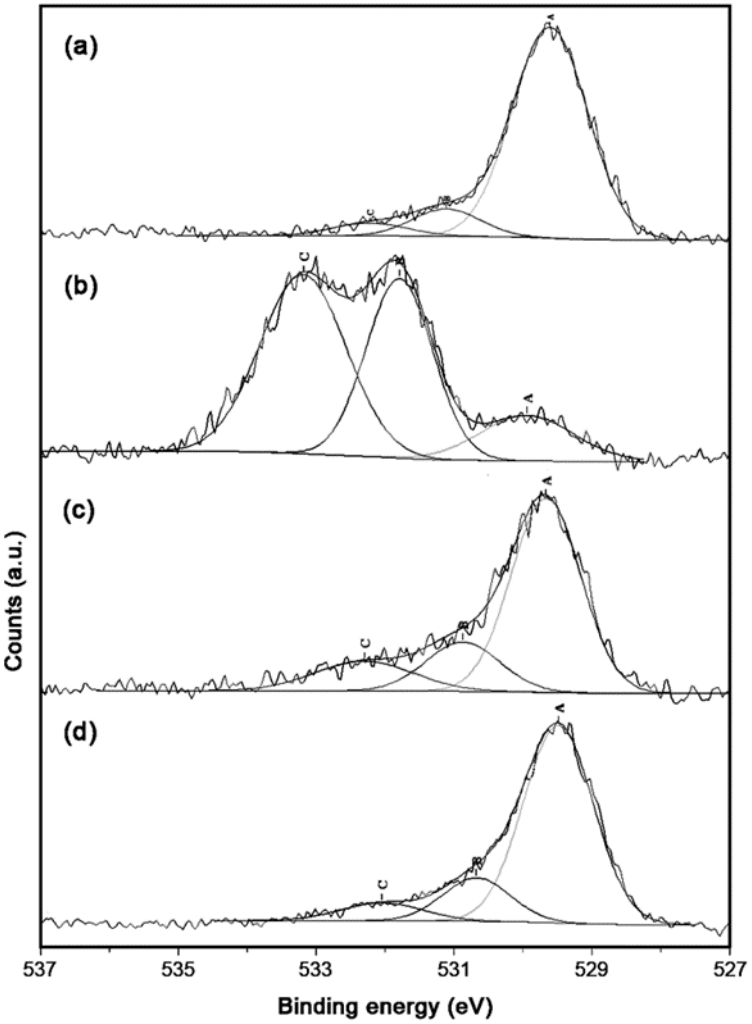

Fig. 4.2. O1s XPS spectra for (a) P25; (b) PC105; (c) 1077; (d) AT-1.

b) Gres tiles characterization

XPS measurement reveals the presence of only Ti(IV) and a Ti/Si ratio of 0.15 for the micro-TiO_2+SiO_2-based compound, which belongs to porcelain grès tiles. The preservation of the pure anatase form was verified by both XRPD and XPS measurements. As reported by Anderson and Bard [37] the presence of SiO_2, together with TiO_2, enhances the formation of

hydroxyl radical $OH^{\cdot}$, which may be achieved via strong Brønsted acid sites at the TiO_2/SiO_2 interface region. Such incorporation inhibits the crystal growth of TiO_2 allowing the preservation of the anatase structure at high temperature. By the investigation of morphological features, the presence of SiO_2-based compound is evident in gres tiles (**Fig. 4.3**), in the form of either small protruding particles or as amorphous coating which covers the TiO_2 particles.

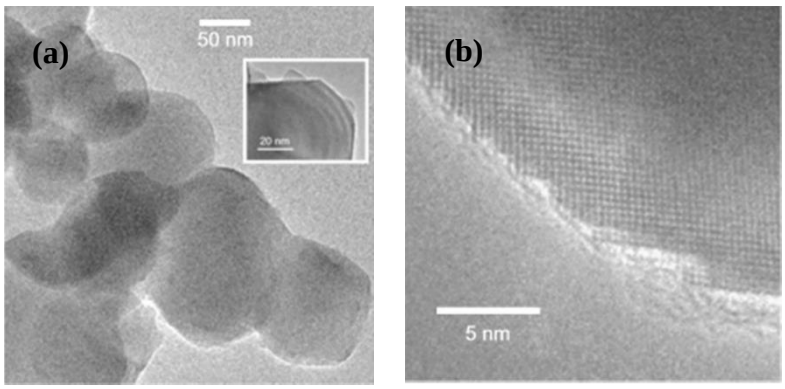

Fig. 4.3. HR-TEM images of the TiO_2 porcelain gres tiles materials. (a) refers to low magnification and (b) to high magnification.

The very thin nature of these particles and/or coating allows to inspect the fringe patterns located below, confirming that the spacing among the fringes are still ascribable to the anatase TiO_2 polymorph.

4.2 Photocatalytic tests

4.2.1 Photocatalytic activity in gas-phase

a) NO_x photoabatement with TiO_2 powders

In this section, several commercial pigmentary powders were tested for NO_x degradation and were compared with the nanometric powders

efficiency (P25 and PC105). At first, the tested concentration of NO_x in the reactor was 1000 ppb, in order to follow the same pollutant concentration requested by the ISO 22197-1 rules [38]. All the samples showed good photocatalytic performances, because the abatement of NO_x was early completed at the end of 3 hours, except the 1071 (by Kronos) sample, which showed lower photodegradation (61.5 %). The efficiency of the other samples was between 90 and 99%: this behavior leads to hypothesize a complete degradation of the pollutant within the chosen limited time of the run (3 h). In particular, it is interesting to observe the photodegradation trend of the only micro-sized samples (1077, AH-R, Hombitam A-Z, Hombitam AN and HombiKat N.10) at 15 min, 30 min, 60 min and 240 min, the most significantly times. In **Fig. 4.4** we can observe the peculiar differences, which arise in the initial period of the degradation. 1077, Hombitam AZ and Hombitam AN seem to be the most active, showing the best efficiency in the first times of reaction (15, 30 min). This behavior can be explained through the physico-chemical features and the amount of hydroxyl radicals that initiate the oxidation of NO. The ratio of OH/O_{tot}, obtained by XPS analysis, resulted to be, in fact, higher than the other micrometric ones (**Table 3.1**). In particular, after 2 h, the NO_x conversion of these samples is higher than 90%, very close to that of P25, which reaches the complete pollutant degradation in the same time. Thus, even if the nano-sized materials (P25 and PC105) show the best performances, the photocatalytic activities of the pigmentary powders are comparable, in agreement with the presence of appreciable amount of surface hydroxyls, which are crucial species for the photooxidation processes [39]. From the trend in the **Fig. 4.4** it is clear that the micrometric samples with the best

photocatalytic performances are the ones showing the largest OH component, the following 1007, Hombitam AZ and Hombitam AN.

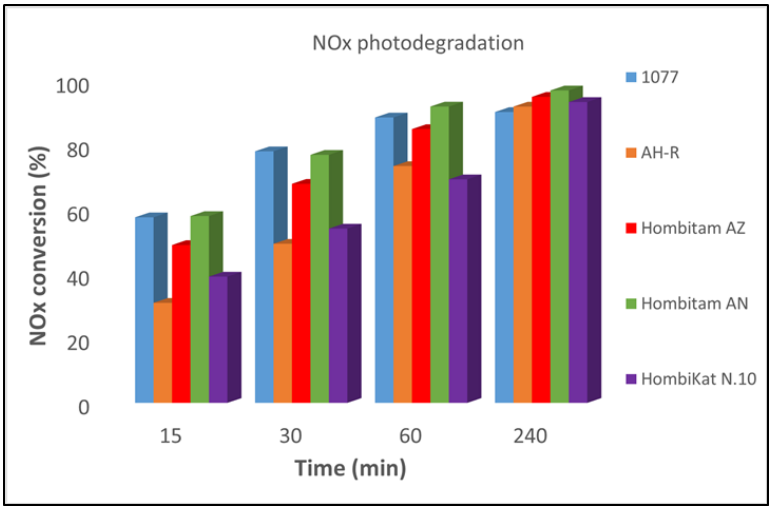

Fig. 4.4. TiO_2 commercial micro-sized powders (1077, AH-R, Hombitam AZ, Hombitam AN, HombiKat N.10) for NO_x abatement at 15, 30, 60, 240 min under UV light irradiation.

b) NO_x photoabatement with photoactive tiles

Another study concerns the application in photocatalysis of building materials. In this PhD work porcelain gres tiles, covered with micrometric TiO_2 powder, were used for the NO_x degradation, under UV light, in static experimental conditions in gas phase. Starting from 1000 ppb of NO_2, i.e. the same amount required by the ISO 22197-1 specification, the 65% of degradation was measured after 6 h. A very interesting trend (**Fig. 4.5**) was observed also following the NO_2 degradation by photocatalytic tiles. NO_2 was chosen as specific reference pollutant instead of the more generic NO_x, because of its higher hazardousness. The continued exposure to high NO_2 levels, in fact, can contribute to the development of acute or chronic bronchitis [40]. More in detail, tests were carried out by using as starting pollutant concentration 106 ppb (value not to be exceeded more than 18

times in a calendar year), and 212 ppb (alert threshold), according to the Directive 2008/50/EC of the European Parliament, which states the guidelines for the protection of the human health. It is possible to observe (**Fig. 4.5**) that, as the amount of starting pollutant is decreased, the time necessary to bring its concentration under the limit required by the European Directive (21 ppb) also decreases. In the **Fig. 4.5 inset** the degradation trend can be observed in the case of an initial pollutant concentration close to the alert threshold.

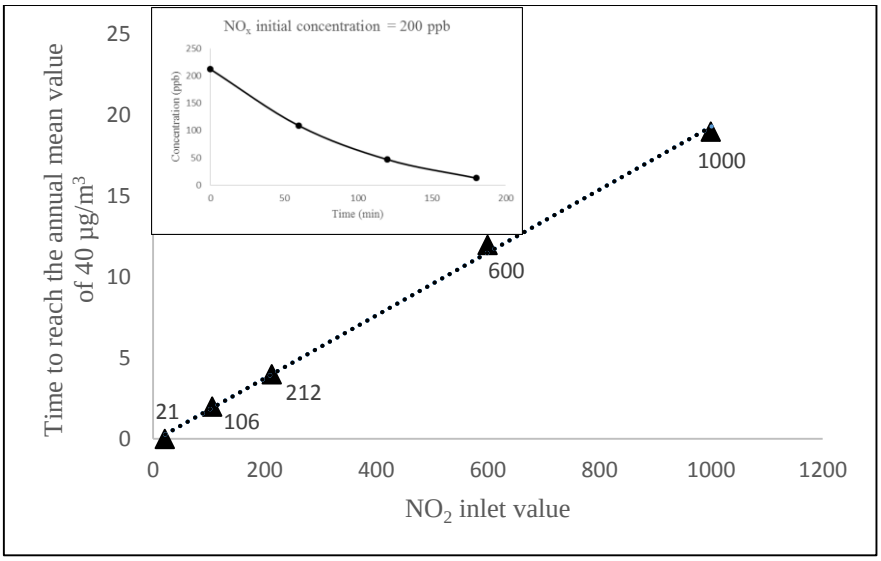

Fig. 4.5. Time necessary to degrade the pollutant and decrease its amount under the limit value required by the Directive 2008/50/EC of the European Parliament and of the council on ambient air quality and cleaner air for Europe (21 ppb); 20 W/m^2, RH 50%, static conditions.

Therefore under real pollution conditions, simulating a day in the absence of wind (static conditions) WGA is able to degrade NO_2 in a very efficient way bringing the pollutant concentration down to the required limit (21 ppb) in a matter of hours [21]. Micro-sized TiO_2 porcelain gres tiles

were also tested in continuous conditions using a plug-flow reactor, whose the operating conditions have been softened cutting the inlet concentration by half (500 ppb, instead of 1000 ppb). It was investigated the role of the flow per hour on the final NO_2 conversion. An interesting aspect revealed: the modification of the flow per hour leads to an evident change of the contact times that is the time the pollutant can stay "in contact" with the catalyst surface. As expected, increasing the contact time, the final conversion proportionally increases. This result is very evident for Orosei Active sample that shows a conversion varying from 1.3% to 82.0% at 180 L h^{-1} and 4.2 L h^{-1}, respectively. The obtained 82% conversion at 4.2 L h^{-1} flow can be consequently considered a very good value.

c) VOCs photoabatement with TiO_2 powders

In order to study the photocatalytic activity of nano- and micro-sized samples, the degradation of three different VOCs, acetone, acetaldehyde and toluene, has been performed. As an illustrative example, it was reported the toluene photodegradation tests. For both nano-and micro-sized TiO_2 powders, the pollutant was not completely degraded, even after 6 h of reaction. Moreover, it is noteworthy that the degradation percentages fell more or less in the same range (46–52%) with a slightly higher value for the nanometric P25 and PC105 catalysts, as it is shown in **Fig. 4.6**. Toluene degradation resulted very difficult due to the complexity of molecule, which presents the aromatic ring. The different catalysts show similar behavior toward the toluene degradation, irrespective of their physico-chemical characteristics. On the contrary, the pollutant mineralization is rather different for almost all samples. Furthermore, a low amount of CO_2 formation confirmed the incompleteness of the degradation reaction. The

possible by-products, which could take form during the degradation, were monitored by FTIR measurements. After the employment in toluene degradation, the spectra of the materials underwent deep changes. In particular, it was possible to recognize signals of unreacted toluene (T) and of several by-products deriving from its degradation, among which benzyl alcohol (BZOH), benzoic acid (BZAc) and benzaldehyde (BZH) [19]. In addition, the signals due to the stretching mode (ν_{OH}) of Ti-OH species free from hydrogen bonding interactions were disappeared with the parallel increase of the broad envelope generated by H-bonded OH groups [31]. Thus, it was possible to state that the catalysts surface underwent irreversible changes after the employment in the photodegradation reaction of toluene: the photo-active "free" Ti-OH sites were completely absent, as a result of their participation to the reaction.

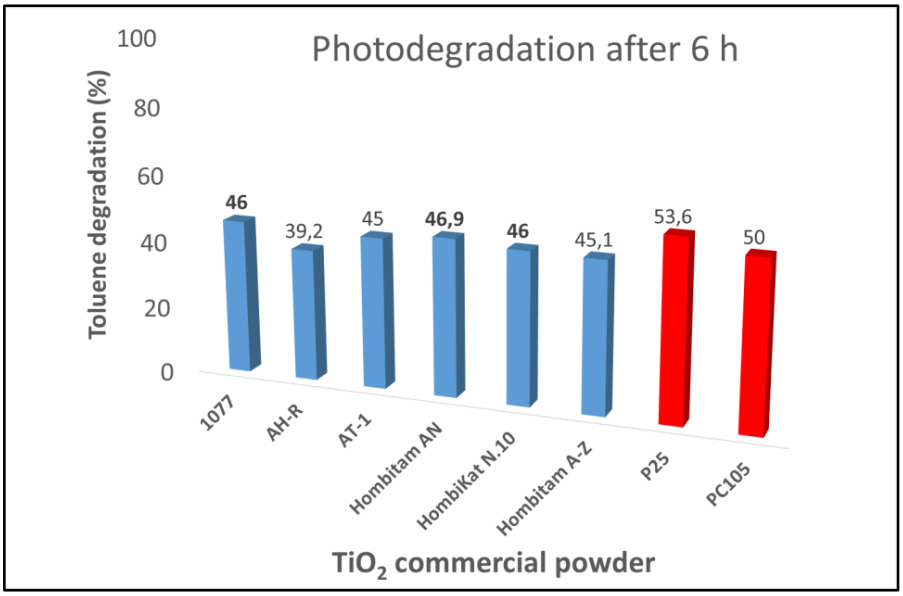

Fig. 4.6. Toluene degradation histogram: photoefficiency achieved with commercial micro-sized TiO_2 and compared to the P25 and PC105 ones (nanometric).

Their disappearance was a clear evidence of why toluene degradation appeared incomplete even after 6 h of reaction for all the samples, regardless of the morphological features of the materials. Therefore, in the case of toluene and in general for all less hydrophilic VOCs, it was well evident that both micro-sized materials and nano-sized ones possess almost the same photocatalytic behavior.

4.2.2 Photocatalytic activity in aqueous-phase

Parallel with photocatalytic tests in gas-phase, photodegradation of surfactants and textile dyes in aqueous phase were performed. In particular, the PFOA (perfluooroctanoic acid) was chosen as surfactant species. The abatement was conducted by using P25 nano-powder as catalyst. The photodegradation trend, monitored at different times, highlighted the incomplete PFOA mineralization. For the entire duration of the photo-abatement process, it was possible to observe a decrease in the PFOA content in solution. However, the mineralization after 4 h settled down: the fluoride content and the percentage mineralization after 6 and 9 h remained equal to 29% and 32%, respectively, as reported by Gatto et al. [29]. Through HPLC-MS analysis was confirmed the presence of the intermediates in the solution that took form through two possible degradation pathways: this surface modification might influence the catalyst reducing the photocatalytic efficiency of TiO_2. Nevertheless, it is important to note that, as reported in the literature, no PFOA abatement was observed working in the presence of TiO_2 as photocatalyst without UV irradiation as

well as under UV irradiation in the absence of photocatalyst (photolysis) [31].

The other interesting study concerns the textile dyes photodegradation, using micro-sized TiO_2 (1077) powders as catalysts. The textile dyes analyzed were Methylene Blue (MhB), Rhodamine B (RhB) and Crystal Violet (CV). Experimental dark tests showed a very low adsorption of all the dyes on both kinds of powders. The contribute of photolysis was almost negligible for MhB and CV, whereas 12% of dye degradation for simple photolysis (10% for P25) was achieved for RhB. Nano-sized powder showed the best results for all the considered dyes achieving the complete decolorizing of the water solution, but also micro-sized sample was able to degrade the pollutants with a good efficiency (ranging from 48 to 58% depending on the dye in six hours) (see **Fig. 4.7**), as reported by Bianchi et al. [30]. In addition, the micro-sized powder can be easily filtered and recovered in order to be immediately reused for further photodegradation reactions. In fact, 1077 was recovered by the simple centrifugation and reused in the same dye degradation test with no loss of photoactivity [30].

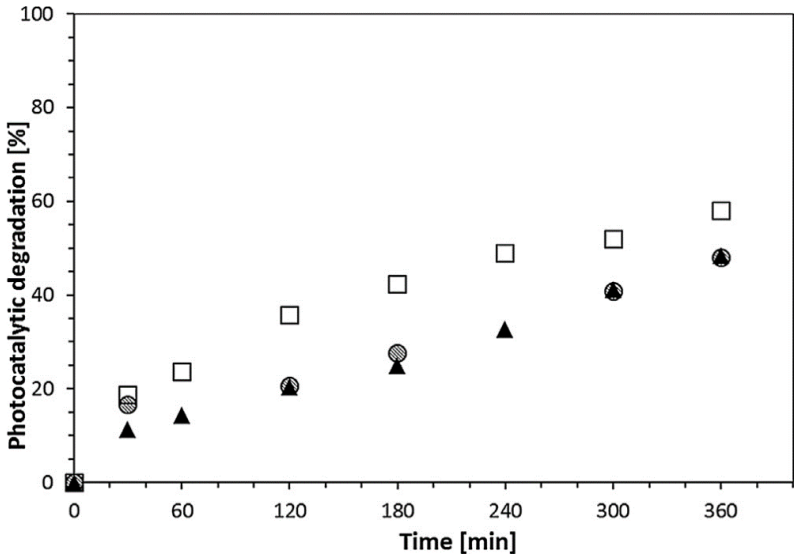

Fig. 4.7. Photocatalysis of dyes performed with powdered micro-TiO_2 catalyst (1077): crystal violet □; methylene blue ▲; rhodamine B ◌.

Another application is relative to the photocatalytic efficiency of TiO_2 porcelain gres tiles, evaluated through UV-vis measurements. This choice reflects the fact that photoactive porcelain gres tiles are covered with the micrometric 1077 powder. It was observed an increase of about 15% of dyes degradation in comparison to the simply photolysis. These porcelain gres tiles can be reused, just after insertion of the tiles in distilled water, and without affecting the photocatalytic activity. In fact, all the tests were done using the same batch of ten samples of industrial tiles, and no loss in their photoactivity was monitored. This indicates that the TiO_2 deposited layers are not deactivated during the reaction either by loss or poisoning of the catalyst, and can be reutilized in subsequent runs. Thus, these new industrial ceramic materials are surely an interesting alternative to TiO_2 suspensions in photocatalytic applications avoiding the removal of the particles at the end of the process.

4.2.3 Self-cleaning effect

A different aspect for the evaluation of gres tiles photo-efficiency is the CA evaluation, measured on micro-sized TiO_2 porcelain gres tiles, after the deposition of oleic acid and irradiation by UV lamp. At first, before the oleic acid (Fluka, >80%) deposition, the pretreatment CA measurements were performed obtaining value of about 31°. The, the catalytic samples were dipped inside the oleic acid solution (0.5 vol%); the presence of oleic acids on the tile surface modify its wettability, the water contact angle in fact increases to about 65°. After UV irradiation it was measured the CA at an appropriate time interval, observing a continuous decrease of the CA values related to a degradation of the polluting agent. We observed that after 76 h of irradiation, the water CA reached the starting value before the oleic acid deposition (about 30°). This highlights the self-cleaning properties of TiO_2 porcelain gres tile [22] and its photocatalytic efficiency for the degradation of organic contaminant deposited on the surface. On the contrary, the same kind of porcelain gres tile (Orosei Active), treated with oleic acid, but maintained in the dark, does not show modifications of CA in the range t_0 and t_{76}. The same procedure, consisting in the deposition of oleic acid solution and irradiation under UV light for 76 h, was performed for a porcelain gres tiles, not containing TiO_2. Even in this case the CA measurement during the UV irradiation remained the same, i.e., the initial CA measured on the oleic acid film (65°). It is justified that the change in the value of the contact angle is due merely to the photodegradation of the oleic acid due to both the action of UV radiation and the photocatalytic efficiency of the used material and not by spontaneous degradation of oleic

acid, induced by non photocatalytic factors. Thus, the photocatalytic process is necessary for the abatement of organic pollutants [17].

4.3 Doping effect on TiO_2 powders

Micro-sized 1077 powder was even doped by the impregnation method. First of all the fluorination effect was investigated, making a comparison with the corresponding nanometric P25 powder: in both powders, after the fluorination, the photocatalytic activity of NO_x and VOCs abatement resulted increased. The simply surface fluorination seems to be a good method to increase the photoactivity in commercial TiO_2 samples, even with large crystallites [41]. In particular, the morphological features evidenced in the HR-TEM images and FT-IR spectral patterns, showed significant features. When the fluorination was carried out on the 1077 sample, there was an increasing of the OH groups interacting by H-bonding in F_2 fluorination and new families of free OH groups involving Ca^{2+} and Na^{+} ions. The simple surface fluorination by fluorination resulted as an easy and good method to increase the photoactivity in commercial TiO_2 samples, even with large crystallites, as reported in **Fig. 4.8**.

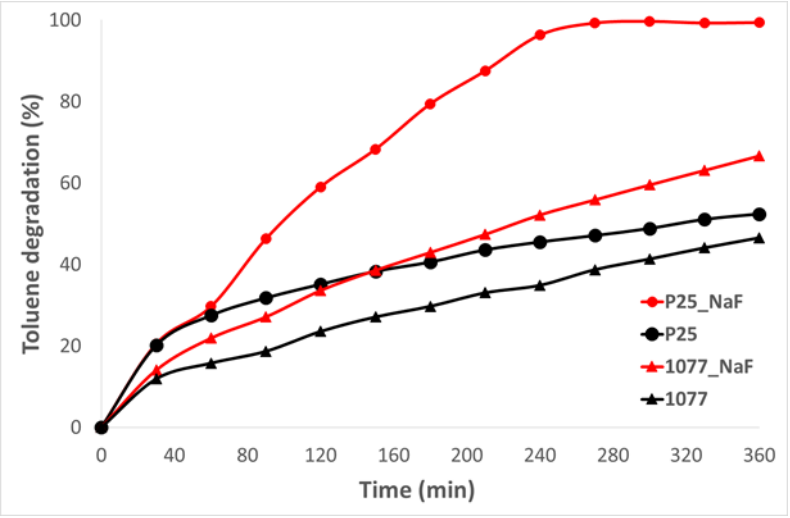

Fig. 4.8. Toluene degradation for both micro- (1077) and nano-sized (P25) TiO_2 samples, naked and fluorinated (NaF precursor).

Physico-chemical characterization demonstrated that the surface fluorination influenced all the surface OH groups, leaving free only some particular OH "families", reasonably the more active in the photocatalytic process. Thus, the driving force of the process is both the presence of active OH population and the efficient adsorption of the pollutant molecules on the photocatalytic semiconductor surface.

Parallel with this, the metal surface deposition with Sn, W and Re lead to an improved photoefficiency. In this case, micro-sized TiO_2 powders exhibited a higher photoactivity compared with the naked TiO_2 one. In particular, an interesting aspect was even the evaluation of photo-efficiency of doped 1077 using the LED light as irradiation source for the pollutant degradation. It has been observed that the photo-abatement efficiency of micro-sized catalysts for VOCs is improved by the presence of metals particles, in particular in the case of rhenium and tungsten. The degradation percentage of acetone was in fact, 37% for 1077_W and 33% for 1077_Re,

compared with the 1077, which showed a negligible photoactivity (~2%), when the catalysts were irradiated by visible light. In **Fig. 4.9** it is possible to see the improved photo-efficiency. In fact, the metal species like W and Re have the main properties of promote the charge transfer and the visible light absorption, which lead to enhanced photocatalytic degradation of pollutants than naked micro-sized TiO_2, even under visible light irradiation [42].

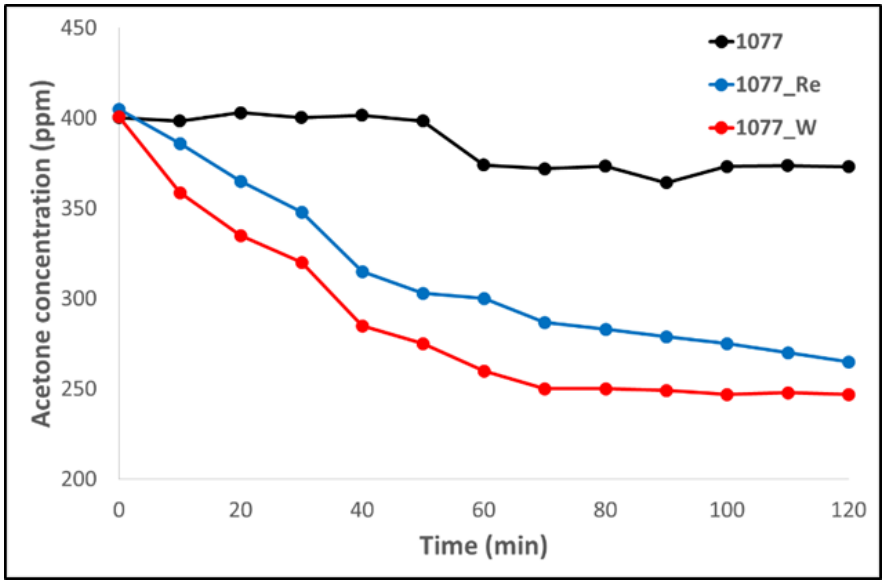

Fig. 4.9. Acetone photodegradation in gas-phase under visible light (performed with a LED lamp).

5. Conclusions

The photocatalytic activity of both nanometric and micrometric TiO_2 powders was evaluated, revealing that nano-sized powders have the best photo-efficiency. However, commercial pigmentary micro-sized TiO_2

powders have given good results proving that they could be good materials in photocatalysis and good alternative to nano-sized catalysts. In particular, 1077, Hombitam AZ and AN are the micro-sized TiO_2 powders with the highest photoactivity for NO_x abatement. The low surface area is not a discriminant factor if other features compensate it; the ratio of OH/O has a specific influence for the pollutants photodegradation together with the morphological features of particles. In fact, nanometric P25 is characterized by a significant higher amount of hydroxyl radicals, in agreement with the optimal efficiency in pollutants photodegradation. However, also pigmentary 1077, Hombitam AZ and AN samples show appreciable amount of $OH^{\cdot}$ groups and this justifies their good catalytic performance. Furthermore, porcelain gres tiles, prepared entrapping micro-TiO_2 at the SiO_2 surface confirmed a stable and reproducible photocatalytic activity toward organic contaminants, such as dyes and NO_x, in both liquid and gas phase. This indicates that these new industrial ceramic materials with micrometric TiO_2 are surely an interesting application, which avoids the use of traditional nanomaterials in powder form for their preparation. In addition, the doping of micrometric TiO_2 powders with anionic or cationic species highlighted the possibility to increase the catalytic performance obtaining comparable results with naked nanometric samples. And, as a consequence of the high demand of the use of LED lamps in the indoor and outdoor areas, the metal particles on the micrometric TiO_2 surface confirmed their ability to adsorb visible light and to be considered sensitizers. To summarize, powders with large particles and low surface area can have good photoefficiency for the depollution abatement.

6. References

[1] Puddu V., Choi H. Dionysiou D.D., Puma G.L. TiO_2 photocatalysts or indoor air remediation: Influence of crystallinity, crystal phase, and UV radiation intensity on trichloroethylene degradation. *Appl. Catal. B: Environ*. **2010**, *94*, 211-218.

[2] Maggos T., Bartzis J.G., Leva P., Kotzias D. Application of photocatalytic technology for NOx removal. *Appl. Phys. A* **2007**, *89*, 81-84.

[3] Gumus D., Akbal F. Photocatalytic degradation of textile dyes and wastewater. *Water Air Soil Pollut*. **2011**, *216*, 117-124.

[4] Gupta S.M., Tripathi M. A review on the synthesis of TiO_2 nanoparticles by solution route. *Central Europ. J. Chem*. **2012**, *10*, 279-294.

[5] Wang X., Liu Y., Hu Z., Chen Y., Liu W., Zhao G. Degradation of methyl orange by composite photocatalysts nano-TiO_2 immobilized on activated carbons of different porosities. *J. Hazard. Mater*. **2009**, *169*, 1061-1067.

[6] Macwan D.P., Dave P.N., Chaturvedi S. A review on nano-TiO_2 sol-gel type synthesis and its applications. *J. Mater. Science* **2011**, *46*, 3669-3686.

[7] Beydoun D., Amal R., Low G., McEvoy S. Role of nanoparticles in photocatalysis *J. Nanoparticle Res.* **1999**, *1*, 439–458.

[8] Di Paola A., García-López E., Marcì G., Palmisano L. A survey of photocatalytic materials for environmental remediation. *J. Hazard.Mater*. **2012**, *211–212*, 3–29.

[9] Love S.A., Maurer-Jones M.A., Thompson J.W., Lin Annu Y-S. Assesing nanoparticle toxicity. *Rev. Anal. Chem*. **2012**, *5*, 181-205.

[10] Park S., Lee S., Kim B., Lee S., Lee J., Sim S., Gu M., Yi J., Lee J. Toxic effects of titanium dioxide nanoparticles on microbial activity and metabolic flux. *Biotechnol. Bioprocess Engin*. **2012**, *17*, 276-282.

[11]] Amoabediny G., Naderi A., Malakootikhah J., Koohi M.K., Mortazavi S.A., Naderi M., Rashedi H. Guidelines for safe handing, use and disposal of nanoparticles. *J. Physics* **2009**, *170*.

[12] Kwon S., Fan M., Cooper A.T., Yang H. Photocatalytic $_{\text{applications}}$ of micro- and nano-TiO_2 in environmental engineering. *Critical Rev. Environ. Sci. Technol*. **2008**, *38*, 197–226.

[13] Rimmer D., Sanderson K.D., Paul T. Coated glass. United States Pat.,WO/2004/108619, **2010**.

[14] Cassar L., Beeldens A., Pimpinelli N., Guerrini G.L. in International RILEM Symposium on Photocatalysis, Environment and Construction Materials, eds. L. Cassar and P. Baglioni, *RILEM*, Florence, **2007**, *1*, 131-145.

[15] Cucitore R., Cangiano S., Cassar L. High durability photocatalytic paving for reducing urban polluting agent. WO/2006/000565, **2006**.
[16] TX Actice Applications - pavements (Italcementi Group), http://www.italcementi.it/ITA/Prodotti+servizi+e+qualita/Prodotti+Fotocatalitici/Realizz azioni/Gallerie_Realizzazioni/Pavimentazioni.htm.
[17] Bianchi C.L., Gatto S., Pirola C.,.Naldoni A, Di Michele A., Cerrato G., Crocellà V., Capucci V. Photocatalytic degradation of acetone, acetaldehyde and toluene in gas-phase: comparison between nano and micro-sized TiO_2. *App. Catal. B: Environ*. **2014**, *146*, 123-130.
[18] Bianchi C.L., Pirola C., Selli E., Biella S. Photocatalytic NO_x abatement: the role of the material supporting the TiO_2 active layer. *J. Hazard. Mater*. **2012**, *211–212*, 203–207.
[19] Bianchi C.L., Gatto S., Pirola C., Scavini M., Vitali S., Capucci V. Micro-TiO_2 as a starting material for new photocatalytic tiles. *Cem. Concr. Comp*. **2013**, *36*, 116-120.
[20] C.L.Bianchi, S. Gatto, S. Nucci, G. Cerrato and V. Capucci, Self-cleaning measurements on tiles manufactured with micro-sized photoactive TiO_2. *Adv. Environ. Res.* **2013**, 2.
[21] Casasola R., Rincón J.M., Romero M. Glass-ceramic glazes for ceramic tiles: a review. *J. Mater. Sci*. **2012**, *47*, 553–582.
[22] Bianchi C.L., Pirola C., Gatto S., Nucci S., Minguzzi A., Cerrato G., Biella S., Capucci V. New surface properties in porcelain gres tiles with a look to human and environmental safety. *Adv. Mater. Sci. Engin*. **2012**, *2012*, 1-8.
[23] Drelich J., Chibowski E. Superhydrophilic and superwetting surfaces: definition and mechanisms of control. *Languir* **2010**, *26*, 18621–18623.
[24] Ren L., Li Y., Hou J., Zhao X., Pan C. Preparation and enhanced photocatalytic activity of TiO_2 nanocrystals with internal pores. *App. Mater. Interfaces* **2014**, *6*, 1608-1615.
[25] Yu J., Wang W., Chen B., Su B.-L. Enhancement of photocatalytic activity of mesoporous TiO_2 powders by hydrothermal surface fluorination treatment. *J. Phys. Chem. C* **2009**, *113*, 6743-6750.
[26] Zhang L., Yan F., Su M., Han G., Kang P. A study on the degradation of methamidophos in the presence of nano-TiO_2 catalyst doped with Re. *Russ. J. Organ. Chem.* **2009**, *54*, 1210-1216.
[27] Choi J., Park H., Hoffmann M.R. Effects of single metal-ion doping on the visible-light photoreactivity of TiO_2. *J. Phys. Chem. C* **2010**, *114*, 783-792.
[28] Gedanken A. Doping nanoparticles into polymers and ceramics using ultrasound radiation. *Ultras. Sonochem*. **2007**, *14*, 418-430.

[29] "ISO 22197-1—test method for air-purification performance of semiconducting photocatalytic materials. Part1: removal of nitric oxide," http://www.iso.org/iso/home.html.
[30] Gatto S., Sansotera M., Persico F., Gola M., Pirola C., Panzeri W., Navarrini W., Bianchi C.L. Surface fluorination on TiO_2 catalyst induced by photodegradation of perfluorooctanoic acid. *Cat. Today* **2014**.
[31] Bianchi C.L., Colombo E., Gatto S., Stucchi M., Cerrato G., Morandi S., Capucci V. Photocatalytic degradation of dyes in water with micro-sized TiO_2 as powder or coated on porcelain gres tiles. *J. Photochem. Photobiol. A: Chem.* **2014**, *280*, 27-31.
[32] Cappelletti G., Bianchi C.L., Ardizzone S. XPS study of the surfactant film adsorbed onto growing titania nanoparticles. *App. Surf. Sci*. **2006**, *253*, 519–524.
[33] Naldoni A., Bianchi C.L., Pirola C., Suslick K.S. Porous TiO_2 microspheres with tunable properties for photocatalytic air purification. *Ultrason. Sonochem*. **2013**, *20*, 445–451.
[34] Morterra C. An infrared spectroscopic study of anatase properties. 6. Surface hydration and strong Lewis acidity of pure and sulphate-doped preparations. *Faraday Trans. 1* **1988**, *84*, 1617–1637.
[35] Angelo J., Andrade L., Madeira L.M., Mendes A. An overview of photocatalysis phenomena applied to NO_x abatement. *J. Environ. Manage*. **2013**, *129*, 522–539.
[36] Diebold U. The surface science of titanium dioxide, *Surf. Sci. Rep*. **2003**, *48*, 53–229.
[37] Anderson C, Bard A. Improved photocatalytic activity and characterization of mixed TiO_2/SiO_2 and TiO_2/Al_2O_3 materials. *J. Phys. Chem. B* **1997**, *101*, 2611–2616.
[38] www.iso.org.
[39] Angelo J., Andrade L., Madeira L.M., Mendes A. An overview of photocatalysis phenomena applied to NO_x abatement. *J. Environ. Manage*. **2013**, *129*, 522–539.
[40] http://www.epa.gov/iaq/no2.html.
[41] Bianchi C.L., Cerrato G., Crocellà V., Gatto S., Pirola C., Stucchi M., Sansotera M., Capucci V. Photoactivity enhancement of commercial micro-sized TiO_2 induced by surface fluorinations. submitted to *ACS Journals* **2014**.
[42] Park H., Park Y., Kim W., Choi W. Surface modification of TiO_2 photocatalyst for environmental applications. *J. Photochem. Photiobiol. C: Photochem. Rev.* **2013**, *15*, 1-20.

Chapter 1

General introduction to photocatalysis

Air and water pollution is a major problem that modern societies are facing. Industrial and anthropogenic activities generate an enormous amount of organic and inorganic pollutants, which inevitably end up in our atmosphere, rivers, seas and soil. Photocatalysis provides the great advantage to be highly environmentally friendly in comparison to other techniques. To oxidize organics and inorganics, the only requirements, beyond the semiconductor photocatalyst, are water, oxygen and light with suitable energy to promote electron transitions in the band structure of the photocatalyst. In this section, the main features of advanced oxidation processes are described after the introduction to the current environmental problems.

1.1 The environmental pollution problem

In the last few decades, the technology has grown considerably becoming of capital importance for air pollution and other environmental problems. Pollution can be a result of human activity, of substances into the air, water or land, which may be harmful to the human health or to the quality of the environment. Human activities, which have bad environmental impact, include [1]:

- power generation (nuclear, hydroelectric, fossil fuel);
- industrial activities (paint and plastic manufacture, fertilizer);
- household refuse, fly ash, sewage, nuclear;
- agricultural practice;
- transportation (motor vehicle derived contamination);
- treatment and transport: e.g. through metal pipes and fitting.

Over the last decades, a large number of studies has investigated the possible adverse effects of ambient air pollution on birth outcomes. Conditions have changed; effective legislation has eliminated most of the air pollution of 50 years ago. 30 years ago, the era of successful abatement of traditional air pollution culminated in a review of the health effects of ambient particulates [2]. However, in the two decades since then, air pollution has re-emerged as a major environmental health issue. One reason is that, although air pollution from combustion of traditional fossil fuel is now present in much lower concentrations than 50 years ago, other components have gained prominence. Oxides of nitrogen produced by the rising number of motorized vehicles have increased until recently. Airborne particles have changed size distribution and composition, altering their toxicity.

Interest in health effects of air pollution became more intense after two US studies suggested that exposure to fine particulate matter in the air was associated with life shortening [3,4]. Both studies were based on observations from the late 1970s to late 1980s, when air pollution concentrations were much lower than the past. On the basis of these values, stringent standards for fine particulate matter have been proposed in the USA. WHO (World Health Organization) estimates that air pollution is responsible for over a million premature deaths worldwide every year [5]. Even brief exposure to air pollution have been associated with increases in cardiovascular mortality [6,7], particularly in susceptible populations. Heart failure is a public health issue that affects more than 23 million people worldwide [8], with an increasing prevalence in old people [9,10].

In 2005 the World Health Organization (WHO) updated the 2000 version [11] of Air Quality Guidelines (AQG) for particulate matter (PM), nitrogen dioxide (NO_2), sulfur dioxide (SO_2) and ozone (O_3) [12]. The WHO AQG are based on a comprehensive review of the evidence on the relationships between air quality and adverse health effects including cardiopulmonary diseases [13,14], cerebrovascular diseases [15,16], cancers [17,18], diabetes [19,20], and adverse birth outcomes [21,22]. They provide guidance to support actions to achieve clean air, which is a basic requirement of human health and well-being and indicate the minimum levels of air quality control needed for the protection of public health. Although the WHO clearly states that the guidelines are neither standards nor legally binding criteria, by 2012, 466 out of 199 cities had complied with the annual AQG for PM_{10} [23]. Short-term AQG were defined as mass concentrations with average times of 1 h (NO_2), 8 h (O_3) and 24 h (PM and

SO_2) based on evidence for the lowest pollutant level associated with observable adverse effects during temporary exposure. At present, the WHO has specified annual AQG for PM and NO_2 only but not for SO_2 and O_3 due to inadequate evidence for chronic health outcomes and data on the properties of air pollutants in different meteorological and emission profiles. It has been conducted a detailed study on the relationships between WHO short-term and annual AQG for particulates (PM_{10} and $PM_{2.5}$) and nitrogen dioxide (NO_2) [24]. It has appeared that there is a deterministic relationship in the current WHO short-term and in annual AQG for PM_{10} and $PM_{2.5}$. They are respectively, in fact 50 $\mu g/m^3$ and 25 $\mu g/m^3$ for the first and 20 $\mu g/m^3$ and 10 $\mu g/m^3$ for the latter one. However, based on this analysis, the short-term AQG of 200 $\mu g/m^3$ for NO_2 cannot provide a regulatory guideline consistent with the annual AQG of 40 $\mu g/m^3$. Based on evidence of adverse health effects of exposure to low levels of NO_2 in adults and infants, WHO has been aware of the need to lower the current annual AQG below 40 µg/ms for NO_2 [25]. There is a considerable temporal as well as spatial variability in nitrogen dioxide levels in the outdoor environment. Outdoor urban levels have an annual mean ranging from 20 to 90 $\mu g/m^3$ and an hourly maximum ranging from 75 to 1015 $\mu g/m^3$. Levels indoors where there are unvented gas combustion appliances may average more than 200 $\mu g/m^3$ over a period of several days. Evidences from animal toxicological studies indicates that long-term exposure to nitrogen dioxide at concentrations above current ambient concentrations has adverse effects. NO_2 has been associated with adverse health effects even when the annual average nitrogen dioxide concentration complied with WHO annual guideline value of 40 $\mu g/m^3$. Many short-term experimental human

toxicological studies show acute health effects at levels higher than 400 µg/m^3, and one meta-analysis has indicated effects at levels exceeding 200 µg/m^3 (**Fig. 1.1**).

Limit values (Annex XI and XII to the European Directive 2008/50/CE)	
Annual limit value (NO_2)	**40 µg/m^3** *equal to* **21,27 ppb**
Hourly limit value (NO_2) (not to be exceeded m ore than 18 times in any calendar year)	**200 µg/m^3** *equal to* **106,36 ppb**
Annual critical level for the (NO_x) protection of vegetation and natural ecosystems	**30 µg/m^3** *equal to* **15,95 ppb**
Alert threshold (NO_2)	**400 µg/m^3** *equal to* **212,72 ppb**

Fig. 1.1. Limit values of NO_2 emissions. Source: EU directive 2008/50/CE.

1.2 Advanced Oxidation Processes (AOPs)

Different solutions for depollution have already been proposed: air scrubbing, adsorption, activated carbon, etc., but some of them only remove the pollutant from one phase to another one and then require additional processes to eliminate toxic compounds [17]. Other conventional techniques including biological, thermal, and physicochemical treatments have been used to remove the aqueous pollutants. Although biological method is widely applied for the treatment of residual wastewaters, it requires long times to a complete depollution and is not suitable to treat the toxic contaminants. In addition, incineration requires an extremely high energy

and gives high emission of other hazardous compounds like dioxin and furan [26]. As a response, the development of newer eco-friendly methods or removal became an imperative task. Even ozonolysis have their own problems and limitations, like the loss of residual effect [27] and generation of chemical compounds that are highly carcinogenic. In the same way, thermally catalytic oxidation requires high temperatures of 200-1200°C for efficient operation and hence expensive. Furthermore, thermally oxidation is not economically feasible, especially at low pollutant concentrations. As a response, the development of newer eco-friendly removal methods became an imperative task.

A valuable alternative might be Advanced Oxidation Processes (AOPs); a highly competitive treatment technology, based on chemical oxidation, for the removal of organic persistent pollutants in both gas and water phase [28]. These processes degrade organic pollutants by forming hydroxyl radicals [28-30.], which are highly reactive and non-selective as reported in some works [31-35].

Thus, the history of photocatalysis is commonly accepted to start with the use of photocatalytic materials for the treatment of contaminated or polluted air or combustion gases. Intensive studies in heterogeneous photocatalysis started three decades ago, after the discovery of the photo-induced splitting of water on TiO_2 electrodes [36,37]. In particular, AOPs rely on generation of highly reactive radical species, mainly $OH^{\cdot}$ by using solar, chemical or other form of energy [38]. A great attention has been especially paid to the reactions that take place on the illuminated surface of semiconductor metal oxides and sulfides, *i.e.*, TiO_2, ZnO, WO_3, CdS, etc. These compounds are semiconductors with a moderate energy band-gap (1-

3 eV) between their valence and conduction bands. Photocatalysis by semiconductor is the result of the interaction of electrons and holes generated in an activated solid with the surrounding medium. Activation is the consequence of light adsorption; thus, electron-hole pairs are formed in the solid particle that can recombine or participate in reductive and oxidative reactions that lead to the decomposition of contaminants. Absorption of a photon by semiconducting solids excites an electron (e^-) from the valence band to the conduction band; if the photon energy, $h\upsilon$, equals or exceeds the band gap of the photocatalyst (band-gap energies of common semiconductors are reported in **Table 1.1**), simultaneously, an electron vacancy or a positive charge, a hole (h^+), is also generated in the valence band (**Fig. 1.2**).

Table 1.1. Band-gap energies for some common semiconductor materials at 0 K [39-41].

Semiconductors	Band-gap energy (eV)	Semiconductors	Band-gap energy (eV)
Diamond	5.4	WO_3	2.76
CdS	2.42	Si	1.17
ZnS	3.6	Ge	0.744
ZnO	3.436	Fe_2O_3	2.3
TiO_2	3.03	PbS	0.286
CdS	2.585	PbSe	0.165
SnO_2	3.54	ZrO_2	3.87
CdSe	1.7	Cu_2O	2.172

Thus, illuminated semiconductor particles completely decompose a variety of organic or inorganic compounds that are known as environmental pollutants.

The key advantages of this technology are summarized in **Table 1.2**, as reported by Kabra et al. [39].

To sum up, in a photocatalytic process a semiconductor is commonly used. Semiconductors are nontoxic, chemically stable, available at reasonable cost, and capable of repeated use without substantial loss of catalytic ability. Furthermore, such reactions are attractive because they do not require high temperature operational conditions and they can be very selective in radiation adsorption. Photocatalytic oxidation is promising technology for air purification because the pollutants can be oxidized to H_2O and CO_2.

Table 1.2. Key advantages of AOPs application [39].

ADVANTAGES OF PHOTOCATALYSIS	Renewable and pollution-free energy
	Harmless products formation
	Application to aqueous- and gaseous-phase treatments
	Mild conditions
	Minimal second waste generation

1.3 TiO_2 semiconductor: an historical background

A great attention, in the last years, it has been paid toward titanium dioxide (TiO_2) semiconductor. Main studies were focused on the utilization of solar energy for the production of hydrogen as a clean fuel from water [40,41]. Even if the first report of some photoreactivity involving these compounds appeared in 1921 [42], it was only in 1972, with the work of Fujishima and Honda that the photocatalytic splitting of water on TiO_2 was discovered [43].

Almost at the same time, also several papers published by Ollis confirmed that a similar approach could be used for degrading organic compounds present in water or air stream [44]. From that moment on, practical applications of TiO_2 photocatalysts have been implemented in both indoor and outdoor environments [45,46]. Thereafter, various researchers [47-49] conducted studies involved to understanding the fundamental processes occurring in photocatalysis and enhancing efficiency of the process adopting TiO_2. There are many reasons for this great interest: TiO_2 has a sufficiently positive valence band edge to oxidize water to oxygen. It is also an extremely stable material even in the presence of aqueous electrolyte solutions, much more so than other types of semiconductor that have been tried. The possibility of solar semiconductor photoelectrolysis was also demonstrated for the first time in 1969, with the system connected to a platinum black counter electrode through an electrical load, exposed to near-UV light [50]. Then, this electrochemical photolysis of water was reported in Nature by analogy with a natural photosynthesis in 1972 [43]. Meantime, crude oil prices ballooned suddenly, and the future lack of crude oil was a serious concern. Thus, the use of TiO_2 has attracted the attention not only of electrochemistry, but also of many scientists in a broad area, and numerous studies were conducted.

1.3.1 Physico-chemical properties

Among different semiconductor photocatalysts, TiO_2 appears as the most active and most suitable one for a wide variety of energy and

environmental applications. TiO_2 has a high oxidation ability, its photo-generated holes being at E_0 = 2.9 V *vs.* NHE (Normal Hydrogen Electrode) at pH 0 [37]; moreover, it is biologically and chemically inert, photostable and cheap. Finally, the location of the bottom of conduction band is suitable for using this material for the photocatalytic production of hydrogen from water, which has received extensive attention in the last decade for its potential application in the field of solar energy harvesting, conversion and storage [40]. After choosing TiO_2 as semiconductor in photocatalytic experiments, the choice of its crystalline form is important as well. Significant progress has been made on investigating the photocatalytic activity of TiO_2 based on its crystal structure and size [51]. The primary physical properties that affect the utility of TiO_2 for industrial applications and use in consumer products include density, melting point, and refractive index.

The crystalline forms of TiO_2 are anatase (tetragonal), rutile (tetragonal) and brookite (orthorhombic).

Brookite is a natural phase, which is quite difficult to synthesize in a laboratory. It is also rare in nature and structurally more complex than the other two polymorphs. It is constituted by an elementary cell containing 8 formula units with an orthorhombic symmetry. The Ti surrounding coordination polyhedron is an octahedron and there is a high oxygen atom packing. It forms very flat small tubular crystals with a variable color, from yellow to brown reddish. This polymorph is metastable: out of a restricted pressure and temperature interval, it is converted into the two other phases (**Fig. 1.3**).

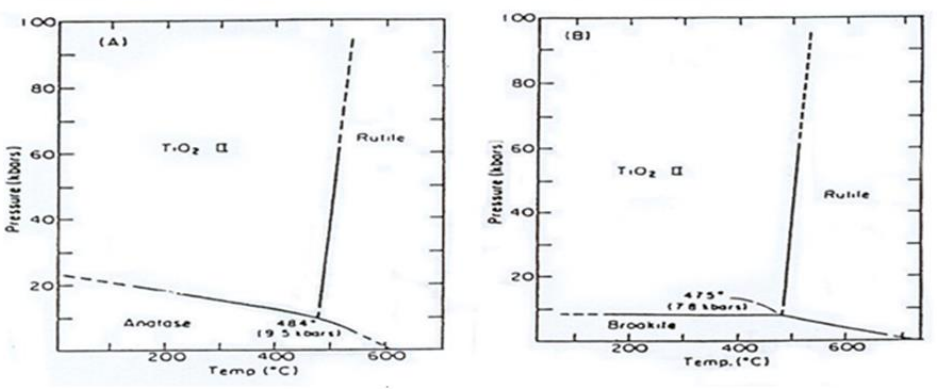

Fig. 1.3. Phase diagrams of TiO_2 at low and high pressures [52].

Anatase and rutile have been the most studied phases of nanostructured TiO_2, while reports on brookite are still scarce [53,54].

The theoretical density of TiO_2 ranges from 3895 kg/m^3 for anatase to 4250 kg/m^3 for rutile [55]. The melting point of rutile ranges from 1830°C to 1850°C. Anatase transition to rutile occurs upon heating before reaching the melting point. This phase change occurs across a broad temperature range of about 500°C to 900°C, depending on the sample. Specifics such as crystallite diameter, weight fraction (if in a mixture), and heat intensity affect the onset and kinetics of the phase transition. The refractive indexes of rutile and anatase are approximately 2.75 and 2.54, respectively.

Rutile is the most common mineral form of TiO_2 in nature. The rutile structure (**Fig. 1.4**) is not compact. Its unit cell is tetragonal: one axis is 30% shorter of than the other two. The structure is a distorted octahedral TiO_6, with oxygen ions shared with other adjacent Ti ions at the edges of an equilateral triangle. It can be envisaged as a central body cubic lattice of Ti

ions that is considerably distorted. The crystallites can be present in nature as black or reddish and also transparent without impurities.

Anatase, also improperly called octahedrite, presents a tetragonal bipyramidal symmetry (**Fig. 1.4**), with a form similar to an elongated octahedron. The structure is based on a polyhedral chain of TiO_6. The difference with rutile is that anatase presents a more distorted structure, where every polyhedron shares 4 units, instead of 2. The anatase crystals are really small, the natural color ranges from blue to yellow-brown [56]. These differences in lattice structures cause diverse mass densities and electronic band structures for the two main TiO_2 polymorphs. In particular, titanium dioxide is characterized by an allowed and indirect band gap, which is equal to 3.2 and 3.0 eV, respectively, for the anatase and rutile phase.

The position of oxygen ions on the exposed crystal surface of anatase shows a triangular arrangement, allowing effective absorption of organics. However, this favorable structure arrangement is not available for rutile structure.

This is one of the reasons why anatase has higher photocatalytic activity than rutile [57]. Furthermore, the anatase polymorph is generally reported to show a highest photoactivity because of the low recombination rate of its photogenerated electrons and holes. Even though anatase is believed to be the most active form of titania, reports suggest that a pure anatase sample would not necessary lead to the best photocatalytic performance [58,59]. The presence of rutile phase introduces mesoporosity and a wider pore size distribution.

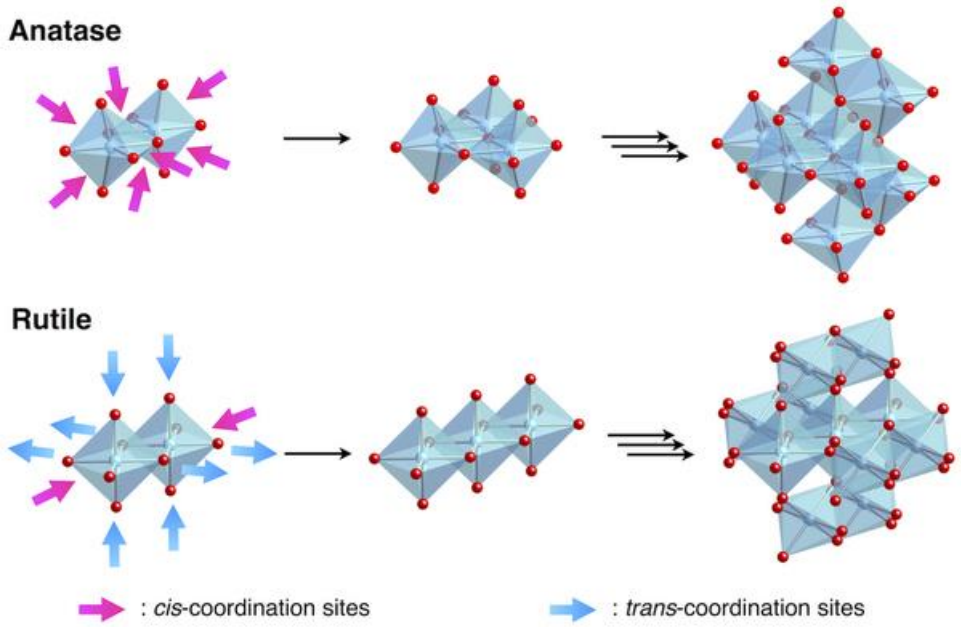

Fig. 1.4. Bulk crystal structure of rutile and anatase.

These factors may be responsible for the increased catalytic activity. A mixture of anatase and rutile would be the best combination to achieve maximum photocatalytic efficiency. Several commercial samples of TiO_2 varying in particle size and purity, were studied to determine catalytic activity by using the TiO_2 catalyst Degussa P25 grade (mixture of 70% anatase, 30% rutile). It has been proved in many works that P25 TiO_2 gives a good degradation efficiency, sometimes better than to other forms [60].

Even the effect of the particle size influences the photocatalytic activity of TiO_2. Several authors report a peak efficiency, for the given reaction, in correspondence of an optimal particle size. A few examples are mentioned in the following. In the photocatalytic degradation of trichloroethylene in the gas phase with particles (in the 2.3-27 nm range), Maira et al. [61] found an optimum particle size of 7 nm. Also, in the oxidation of

trichloromethane, Zhang et al. [62] reported the best efficiency for an anatase size of 11 nm. On the contrary, Almquist and Biswas [63], in the photodegradation of phenol, instead report a much larger optimal particle size in the 25-40 nm range. Furthermore, other authors report a continuous increase in the photocatalytic activity with lowering of the particle size. For example, Anpo et al. [64] in the hydrogenation of CH_3COH report an increase in conversion when the particle size of anatase TiO_2 decreased from 11 to 3.8 nm. The recent results by Lin et al. [65] are relevant to this debate: the band gap of anatase TiO_2 was observed to decrease monotically from 3.239 to 3.173 eV when the particle size decreased from 29 to 17 nm and then to increase from 3.173 to 3.289 eV as the particle size decreased from 17 to 3.8 nm, in agreement with the red and blue shifts of the band gap reported by other researchers.

1.3.2 TiO_2 as photocatalyst

The semiconductor TiO_2 has been widely utilized for inducing a series of reductive and oxidative reactions on its surface. When photon energy ($h\upsilon$) of greater than or equal to the band-gap energy of TiO_2 is illuminated onto its surface (3.2 eV for anatase and 3.0 eV for rutile), the electron will be photoexcited to the empty conduction band. **Fig. 1.5** concerns the mechanism of the electron-hole pair formation when the TiO_2 particle is irradiated with adequate $h\upsilon$. The light wavelength for such photon energy usually corresponds to $\lambda < 400$nm. The photonic excitation leaves behind an empty unfilled valence band, and thus creates the electron-hole pair ($e^- - h^+$).

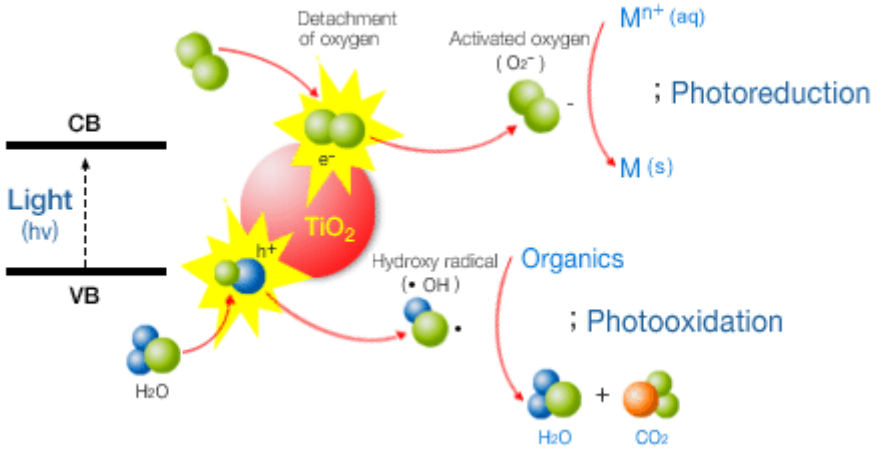

Fig. 1.5. TiO_2 sensitised photoreactions of both reduction and oxidation.

The following chain reactions have been widely postulated.

Photoexcitation: $TiO_2/SC + h\upsilon \rightarrow e^- + h^+$ **(2.1)**

Oxygen ionosorption: $(O_2)_{ads} + e^- \rightarrow O_2^{\cdot -}$ **(2.2)**

Oxidation of hydroxyls: $OH^- + h^+ \rightarrow OH^{\cdot}$ **(2.3)**

Photodegradation by $OH^{\cdot}$: $R\text{-}H + OH^{\cdot} \rightarrow R^{\cdot} + H_2O$ **(2.4)**

Ionization of water: $H_2O \rightarrow OH^- + H^+$ **(2.5)**

Direct photoholes: $R + h^+ \rightarrow R^{+\cdot} \rightarrow$ interm.(s)/Final degradat. Products **(2.6)**

Protonation of superoxides: $O_2^{\cdot -} + H^+ \rightarrow HOO^{\cdot}$ **(2.7)**

The hydroperoxyl radical formed (2.7) also has scavenging property as O_2 thus doubly prolonging the lifetime of photohole:

$HOO^{\cdot} + e^- \rightarrow HO_2^-$ **(2.8)**

$HOO^- + H^+ \rightarrow H_2O_2$ **(2.9)**

Both the oxidation and reduction can take place at the surface of the photoexcited semiconductor photocatalyst (**Fig. 1.5**). Recombination

between electron and hole occurs until oxygen is available to give the electrons to form superoxides ($O_2^{\cdot -}$), its protonated form the hydroperoxyl radical (HO_2^-) and subsequently H_2O_2. Thus, the presence of electron scavengers is vital for prolonging the recombination and successful functioning of photocatalysis. Eq. (2.2) reports how the presence of oxygen prevent the recombination of electron-hole pair, while allowing the formation of superoxide radicals ($O_2^{\cdot -}$). This $O_2^{\cdot -}$ radical can be protonated to form the hydroperoxyl radical (HO_2^-) and subsequently H_2O_2 as shown in Eqs (2.7) and (2.8), respectively. However, it should be noted that all these expressions in photocatalysis were attributed to the presence of both oxygen and water molecules. Without the presence of water molecules, the highly reactive radicals (OH) could not be formed and this would prevent the photodegradation of organic chemical compounds.

1.3.3 Thermodynamics and kinetics in TiO_2 photocatalyst

As already reported in the last paragraph, the first step of every semiconductor sensitized photoreactions is the photoactivation of the semiconductor photocatalyst through optical excitations. When the optical transition occurs, valence band positive holes and conductance band free electrons are generated in the TiO_2 band structure. From a great number of experimental studies [66-68], it is known that rarely organics and inorganics react directly with positive holes and free electrons, but the oxidation reactions, that undergo on photoactivated TiO_2 surfaces, are mainly driven by highly oxidative species like hydroxyl radicals, $^{\cdot}OH$, superoxydes, $O_2^{\cdot -}$,

peroxides, HO_2^-, etc., all generated by initial interaction of oxygen with conductance band electrons and water and/or surface OH groups with valence band positive holes.

Even though the kind of reaction and relative species involved, a general photocatalytic mechanism can be represented as the following:

$$A + D \xrightarrow{h\upsilon,\ semicond.} A^- + D^+ \qquad \textbf{(2.10)}$$

where hυ, the energy of the incident light, must be equal or higher than the semiconductor band gap. To catalyze reactions, the redox potential of valence band holes must be higher than the half/cell D^+/D and the redox potential of the conductance band electrons lower than A/A^-.

Photocatalytic oxidation of organics and inorganics proceeds through initial interactions of oxygen and water with the photogenerated charge carriers in the band structure of the TiO_2 forming oxygen-based species which oxidise the pollutant molecule. However, it could happen that the photogenerated electron-hole pairs recombine re-establishing the initial ground state. According to Hoffmann et al. [69], the following general mechanism for heterogeneous photocatalysis on TiO_2 is characterized by different times for each step (**Table 1.3**).

The kinetics of the whole photocatalytic processes can be described and studied according to a *Langmuir-Hinshelwood* (L-H) approach. For the generic reaction Equation 1, the rate of reaction is derived through Eq. 2.11:

$$r = k_{overall} \frac{K_A K_D C_A C_D}{(1 + K_A C_A + K_D C_D)} \qquad \textbf{(2.11)}$$

where r is the reaction rate, $k_{overall}$ an overall rate kinetic constant, K_A and K_D the Langmuir adsorption constants for the reactants A and D and C_A and C_D the concentrations of the same reactants.

The L-H kinetics implies that both the reactants are first adsorbed on the TiO_2 surface and subsequently react generating the products that eventually desorb from the surface. Furthermore, the model assumes fast adsorption/desorption equilibrium steps and a slow surface step [70].

Table 1.3. Primary processes and associated characteristics times domains in the TiO_2-sensitizied photoreactions.

Primary Process	***Characteristic Time***
Charge carrier generation	
$TiO_2 + h\nu \rightarrow h^+ + e^-$	fs (very fast)
Charge carrier trapping	
$h^+ + Ti^{IV}OH \rightarrow \{ Ti^{IV}OH^{\cdot} \}^+10$	ns (fast)
$e^- + Ti^{IV}OH \leftrightarrow \{ Ti^{III}OH \}1$	ps (dynamic equilibrium)
$e^- + Ti^{IV} \rightarrow Ti^{III}10$	ns (deep trap)
Charge carrier recombination	
$e^- + \{ Ti^{IV}OH^{\cdot} \}^+ \rightarrow Ti^{IV}OH100$	ns (slow)
$h^+ + \{ Ti^{III}OH \} \rightarrow Ti^{IV}OH10$	ns (fast)
Interfacial charge carrier	
$\{ Ti^{IV}OH^{\cdot} \}^+ + org \rightarrow Ti^{IV}OH + ox\ org100$	ns (slow)
$\{ Ti^{III}OH \} + O_2 \rightarrow Ti^{IV}OH + O_2^{\cdot -}$	ms (very slow)

1.4 Depollution effects with TiO_2 photocatalyst

The World Health Organization recently estimated that 2.4 million people worldwide die annually from causes directly attributed to air pollution, as just mentioned above (WHO, 2012). Weighing in closer to home, the American Lung Association, in its prominent 2011 "State of the Air" study, found that more than 154 million people (over half the nation) still suffer pollution levels that are often dangerous to breathe [71]. The American Lung Association cites numerous health concerns and conditions caused by smog. They include premature births, infant deaths, chronic obstructive pulmonary disease, allergies, asthma, reduced lung function, premature death, lung cancer, heart disease, and heart attacks.

Photocatalytic processes are widely recognized and used as valid solutions for environmental problems [72]. Previous photocatalysis studies have mainly focused on the photodegradation mechanism, catalyst deactivation and catalyst preparation [73-75]. For example, the harmful NO_x gases are oxidized to nitrates by using UV irradiation, which activate TiO_2 semiconductor to remove NO_x from the air. These types of materials have gained increased attention, given the wide range of possible applications. TiO_2 photocatalysts can be used in roadway structures, as outer material on buildings, having the capacity to "clean" the air along the roadway that are polluted by automobile exhaust gases, using only the solar energy [76,77]. So, in recent years titanium dioxide has been used as a catalyst for the UV induced photocatalysis of organic chemical compounds.

1.4.1 Indoor air pollution

Indoor air pollution is a major risk factor, accounting for about 4% of the global burden of disease [78]. It is caused by the use of low-cost, widely available traditional energy sources such as coal and bio-mass (wood, dung, crop residues) for cooking and home heating. Bio-mass is still the main source of energy for 60 to 90% of households in developing countries, about 3.5 billion people.

In the last century, dramatic episodes of excess mortality caused by ambient air pollution established that atmospheric contamination by human activities could adversely affect health. In many countries, governmental regulations implemented in response to the adverse health effects of air pollution have resulted in strong trends towards improved air quality. Research directed at indoor air pollution began in the late 1960s and early 1970s [79,80]. Investigations in this area were stimulated and developed up to now, where a large body of literature is available on diverse aspects of indoor air pollution: sources, concentrations, health effects and policy.

Indoor air pollutants mainly include nitrogen oxides, volatile organic compounds (VOCs) and particulates. Numerous sources of airborne contaminants have been identified in indoor environments: in home, office and transportation environments. Unvented combustion, evaporations of solvents and abrasion can produce gaseous and particulate pollution indoors. Biological sources include fungi, bacteria, insects. Even household products such as detergents, disinfectants, paints, perfumes and cosmetics released in the indoor atmosphere during normal usage and storage, represent pollution source. Active photocatalytic surfaces can help to reduce the proliferation of moisture-induced mold colonies, bacteria and fungi thanks to the oxidative

power of the photocatalyst once irradiated with light of sufficient energy [81-83].

1.4.2 Outdoor air pollution

Outdoor air pollution is a mixture of multiple pollutants generating from both natural and anthropogenic sources. Transport, power generation, industrial activity, biomass burning and domestic heating are the main anthropogenic sources [84]. In October, 2013, 24 experts from 11 countries met at the International Agency fro Research on Cancer (IARC), Lyon, France, to assess the carcinogenicity of outdoor air pollution. This assessment was the last in a series that began with specific combustion products and sources of air pollution and concluded with the complex mixture that contains all of them [85]. Studies in series, conducted for a long time, period have found that the mix of pollutants in outdoor air varies substantially over space and time, showing not only the diversity of sources, but the effect of atmospheric processes, including oxidation and weather [86,87]. Outdoor pollutants with health effects include particulate matter (PM_{10} and $PM_{2.5}$), nitrogen dioxide (NO_2), sulfure dioxide (SO_2) and ozone (O_3) [88]. For 2005, nationwide estimated traffic emissions attributable to time spent in traffic congestion include approximately 1.2 million tons of NO_x, 34,000 tons of SO_2, and 23,000 tons of $PM_{2.5}$. The relative proportion of the impact attributable to different pollutants varies significantly across urban areas. Examining time trends in mortality risk attributable to congestion (**Fig 1.6**), there is a steady decline from 2000 until 2020, with an

estimated 4,000 premature deaths in 2000 and an estimated 1,600 premature deaths in 2020 [89].

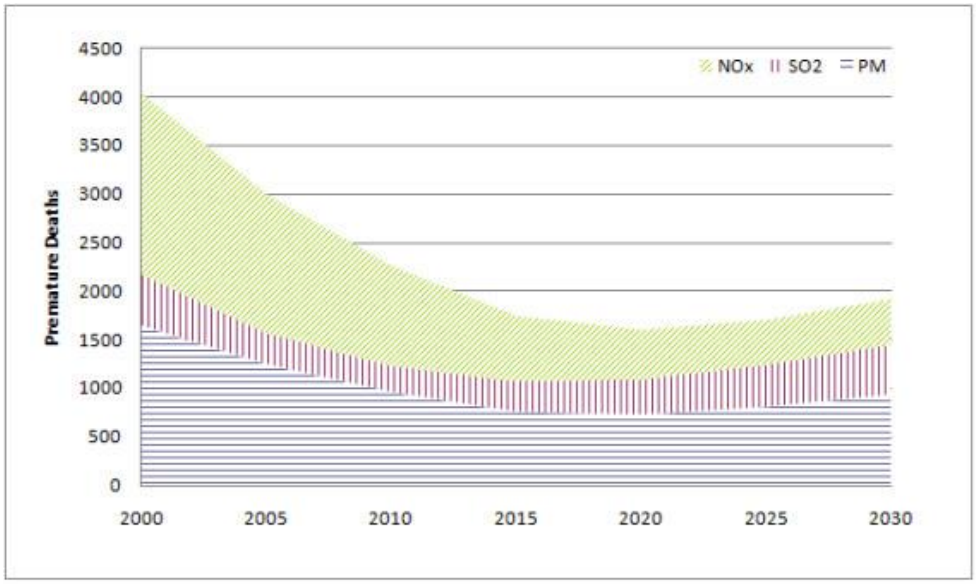

Fig. 1.6. Time trends related to emitted pollutants attributable to traffic congestion nationwide.

In particular, nitrogen oxides (NO_x) play a key role in the atmospheric reactions that create ground-level ozone and acid rain. These chemical pollutants can be effectively removed by photocatalytic oxidation on titanium dioxide [90]. NO_x is a term used in atmospheric chemistry to indicate the sum of NO and NO_2. NO originates directly from sources such as high temperature combustion in transport and industry [91-93]. NO_2 is formed in the atmosphere by reaction between NO and O_3 or molecular oxygen (even though the reaction with the latter is kinetically slow) assisted by sunlight [94-96]. Further reactions in the atmosphere can transform NO and NO_2 into nitric acid, HNO_3, peroxyacyl nitrates (PANs), $RC(O)OONO_2$, peroxynitric acid, HNO_4, etc... The sum of all these species and NO_x is

known as NO_y, *reactive nitrogen compounds*. NO_x are mainly responsible for *photochemical smog* [97] (a mixture of hazardous chemicals derived from the interaction of sunlight with atmospheric pollutants, **Fig. 1.7**). Direct exposure, or to acid vapours arising from their interaction with atmospheric moisture, can cause emphysemas and bronchitis in humans [97,98].

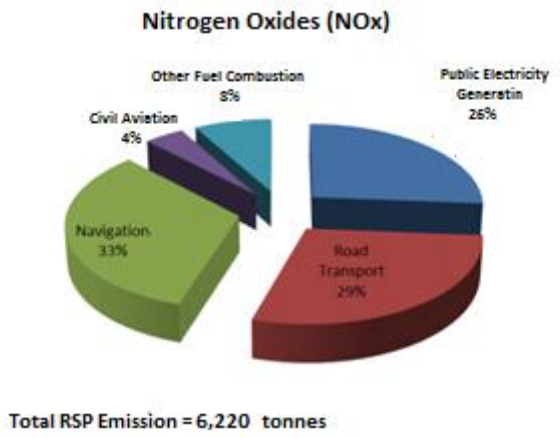

Fig. 1.7. The major emitters of NO_x. Source: EPA – The Government of the Hong Kong, Special Administrative Region, March 2013.

The control and remediation of atmospheric NO_x has been largely investigated. In particular, photocatalytic oxidation using TiO_2 as semiconductor photocatalyst has become an optimal alternative, as confirmed by the growing number of increasing research reports [99-104]. The general mechanism for NO_x degradation by photocatalysis implies the oxidation of the nitric monoxide to nitric or to nitrous acid induced by oxygen species produced at the TiO_2 surface [105]. The reaction path for NO_x conversion is similarly mediated by OH radicals:

$$NO_2 + OH^{\cdot} \rightarrow HNO_3$$

$$NO + OH^{\cdot} \rightarrow HNO_2$$

According to Ardizzone et al. [106], the best activity for NO_x degradation is shown by the catalysts displaying the highest OH/O_{tot} surface ratios. An efficient adsorption of the pollutant molecule at the semiconductor surface may promote the photocatalytic reaction. The adsorption of NO at oxide surface, in the presence of oxygen, implies the formation of both surface bridged nitrates and bidentate nitrates. So, a large OH population can be expected to promote the molecule adsorption.

1.4.3 Wastewater effluent

The reuse and recycling of wastewater effluent is rapidly growing and becoming a necessity for water utilities in the world to augment our limited fresh water supply, which is currently under pressure due to rapid population growth [106-108]. "Dyes" are generally defined as compounds that undergo chemical interaction with the substrate to be dyed. They are usually dissolved or dispersed in a solvent, and the substrate is treated in this solution. “Pigments" do not form chemical bonds with the substrate; in order to adhere to the surface of a substrate they have to be mixed with an adhesive. "Colorant" is a term used for both dyes and pigments [109]. Men have made use of dyes since prehistoric times, for example in decorating their bodies and in coloring the furs and skins that they wore. This clearly shows that dyes had and still have a profound anthropological, esthetic, functional and economic impact on society. The demand and the usage for

dyes have continuously increased in many industries such as textile, paper, plastics and cosmetics. The textile industry includes a wide range of activities, from preparation of raw material to pre-treatment, dyeing and finishing of textile material. All these activities consume water and energy, and are highly polluting. The presence of dyes in water, even in trace quantities, is highly undesirable as it reduces the light penetration into water thereby decreasing the efficiency of photosynthesis in aquatic plants and resulting in impairment on their growth. Thus, the ecosystem of streams can be seriously affected. Consequently, water contamination originated from the dyeing and finishing in textile industry has become a major concern [110]. Also, phenols, others polluting contaminants, are continuously introduced into the aquatic environment through various anthropogenic inputs [111].

Since the early 1900, the most of dyes started to employ even in the alimentary industry [112]. Most of synthetic dyes are azo-dyes and are suspected to be carcinogenic [113]. Since 1908, amaranth (E123) had been used as a food dye. However, in 1970, Russian studies [114] showed that amaranth was carcinogen. In 1977, Italian legislation (DM 21/03/77, G.U., No. 92, 05/04/77, p. 2355) banned its use in most food and beverages: the dye could only be used in caviar. On the other hand, this dye was still allowed in other European countries. In 1994, the European community decided to unify the legislation about food dyes (DIR No. 94/36/CEE, 30/06/94, G.U.C.R. L-237, 10/09/94, p. 13). The release of colored wastewaters in the ecosystem is a dramatic source of esthetic pollution, eutrophication, and perturbations in aquatic life. Environmental problems related to the textile industry are numerous and well documented. Despite

the high volume of waste and its high organic load, the main problem of textile industry effluents is related to the colour generated by unfixed dyes during textile processing and directly released to the effluent.

Colour is the first contaminant to be recognized in wastewater. The presence of very small amounts of dyes in water (less than 1 ppm for some dyes) is highly visible and affects not only the aesthetic aspect and water transparency, but also the absorption and reflection of sunlight. All dyes used in the textile industry are synthesized to be chemically and photolytically stable, i. e., to resist to light exposure, water, various chemicals, including oxidizing agents, and microbial attack. According to Suteu [115], the removal of dyes from industrial effluents, before the discharged into water systems, is strictly required. In fact, the dye fixation on the fibers during the dyeing process is not total, leading to the dye release into wastewater. However, the remediation process of wastewaters polluted by dyes is not easy, since the complex structure, the synthetic origin and the recalcitrant nature of dyes, make their bleaching very difficult. It is developing a massive search of more effective treatment methods for the removal of dyes from wastewaters in order to meet the established limits.

In 2006 the EU Regulation 1907/2006, commonly known as REACH, was introduced and this regulation is mandatory for all EU countries. The REACH regulation included all the existing EU Directives on chemicals, so this means the EU Directives regulating azo colorants (2004/21/EC, 2003/3/EC and 2002/61/EC) are automatically included in the REACH regulation. The EU Directive 2004/21/EC established harmonized testing methods within the EU. For leather the official European analytical method is EN ISO 17234-1 : 2010 (an up-dated version of the CEN ISO/TS 17234 :

2003). Furthermore, several countries introduced a specific brand to certain chemical compounds, in order to mark products with less environmental impact. In Europe this Community Mark is named ECOLABEL, recognizable with a peculiar sign. Criteria to recognize the Community Mark have been established by Commission 1999/178/CE, modified in 2002. Thus, it is very fundamental, both for the industries and consumers the development of new procedures for reducing or eliminating the emission of harmful chemical compounds in the environment.

Photocatalytic oxidation method appears to be a promising route for the treatment of wastewater contaminated with phenols and dyes [116-120]. However, also for this method many drawbacks are reported; first of all the catalysts (TiO_2 especially) are characterized by a low quantum efficiency due to inefficient visible light harvesting [121]. Further the design of photoreactor can be very complex and expensive [122] and the recovery and reuse of titanium dioxide sometimes is impossible [123]. Lastly also the generation of toxic intermediates in the case of a not-complete degradation of the pollutants [124], as well the catalyst deactivation [125-127], have to be considered as major drawbacks. The correct photocatalytic degradation of pollutants like pesticides, phenols, and dyes is largely dependent on their concentration inside the solution, together with the solution pH and ionic composition. Moreover, the types of catalysts, their loading and the light intensity are critical parameters [128,129]. Therefore, understanding the impacts of the various process parameters that govern the photocatalytic degradation efficiency is of fundamental importance.

1.5 Role of particle size in TiO_2 photocatalyst

Particle size is an important parameter in general for catalysis since it directly affects the specific surface area of the catalyst. Reduction in particle size leads to larger surface area, which increases the available surface active sites, favoring the surface charge carrier transfer. However, as previously reported by Zhang et al. [130], the photocatalytic efficiency does not monotonically increase with the decreasing of particles size, because of the increased surface electron/hole (e^-/h^+) recombination rate. To increase the quantum yield of photocatalysts, the e^-/h^+ recombination rate has to be reduced. As a consequence, is necessary to perform a systematic study of the particles size effect on the photodegradative activity of the catalysts.

1.5.1 Recent studies on nanoparticles effects

Nanotechnology is expanding rapidly and will affect many aspects of everyday life. For example, nanoparticles have been successfully used for sporting equipment fabrication and for cosmetics and electronics production [131-135]. It was estimated that there are at least 1,300 commercially available products containing nanomaterials [136] and it is anticipated that commercialization of nanomaterials will grow into a $1 trillion per year by 2015 [137]. With the rapid growth of nanotechnology and future bulk manufacture of nanomaterials comes the need to determine, understand and counteract any adverse health effects of these materials that may occur during manufacture, during use, or accidentally. Nanoparticles come from many different sources: they are found naturally in the environment (forest

fires, volcanoes), are produced as byproducts of industrial or combustion processes (engines, power plants, incinerators), and are potentially made for various industrial or consumer product applications (pigments, chemical catalysis).

The concept of "nanotechnology" is derived, in part, from the Greek word "nano", meaning "dwarf". From a materials science point of view, the generation of new products using engineered nanomaterials is stimulating because as one moves down the nanoscale, i.e. reducing the particle size range below 100 nm, the properties are known to change and implementation of them can provide products with enhanced applications [138]. Nanoparticles (sometimes referred to as ultrafine particles) generally have been defined as particle-types in the size range < 100 nanometers, in at least one dimension. A nanometer (nm) is roughly the width of 10 hydrogen atoms [139]. The term of "ultrafine" and "nano" have frequently been used interchangeably, with the latter being viewed as a more contemporary nomenclature. This has led to some confusion, as some investigators have referred to the term "ultrafine" to particles generated via combustion sources, while engineered nanoparticles-types are often intentionally manufactured to specific particle size ranges for specific applications. However, the potential for human and ecological toxicity associated with nanomaterials and ultrafine particles is a growing area of investigation. Man-made nanostructured materials such as fullerenes, nanoparticles, nanopowders, nanotubes, nanowires, nanorods, nanofibers, quantum dots, dendrimers, nanoclusters, nanocrystals, and nanocomposites are globally produced in large quantities due to their wide potential applications. Human exposure to these nanostructured materials is inevitable, as they can enter

the body through the lungs or other organs via food, drink, air, and medicine. The nanopowders exposure affects different organs and tissues such as the brain, liver, kidney, heart, blood, and it causes cytotoxic effects; for example, deformation and inhibition of cell growth leading to various diseases in both humans and animals.

The existing research raises some concerns about the safety of nanomaterials and has led to increase interest in studying the toxicity of nanomaterials for use in risk assessment and protection of human health in the environment. A new field of nanotoxicology has been developed to investigate the possibility of harmful effects due to exposure to nanometarials [140]. The different routes of exposure, including inhalation, dermal uptake, ingestion and injection can present unique toxicological outcomes that vary with the physicochemical properties of the nanoparticles. Since a wide variety of nanostructured materials exists, their interactions with biological systems and possible toxicity largely depend upon their properties, such as particle size, concentration, solubility, chemical and biological properties, and stability [141].

The earliest studies investigating the toxicity of nanoparticles focused on atmospheric exposure of humans and environmentally relevant species to heterogeneous mixtures of environmentally produced ultrafine particulate matter (having a diameter < 100 nm). These studies examined pulmonary toxicity associated with particulate matter deposition in the respiratory tract of target organisms [142-146]. Trouiller et al. [147] investigated TiO_2 nanoparticles-induced genotoxicity, oxidative DNA damage and inflammation, in a mice model. Epidemiological assessments of the effects of urban air pollution exposure focusing on particulate matter produced as a

byproduct of combustion events, such as automobile exhaust and other sources of urban air pollution, showed a link in test populations between mortality and amount of particulate matter as reported by MacNee and Zhu [148-150]. TiO_2 nanoparticles have been even extensively utilized in the nanotechnological and pharmaceutical areas and are one of the main components in many household commodities and personalized products [151]. Nanoparticles can infiltrate multiple organs, potentially directly stimulating mast cells, exacerbating pathological consequences [152]. The inhaled nanoparticles can circulate and accumulate in various organs thereby elevating the risks of activating mast cell degranulation in other tissues [153-156].

As reported by Park et al. [157], TiO_2 toxicity was estimated, not only on the bacteria surface, but also through numbers of dead/live cells, and an *in vivo* metabolite quantitative analysis was estimated. It was demonstrated that nanoparticles could inhibit the metabolic pathway of cells even at lower concentrations of TiO_2 that were not enough to kill the cells.

1.5.2 Emissions regulation and guidelines for nanoparticles

Despite the wide range of potential exposure situations and therefore potential risks, specific regulation has been slow to emerge. One of the issue is that because of the width of applications, from paints to cosmetics, many different regulatory frameworks have to be applied. For example, in Europe, this would include regulations on worker safety, chemicals, general products, cosmetics, food, pollution, biocides and water waste. However, reviews of regulations like the BRASS report in the UK [158], highlight that

the regulations do not well agree with the specifics of nano-sized materials. In only few of them the particle size is referred as a key considerable factor. In many cases, in fact, there is nothing within the regulations that would cause any need for change of notification requirements if a micro-sized material is replaces by a nano-sized one of the same chemical specie. However, in 2011 European Parliament established to review all relevant legislations to ensure safety for all applications of nanomaterials in products with potential health effects [159]. The European Commission has published a recommendation aimed at all those involved in nanotechnology research including funding organizations, industry and academic groups. The code recognizes many of the uncertainties involved and comprises a general exhortation towards good practice. Among these it is the principle that "research activities should be conducted in accordance with the precautionary principle, anticipating potential environmental, health and safety impacts of nanoscience and nanotechnology outcomes and taking due precautions". Moreover, the code states that "Students, researchers and research organizations involved in nanoscience and nanotechnology research should take specific health, safety and environmental measures adapted to the particularities of the nano-objects manipulated. Specific guidelines on the prevention of pathologies induced by nano-objects should be developed in line with the Community Strategy 2007-2014 on Health and Safety at Work".

US-EPA (*United States Environmental Protection Agency*) has identified particular types of nanomaterials for investigation on their health effect on human and ecosystems, since these nanomaterials are used in more than 500 consumer products and the number is expected to grow.

Specifically, research want to determine if there are environmental hazard and how these materials may be modified or managed to avoid potential humans or ecosystem effects [160,161]. Nano-sized TiO_2 is currently used in many products. Depending on the type of particle, it may be found in sunscreens, cosmetics, paints and coatings. It is also being investigated for use in removing contaminants from drinking water.

1.5.3 Micro-sized TiO_2 catalyst as real substitute

Considerations of the above issues leads to the conclusions that nanoparticles, although they are produced because their small size confers certain advantageous chemical or physical properties, might have different actions in biological systems with respect to those of the same material at larger dimensions and that in some cases these may lead to unexpected toxic effects [162]. It should be borne in mind that workers with industrial diseases have usually been exposed to high doses of the materials over years and this is a critical point in determining toxicity. A fundamental method for avoiding harms arms is thus a reduction of the use of nanoparticles or a complete substitution of them with the other one of larger size. In fact, in the last three years there was a great decrease on the literature publication of nano-sized TiO_2 focusing, instead, on the study of larger particles application (**Fig. 1.8**).

Fig 1.8. Research on the nano-TiO_2 publications in photocatalysis (source: http://SciFinder.cas.org).

However, it is worth to observe that micro- and nano-sized materials evidence unusual and different chemical, mechanical, optical, electrical and magnetic properties. As just mentioned, since considerable research has shown that many applications of micro- and nanomaterial properties depend on their specific surface area, it is clear that a decrease in particle size will lead to improved and expanded application [163]. The main question is if it is necessary the use of nano-sized particles in an exclusive way. Kwon et al. [164] stated that nanocatalysts having small particle size, high surface area, and a high density of surface unsaturated coordination sites offer improved catalytic performance over microscales catalysts. However, this does not imply the impossibility a priori to use the latter ones in selected conditions.

Actually, several researchers have tried to synthesize TiO_2-based catalysts modulating and changing the particles size. Li et al. [165]

fabricated a type of TiO_2 microspheres for improving the separation and the dispersion; by air bubbling it is in fact easy to suspend this microspheres, which then rapidly settle on the reactor bottom with the aid of gravity eliminating the air bubbling. It has been demonstrated that TiO_2 microspheres can degrade some organic compounds that are strongly adsorbed onto TiO_2 compounds that are strongly adsorbed, such as sulfosalicylic acid (SSA) and salicylic acid (SA), with an equivalent efficiency to the nanopowder counterpart. These results demonstrate that is possible to use micro-sized particles for efficient photocatalysts production, with undeniable advantages in the exhausted catalyst recovering, by accurately choosing the organic pollutant to degrade.

Mesoporous materials with tailored pore structures and high surface areas have even many applications in the area of adsorption and catalysis. Although most studies on the preparation of mesoporous materials appear to be focused on silica because it is more difficult to synthesize mesoporous metal oxides [166,167], in the recent years it has been conducted a work on the synthesis mesoporous TiO_2 microspheres. The obtained products could be easily separated and also showed good catalytic performances degrading bisphenol A [168]. However, photocatalytic degradation of bisphenol A using mesoporous TiO_2 microspheres in aqueous suspension has not been fully understood. Hence, detailed and further photocatalytic degradation studies have to be carried with the helpful of computing simulation.

So, a great attention is focused on the potential of TiO_2 micro-sized powders to be used as photocatalyst for the degradation of organic chemical compounds. Bianchi et al. published articles concerning the use of micro-sized TiO_2 powders for pollutant removal [169-171] The possibility to

substitute nanopowders with micro-sized one is considered of great importance, because actually the health risks related to nano-sized particles can be avoided. Moreover, such a micro-sized powder can be easily filtered and recovered, in order to be immediately reused for further photodegradation reactions, opening also the way of a fully industrial use of photocatalysis in environmental remediation. Micro-sized TiO_2 can be really used as a valid choice for antipollutant photocatalytic processes avoiding the intrinsic ricks due to the nanometric dimension. In this way, all risks to human health and to the environment associated with the nanometric dimensions, especially during industrial application and utilization, are reduced. Therefore, the possibility to prepare and use micro-sized TiO_2 opens a new generation of material intrinsically safer than the traditional photocatalytic products for both workers in the factories and public safety.

1.5.4 TiO_2 modification and doping

However, even if the micro-sized TiO_2 samples are extremely appeal to environmental applications, the possibility to increase their photocatalytic performance of the micro-sized sample is relevant. The improvement study has been already investigated, as suggested by many authors [172-174], through the simple surface fluorination. Surface fluorination was found to have a deep impact on the surface properties of TiO_2 by decreasing the amount of surface hydroxyl groups through the formation of Ti F species [175], which dominate at acidic pH [176] and cause significant variations of the photocatalytic behavior of the semiconductor. In fact, fluoride ions, substituting for surface–OH groups, inhibit surface trapping of

photogenerated holes. Consequently valence band holes, which are not able to oxidize the F–anion because of the high oxidation potential of the F•/F− couple, directly react with water molecules at the interface producing relatively large amounts of •OH radicals. Furthermore, according to Kim [177], fluoride anions adsorbed on the photocatalyst surface have the effect of favoring the generation of free OH radicals (not surface-bond •OH), which are responsible for the enhanced oxidation.

Simultaneously, noble metals, such as Ag, Ni, Cu, Pt, Pd, Rh, with Fermi level lower than TiO_2 (**Fig. 1.9**) have been deposited on the TiO_2 surface for enhanced charge separation [178]. The doping of TiO_2 with metals, not only retards the fast recombination of electron-hole pair, but also enhances the adsorption of visible light by providing defective states in the band-gap [179]. In some cases it has been demonstrated that modifications of the TiO_2 surface with noble metals improves the photocatalytic activity, increasing, so, the quantum yield due to an increase of the rate of electron transfer to the oxidant reagent. It's worth to note, indeed, that the incorporation of metal within TiO_2 may be in two different ways: doping (or substitution) [180,181] and metal impregnation [182-184]. The main difference between the two deposition methods is that the "doping" requires in situ synthesis of TiO_2 catalyst in presence of metal ions at high temperature [185], while the "impregnation" may be achieved by reducing the metal chemically or photochemically. According to Saha at al. [186], the improvement with metal insertion depends on the several factors, such as the catalyst dose, the amount of metal, the pH, and the pollutant type. For example, when metal concentration is very high, negative effect on the photocatalyst surface can occur: semiconductor surface is covered by metal

particles decreasing the light that reaches its surface and, so, the number of photogenerated electron-hole pairs [187]. In addition, metal deposits can occupy the semiconductor surface active centers [188]. For these reasons in the literature it is highlighted an optimum amount of metal above which the photoefficiency decrease. Contradictory results, in fact, can be found in the literature about the effects of a particular metal, and there are no general rules as to whether one metal is better than another one or what their optimum concentrations are. Concerning the addition of silver ions, Kondo et al. [189] reported that Ag/TiO_2 was more effective than bare TiO_2 in chloroform degradation; Sahoo et al. [190] in the degradation of C.I. Basic Violet 3; Behnajady et al. [191] in the degradation of Acid Red 88 dye, and so on.

In this research work, the doping by "impregnation" method was performed through the fluorination of the naked micrometric TiO_2 commercial catalysts, using different fluoride precursors, which will be described in the **Chapter 7**. In respect to metal doping, W, Re and Sn were chosen to improve the photoactivity of micro-sized TiO_2.

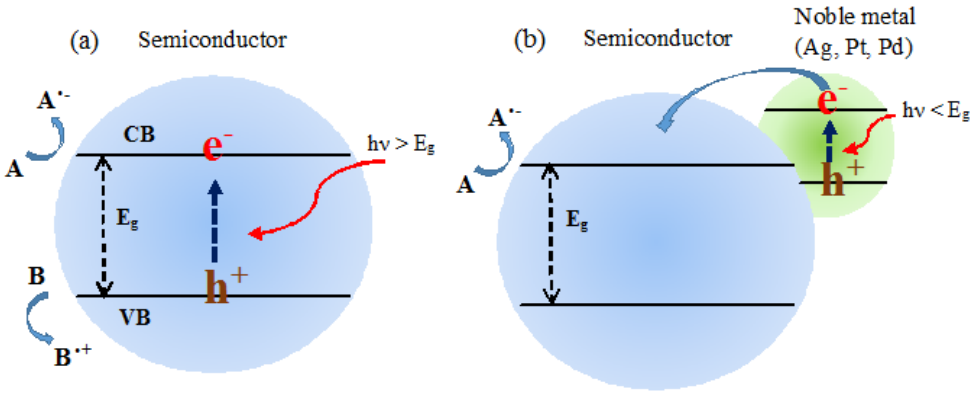

Fig. 1.9. Photocatalytic processes on a naked semiconductor (a) and doped ones (b).

1.6 Industrial research and new gres-tiles materials

The environmental pollution in urban areas is one of the causes for indoor air quality in buildings. Moreover, gaseous emissions from daily traffic in the same areas are increasing often exceeding the limit concentration in the atmosphere, raising public concerns and problems to the traffic itself. The development of photocatalytic construction materials, such as porcelain gres tiles, can contribute to clean the air and to degrade the chemical pollutants.

Porcelain gres tiles are characterized by a very low water absorption rate (less than 0.5%) and are manufactured under high pressure by dry-pressing fine processed ceramic raw materials with large proportions of quartz, feldspar, and other fluxes. Afterwards, the body of these materials is fired at very high temperatures (1200–1300°C) in kilns [192]. Final material is thus characterized by lack of porosity, complete water-proofing, durability, hardness, wear resistance properties, and a complete frost resistance.

In the past decades, porcelain gres tiles underwent significant transformations in terms of appearance and size. At the beginning of the industrial productions, porcelain gres tiles were considered as just a technical material characterized by strong resistance to both abrasion and acid attack, almost lack of porosity, but aesthetically not very beautiful. Today thanks to new industrial production methods, both properties and beauty of these materials completely fit the market requests. In particular, the possibility to prepare slabs of large sizes is the new frontier of building materials.

1.6.1 Gres-tiles photocatalytic applications

The use of photocatalysts together to construction materials started from the early 1990s. The main effects related to the nature of photoactive TiO_2 coatings concern photocatalytic water and air purifications, self-cleaning and photocatalytic anti-bacterial effect. All these properties can be attributed to two fundamental photochemical phenomena that occur on the surface of photocatalyst under ultraviolet (UV) irradiation. One is the photodegradation of adsorbed organic substances, and the other is the photo-induced super-hydrofilicity. The synergy of these two properties stimulate the application in building materials. The versatile function of TiO_2, which can both serve as photocatalytic and structural materials, has facilitated its application in exterior construction and interior furnishing materials, such as cement mortar, exterior tiles, paving blocks, glass and PVC fabric. The advantages of affixing TiO_2 into building materials have attracted many industrial interests. In 2003, the sales of photocatalytic building materials accounted for 60% of the whole photocatalytic market share in Japan [193]. Photocatalytic building materials represent a new era in air quality improvement, since photocatalysis is able to accelerate natural oxidation process, promoting a faster decomposition of pollutants [194,195]. When this type of cement is used in concrete structures, a charge is created on the surface that reacts with external substances to decompose air pollutants such as NO_x [196]. TiO_2 can be integrated within the concrete pavement surface to act as an accelerator of a natural oxidation process. It promotes faster decomposition of NO_x and SO_x from the air [197]. According to Folli et al. [198] two important effects related to the nature of photoactive TiO_2 coatings have been pointed out. Firstly, a self-cleaning effect due to redox

reactions promoted by sunlight, or in general weak ultraviolet light (**Fig. 1.10a**), on the photocatalytic surface is evident [199]. Secondly, photo-induced hydrophilicity of the catalyst surface enhances the self-cleaning effect, since inorganics causing dirt and stains on surfaces can be easily removed due to rainwater soaking between the adsorbed substance and the TiO_2 surface (**Fig. 1.10b**). Recently, photocatalytic building materials have been patented by Mitsubishi Corp.(NO_xer^{TM}), and Italcementi SpA (TX-Aria^{TM} and TX-Arca^{TM}) [200-202]. In all these construction materials, the active photocatalyst is anatase TiO_2 (the most active between the three TiO_2 polymorphs: anatase, rutile and brookite).

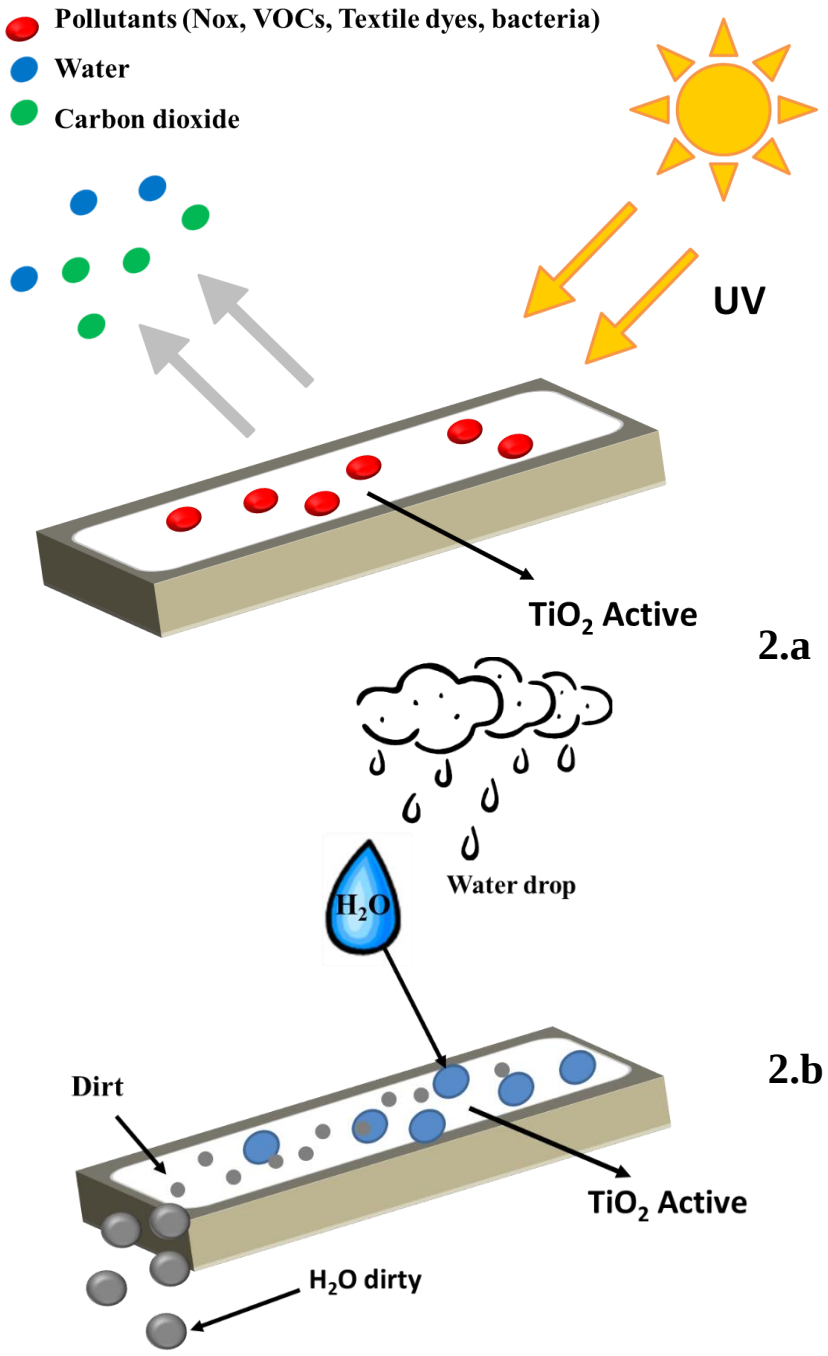

Fig. 1.10. (a) Photocatalytic and (b) self-cleaning mechanisms of TiO_2 catalysts.

The application of TiO_2 photocatalysis leads to the air purification, self-cleaning and self-disinfecting. The first application of photocatalytic building materials has certainly been the "Dives of Misericordia" church in Rome for which, on demand of arch. Richard Meier, CTG Laboratories developed a white concrete possessing a prolonged maintenance of colour over time (**Fig. 1.11**). Another breakthrough for this innovation consists in the funded European research project PICADA ("Photocatalytic Innovative Coverings Applications for Depollution Assessment", 2002-2005), through which a pilot scale experience (street canyon) was carried out for the evaluation of depolluting performances of coating materials in real conditions. The research was aimed to develop products capable to obtain a surface degradation of gaseous polluting agents (NO_x, VOCs, SO_x), so that several commercial products (pavements, roofing and coatings) are now available on the market.

Fig 1.11. Church "Dives in Misericordia", (Rome).

The trend in volume consumption show a shift from paving blocks plus paint, to ready mix and precast concrete manufacts. This means that there has been a breakthrough in consumption that does not correspond to a proportional increase in the surface covered. Paints and coatings represent a small amount of the product (cement) used, but in terms of photocatalytic surfaces they represent more than 50% of the total. Currently, about 60 Companies are TX Active® partners in Italy, and more than 100 in the world (France, USA, Spain, Belgium, Morocco).

Fig. 1.12. CT Millenium cement – gray cement was used in France for the construction of the Music and Arts City Halls in Chambéry.

According to a reliable research, the photocatalytic surfaces produced in Europe with cement-based materials until 2009 result to be over 1.5 million m^2. Another example of photocatalytic materials containing TiO_2 is the Music and Arts City Hall in Chambéry, France (**Fig. 1.12**). Brilliancy tests carried out so far show the aesthetic treatability of concrete elements made

in white cements, exposed within an urban environment for five years. After 30 months the level of brilliance of the façade is well maintained and no significant variation compared to the initial values are observed.

Concrete pavement surfaces and external building surfaces are optimal media for applying the photocatalytic materials because the relatively flat configuration of the building materials can facilitate the exposure of the photocatalyst to sunlight. Under irradiation of solar light, gaseous pollutants can be degraded on the surface of construction materials which can be eventually washed away by rain (**Fig. 1.13**). The whole removal process of pollutants is driven by natural energy alone [203].

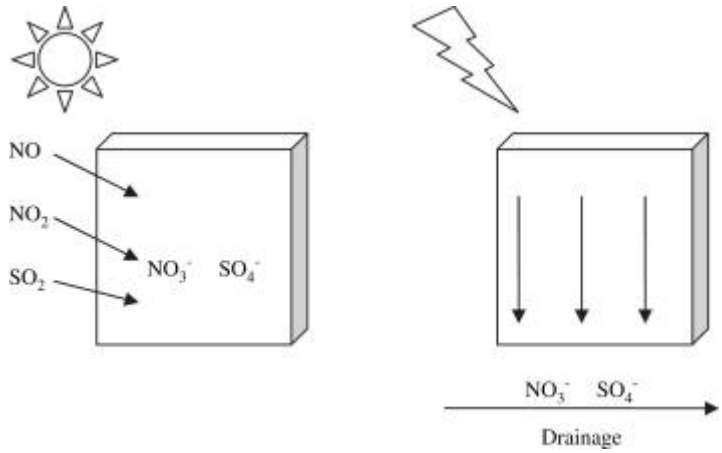

Fig. 1.13. Illustration of pollutant removal by photocatalytic building materials in natural environment.

1.6.2 Air depollution

The depollution effect of photocatalytic cementitious materials has been demonstrated by many laboratory studies [204-210]. Nitrogen oxides (NO_x)

and volatile organic compounds (VOCs) have been chosen by most studies as representative airborne pollutants due to their potential health risks and ability to generate photochemical smog.

The NO_x removal applying cement mortars with TiO_2 was evaluated by Staub de Melo et al. [211]. The study evaluated, experimentally, the influence of different environmental conditions (UV-A radiation, relative humidity and flow rate) on the efficiency of photocatalytic mortar in the degradation of NO_x. The experimental study found that the change in environmental conditions significantly affects the efficiency of the photocatalytic mortar. With higher levels of UV-A radiation, there are greater amounts of active TiO_2 sites on the surface, improving the performance in the degradation of the pollutants. The environmental conditions are crucial to the photoefficiency. Thus, for the application of such materials, location with specific humidity values, incidence of solar radiation and air mass movement are required to be monitored in order to provide better conditions for the high efficiencies of the building mortars. When TiO_2 is activated by UV light, in a catalytic reaction it first breaks down NO_x gases into nitric acid (HNO_3) that then adhere to water droplets. These water droplets will then be washed away by rain. Photocatalytic effect is associated with a reduced nitric oxide (NO) oxidation to nitrates and these ions are flushed from the surface as a weak HNO_3. The whole reaction results in a significant reduction in the concentration of pollutants from the atmosphere when used on or in a concrete structure that is exposed to UV-A and placed close to the pollution source [212]. Bianchi et al. [213,214] tested micro-sized TiO_2 porcelain gres tiles photoefficiency for the NO_x photoabetement, hiting a good photocatalytic performances.

Regarding the degradation of VOCs, Aissa et al. [215] used self-cleaning mortars and concretes for the removal of formaldehyde as a representative VOC air pollutant. It has been clearly demonstrated that cementitious materials containing TiO_2 could not only be self-cleaning as previously described [216-219], but could also participate to the cleaning of ambient air containing VOCs, such as formaldehyde which is the most commonly found air pollutant in outdoor urban atmospheres. It was evaluated an optimum weight percentage of TiO_2 into the cement. It was shown that formaldehyde can be adsorbed by the mortar, and some intermediates like formic acid, can follow the same way as well as the final CO_2, but this corresponds to the surface properties of mortars and concretes.

1.6.3 Limitations

It is well-known that innovative materials can have some limitations in their commercial applications. Reference standards are absolutely necessary to define their performances required in specifications and projects and to compare different building materials. So, it is in progress an accurate standardization activity (ISO) of, also, photocatalytic materials. The standardization activity started in Italy for the determination of photocatalytic activity of cementitious products (NO_x test, UNI 11247-2009, Volatile Organic Compounds tests, UNI 11238-1-2007) and of azo dyes (Rhodamine B tests, UNI 11259-2008).

Nonetheless, in a sensory assessment of indoor air quality performed on cement-based paints, a negative effect of the photocatalyst on air quality

was perceived: the reason was found in previous experimental works, which described an incomplete degradation of VOCs and other pollutants giving rise to undesired byproducts, manly harmful carbonyls (e.g., acetaldehyde and formaldehyde) [220]. Furthermore, the most challenging aspects relate to the durability of such coatings, which are likely to undergo surface erosion caused by environmental agents, in opposition to the greatest stability of bulk admixtures; unfortunately, few information is available on the durability of construction materials and of photoactive coatings applied to building materials [221]. The type and quantity of photocatalyst and characteristics of the different building matrixes play a key role on the photocatalytic activity. For example, technical aspects limit the large scale application and therefore the price of this light-driven technology. In fact, it is not clear yet what is the most efficient way to incorporate the TiO_2 photocatalyst in the cementitious materials. Current research is conducted to minimize the amount of TiO_2 while enhancing the photocatalytic activity for the different applications. Maury-Ramirez et al. [222] investigated two different coating techniques (dip-coating and a novel vacuum saturation method). This type of research was helpful to better assess the real application potential of innovative cementitious materials for long-term air-purifying purposes. In parallel with this, Bianchi et al. [223] investigated an aspect of building coatings: the photoactivity lifetime. Stability over long periods of time is a crucial parameter that must be estimated to assess the suitability of the materials composites to be used as photoactive building coatings. In fact, the hydroxyl radicals produced by photoexcitation are not selective and can then degrade the matrix of the material as well as the air pollutants [224]. Therefore, Bianchi et al. selected two different kinds of

coatings, mixed with the same quantity of photocatalyst TiO_2. The evaluation of pollutant removal (NO_x) was monitored over 1 year. The correct evaluation of the durability parameter is highly important to understand the times required for photocatalyst replacement or for refreshing it. In fact, the durability of building coatings resulted strongly influenced by the different stability of the used matrix. According to Diamanti et al. [225] a good compromise may be found in the addition of TiO_2 to finishing layers of mortar or plasters. However, it is yet not clear how the presence of hydroxides or other chemical species may hinder TiO_2 photoactivity, such as a reduced adsorption of pollutants on the catalyst surface, or the introduction of recombination sites for the photogenerated reactive species [226-228].

1.7 References

[1] Seinfeld J.H., Pandis S.N. Atmospferic chemistry and physics: from air pollution to climate change. **2012**.
[2] Holland W.W., Bennett A.E., Cameron I.R., et al. Health effects of particulate pollution: reappraising the evidence. *Am. J. Epidemiol*. **1979**, *110*, 527–659.
[3] Dockery D.W., Pope C.A. 3rd, Xu X, et al. An association between air pollution and mortality in six US cities. *N. Engl. J. Med*. **1993**, *329*, 1753–1759.
[4] Pope C.A. 3rd, Thun MJ, Namboodiri MM, et al. Particulate air pollution as a predictor of mortality in a prospective study of US adults. *Am. J. Respir. Crit. Care Med*. **1995**, *151*, 669–674.
[5] Global Health Observatory Data Repository. Urban outdoor air pollution: burden of disease by country. Geneva: World Health Organization, 2008. http://apps.who.int/gho/data/node.main.285, accessed Sept 1, **2012**.

[6] Samet J.M., Dominici F., Curriero F.C., Coursac I., Zeger S.L. Fine particulate air pollution and mortality in 20 US cities, 1987–1994. *N. Engl. J. Med*. **2000**, *343*, 1742–1749.
[7] Peters A., Dockery D.W., Muller J.E., Mittleman M.A. Increased particulate air pollution and the triggering of myocardial infarction. *Circulation* **2001**, *103*, 2810–2815.
[8] Berry C., Murdoch D.R., McMurray J.J. Economics of chronic heart failure. *Eur. J. Heart Fail* **2001**, *3*, 283–291.
[9] Davies M., Hobbs F., Davis R., et al. Prevalence of left-ventricular systolic dysfunction and heart failure in the Echocardiographic Heart of England Screening study: a population based study. *Lancet* **2001**, *358*, 439–444.
[10] Redfi eld M.M., Jacobsen S.J., Burnett J.C. Jr, Mahoney D.W., Bailey K.R., Rodeheff er R.J. Burden of systolic and diastolic ventricular dysfunction in the community: appreciating the scope of the heart failure epidemic. *JAMA* **2003**, *289*, 194–202.
[11] WHO. Criteria used in establishing guideline value. Air quality guidelines for Europe. 2nd ed. Copenhagen: WHO Regional Office for Europe; **2000**a., 11–31.
[12] WHO. Introduction. Air quality guidelines for Europe. 2nd ed. Copenhagen:WHO Regional Office for Europe; **2000**b., 5–7.
[13] Dockery D.W., Pope C.A., Xu X.P., Spengler J.D., Ware J.H., Fay M.E., Ferris B.G., Speizer F.E. An association between air-pollution and mortality in 6 United-States Cities. *New Engl. J. Med.* **1993**, *329*, 1753–1759.
[14] Pope C.A., Burnett R.T., Thurston G.D., Thun M.J., Calle E.E., Krewski D., Godleski J.J. Cardiovascular mortality and long-term exposure to particulate air pollution—epidemiological evidence of general pathophysiological pathways of disease. *Circulation* **2004**, *109*, 71–77.
[15] Dominici F., Peng R.D., Bell M.L., Pham L., McDermott A., Zeger S.L., Samet J.M. Fine particulate air pollution and hospital admission for cardiovascular and respiratory diseases. *JAMA* **2006**, *295*, 1127–1134.
[16] Wordley J., Walters S., Ayres J.G. Short termvariations in hospital admissions and mortality and particulate air pollution. *Occup. Environ. Med*. **1997**, *54*, 108–116.
[17] Laden F., Schwartz J., Speizer F.E., Dockery D.W. Reduction in fine particulate air pollution and mortality: extended follow-up of the Harvard Six Cities study. *Am. J. Respir. Crit. Care Med*. **2006**, *173*, 667–672.
[18] Pope C.A., Burnett R.T., Thun M.J., Calle E.E., Krewski D., Ito K., Thurston G.D. Lung cancer, cardiopulmonary mortality, and long-term exposure to fine particulate air pollution. *JAMA* **2002**, *287*, 1132–1141.

[19] Brook R.D., Jerreft M., Brook J.R., Bard R.L., Finkelstein M.M. The relationship between diabetes mellitus and traffic-related air pollution. *J. Occup. Environ. Med*. **2008**, *50*, 32–38.
[20] Ostro B., Broadwin R., Green S., Feng W.Y., Lipsett M. Fine particulate air pollution and mortality in nine California counties: results from CALFINE. *Environ. Health Perspect*. **2006**, *114*, 29–33.
[21] Bobak M. Outdoor air pollution, low birth weight, and prematurity. *Environ. Health Perspect.* **2000**, *108*, 173–176.
[22] Woodruff T.J., Grillo J., Schoendorf K.C. The relationship between selected causes of postneonatal infant mortality and particulate air pollution in the United States. *Environ. Health Perspect*. **1997**, *105*, 608–612.
[23] WHO. Exposure: city level by country. World Health Organization; **2012** [http://apps. who.int/gho/data/view.main.34201.
[24] Lai H.-K., Hedley A.J., Thach T.-Q., Wong C.-M. A method to derive the relationship between the annual and short-term air quality limits – Analysis using the WHO Air Quality Guidelines for health protection, *Environ. Int*. **2013**, *59*, 86-91.
[25] WHO. Nitrogen dioxide. Air quality guidelines global update 2005: particulate matter, ozone, nitrogen dioxide and sulfur dioxide. Copenhagen: WHO Regional Office for Europe; **2006**d., 375.
[26] Debellefontaine H., Chakchouk M., Foussard J.N., Tissot D., Striolo P., Treatment of organic aqueous wastes: wet air oxidation and wet peroxide oxidation(R). *Environ. Pollut*. **1996**, *92*, 155–164.
[27] Hung H.-M., Tang C.-W. Effects of temperature and physical state on heterogeneous oxidation of oleic acid droplets with ozone. *J. Phys. Chem. A* **2010**, *114*(50), 13104-13112.
[28] Oller I., Malato S., Sànchez-Pérez J.A. Combination of advanced oxidation processes and biological treatments for wastewater decontamination – A review. *Sci. Tot. Environ.* **2011**, *409*, 4141–4166.
[29] Balcioglu I.A., Arslan I., Sacan M.T. Homogeneous and heterogeneous advanced oxidation of two commercial reactive dyes. *Environ. Technol*. **2001**, *22*, 813–822.
[30] Bhatkhande D.S., Pangarkar V.G., Beenackers A.A.C.M. Photocatalytic degradation for environmental applications: a review. *J. Chem. Technol. Biotechnol*. **2002**, *77*, 102–116.
[31] García-Montaño J., Ruiz N., Muñoz I., Doménech X., García-Hortal J.A., Torrades F., et al. Environmental assessment of different photo-Fenton approaches for commercial reactive dye removal. *J. Hazard. Mater*. **2006**a, *138*, 218–225.

[32] Gogate P.R., Pandit A.B. A review of imperative technologies for wastewater treatment I: oxidations technologies at ambient conditions. *Adv. Environ. Res*. **2004**a, *8*, 501–551.
[33] Gogate P.R., Pandit A.B. A review of imperative technologies for wastewater treatment II: hybrid methods. *Adv. Environ. Res.* **2004**b, *8*, 553–597.
[34] Pera-Titus M., García-Molina V., Baños M.A., Giménez J., Espulgas S. Degradation of chlorophenols by means of advanced oxidation processes: a general review. *Appl. Catal. B Environ*. **2004**, *47*, 219–256.
[35] Devipriyas S, Yesodharan S. Photocatalytic degradation of pesticide contaminants in water. *Sol. Energy Mater. Sol. Cells* **2005**, *86*, 309–348.
[36] Pignatello J.J., Oliveros E., MacKay A. Advanced oxidation processes for organic contaminant destruction based on the Fenton reaction and related chemistry. *Crit. Rev. Env. Sci Technol*. **2006**, *36*, 1-84.
[37] Fujishima A., Honda K., Kikuchi S. Photosensitized electrolytic oxidation on TiO_2 semiconductor electrode. *J. Chem. Soc. Japan* (Kogyo Kagaku Zasshi) **1969**, *72*, 108–109.
[38] Fujishima A., Honda K. Electrochemical photolysis of water at a semiconductor electrode. *Nature* **1972**, *238*, 37–38.
[39] Kabra K., Chaudhary R., Sawhney R.L. Treatment of hazardous organic and inorganic compounds through aqueous-phase photocatalysis: a review. *Ind. Eng. Chem. Res*. **2004**, *43*, 7683-7696.
[40] Kawai T., Sakata T. Hydrogen evolution from water using solid carbon and light energy. *Nature* **1979**, *282*, 283–284.
[41] Sato S., White J.M. Photodecomposition of water over Pt/TiO_2 catalyst. *Chem. Phys. Lett*. **1980**, *72*, 83–86.
[42] Renz C. Photo-reactions of the oxides of titanium, cerium and earth-acids. *Helv. Chim. Acta* **1921**, *4*, 961-968.
[43] Fujishima A., Honda K. Electrochemical photolysis of water at a semiconductor electrode. *Nature* **1972**, *238*, 37–38.
[44] Turchi C.S., Ollis D.F. Photocatalytic degradation of organic water contaminants: mechanisms involving hydroxyl radical attack. *J. Catal*. **1990,** *122*, 178-192.
[45] Fujishima A., Hashimoto K., Watanabe T. TiO_2 photocatalysis: fundamentals and applications. *Tokyo: BKC*, Inc., **1999**.
[46] Fujishima A., Zhang X. TiO_2 photocatalysis: present situation and future perspectives. *C. R. Chimie* **2006**, *9*, 750–760.
[47] Herrmann J.M., Disdier J., Mozzanega M.-N., Pichat P. Heterogeneous Photocatalysis: in situ photoconductivity study of TiO_2 during oxidation of isobutene into acetone. *J. Catal*. **1979**, *60*, 369-377.

[48] Hsiaio C.Y., Lee C.L., Ollis D.F. Heterogeneous photocatalysis: degradation of diluite solutions of dichloromethane, choloroform and carbon tetrachloride with illuminated TiO_2 photocatalyst. *J Catal*. **1983,** *82*, 418.
[49] Matthews R.W. Photooxidation of organic material in aqueous suspensions of titanium dioxide. *Water Res.* **1986**, *20*(5), 569-578.
[50] Fujishima A., Honda K., Kikuchi S. Photochemical reactions of semiconductors. I. Photosensitized electrolytic oxidation on semiconducting n-type TiO_2 electrode. *Kogyo Kagaku Zasshi* **1969,** *72,* 108-113.
[51] Kaneko M., Okuru N. Photocatalysis: Science and technology. *Kodansha Ltd,* Japan **2002**, *356*.
[52] Dachille F., Simons P.Y., Roy R. Pressure-temperature studies of anatase, brookite and rutile and TiO2-II. Am. Mioneral **1968**, *53*.
[53] Sun B., Smirniotis P.G. Interaction of anatase and rutile TiO_2 particles in aqueous photooxidation. *Catal. Today* **2003**, *88*, 49-59.
[54] Bavykin D.V., Friedrich J.M., Walsh F.C. Protonated titanates and TiO_2 nanostructured materials: synthesis, properties and applications. *Adv. Mater*. **2006**, *18*, 2807-2824.
[55] Titanium Compounds, Inorganic. In *Kirk-Othmer Encyclopedia of Chemical Technology*, (Online) ed.; Wiley: New York, **2000**, 1-58.
[56] Mo S.D., Ching W.Y. Electronic and optical properties of three phases of titanium dioxide: rutile, anatase and brookite. *Phys. Rev. B* **1995**, *51*, 13023-13031.
[57] Weng T. Photocatalytic purification and treatment of water and air. *Elsevier Publishers*, Amsterdam **1993**.
[58] Bickley R.I., Gonzalez-Carreno T., Lees J.S., Palmisano L., Tilley R.J.D. A structural investigation of titanium dioxide photocatalysts. *J. Sol. St. Chem*. **1991**, *92*, 178-190.
[59] Beska R.R., Kiwi J. *App. Catal. B: Environ.* **1998,** *16*, 19.
[60] Yamazaki S., Matsunaga S., Hori K. Photocatalytic degradation of trichloroethylene in water using TiO_2 pellets. *Water Res*. **2001**, *35*, 1022-1028.
[61] Maira A.J., Yeung K.L., Lee C.Y., Yeu P.L., Chan C.K. Size effects in gas-phase photooxidation of trichloroethylene using nanometer-sized TiO_2 catalysts. *J. Catal*. **2000**, *192*(1), 185-196.
[62] Zhang Z., Wang C.C., Zakaria R., Ying J.Y. Role of particle size in nanocrystalline TiO_2-based photocatalysts. *J. Phys. Chem. B* **1998**, *102*(52), 10871-10878.
[63] Almquist C.B., Biswas P. Role of synthesis method and particle size of nanostructured TiO_2 on its photoactivity. *J. Catal*. **2002**, *212*, 145-156.
[64] Anpo M., Shima T., Kodama S., Kubokawa Y. Photocatalytic hydrogenation of propyne with water on small-particle titania: size quantization effects and reaction intermediates. J. *Phys. Chem*. **1987**, *91*, 4305-4310.

[65] Lin H., Huang C.P., Li W., Ni C., Ismat Shah S., Tseng, Y.H. Size dependency of nanocrystalline TiO_2 on its optical property and photocatalytic reactivity exemplified by 2-chlorophenol. *Appl. Catal. B* 2006, *68*, 1-11.
[66] Mills A., Le Hunte S. An overview of semiconductor photocatalysis. *J. Photochem. Photobiol. A* **1997**, *108*, 1-35.
[67] Fujishima A., Rao T. N., Tryk D. A. Titanium dioxide photocatalysis. *J. Photochem. Photobiol. C* **2000,** *1*, 1-21.
[68] Fujishima A., Hashimoto K., Watanabe T. TiO_2 Photocatalysis: Fundamentals and Application, 1 edn., BKC, Tokyo, **1999**.
[69] Hoffmann M.R., Martin S.T., Choi W., Bahnemann D.W. Environmental applications of semiconductor photocatalysis. *Chem. Rev*. **1995**, *95*, 69-96.
[70] Emeline A.V., Ryabchuk V.K., Serpone N. Dogmas and misconceptions in heterogeneous photocatalysis. Some enlightened reflections. *J. Phys. Chem. B* **2005**, *109*, 18515-18521.
[71] Cantor J., Mikkelsen L., Simons B., Waters R. How can we pay for a healthy population?. *Prev. Inst*. **2013**.
[72] Nath R.K., Zain M.F.M., Kadhum A.A.H. Photocatalysis - a novel approach for solving various environmental and disinfection problems: a brief review. *J. App. Scie. Res*. **2012**, *8*(8), 4147-4155.
[73] Hashimoto K., Wasada K., Toukai N., Kominami H., Kera Y. Photocatalytic oxidation of nitrogen monoxide over titanium(IV) oxide nanocrystals large size areas. *J. Photochem. Photobiol*. **2000**, *136*, 103-109.
[74] Cao L., Gao Z., Suib S., Obee T., Hay S., Freihaut J. Photocatalytic oxidation of toluene on nanoscale TiO_2 catalysts: studies of deactivation and regeneration. *J. Catal*. **2000**, *186*, 253-261.
[75] Rao K., Subrahmanyam M., Boule P. Immobilized TiO_2 photocatalyst during long-term use: decrease of its activity. *Appl. Catal. B* **2004**, *49*, 239-249.
[76] Chen J., Poon C. Photocatalytic construction and building materials: from fundamentals to applications. *Building and Environment* **2009**, *44*, 1899-1906.
[77] Maggos T., Bartzis J.G., Leva P., Kotzias D. Application of photocatalytic technology for NO_x removal. *App. Phys. A* **2007**, *1*, 81-84.
[78] Smith K.R., Mehta S. The burden of disease from indoor air pollution in developing countries: comparison of estimatos. *Int. J. Hygiene Environ*. **2003**, *206*, 279-289.
[79] Benson F.B., Henderson J.J., Caldwell D.E. Research Triangle Park, *NC: U.S. Environmental Protection Agency* **1972** Publication No. AP-112.
[80] Henderson J.J., Benson F.B., Caldwell D.E., *NC: U.S. Environmental Protection Agency* **1973** Publication No. AB-112B.
[81] Irie H., Tee S. P., Shibata T., Hashimoto K. *Electrochem. Solid-State Lett*. **2005**, *8*, 23-25.

[82] Mills A., Le Hunte S. An overview of semiconductor photocatalysis. *J. Photochem. Photobiol. A* **1997**, *108*, 1 – 35.
[83] Hoffmann M.R., Martin S.T., Choi W., Bahnemann, D.W. Environmental applications of semiconductor photocatalysis. *Chem. Rev*. **1995**, *95*, 69-96.
[84] Unger N., Bond, T.C., Wang, J.S. Attribution of climate forcing to economic sectors. *Proc Natl Acad Sci USA* **2010**, *107*, 3382-3387.
[85] IARC. IARC monographs on the evaluation of carcinogenic risks to humans. Volume 109. Outdoor air pollution. Lyon: International Agency for Research on Cancer (in press).
[86] Lianou M., Chalbot M.-C., Kotronarou A., Kavouras I., Karakatsani A., Katsouvanni K., Puustinnen A., Hameri K., Vallius M., Pekkanen J. Dependence of home outdoor particulate mass and number concentrations on residential and traffic features in urban areas. *J. Air & Waste Manag. Assoc*. **2007**, *57*, 1507-1517.
[87] Setton E., Marshall J.D., Brauer M., Lundquist K.R., Hystad P., Kelelr P., Cloutier-Fisher D. The impact of daily mobility on exposure to traffic-related air pollution and health effect estimates. *J. Expos. Sci. Environ. Epidem*. **2010**, 1-7.
[88] Brunekreef B., Holgate S.T. Air pollution and health. *The Lancet* **2002**, *360*, 1233-1242.
[89] Levy J., Buonocore J.J., Von Stackelberg K. Evaluation of the public health impacts of traffic congestion: a health risk assessment. *Envir. Health* **2010**, *9*, 1-12.
[90] Kitano M., Matsuoka M. Ueshima M., Anpo M. Recent developments in titanium oxide-based photocatalysts. *Appl. Catal. A* **2007**, *325*, 1-14.
[91] Seinfeld J.H., Pandis S.N. Atmospheric chemistry and physics: from air pollution to climate changes. **2012**.
[92] Neff J.C., Holland E.A., Dentener F.J., Mc Dowell W.H. The origin, composition and rates of organic nitrogen deposition: a missing piece of the nitrogen cycle?. *Biogeochem*. **2002**, *57-58*, 99-136.
[93] Crutzen P.J. The role of NO and NO_2 in the chemistry of the troposphere and stratosphere. *An. Rev. Earth Planet. Sci*. **1979**, *7*, 443-472.
[94] Harrison R.M. Pollution: causes, effects and control, 2 edn., *The Royal Society of Chemistry*, Cambridge, **1992**.
[95] Cotton F.A., Wilkinson G. Advanced Inorganic Chemistry, 5 edn., Wiley-Interscience, USA, 1988, Elsom D. *Atmospheric Pollution*, 1 edn., Basil Blackwell, New York, **1987**.
[96] Seinfeld J.H. Atmospheric chemistry and physics: from air pollution to climate change, 1 edn., Wiley, New York, **1998**.
[97] Cheng Y., Weixiong H., Changjin G., Xuejun P., Shixin H., Zhang W. Experimental study of photochemical reaction in smog chamber using a Chernin multipass cell. *Guangxue Xuebao* **2013**, *33*, 1-8.

[98] Gautam A., Mahajan M., Garg S. Impact of air pollution on human health in Dehra Doon City. *Res. Sci. & Res. Ass*. **2009**, 1-6.
[99] Menzel D.B. The toxicity of air pollution in experimental animals and humans: the role of oxidative stress. *Toxicol. Letters* **1994**.
[100] Bianchi C.L., Pirola C., Selli E., Biella S. Photocatalytic NO_x abatement: The role of the material supporting the TiO_2 active layer. *J. Hazard. Mater*. **2012**, *211-212*, 203-207.
[101] Naldoni A., Bianchi C.L., Pirola C., Suslick K.S. Porous TiO_2 microspheres with tunable properties for photocatalytic air purification. *Ultras. Sonochem*. **2013**, *20*, 445-451.
[102] Juengsuwattananon K., Rujitanaroj P., Supaphol P., Pimpha N., Matsuzawa S. Preparation of ultrafine TiO2 nanofibers and their application in removal of NO_x in air. *Mat. Sci. Forum* **2008**, *569*, 25-28.
[103] Wang H., Wu Z., Zhao W., Guan B. Photocatalytic oxidation of nitrogen oxides using TiO_2 loading on woven glass fabric. *Chemosphere* **2007**, *66*, 185–190.
[104] Wu Q., Van de Krol R. Selective photoreduction of nitric oxide to nitrogen by nanostructured TiO_2 photocatalysts: role of oxygen vacancies and iron dopant. *J. Am. Chem. Soc.* **2012**, *134*, 9369-9375.
[105] Huang C.-H., Bai H., Liu S.-H., Huang Y.-L., Tseng Y.-H. Synthesis of neutral SiO_2/TiO_2 hydrosol and its photocatalytic degradation of nitric oxide gas. *Micro & Nano Lett.* **2011**, *6*, 646-649.
[106] Ardizzone S., Bianchi C.L., Cappelletti G., Gialanella S., Pirola C., Ragaini V. Tailored anatase/brookite nanocrystalline TiO_2. The optimal particle features for liquid- and gas-phase photocatalytic reactions. *J. Phys. Chem. C* **2007**, *111*, 13222-13231.
[107] Radcliff J. Future directions for water recycling in Australia. *Desalination* **2006**, *187*, 77–87.
[108] Mitchell V.G., Mein R.G., Mcmahon T.A. Utilising storm water and wastewater resources in urban areas. *Aust. J. Wat. Res*. **2002**, *6*, 31–43.
[109] DEH (Department of Environment and Heritage). Introduction to urban stormwater management in Australia, prepared under the stormwater initiative of the living cities PROGRAM 2002. **2002**.
[110] Séquin-Frey M. The chemistry of plant and animal dyes. *J. Chem. Educ*. **1981**, *58*, 301-305.
[111] Ong S.-T., Lee C.-K., Zainal Z., Keng P.-S., Ha S.-T. Photocatalytic degradation of basic and reactive dyes in both single and binary systems using immobilized TiO_2. *J. Fund. Sci*. **2009**, *5*, 88-93.
[112] Eriksson E., Baun A., Mikkelsen P.S., Ledin A. Risk assessment of xenobiotics in stormwater discharged to Harrestup Ao. Denmark. *Desalination* **2007**, *215*, 187–197.

[113] Capon M., Courilleau V., Valette C., Cachan E.N.S. Chimie des Couleurs et Des Odeurs, Cultures et Techniques, Nantes, France, **1993**.
[114] Brown M.A., De Vito S.C. Predicting azo dye toxicity. *Crit. Rev. Environ. Sci. Technol.* **1993**, *23*, 249-324.
[115] Pérez-Urquiza M., Beltran J.L. Determination of dyes in foodstuffs by capillary zone electrophoresis. *J. Chromatogr. A* **2000**, *898*, 271-275.
[116] Delée W., O'Neill C., Hawkes F.R., Pinheiro H.M. Anaerobic Treatment of textile effluents: a review. *J. Chem. Technol. Biotechnol*. **1998**, *73*, 323-335.
[117] More A.T., Vira A., Fogel S. *Environ. Sci. Technol.* **1989**, *23*, 403.
[118] Slokar Y.M., Le Marechal A.M. Methods of decoloration of textile wastewaters. *Dyes Pigments* **1998**, *37*, 335-356.
[119] Esplugas S., Giménez J., Contreras S., Pascual E., Rodriguez M. Comparison of different advanced oxidation processes for phenol degradation. *Wat. Res*. **2002**, *36*, 1034-1042.
[120] Swaminathan M., Muruganandham M., Sillanpaa M. Advanced oxidation processes for wastewater treatment. *Int. J. Photoen*. **2013,** *2013*, 1-3.
[121] Muruganandham M., Suri R.P.S., Jafari S., Sillanpaa M., Lee G.J., Wu J.J., Swaminathan M. Recent developments in homogeneous advanced oxidation processes for water and wastewater treatment. *Int. J. Photoen*. **2014**, *2014*, 1-21.
[122] Sun L., Bolton J.R. Determination of the quantum yield for the photochemical generation of hydroxyl radicals in TiO_2 suspensions. *J. Phys. Chem*. **1996**, *100*, 4127-4134.
[123] Mukherjee P.S., Ray A.K. Major challenges in the design of a large scale photocatalytic reactor for water treatment. *Chem. Engin. Technol*. **1999**, *22*, 253-260.
[124] Moctezumaa E., Leyva E., Palestino G., Lasa H.D. Photocatalytic degradation of methyl parathion: Reaction pathways and intermediate reaction products. *J. Photochem. Photob. A: Chem*. **2007**, *186*, 71-84.
[125] Konstantinou I.K., Albanis T.A. Photocatalytic transformation of pesticides in aqueous titanium dioxide suspensions using artificial and solar light: Intermediates and degradation pathways. *App. Cat. B: Environ.* **2003**, *42*, 319-355.
[126] Legrini O., Oliveros E., Braun A.M. Photochemical for water treatment. *Chem. Rev*. **1993**, *93*, 671-698.
[127] Rincon A.-G., Pulgarin C. Effect of pH, inorganic ions, organic matter and H_2O_2 on E. coli K12 photocatalytic inactivation by TiO_2. *App. Cat. B: Envir*. **2004**, *51*, 283-302.
[128] Doll T.E., Frimmel F.H. Photocatalytic degradation of carbamazepine, clofibric acid and iomeprol with P25 and Hombikat UV100 in the presence of natural organic matter (NOM) and other organic water constituents. *Wat. Res.* **2005**, *39*, 403-411.

[129] Shakthivel S., Janczarek M., Kisch H. Visible light activity and photoelectrochemical properties of nitrogen-doped TiO_2. *J. Phys. Chem. B* **2004**, *108*, 19384-19387.
[130] Byrappa K., Subramania A.K., Ananda S., Rai K.M.L., Dinesh R., Yushimura M. Photocatalytic degradation of Rhodamine B dye using hydrothermally synthesized ZnO. *Bulletin Mat. Sci*. **2006**, *29*, 433-438.
[131] Zhang Z., Wang C.-C., Zakaria R., Ying J.Y. Role of particle size in nanocrystalline TiO_2-based photocatalysts. *J. Phys. Chem. B* **1998**, *102*, 10871-10878.
[132] Serpone N., Lawless D., Khairlutdinov R., Pelizzetti E. Size effects on the photophysical properties of colloidal anatase TiO_2 particles: size quantization versus direct transitions in this indirect semiconductor? *J. Phys. Chem*. **1995**, *99*, 16646-16654.
[133] Mu L., Sprando R. Application of nanotechnology in cosmetics. *Pharm. Res.* **2010**, *27*, 1746-1749.
[134] Pitkethly M.J. Nanomaterials – the driving force. *MaterialsToday*, **2004**, *7*, 20-29.
[135] Markarian J. Automotive and packaging offer growth opportunities for nanocomposites. *Plastics, Addit. Comp*. **2005**, *7*, 18-21.
[136] Xia T., Kovochich M., Brant J., Hotze M., Sempf J., Oberley T., Sioutas C., Yeh J., Wiesner M., Nel A. Comparison of the abilities of ambient and manufactured nanoparticles to induce cellular toxicity according to an oxidative stress paradigm. *Nano Letters*, **2006**, *6*, 1794-1807.
[137] Meng H., Xia T., George S., Nel A.E. A predictive toxicological paradigm for the safety assessment of nanomaterials. *ACS Nano* **2009**, *3*, 1620–1627.
[138] Madl A.K., Pinkerton K.E. Health effects of inhaled engineered and incidental nanoparticles. *Crit. Rev. Toxicol*. **2009**, *39*, 629-658.
[139] Warheit D.B., Sayes C.M., Reed K.L., Swain K.A. Health effects related to nanoparticle exposures: Environmental, health and safety considerations for assessing hazards and risks. *Pharmac. Therap*. **2008**, *120*, 35-42.
[140] Xia T., Li N., Nel A.E. Potential health impact of nanoparticles. *Nanomat.* **2009**, *30*, 137-150.
[141] Donaldson K., Stone V., Tran C.L., Kreyling W., Born P.J. *Nanotoxicology. Occup. Environ. Med*. **2004**, *61*, 727-728.
[142] Singh S., Nalwa H.S. Nanotechnology and health safety-toxicity and risk assessments of nanostructured materials on human health. *J. Nanosci. Nanotechnol*. **2007**, *7*, 3048-3070.
[143] Cheng Y.S., Hansen G.K., Su Y.F., Yeh H.C., Morgan K.T. Deposition of ultrafine aerosols in rat nasal molds. *Toxicol. Appl. Pharmacol*. **1990**, *106*, 222-233.

[144] Kelly J.T., Asgharian B. Nasal molds as predictors of fine and coarse particle deposition in rat nasal airways. *Inhal. Toxicol*. **2003**, *15*, 859-875.
[145] Bermendez E., Mangum J.B., Wong B.A., Asgharian B., Hext P.M., Warheit D.B. Pulmonary responces of mice, rats and hamsters to subchronic inhalation of ultrafine titanium dioxide particles. *Toxicol. Sci*. **2004**, *77*, 347-357.
[146] Donaldson K., Brown D., Clouter A., Duffin R., MacNee W., Renwick L. The pulmonary toxicology of ultrafine particles. *J. Aerosol Med*. **2002**, *15*, 213-220.
[147] Oberdorster G., Oberdorster E., Oberdorster J. Nanotoxicology: an emerging discipline evolving from studies of ultrafine particles. *Environ. Health Perspect*. **2005**, *113*, 823-839.
[148] Trouiller B., Reliene R., Westbrook A., Solaimani P., Schiestl R. H., Titanium dioxide nanoparticles induce DNA damage and genetic instability in vivo in mice. *Cancer Research* **2009**, *69*, 8784–8789.
[150] MacNee W., Donaldson K. How can ultrafine particles be responsible for increased mortality?. *Monaldi Arch. Chest. Dis*. **2000**, *55*, 135-139.
[151] Zhu Y., Hinds W.C., Krudysz M., Kuhn T., Froines J. Sioutas C. Penetration of freeway ultrafine particles into indoor environments. *J. Aerosol Sci*. **2005**, *36*, 303-322.
[152] Wichmann H.E., Spix C., Tuch T., Wolke G., Peters A., Heinrich J. Daily mortality and fine and ultrafine particles in Erfurt, Germany part I: role of particle number and particle mass. *Res. Rep. Health Eff. Inst*. **2000**, 5-86.
[153] Chen E.Y., Garnica M., Wang Y.C., Chen C.S., Chin W.C. Mucin secretion induced by titanium dioxide nanoparticles. *PLOS. One* **2011**, *6*, 1-8.
[154] Pujalte I., Passagne I., Brouillaud B., Treguer M., Durand E., Ohayon-Courtes C., L'Azou B. Cytotoxicity and oxidative stress induced by different metallic nanoparticles on human kidney cells. *Part. Fibre Toxicol*. **2011**, *8*, 1-16.
[155] Choi H.S., Ashitate Y., Lee J.H., Kim S.H., Matsui A., Insin N., Bawendi M.G., Semmler-Behnke M., Frangioni J.V., Tsuda A. Rapid translocation of nanoparticles from the lung airspaces to the body. *Nat. Biotechnol*. **2010**, *28*, 1300-1303.
[156] Kumar R., Roy I., Ohulchanskky T.Y., Vathy L.A., Bergey E.J., Sajjad M., Prasad P.N. In vivo biodistribution and clearance studies using multimodal organically modified silica nanoparticles. *ACS Nano* **2010**, *4*, 699-708.
[157] Hansson G.K., Robertson A.K., Soderberg-Naucler C. Inflammation and atherosclerosis. *Annu. Rev. Pathol*. **2006**, *1*, 297-329.
[158] Ozben B., Erdogan O. The role of inflammation and allergy in acute coronary syndromes. *Inflamm. Allergy Drug Targets* **2008**, *7*, 136-144.
[159] Park S., Lee S., Kim B., Lee S., Lee J., Sim S., Gu M., Yi J., Lee J. Toxic effects of titanium dioxide nanoparticles in microbial activity and metabolic flux. *Biotechnol. Bioprocess. Engin*. **2012**, *17*, 276-282.

[160] Frater, L., Stokes, E., Lee, R. & Oriola, T. An overview of the framework of current regulation affecting the development and marketing of nanomaterials. Cardiff, *UK: ESRC Centre for Business Relationships Accountability Sustainability and Society (BRASS)*, Cardiff University **2006**.
[161] Linsinger T., Roebben G., Gilliland D., Calzolai L., Rossi F., Gibson P., Klein C. Requirements on measurements for the implementation of the European Commission definition of the term "nanomaterial". *EUR 25404 EN. Luxembourg: Publications Office of the European Union*; **2012**.
[162] Seaton A., Tran L., Aitken R., Donaldson K. Nanoparticles, human health hazard and regulation. *J. R. Soc. Interface* **2010**, *7*, 119-129.
[163] Li P., Miser D.E., Rabiei S., Yadav R.T., Hajaligol M.R. The removal of carbon monoxide by iron oxide nanoparticles. *Appl. Catal. B Environ.* **2003**, *43*, 151–162.
[164] Kwon S., Fan M., Cooper A.T., Yang H. Photocatalytic applications of micro- and nano-TiO_2 in environmental engineering. *Crit. Rev. Environ. Sci Technol*. **2008**, *38*, 197-226.
[165] Li X.Z., Liu H., Chenge F. Photocatalytic oxidation using a new catalyst TiO_2 microsphere for water and wastewater treatment. *Environ. Sci. Technol*. **2003**, *37*, 3989-3994.
[166] Elder S.H., Gao Y., Li X., Liu J., McCready D.E., Windisch C.F. Zirconia-stabilized 25-angstrom TiO_2 anatase crystallites in a mesoporous structure. *Chem. Mater*. **1998**, *10* (10), 3140–3145.
[167] Yada M., Ohya M., Machida M., Kijima T. Mesoporous gallium oxide structurally stabilized by yttrium oxide. *Langmuir* **2000**, *16* (10), 4752–4755.
[168] Guo C., Ge M., Liu L., Gao G., Feng Y., Wang Y. Directed synthesis of mesoporous TiO_2 microspheres: catalysts and their photocatalysis for bisphenol A degradation. *Environ. Sci. Technol*. **2010**, *44*, 419-425.
[170] Bianchi C.L., Gatto S., Pirola C., Naldoni A., Di Michele A., Cerrato G., Crocellà V., Capucci V. Photocatalytic degradation of acetone, acetaldehyde and toluene in gas-phase: comparison between nano and micro-sized TiO_2. *App. Catal. B: Environm.* **2014**, *146*, 123-130.
[171] Bianchi C.L., Colombo E., Gatto S., Stucchi M., Cerrato G., Morandi S., Capucci V. Photocatalytic degradation of dyes in water with micro-sized TiO_2 as powder or coated on porcelain-gres tiles. *J. Photochem. Photobiol. A: Chem.* **2014**, *280*, 27-31.
[172] J.S. Park, W. Choi Enhanced remote photocatalytic oxidation on surface-fluorinated TiO_2. *Langmuir*, **2004**, *20*, 11523-11527.
[173] D. Monllor-Satoca, R. Gomez Electrochemical Method for Studying the Kinetics of Electron Recombination and Transfer Reactions in Heterogeneous

Photocatalysis: The Effect of Fluorination on TiO_2 Nanoporous Layers. *J. Phys. Chem. C* **2008**, *112*, 139-147.

[174] M.V. Dozzi, E. Selli Doping TiO_2 with p-block elements: effects on photocatalytic activity. *J. Photochem. Photobiol.* C. **2013**, *14*, 13-28.

[175] M. Hermann, U. Kaluza, H.P. Boehm, Z. On the chemistry of the surface of the titanium dioxide. IV. Exchange of hydroxide for fluoride ions. *Anorg. Chem*. **1970**, *372*, 308-313.

[175] C. Minero, G. Mariella, V. Maurino, E. Pelizzetti Photocatalytic Transformation of Organic Compounds in the Presence of Inorganic Anions. 1. Hydroxyl-Mediated and Direct Electron-Transfer Reactions of Phenol on a Titanium Dioxide−Fluoride System. *Langmuir* **2000**, *16*, 2632-2641.

[176] Kim H., Choi W. Effects of surface fluorination of TiO_2 on photocatalytic oxidation of gaseous acetaldehyde. *Appl. Catal. B: Environ*. **2006**, *69*, 127-132.

[177] Loganathan K., Bommusamy P., Muthaiahpillai P., Velayutham M. The synthesis, characterization and photocatalytic activities of silver, platinum and gold doped TiO_2 nanoparticles. *Environ. Engin. Res.* **2011**, *16*, 81-90.

[178] Kumar S.G., Devi L.G. Review on modified TiO_2 photocatalysis under UV/visible light: selected results and related mechanisms on interfacial charge carrier transfer dynamics. *J. Phys. Chem. A* **2011**, *115*, 13211-13241.

[179] Roy S., Hegde M.S., Ravishankar N., Madras G. Creation of redox adsorption sites by Pd^{2+} ion substitution in nano TiO_2 for high photocatalytic activity of CO oxidation, NO oxidation, and NO decomposition. *J. Phys. Chem. C* **2007**, *111*, 8153–8160.

[180] Vinu R., Madras G. Photocatalytic activity of Ag-substituted and impregnated nano-TiO_2. *Appl. Catal. A: Gen*. **2009**, *366*, 130–140.

[182] Melián E.P., Díaz O.G., Rodríguez J.M.D., Colón G., Navío J.A., Macías M., Peña J.P. Effect of deposition of silver on structural characteristics and photoactivity of TiO_2-based photocatalysts. *Appl. Catal. B: Environ*. **2012**, *127*, 112-120.

[183] Li X., Wang L., Lu X. Preparation of silver-modified TiO_2 via microwave-assisted method and its photocatalytic activity for toluene degradation. *J. Haz. Mater*. **2010**, *177*, 639-647.

[184] Schüler E., Gustavsson A.-K., Hertenberger S., Sattler K. Solar photocatalytic and electrokinetic studies of TiO_2/Ag nanoparticle suspensions. *Solar Energy* **2013**, *96*, 220-226.

[185] Vinu R., Madras G. Photocatalytic activity of Ag-substituted and impregnated nano-TiO_2. *Appl. Catal. A: Gen*. **2009**, *366*, 130–140.

[186] Saha S., Wang J.M., Pal A. Nano silver impregnation on commercial TiO_2 and a comparative photocatalytic account to degrade malachite green. *Separ. Purif. Technol*. **2012**, *89*, 147-159.

[187] Sclafani A., Herrmann J.M. Influence of metallic silver and of platinum-silver bimetallic deposits on the photocatalytic activity of titania (anatase and rutile) in organic and aqueous media. *J. Photochem. Photobiol*. **1998**, *113*, 181–188.
[188] Carp O., Huisman C.L., Reller A. Photoinduced reactivity of titanium dioxide. *Prog. Solid State Chem*. **2004**, *32*, 133–177.
[189] Kondo M.M., Jardim W.F. Photodegradation of chloroform and urea using Ag-loaded titanium dioxide as catalyst. *Wat. Res*. **1991**, *25*, 823–827.
[190] Sahoo C., Gupta A.K., Pal A. Photocatalytic degradation of a mixture of Crystal Violet (Cl Basic Violet 3) on silver ion doped TiO_2. *Dyes Pigments* **2005**, *66*, 189–196.
[191] Behnajady M.A., Modirshahla N., Shokri M., Rad B. Enhancement of photocatalytic activity of TiO_2 nanoparticles by silver doping: photodeposition versus liquid impregnation methods. *Global Nest J*. **2008**, *10*, 1–7.
[192] Casasola R., Rincòn J.M., Romero M. Glass-ceramic glazes for ceramic tiles: a review. *J. Mater. Sci*. **2012**, *47*, 553-582.
[193] Fujishima A, Zhang XT Titanium dioxide photocatalysis: present situation and future approaches. *Comptes Rendus Chimie* **2006**, *9*(5–6), 750–60.
[194] Cassar L. Photocatalysis of cementitious materials: Clean buildings and clear air. *Mater. Res. Soc. Bulletin* **2004**, *29*, 328-331.
[195] Sugranez R., Cruz-Yusta M., Marmol I., Martin F., Morales J., Sànchez L. Use of industrial waste for the manufacturing of sustainable building materials. *ChemSusChem* **2012**, *5*, 694-699.
[196] Chusid M. Words you should know: depollution, photocatalysis. *Concrete* **2006**.
[197] Essroc Italcementi Group "Concrete that cleans itself and the environment", presentation on behalf of Essroc Italcementi Group at CONSTRUCT2009, Indiana Convention Center, Indianapolis, IN, **2009**.
[198] Folli, A., Pade C., Bæk Hansen T., De Marco T., Macphee D.E. TiO_2 photocatalysis in cementitious systems: Insights into self-cleaning and depollution chemistry. *Cem. Conc. Res*. **2012**, *42*, 539-548.
[199] Fujishima A., Hashimoto K., Watanabe T. TiO_2 photocatalyst, fundamentals and applications BKC Inc., **1999**, Tokyo, *66*.
[200] Cucitore R., Cangiano S., Cassar L. High durability photocatalytic paving for reducing urban polluting agent. WO/2006/000565, **2006**.
[201] Murata Y., Tawara H., Obata H., Murata K. NO_X-cleaning paving block, EP0786283, **2003**.
[202] Guerrini G.L., Plassais A., Pepe C., Cassar L., Environment and Construction Materials, in *International RILEM Symposium on Photocatalysis*, eds. L. Cassar and P. Baglioni, RILEM, Florence **2007**, *1*, 219-226.

[203] Chen J., Poon C. Photocatalytic construction and building materials: from fundamentals and applications. *Build. Envir*. **2009**, *44*, 1899-1906.
[204] Poon C.S., Cheung E. NO removal efficiency of photocatalytic paving blocks prepared with recycled materials. *Cons. Build. Mater*. **2006**, *21*(8), 1746–1753.
[205] Poon C.S., Cheung E. Performance of photo-catalytic paving blocks made from waste. *Waste Res. Manag*. **2006**, *159*, 165–171.
[206] Beeldens A. Air purification by road materials: results of the test project in Antwerp. In: Baglioni P, Cassar L, eds. *RILEM Int. Symp. On photocatalysis, environment and construction materials*. Italy; **2007**, 187–194.
[207] Husken G., Hunger M., Brouwers H. Comparative study on cementitious products containing titanium dioxide as photo-catalyst. In: Baglioni P, Cassar L, eds. *RILEM Int. Symp. On Photocatalysis, environment and construction materials*. Italy; **2007**, 147–154.
[208] Kawakami M., Furumura T., Tokushige H. NO_x removal effects and physical properties of cement mortar incorporating titanium dioxide powder. In: Baglioni P, Cassar L, eds. *RILEM Int. Symp. On photocatalysis, environment and construction materials*. Italy; **2007**, 163–170.
[209] Strini A., Cassese S., Schiavi L. Measurement of benzene, toluene, ethylbenzene and o-xylene gas phase photodegradation by titanium dioxide dispersed in cementitious materials using a mixed flow reactor. *Appl. Catal. B: Envir*. **2005**, *61*(1–2), 90–97.
[210] Demeestere K., Dewulf J., Witte B.D., Beeldens A., Langenhove H.V. Heterogeneous photocatalytic removal of toluene from air on building materials enriched with TiO_2. *Build. Envir*. **2008**, *43*(4), 406–414.
[211] Staub de Melo J.V., Triches G. Evaluation of the influence of environmental conditions on the efficiency of photocatalytic coatings in the degradation of nitrogen oxides (NO_x). *Build. Envir*. **2012**, *49*, 117-123.
[212] Hassan M.M., Dylla H., Mohammad L.N., Rupnow,T. Evaluation of the durability of titanium dioxide photocatalyst coating for concrete pavement. *Cons. Build. Mater*. **2010**, *24*, 1456-1461.
[213] Bianchi C.L., Pirola C., Gatto S., Nucci S., Minguzzi A., Cerrato G., Biella S., Capucci V. New surface properties in porcelain gres tiles with a look to human and environmental safety. *Adv. Mater. Sci. Engin.* **2012**, *2012*, 1-8.
[214] Bianchi C.L., Gatto S., Pirola C., Scavini M., Vitali S., Capucci V. Micro-TiO_2 as a starting material for new photocatalytic tiles. *Cem. Conc. Comp.* **2013**, *36*
[215] Aissa A.H., Puzenat E., Plassais A., Herrmann J.-M., Haehnel C., Guillard C. Characterization and photocatalytic performance in air of cementitious materials containing TiO_2. Case study of formaldehyde removal. *App. Catal. B: Envir*. **2011**, *107*, 1-8.

[216] Watanabe T., Nakajima A., Wang R., Minabe M., Koizumi S., Fujishima A., Hashimoto K. Photocatalytic activity and photoinduced hydrophilicity of titanium dioxide coated glass. *Thin Solid Films* **1999**, *351*, 260–263.
[217] Peruchon L., Puzenat E., Herrmann J.M., Guillard C. Photocatalytic efficiencies of self-cleaning glasses. Influence of physical factors. *Photochem. Photobiol. Sci*. **2009**, *8*, 1040-1046.
[218] Cassar L. Photocatalysis of cementitious materials: clean buildings and clean air. *MRS Bulletin* **2004**, *29*, 328–331.
[219] Wang K.H., Tsai H.H., Hsieh Y.H. A study of photocatalytic degradation of trichloroethylene in vapor phase on TiO_2 photocatalyst. *Chemosphere* **1998**, *36*, 2763–2773.
[220] Kolarik J., Toftum J. The impact of a photocatalytic paint on indoor air pollutants: sensory assessments. *Build. Environ*. **2012**, *57*, 396–402.
[221] Salthammer T., Fuhrmann F. Photocatalytic surface reactions on indoor wall paint. *Environ. Sci. Technol*. **2007**, *41*, 6573–6578.
[222] Maury-Ramirez A., Demeestere K., De Belie N. Photocatalytic activity of titanium dioxide nanoparticle coatings applied on autoclaved aerated concrete: effect of weathering on coating physical characteristics and gaseous toluene removal. *J. Hazard. Mater.* **2012**, *211–212*, 218–225.
[223] Pirola C., Boffito D.C., Vitali S., Bianchi C.L. Photocatalytic coatings for building industry: study of 1 year of activity in the NO_x degradation. *J. Coat. Technol. Res*. **2012**, *9*, 453–458.
[224] Yuranova T., Sarria V., Jardim W., Rengifo J., Pulgarin C., Trabesinger G. Photocatalytic discoloration of organic compounds on outdoor building cement panels modified by photoactive coatings. *J. Photochem. Photobiol. A* **2007**, *188*, 334–341.
[225] Diamanti M.V., Ormellese M., Pedeferri M.P. Characterization of photocatalytic and superhydrophilic properties of mortars containing titanium dioxide. *Cem. Concr. Res.* **2008**, *38*, 1349–1353.
[226] Lackhoff M, Prieto X, Nestle N, Dehn F, Niessner R. Photocatalytic activity of semiconductor-modified cement-influence of semiconductor type and cement ageing. *Appl. Catal. B* **2003**, *43*, 205–216.
[227] Rachel A, Subrahmanyam M, Boule P. Comparison of photocatalytic efficiencies of TiO_2 in suspended and immobilised form for the photocatalytic degradation of nitrobenzenesulfonic acids. *Appl. Catal. B* **2002**, *37*, 301–308.
[228] Nagaveni K, Hegde MS, Madras G. Structure and Photocatalytic activity of $Ti_{1-x}M_xO_{2\pm\delta}$ (M = W, V, Ce, Zr, Fe, and Cu) synthesized by solution combustion method. *J. Phys. Chem. B* **2004**, *108*, 20204–20212.

Chapter 2

PhD's work project

It is presented the main purposes of this PhD's research, considering the actual key questions, yet unanswered, concerning the photocatalytic action and related performances of TiO_2 catalyst. The effort to conduct a research on this field is connected to the actual demand for a greater improvement of application of these semiconductor materials, especially for the industrial applications. For this aim, even commercial porcelain tiles covered with micro-sized TiO_2 were tested and studied in detail, in parallel with the photocatalytic TiO_2 powders.

2.1 Brief foreword

Powders of TiO_2 have been commonly used as white pigments from ancient times [1]. TiO_2 is a very important semiconductor with a high potential for applications in photocatalysis, solar cells, photochromism, and various other areas of nanotechnology [2,3]. Nowadays, TiO_2 is widely used as photocatalyst in air purification devices and a surface treatment and additive in ceramics, cement, transportation infrastructure and glass. These products are used or evaluated for their depollution, self-cleaning, antifungal, and environmental improvement attributes [4]. These applications can be classified into two remarkable classes: "energy" and "environment". Their catalytic performances not depend only on TiO_2 material as it is, but even on the possible modifications that could generated on it by the addition of proper chemical doping species or by the interaction of TiO_2 catalyst with the surrounding environment. So, in the last years there has been a big effort for the synthesis of TiO_2 with controlled dimensions and physico-chemical characteristics, such as surface area, porosity, crystallographic phase [5]. The mentioned above characteristics, have important effects on the photocatalytic performance; thus, the improvement of performance by adjusting these factors is still a major focus of photocatalysis research [6]. The performance of TiO_2-based materials is largely influenced even by the size of TiO_2 particles. For example, the synthesis by sol-gel method provided the possibility to study the correlation between the characteristics and properties of TiO_2 as photocatalyst, especially in the environmental remediation as mentioned above (pollutant degradation in gas and liquid-phase) [7]. In fact, the sol-gel synthesis

supports an accurate control of the final characteristics of synthesized product, by varying the kind of solvent (ratio water/alkoxide, water/solvent), time and calcination temperature [8]. Granted that, the essential of TiO_2 photocatalyst is to provide for the photoabatement of various environmental pollutants breaking down them into less harmful chemical products, or even carbon dioxide and water in the optimal work conditions [9]. However, the large band gap (3.0 to 3.2 eV) of unmodified titanium dioxide made it too inefficient to produce hydrogen from sunlight due to the small number of sufficiently energetic photons. There have been several efforts to modify TiO_2 so that visible light could possibly be used. For this aim, the doping with metal ions is widely being used, because of their specific capacities to adsorb photons of higher wavelength waves (nm). In this way, the spectral region of adsorption shifts towards the visible region.

Because of the advantages given by TiO_2 photocatalyst in the environmental depollution, in the recent literature there has been a great interest of TiO_2-containing cements for self-cleaning and air depollution [10]. Cement is one of the most used manufactured substances, applied on a large scale in the production of spectra of cement-based construction materials (mortars, concrete, and renders). Cement based-coatings including TiO_2 particles for exterior surfaces of the buildings are therefore attracting increasing interests. Large surfaces of cement-based materials in build environment and infrastructural objects (buildings, pavements, roads, bridges, etc.) are exposed to polluted environment, causing gradual deterioration of both surface properties and structural characteristics of different construction materials. In recent years, the increasing interest combining photocatalytic active materials with cementitious materials has

been recognized in a number of publications [11-13]. Most of the published research refers to the application of nano-sized TiO_2 semiconductor as photocatalytic active material [14,15], trying to develop challenges in order to achieve stable photocatalytic activity and adequate compatibility with the substrate and therefore durability during the time. Different techniques for TiO_2 application in the cement-based matrix have been used, such as: mixing with the cementitious materials, sputtering, spray coating and sol–gel dip coating [16].

2.2 Novelty of PhD's project

For a long time, new synthesis routes have been developing to prepare nano-TiO_2 samples in order to enhance the photocatalytic efficiency. The enhancement of the photocatalytic efficiency is due to the small particles and, therefore to the high surface area [17-19]. However, in recent years many papers published the possible dangerous of nano-sized materials [20,21]. Small size, shape, solubility and agglomeration degree of nano-sized materials can lead to the process in which nanoparticles cross the cell boundaries or pass directly from the lungs into the blood stream and finally reach all the organs in the body. Moreover, these reasons may raise more serious problems than when materials with larger particles are used. One of the possible way to nanoparticles exposure is inhalation by breathing [22]. So, it becomes essential to look for alternative materials maintaining photocatalytic properties.

The novelty of this PhD's work is to test larger-sized TiO_2 compounds in order to compare with nano-sized. Moreover, it is important to evaluate the possibility of using micro-sized TiO_2, which results in a greater environmental impact and higher production costs compared to the nano-sized particles. Therefore, the photocatalytic behavior of different commercial powdered TiO_2 was compared. On the one hand, nano-sized photoactive TiO_2 samples were randomly chosen among all the commercially available. On the other hand, micro-sized materials were chosen among the commercial titania-based pigmentary products having some specific features: pure anatase polymorph, particle size over 100 nm, absence of ultrafine particles, no specific post-treatment on the material surface for the stabilization after the preparation, no addition of dopants. Photocatalytic tests with TiO_2 were carried out to evaluate the degradation of both VOCs and NO_x pollutants in gas phase, and organic dyes and surfactants in aqueous phase.

In addition, TiO_2 powders were doped with cations, such as rhenium (Re), and anions like fluoride ions (F^-) in order to improve the photoactivity. Ren at al. [23] demonstrated that the fluorination of TiO_2 nanocrystals gave a photocatalytic enhancement due to the higher separation efficiency of photogenerated electrons and holes in the former. The fluorination of TiO_2 can have promising potential applications in environmental remediation, solar cell, renewable clean energy applications owing to their unique properties. In the literature is even reported that Re dopant could effectively inhibit the recombination of the photoinduced electrons and holes [24]. Re can act as electron trap and promote the interfacial charge transfer processes in the composite systems, which reduces the recombination of photoinduced

electron-hole pairs, thus improving the photocatalytic activity of TiO_2. It also results in the extension of their wavelength response towards the visible region. Moreover, noble metal particles can facilitate the electron excitation by creating a local electrical field. So, a further study was involved irradiating the TiO_2 catalysts with only visible light (LED light), evaluating their photoefficiency.

A further important industrial application is the preparation and characterization at the base of a new kind of fired tiles able to reduce polluting molecules present in air thanks to their new photocatalytic properties. The extreme originality of these products is the surface presence of micro-sized TiO_2. The possibility to use micro-sized TiO_2 in a commercial manufactured product opens a new generation of material intrinsically safer than the traditional photocatalytic products for both workers in the factories and public safety, even though, with such materials that are surface vitrified, the release of TiO_2 particles is extremely remote. In this PhD work, new industrial photocatalytic tiles were tested for the degradation of environmental pollutants. The porcelain gres slabs are prepared with the commercial TiO_2 pigmentary powder with crystallites larger than the classical nanoparticles usually used in photocatalysis. The final heat treatment at 680°C assures a perfect and stable fixation of the TiO_2 particles. Then, the photocatalytic properties of this material have been verified through depollution and self-cleaning tests.

In conclusion, the research has dealt with different typologies of catalysts: simple micrometric TiO_2 powders and gres porcelain tiles covered with micro-sized TiO_2. The photocatalytic efficiency was verified evaluating the degradation of several ubiquitous pollutants, such as NO_x,

VOCs. To understand properly the influence of many parameters as the distribution of particles on the catalyst surface or the amount of hydroxyl radicals species on the photocatalytic process, a deep catalysts characterization study has been made using different techniques (BET, TEM, SEM, FT-IR, XPS, XRD, photoelectrochemical analysis). It was so possible to correlate the photoefficiency with the catalysts properties. All the catalysts in shape of powders were tested depositing them in glass laminas as it will be explained in the Chapter 4 (see paragraph 4.1.1), whereas the addition of anionic or cationic species have been made through the simple surface impregnation method. Both UV and visible light (LED lamp) were used as irradiation source for the photodegradation with TiO_2 catalysts.

2.3 References

[1] Pfaff G., Reynders P. Angle-dependent optical effects deriving from submicron structures of films and pigments. *Chem. Rev*. **1999**, *99*, 1963-1982.
[2] Ismail A.A., Bahnemann D.W. Mesoporous titania photocatalysts: preparation, characterization and reaction mechanisms. *J. Mater. Chem*. **2011**, *21*, 11686-11707.
[3] Kumar A., Madaria A.R., Zhou C. Growth of aligned single-crystalline rutile TiO_2 nanowires on arbitrary substrates and their application in dye-sensitized solar cells. *J. Phys. Chem. C* **2010**, *14*, 7787-7792.
[4] Chen P. Hu X., Chen C., Gu J., Chen Y. Research progress in supported TiO_2 photocatalysts. *Cailiao Kaifa Yu Yingyong* **2013**, *28*, 117-124.
[5] Chen X., Mao S.S. Titanium dioxide nanomaterials: synthesis, properties, modifications and applications. *Chem. Rev*. **2007**, *107*, 2891-2959.

[6] Fujishima A., Nakata K., Ochiai T., Manivannan A., Tryk D.A. Recent aspects of photovoltaic technologies for solar fuels, self-cleaning, and environmental cleanup. *The Electrochm. Soc. Inter*. **2013**, 51-56.
[7] Macwan D.P., Dave P.N., Chaturvedi S. A review on nano-TiO_2 sol-gel type synthesis and its applications. *J. Mater. Sci.* **2011**, *46*, 3669-3686.
[8] Mayo M. J., Hague D.C., Chen D.-J. Processing nanocrystalline ceramics for applications in superplasticity. *Mater. Sci. Engin*. **1993**, *166*, 145-159.
[9] Miranda-Garcia N., Suarez S., Sanchez B., Coronado J.M., Malato S., Maldonado M.I. Photocatalytic degradation of emerging contaminants in municipal weastewater treatment plant effluents using immobilized TiO_2 in a solar pilot plant. *App. Catal. B: Environm*. **2011**, *103*, 294-301.
[10] Krishnan P., Zhang M.-H., Yu L., Fenh H. Photocatalytic degradation of particulate pollutants and self-cleaning performance of TiO_2-containing silicate coating and mortar. *Construct. Build. Mater.* **2013**, *44*, 309-316.
[11] Chen J., Poon C.S. Photocatalytic cementitious materials: influence of the microstructure of cement paste on photocatalytic pollution degradation. *Environ. Sci. Technol*. **2009**, *43*, 8948–8952.
[12] Chen J., Kou S.C., Poon C.S. Photocatalytic cement-based materials: comparison of nitrogen oxides and toluene removal potentials and evaluation of self-cleaning performance. *Build. Environ*. **2011**, *46*, 1827–1833.
[13] Ruot B., Plassais A., Olive F., Guillot L., Bonafous L. TiO_2 – containing cement paste and mortars: measurements of the photocatalytic efficiency using rhodamine B-based colorimetric test. *Solar Energy* **2009**, *83*, 1794–1801.
[14] Diamanti M.V., Ormellese M., Pedeferri M. Characterization of photocatalytic and superhydrophilic properties of mortars containing titanium dioxide. *Cem. Concr. Res.* **2008**, *38*, 1349–1353.
[15] Nazari A., Riahi S. TiO_2 nanoparticles effects on physical, thermal and mechanical properties of self compacting concrete with ground granulated blast furnace slag as binder. *Energ. Build*. **2011**, *43*, 995–1002.
[16] Vulic T., Hadnadjev-Kostic M., Rudic O., Radeka M., Marinkovic-Neducin R., Ranogajec J. Improvement of cement-based mortars by application of photocatalytic active Ti–Zn–Al nanocomposites. *Cement Conc. Compos*. **2013**, *36*, 121–127.
[17] Gupta S.M., Tripathi M. A review on the synthesis of TiO_2 nanoparticles by solution route. *Central European J. Chemistry* **2012**, *10*, 279-294.

[18] Wang X., Liu Y., Hu Z., Chen Y., Liu W., Zhao G. Degradation of methyl orange by composite photocatalysts nano TiO_2 immobilized on activated carbons of different porosities. *J. Hazard. Mater*. **2009**, *169*, 1061-1067.
[19] Macwan D.P., Dave P.N., Chaturvedi S. A review on nano TiO_2 sol-gel type synthesizes and its applications. *J. Mater. Science* **2011**, *46*, 3669-3686.
[20] Love S.A., Maurer-Jones M.A., Thompson J.W., Lin Y-S. Assessing nanoparticle toxicity. *Annu. Rev. Anal. Chem.* **2012**, *5*, 181-205.
[21] Park S., Lee S., Kim B., Lee S., Lee J., Sim S., Gu M., Yi J., Lee J. Toxic effects of titanium dioxide nanoparticles on microbial activity and metabolic flux. *Biotechnol. and Bioprocess Engin*. **2012**, *17*, 2, 276-282.
[22] Amoabediny G., Naderi A., Malakootikhah J., Koohi M.K., Mortazavi S.A., Naderi M., Rashedi H. Guidelines for safe handling, use and disposal of nanoparticles. *J. Physics* **2009**, *170*, 1-13.
[23] Ren L., Li Y., Hou J., Zhao X., Pan C. Preparation and enhanced photocatalytic activity of TiO_2 nanocrystals with internal pores. *App. Mater. Interfaces* **2014**, *6*, 1608-1615.
[24] He H., Liu C., Dubois K.D., Jin T., Louis M.E., Li G. Enhanced charge separation in nanostructured TiO_2 materials for photocatalytic and photovoltaic applications. *I&EC Res.* **2012**, *51*, 11841-11849.

Chapter 3

Characterization methods and results

Here, we focus on the photocatalytic commercial powders and gres-tiles physico-chemical properties. At first, the characterization techniques, used for a proper study and understanding of the catalytic systems behavior, are illustrated, such as microscopic (HR-TEM, SEM), spectroscopic (FT-IR, UV-VIS, XRD) and chromatographic (HPLC-MS) techniques. Then, brief description even on the basics of electrochemical technique (cyclic voltammetry) used to gain additional information on the specific photoefficiency of the various catalytic TiO_2 powders. Finally, there will be shown the characterization results, made on both powders and porcelain gres tiles.

3.1 Catalysts characterization: introduction and theory

According to Fadoni [1], the basic characterization involves two main steps: the investigation on the porous nature of catalyst support (physical properties) and on the properties of the active sites that are dispersed on the support surface (**Table 3.1**).

Table 3.1. General scheme of catalysts characterization

Catalyst texture			
Physical properties		**Chemical properties**	
Result	**Technique**	**Result**	**Technique**
Geometry and shape	- Optical microscopy	Chemical composition	-Electron spectroscopy -Atomic adsorption
Total specific surface area	-Gas physisorption -Mercury porosimetry	Degree of dispersion	-Selective chemisorption -X-ray -Electron microscopy -Magnetisation analysis
True density	-X-ray analysis -Neutron diffraction	Degree of dispersion	-Selective chemisorption -X-Ray -Electron microscopy -Magnetisation analysis
Bulk and apparent density	-Helium pycnometry -Mercury porosimetry -Liquid displacement	Surface Energy	-Thermal analysis test -Temperature programmed desorption and reaction calorimetry
-Pore specific volume -Porosity	-Mercury porosimetry -Gas adsorption	Acid-base sites	-Selective chemisorption -Temperature programmed desorption
Pore size and mean pore size	-Mercury porosimetry -Gas Adsorption	Redox sites	-Spectroscopic methods -Temp. programmed reduction -Temp. Programmed oxidation
Particle size	-Sieves -Laser scattering -Sedimentation -Electrical sensing zone -Etc.	-Catalytic properties -Activity -Selectivity	Reactor tests and simulation
Surface structure	-Optical microscopy -Electron microscopy -X-Ray analysis		
Surface change	Z potential		

The complete and accurate knowledge of the properties of a catalyst is fundamental for evaluating its performance. In this work there were used several techniques to investigate their physical and chemical properties.

The used techniques were BET (adsorption method for surface area evaluation), SEM and TEM (electron microscopy), XPS (electron spectroscopy for the evaluation of electronic state of the elements on the catalysts surface), FT-IR (vibrational spectroscopy for chemistry of surface groups), XRD (spectroscopic technique for the information about the structure of crystalline materials). In this chapter, the catalyst characterization techniques will be reported and discussed. Further, in **Paragraph 3.3** the photoelectrochemical characterization technique, useful for discussion of specific studies, will be shown.

3.1.1 Brunauer Emmett Teller (BET) technique

According to Nelsen et al. [2] the most widely used method for determining surface area involves measuring the amount of gas adsorbed on a solid surface at a temperature close to the boiling point of the gas. Nitrogen is most commonly used as the adsorbate. Adsorption methods may be used to provide information about the total surface area of a catalyst, the surface area of the phase carrying the active sites, or possibly even the type and number of active sites. The interaction between the adsorbate and the adsorbent may be chemical (chemisorption) or physical (physisorption) in nature and ideally should be a surface-specific interaction. Physical adsorption is used in the BET method to determine total surface areas [3].

This technique of characterization of solid has the acronym derived from authors (Brunauer, Emmett and Teller [4], 1938) of the particular equation that allows to determine a parameter of great importance in the study of the solid ones, that is the superficial specific area. Such parameter expresses the relationship between the total surface of the catalyst and the weight of the same one and usually is expressed in m^2/g. Technique BET uses the principle of the physical inert gas adsorption (nitrogen) to varying of the relationship between the partial pressure of nitrogen and its vapor pressure to the temperature of liquid nitrogen. BET theory is a well-known rule for the physical adsorption of gas molecules on a solid surface that is basis for an important analysis technique for the measurement of the specific surface area of a material. The concept of the theory is an extension of the Langmuir theory, which is a theory for monolayer molecular adsorption, to multilayer adsorption with the following hypotheses: (a) gas molecules physically adsorb on a solid in layers infinitely; (b) there is no interaction between each adsorption layer; and (c) the Langmuir theory can be applied to each layer. The resulting BET equation is the following:

$$\frac{V}{V_m} = \frac{c\frac{p}{p^\circ}}{\left[1-\left(\frac{p}{p^\circ}\right)\right]\left[1+(c-1)\frac{p}{p^\circ}\right]} \qquad \textbf{(3.1)}$$

Where:

V = volume of adsorbed gas at pressure P
p° = gas saturation pressure, at temperature T
p/p° = relative pressure
C = BET constant, expressed by the following:

$$C = \exp((q_1 - q_L)/RT) \quad \textbf{(3.2)}$$

Where

q_1 = heat of adsorption of the first layer
q_L = heat of adsorption of the second and higher layers

For the V_m calculation the (3.2) must be linearized and the linear relationship of this equation is maintained only in the range of $0.05 < P / P_0 < 0.35$:

$$\frac{\frac{p}{p^\circ}}{V\left[1-\left(\frac{p}{p^\circ}\right)\right]} = \frac{1}{CV_m} + \frac{(c-1)\frac{p}{p^\circ}}{cV_m} \quad \textbf{(3.3)}$$

Equation (3.3) is an adsorption isotherm and can be plotted as a straight line with $1 / V[(P^\circ / P) - 1]$ on the y-axis and P / P_0 on the x-axis according to experimental results. The specific surface area is determined on the V_m basis:

$$S.A. = \frac{V_m . N_{AV} . A_{mol}}{V_{mol}} \quad \textbf{(3.4)}$$

Where:

N_{AV} = Avogadro's number
A_{mol}= adsorption cross section (for N_2 = 16.2 Å^2)
V_{mol}= molar volume of gas (22414 ml/mol)

Experimental: The samples have been analysed using a Costech Sorptometer 1042 "KELVIN", using liquid nitrogen. Before the analysis, the catalyst is put in oven (T = 110°C for 16 h) to remove the adsorbed water. Then a quantity between 0.08 g and 0.2 g in analyzed in the instrument. The sample is pre-treated for 2 h at T = 200°C in a N_2 flow to

remove all the impurity, then a check with helium is made to calibrate the interspatial volume.

3.1.2 Spectroscopic techniques

There exist different parameters to describe light adsorption, as transmittance and absorbance (for transparent samples) and diffuse reflectance and Kubelka-Munk transformation (for scattering samples).

The transmittance (*T*) is the fraction of incident light at a specified wavelength (λ) that passes through a sample:

$$\boldsymbol{T = \frac{I}{I_0}} \qquad \textbf{(3.5)}$$

where I_0 is the intensity of incident radiation and *I* the intensity of the radiation passing through the sample. Likewise, the absorbance (*A*) is defined by the equation:

$$\boldsymbol{A = -logT = -log\frac{I}{I_0}} \qquad \textbf{(3.6)}$$

It is worth noting that the absorbance measured at a particular λ is directly proportional to the optical length (*l*) and to the concentration (*c*) and molar absorptivity (*ε*) of the light absorbing species. The molar absorptivity is an intrinsic property of the absorbing species and depends on the incident wavelength. Therefore *A* at a given wavelength can be expressed via the so-called *Lambert-Beer law* as follows:

$$\boldsymbol{A = \varepsilon(\lambda)\cdot l\cdot c} \qquad \textbf{(3.7)}$$

However, these concepts cannot be used when characterizing samples with strong light scattering, since part of the incident light is lost by processes that differ from absorption. In these cases, when incident light

reaches the sample surface, it is, aside from partially transmitted and absorbed, dispersed. This idea is summarized in the following relation:

$$\boldsymbol{A + T + R = 1} \qquad \textbf{(3.8)}$$

where it is indicated that once the light reaches the sample, part of the radiation is absorbed (*A*), part is transmitted (*T*) and other part is reflected (*R*). The dispersion of the radiation can be specular (the angle of incidence equals the angle of reflection) and/or diffuse (radiation is dispersed in many directions). In order to obtain the UV-vis spectra of light-scattering samples it is necessary to use an integrating sphere. As shown in **Fig. 3.1**, with this accessory all the radiation dispersed from the sample can be efficiently harvested in the detector because the sphere is coated with a highly dispersive material with poor light absorption. In this way, the *diffuse reflectance spectra* of the sample can be obtained. It is useful to calculate the Kubelka-Munk transformation of the diffuse reflectance (*R*) values using the following equation:

$$\boldsymbol{F(R) = \frac{(1-R)^2}{2R}} \qquad \textbf{(3.9)}$$

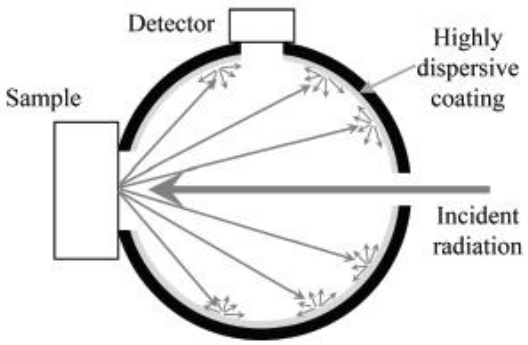

Fig. 3.1. Illustration of an integrating sphere.

The transformed spectra resemble typical absorption spectra, facilitating their analysis (and comparisons with true absorption spectra). In general, the absorption spectroscopy delivers spectra where either the absorbance or the reflectance is plotted against the wavelength. It is important to emphasize that light absorption features contain relevant information regarding the electronic structure of the samples.

3.1.2.1 X-ray photoelectron spectroscopy (XPS)

XPS is a quantitative technique that allow us to obtain information about the atomic composition, chemical environment and electronic state of the elements forming the sample, especially those located in its surface.

This technique involves the irradiation of the sample with a monochromatic beam of X-rays, causing the emission of electrons from the core of the atoms and simultaneously measuring the kinetic energy (KE) and number of electrons that escape from the top 1 to 10 nm of the material being analyzed. The analysis of these electrons, known as the photoelectrons, is the basis of the XPS analysis. Note that given that the energy of the X-ray irradiating the sample is known, the electron binding energy (E_b) of each emitted electron can be determined by using the following equation:

$$\boldsymbol{E_b = h\nu - (E_k + \Phi)} \qquad \textbf{(3.10)}$$

where $h\nu$ is the energy of the incident X-ray photons, E_k is the kinetic energy of photoelectrons emitted from the sample and Φ is the work function of the spectrophotometer.

XPS requires ultra-high vacuum (UHV) conditions. XPS is a surface chemical analysis technique that can be used to analyze the surface chemistry of a material in its "as received" state. XPS is also known as ESCA, an abbreviation for Electron Spectroscopy for Chemical Analysis. XPS detects all elements with an atomic number (Z) between those of lithium (Z=3) and lawrencium (Z=103). This limitation means that it cannot detect hydrogen (Z=1) or helium (Z=2). XPS is used to measure elemental composition of the surface (1–10 nm usually), empirical formula of pure materials, elements that contaminate a surface, chemical or electronic state of each element in the surface.

XPS technique is based on the analysis of the kinetic energy distribution of core level photoelectrons ejected as the result of irradiation with monochromatic or narrow band X-rays [3]. The best sensitivity is of the order of a few percent of a monolayer and for most instruments. spatial resolution is around 0.2 mm. With suitable calibration procedures, elemental surface concentrations can be measured with an accuracy of the order of 20%. It constitutes a major tool in catalysts characterization. The major interest is centred on observations of “chemical shift” effects, which reflect the oxidation state, and the chemical environment of the emitter. Quantitative applications, especially to complex systems such as catalysts, can involve problems due to sample charging and to the choice of calibration procedures. XPS has been widely used in catalyst research to provide general qualitative analyses, to investigate the depth profile distribution of active species, to obtain estimates of dispersion, clustering and other morphological variations, to study metal-metal and metal-support interactions and to examine the chemical states of additives, poisons and

transition metal ions in zeolites. Proven measurement techniques and models for interpolation [5,6] are available.

XPS spectra are obtained by recording the quantity of photoelectrons emitted as a function of the binding energy. These spectra are formed by different peaks corresponding to different atoms. Moreover, the position of these peaks depends on the chemical environment, *i.e.* the number of valence electrons and type of bonds with neighbouring atoms. In such a way it is possible to discern not only different elements, but also, different oxidation states.

Experimental: XPS measurements were performed in a M-Probe Instrument (SSI) equipped with a monochromatic Al Ka source (1486.6 eV) with a spot size of 200mm - 750 mm and a pass energy of 25 eV, providing a resolution for 0.74 eV. The accuracy of the reported binding energies (BE) can be estimated to be 0.2 eV. The quantitative data were checked accurately and reproduced several times (at least 10 times for each sample).

3.1.2.2 FT-IR analysis

Infrared spectroscopy is the subset of spectroscopy that deals with the infrared region of the electromagnetic spectrum. It covers a range of techniques, the most common being a form of absorption spectroscopy. As with all spectroscopic techniques, it can be used to identify compounds or investigate sample composition. Infrared spectroscopy correlation tables are tabulated in the literature.

The infrared portion of the electromagnetic spectrum is divided into three regions; the near-, mid- and far- infrared, named for their relation to the visible spectrum. The far-infrared, approximately 400-10 cm^{-1} (1000–30 μm), lying adjacent to the microwave region, has low energy and may be used for rotational spectroscopy. The mid-infrared, approximately 4000-400 cm^{-1} (30–1.4 μm) may be used to study the fundamental vibrations and associated rotational-vibrational structure. The higher energy near-IR, approximately 14000-4000 cm^{-1} (1.4–0.8 μm) can excite overtone or harmonic vibrations. Infrared spectroscopy exploits the fact that molecules have specific frequencies at which they rotate or vibrate corresponding to discrete energy levels. These resonant frequencies are determined by the shape of the molecular potential energy surfaces, the masses of the atoms and by the associated vibronic coupling. In order for a vibrational mode in a molecule to be IR active, it must be associated with changes in the permanent dipole. In particular, in the Born-Oppenheimer and harmonic approximations, i.e. when the molecular Hamiltonian corresponding to the electronic ground state can be approximated by a harmonic oscillator in the neighborhood of the equilibrium molecular geometry, the resonant frequencies are determined by the normal modes corresponding to the molecular electronic ground state potential energy surface. Nevertheless, the resonant frequencies can be in a first approach related to the strength of the bond, and the mass of the atoms at either end of it. Thus, the frequency of the vibrations can be associated with a particular bond type.

Molecules that are more complex have many bonds and vibrations can be conjugated, leading to infrared absorptions at characteristic frequencies that may be related to chemical groups. The infrared spectra of a sample are

collected by passing a beam of infrared light through the sample. Examination of the transmitted light reveals how much energy was absorbed at each wavelength. This can be done with a monochromatic beam, which changes in wavelength over time, or by using a Fourier transform instrument to measure all wavelengths at once. From this, a transmittance or absorbance spectrum can be produced, showing at which IR wavelengths the sample absorbs. Analysis of these absorption characteristics reveals details about the molecular structure of the sample. This technique has been used for the characterization of very complex mixtures.

This vibrational spectroscopy is used for characterisation of high area supported or unsupported catalysts, including zeolites. Information is available, either directly or by study of "probe" adsorbates, on the chemistry of surface groups (particularly on oxides). Problems include low transmission at high metal loadings and strong oxide scattering. Absorption at lower wavenumbers often prevents observation of modes such as adsorbate-metal stretching. Fourier Transform (FIIR) spectrometers offer two pronounced advantages over dispersive instruments: higher energy throughput and faster data acquisition or higher signal-to-noise ratio. Data processing is easy. These features are significant when examining very strongly absorbing and scattering solids and when following dynamic processes. Much IR transmission work, however, requires examination of only limited frequency ranges at medium resolution and computerised dispersive spectrometers may then be preferable.

Experimental: the IR analysis were performed in collaboration with the **University of Turin (Prof.ssa Cerrato, Dr.ssa Crocellà, Dr.ssa**

Morandi). Absorption/transmission IR spectra have been obtained on a Perkin-Elmer FT-IR System 2000 spectrophotometer equipped with a Hg-Cd-Te cryo-detector, working in the range of wavenumbers 7200-580 cm^{-1} at a resolution of 2 cm^{-1} (number of scans ~20) (**Fig. 3.2**). For IR analysis powder catalyst has been compressed in self-supporting disc (of about 10 mg cm^{-2}) and placed in a homemade quartz cell, equipped with KBr windows, connected to a conventional high-vacuum line (UHV). Spectra were recorded at room temperature (RT) on the samples in air and after prolonged outgassing at RT.

Fig. 3.2. FTI-IR model Perkin-Elmer FT-IR System 2000 spectrophotometer.

3.1.2.3 X-ray diffraction (XRD)

X-ray powder diffraction (XRPD) is a non-destructive analytical technique widely applied for the characterization of crystalline materials [7-9]. This method has been traditionally used for phase identification,

quantitative analysis and the determination of structure imperfections of powdered solid samples.

Powder diffraction is commonly used to identify unknown substances, by comparing diffraction data with those in the international data base. In fact, each crystalline solid produces distinctive diffraction patterns. When a monochromatic X-ray beam passes through a crystalline sample, it interacts with the electrons in the atoms, resulting in scattering of the radiation. If the matter is crystalline, *i.e.* the atoms are organized in planes and the distances between the atoms are of the same magnitude as the X-rays wavelength, constructive and destructive interference will occur. The process of diffraction is described in terms of incident and reflected (or diffracted) rays, each forming an angle, q, with a fixed crystal plane. In particular, when the interaction of the incident rays with the sample produces constructive interference (**Fig. 3.3**), the diffraction phenomena satisfy the so-called Bragg law [10,11]:

$$n\lambda = 2dsen\theta \qquad \textbf{(3.11)}$$

where:

λ = incident light wavelength
n = integer positive number (0,1,2,3,etc.)
d = interplane spacing
θ = angle between the incident radiation and the planes (h,k,l)

The incident angle is chosen by rotating the crystal relative to the beam, the wavelength is fixed and thus the interplanar spacing d is obtained. The conclusion is that any set of planes in a crystal will reflect an X-ray beam if the set of planes is at right angle to the incident beam.

The intensity of the reflected beam is proportional to the product of the intensity of the incident beam and the concentration of electrons in the

reflecting plane. Thus if the unit cell dimensions are known and, subsequently, the atomic number of each of the atoms, it is possible to calculate the concentration of electrons and hence the intensity of the reflected beam. In powder diffraction it's important to have samples with a smooth plane surface, with the crystallites randomly distributed. The powder sample is filled in a small disc and placed in the analysis equipment. The monochromatic X-ray source is placed on a rotating arm, in order to light the sample with a variable angle q. The reflected radiation is collected by the detector, even fixed on a rotating arm, placed at twice this angle. As 2θ is the angle measured between the detector and the incident beam, as shown in **Fig. 3.3**, the diffracted radiation is collected by the detector at the very same incident angle θ.

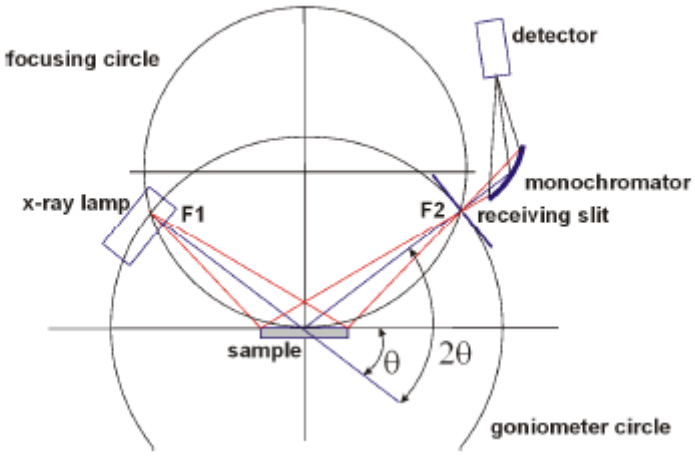

Fig. 3.3. Schematic diagram of an X-ray diffractometer.

Moreover from XRPD patterns, crystallite sizes can be calculated. Generally as the size of the crystallite decreases, the angular spread of the reflection increases. In this thesis the value of the FWHM (full width at half maximum) of the most intensive line of each phase was used in order to

measure the mean particle (crystallite) size, by applying the Scherrer formula:

$$d_{hkl} = \frac{0.9\lambda}{\beta cos\theta} \quad \textbf{(3.12)}$$

where:

$d_{(hkl)}$ = size (nm) of particles in the direction vertical to the corresponding lattice plane.
l = X-ray incident wavelength.
b = line broadening at half maximum intensity (FWHM) expressed in rad.
q = incident angle.

Experimental: The crystalline nature of the samples was investigated by X-ray diffraction (XRD) using a PW3050/60 X'Pert PRO MPD diffractometer from PAN analytical working Bragg-Brentano, using as source the high power ceramic tube PW3373/10 LFF with a Cu anode equipped with Ni filter to attenuate Kβ. Scattered photons have been collected by a RTMS (Real Time Multiple Strip) X'celerator detector. The calculation of the crystallite size is given by the Scherrer equation: $t = 0.9\ \lambda/(\beta_{h\,k\,l} \times \cos\theta_{h\,k\,l})$, where t is the crystallite size, λ is the X-ray wavelength of radiation for CuKβ, $\beta_{h\,k\,l}$ is the full width at half maximum (FWHM) at ($h\ k\ l$) peak and $\theta_{h\,k\,l}$ is the diffraction angle.

3.1.3 HPLC-MS

High-Performance Liquid Chromatography (HPLC) was initially discovered as an analytical technique in the early twentieth century and was first used as a method of separating colored compounds. This is where the name chromatography "chroma" means color, "graphy" means writing, was

derived. A Russian botanist named Mikhail S. Tswett used a rudimentary form of chromatographic separation to purify mixtures of plant pigments into the pure constituents [12]. He separated the pigments based on their interaction with a stationary phase, which is essential to any chromatographic separation. The result of this process most crucial to his investigation was that the plant pigments separated into bands of pure components as they passed through the stationary phase. Modern high performance liquid chromatography or HPLC has its roots in this separation, the first form of liquid chromatography.

All chromatographic separations, including HPLC operate under the same basic principle; every compound interacts with other chemical species in a characteristic manner [12]. Chromatography separates a sample into its constituent parts because of the difference in the relative affinities of different molecules for the mobile phase and the stationary phase used in the separation. In general, chromatography involves moving a sample through the system over a stationary phase. HPLC is a type of liquid chromatography used to separate and quantify compounds that have been dissolved in solution. It is used to determine the amount of a specific compound in a solution. In HPLC and liquid chromatography, where the sample solution is in contact with a second solid or liquid phase, the different solutes in the sample solution will interact with the stationary phase. Thus, the differences in interaction with the column can separate different sample components from each other.

Retention or elution volume is the quantity of the mobile phase required to pull the sample through the column. Retention time is defined as how long a component is retained in the column by the stationary phase relative

to the time it resides in the mobile phase. The retention is best described as a column capacity ratio (k'), which can be used to evaluate the efficiency of columns. The longer a component is retained by the column, the greater is the capacity factor. The column capacity ratio of a compound (A) is defined by the following equation:

$$\boldsymbol{k' = \frac{T_A - T_0}{T_0} = \frac{V_A - V_0}{V_0}} \qquad \textbf{(3.13)}$$

where V_A is the elution volume of the component A and V_0 is the elution volume of a non retained compound. At constant flow rate, retention times (T_A and T_0) can be used instead of retention or elution volumes.

Resolution is the ability of the column to separate peaks on the chromatograph. Resolution (R) is expressed as the ratio of the distance between two peak maxima to the mean value of the peak width at the base line:

$$\boldsymbol{R = \frac{(T_B - T_A)^2}{w_{A+} w_B}} \qquad \textbf{(3.14)}$$

where T_B is the retention time of component B, T_A is the retention time of the component A, w_A is the peak width of component A and w_B is the peak width of component B. If R is equal to or more than 1, then components are completely separated, but if R is less than 1, then components overlap.

Sensitivity is a measure of the smallest detectable level of a component in a chromatographic separation and is dependent on the signal-to-noise ratio in a given detector.

HPLC instrumentation includes a pump, injector, column, detector and integrator or acquisition and display system as reported in **Fig. 3.4**. The heart of the system is the column where separation occurs. Since the stationary phase may be composed of micron-sized porous particles, a high-

pressure pump is required to move the mobile phase through the column. The chromatographic process begins by injecting of the solute into the injector at the end of the column. Separation of components occurs as the analytes and mobile phase are pumped through the column. Eventually, each component elutes from the column as a peak on the data display. The response of the detector to each component is displayed on a computer screen and is known as a chromatogram.

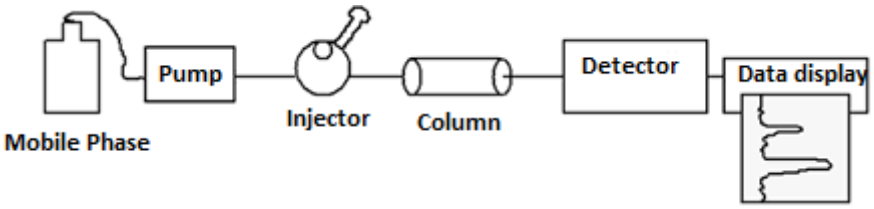

Fig. 3.4. Schematic of a High-Performance Liquid Chromatograph.

Experimental: it has been used the Agilent 1100 Series HPLC instrument. The separations were performed using isocratic eluent that is an eluent with unchanging composition during the analysis. In this work, the used eluent has the following composition: acetonitrile, ice acetic acid, water, in equal ratios; the solvent useful to dissolve the powders has the same chemical composition.

3.1.4 Microscopic techniques

These techniques help to give an insight into the morphology and the composition of the samples under study. The main techniques employed in

this work uncover the shape and the morphology of TiO_2 powders and gres-tiles are shown below.

3.1.4.1 High-Resolution Transmission Electron Microscopy (HR-TEM)

Transmission electron microscopy (TEM) is a microscopy technique whereby a beam of electrons is transmitted through an ultra thin specimen, interacting with the specimen as it passes through it [13]. An image is formed from the electrons transmitted through the specimen, magnified and focused by an objective lens and appears on an imaging screen, a fluorescent screen in most TEMs, plus a monitor, , or to be detected by a sensor such as a CCD camera. The first practical transmission electron microscope was built by Albert Prebus and James Hillier at the University of Toronto in 1938 using concepts developed earlier by Max Knoll and Ernst Ruska.

Theoretically, the maximum resolution that one can obtain with a light microscope has been limited by the wavelength of the photons that are being used to probe the sample and the numerical aperture of the system. Early twentieth century scientists theorized ways of getting around the limitations of the relatively large wavelength of visible light (wavelengths of 400–700 nanometers) by using electrons. Like all matter, electrons have both wave and particle properties (as theorized by Louis-Victor de Broglie), and their wave-like properties mean that a beam of electrons can be made to behave like a beam of electromagnetic radiation. Electrons are usually generated in an electron microscope by a process known as thermionic emission from a filament, usually tungsten. Electrons are then accelerated by an electric potential (measured in V, or volts) and focused by electrostatic and

electromagnetic lenses onto the sample. The beam interacts variously with the sample due to differences in density or chemistry. The beam that is transmitted through the sample contains information about these differences, and this information in the beam of electrons is used to form an image of the sample. The contrast in a TEM image is not like the contrast in a light microscope image. A crystalline material interacts with the electron beam mostly by diffraction rather than absorption, although the intensity of the transmitted beam is still affected by the volume and density of the material through which it passes. The intensity of the diffraction depends on the orientation of the planes of atoms in a crystal relative to the electron beam; the electron beam may be diffracted or transmitted. TEM is still suitable for examination of supported catalysts with particle sizes down to 2-3 nm, giving information on particle location over the support, on particle-size distributions in favourable cases, on particle and support morphology and on the nature and distribution of deposits having a thickness of the order of 2-3 nm. Surface topography can be examined using replication techniques.

Experimental: the HR-TEM analysis have been made in collaboration with the **University of Turin (Prof.ssa Cerrato, Dr.ssa Crocellà, Dr.ssa Morandi)** using their instrument. HR-TEM analysis were made using a JEOL 3010-UHR instrument (acceleration potential: 300 kV; LaBs filament). Samples were “dry” dispersed on lacey carbon Cu grids.

3.1.4.2 Scanning Electron Microscopy (SEM)

The scanning electron microscope (SEM) is a type of electron microscope that creates various images by focusing a high energy beam of

electrons onto the surface of a sample and detecting signals from the interaction of the incident electrons with the sample's surface. The type of signals gathered in a SEM varies and can include secondary electrons, characteristic X-rays, and back scattered electrons. In a SEM, these signals come not only from the primary beam impinging upon the sample, but from other interactions within the sample near the surface. The SEM is capable of producing high-resolution images of a sample surface in its primary use mode, secondary electron imaging. Due to the manner in which this image is created, SEM images have great depth of field yielding a characteristic three-dimensional appearance useful for understanding the surface structure of a sample. Characteristic X-rays are emitted when the primary beam causes the ejection of inner shell electrons from the sample and are used to tell the elemental composition of the sample. The back-scattered electrons emitted from the sample may be used alone to form an image or in conjunction with the characteristic X-rays as atomic number contrast clues to the elemental composition of the sample. The SEM was pioneered by Manfred von Ardenne in 1937 [14]. The instrument was further developed by Charles Oatley and first commercialized by Cambridge Instruments. The spatial resolution of the SEM depends on the size of the electron spot, which in turn depends on both the wavelength of the electrons and the magnetic electron-optical system which produces the scanning beam. The resolution is also limited by the size of the interaction volume, or the extent to which the material interacts with the electron beam. The spot size and the interaction volume both might be large compared to the distances between atoms, so the resolution of the SEM is not high enough to image individual atoms, as is possible in the shorter wavelength (i.e. higher energy)

transmission electron microscope (TEM). The SEM has compensating advantages, though, including the ability to image a comparatively large area of the specimen; the ability to image bulk materials (not just thin films or foils); and the variety of analytical modes available for measuring the composition and nature of the specimen. Depending on the instrument, the resolution can fall somewhere between less than 1 nm and 20 nm. In general, SEM images are easier to interpret than TEM images.

Experimental: SEM analysis have been made in collaboration with **University of Perugia (Dr. Di Michele)** using their instrument. SEM images were measured using an electron microscopy Philips XL-30CP with RBS detector of back-scattered electrons and EDS analyzer was used to describe the surface and elemental composition of catalysts.

3.1.5 Photoelectrochemical measurements

In this section, it will be explained the equipment utilized to carry out photoelectrochemical experiments in three-electrode cell configuration, specifying the specific electrochemical set-up employed in this research work.

3.1.5.1 Electrode films preparation

Four different types of commercial TiO_2, two nanometric (AEROXIDE® TiO_2 P25 by Evonik Ind. and PC105 by CrystalGlobal) and two micrometric (1077 by Kronos and AH-R by Hundsman) have been used for preparing

TiO_2 electrode films. TiO_2 electrodes were prepared by spreading an aqueous slurry of commercial nano- or micro-sized TiO_2 over a fresh cleaned conductive glass (fluorine-doped tin oxide, FTO glass). TiO_2 films were prepared by spreading (*doctor blading*) an aqueous slurry of TiO_2 powder over the substrates. In order to gain the same thickness on the electrodes surface, the suspension was prepared by adding 0.25 g. or 0.5 g. of TiO_2 powder, respectively for nanoparticles and microparticles of TiO_2, with an amount of H_2O (1.25 ml. for nanopowders and 1 ml for micropowders), 15 µL of acetylacetone (99 + % Aldrich), and 15 µL of Triton X100 (Aldrich). In general, 15 µL of this suspension were applied for FTO glass and a thin film of TiO_2 was obtained using the doctor blade method (the slurry was spread using a Pasteur pipette). Afterwards, the films were annealed and sintered for 2 h at 450°C in air. The average thickness (in µm) was measured with a Perfilomiter Instrument (KLA Tencor D-100) in two different portion of the TiO_2 annealed film, resulting to be ~ 3 µm. Then it is measured also the surface area in cm^2 of the TiO_2 film for the different TiO_2 samples and electrodes annealed on the FTO glass. The geometric area of electrodes was ~ 1 cm^2.

3.1.5.2 Three-electrode cell configuration

The photoelectrochemical cell used is made of two compartments; one including the working and the counter electrodes and the other for the reference electrode. It is shown in **Fig. 3.5**. In all cases, an Ag/AgCl/KCl(sat.) electrode was used as a reference, whereas a Pt wire was employed as a countered electrode.

The experiments were performed in acid media, by employing a $HClO_4$ water solution (0.1M). The electrolyte was purged either with N_2 for 30 min before measurements, keeping a N_2 flow over it, or with O_2 to saturate the electrolyte solution, depending on the cases of investigation.

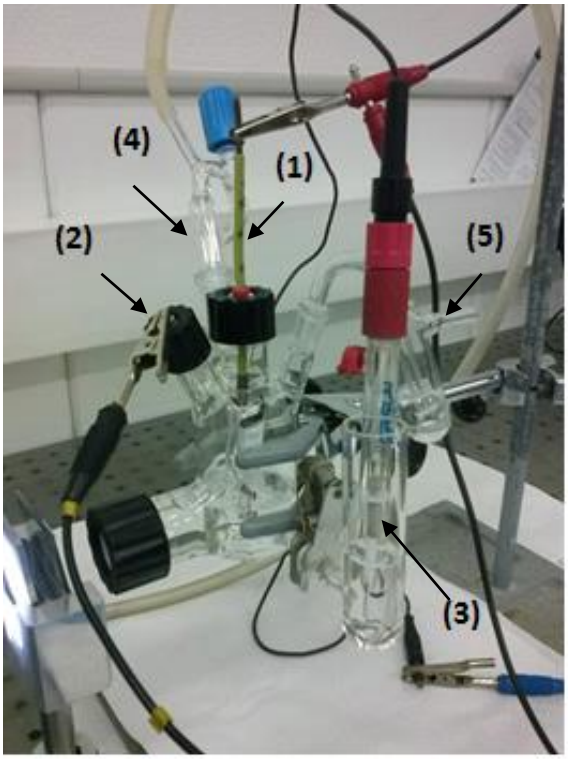

Fig. 3.5. Photoelectrochemical cell: (1) working electrode, (2) counter electrode, (3) reference electrode, (4) gas bubbler, (5) gas outlet.

3.1.5.3 Cyclic voltammetry

Cyclic voltammetry (CV) has become an important and widely used electroanhalitical technique in many area of chemistry. The high versatility of cyclic voltammetry is the result of the possibility of rapidly provide a

considerable number of information on the thermodynamics of redox processes, the kinetics of heterogeneous electro-transfer reactions, coupled chemical reactions, adsorption processes etc. CV measures the current that develops in an electrochemical cell between the working and the counter electrode, after the potential applied to the working electrode is varied.

The potential of the working electrode is varied and measured against a reference electrode, which maintains a constant potential, as shown in Fig. 4.6 The potential fist scans negatively, starting from a value (a) and ending at a final potential (b), and then the potential is reversed in opposite direction from (b) to (c). The potential extreme (b) is call the switching potential, where the voltage is sufficient to have caused an oxidation or reduction of an analyte. **Fig. 3.6** shows a typical reduction occurring from (a) to (b) and an oxidation from (b) to (c). This cycle can be repeated, and the scan rate can be varied.

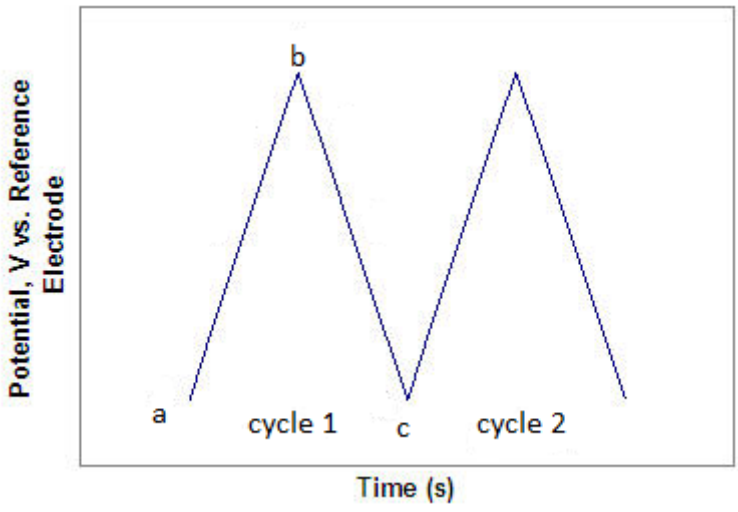

Fig. 3.6. Schematic of the variation of the potential of the working electrode with time in CV.

The time is converted to potential, and the resulting plot is to record current *vs.* potential, named cyclic voltammetry (**Fig. 3.7**). The reduction process starts from initial positive potential to negative values, reaching to the point, called cathodic peak potential (E_{pc}), at which all the substrate at the surface of the electrode has been reduced. Reversely, the potential scans positively from negative to positive values, leading to the anodic peak potential (E_{pa}), where all of the substrate at the electrode surface has been oxidized.

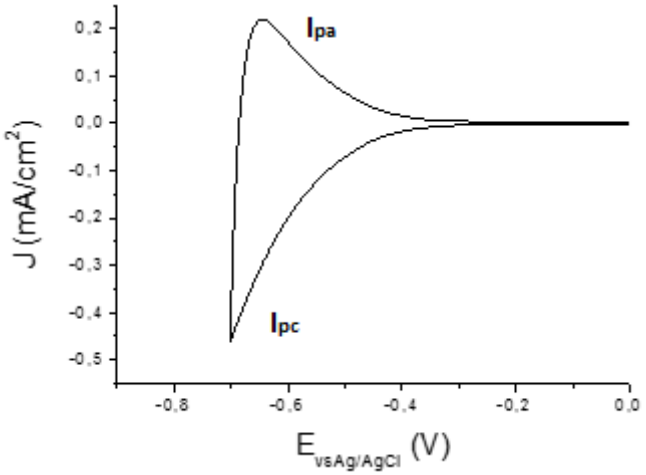

Fig. 3.7. Example of cyclic voltammogram obtained for a TiO_2 film at a scan rate of 20 $mV \cdot s^{-1}$ under N_2 flux in the dark ($HClO_4$ 0.5M).

The peak current (i_p) is given by:

$$\boldsymbol{i_p = \left(2.69 \times 10^5\right) n^{3/2} A D^{1/2} v^{1/2} C} \qquad \textbf{(3.15)}$$

where i_p is the peak current (in amperes), **n** is the number of electrons passed per molecule of analyte oxidized or reduced, *A* is the electrode area (in cm^2), *D* is the diffusion coefficient of analyte (in cm^2/sec), *v* is the

potential sweep rate (in volts/sec), and *C* is the concentration of analyte in bulk solution (in moles/cm^3).

Moreover, the charge density (*q*) exchanged during the potential excursion can be extracted from the voltammogram [15]. The current density (*j*) is defined as the rate at which charge (*Q*) flows per unit surface area (*A*):

$$\boldsymbol{j = \frac{1}{A}\frac{dQ}{dt} = \frac{dq}{dt}} \quad \textbf{(3.16)}$$

This expression can be rewritten as:

$$\boldsymbol{dq = jdt} \quad \textbf{(3.17)}$$

Since: $\boldsymbol{v = \frac{dE}{dt}}$ **(3.18)**

By the integration in the potential range, the charge density can be determined as:

$$\boldsymbol{q = \int_{E_1}^{E_2} \frac{j}{v} dE = \int_{E_1}^{E_2} \frac{I}{Av} dE} \quad \textbf{(3.19)}$$

Experimental: CV analysis were performed with the collaboration of **University of Alicante, Spain (Prof. P. Bonete and R. Gomez)**, where there were performed a serious of photoelectrochemical analysis during the beginning of the third year of the PhD. To perform photoelectrochemical measurements, Xe arc lamp of 150 W was used as illumination source. A quartz window on the voltammetric cell was utilized for photoelectrochemical experiments. The electrochemical measurements were carried out using a computer-controlled Autolab PGSTAT30 potentiostat in

most of the cases. All the cyclic voltammograms were recorded at a scan rate of 20 $mV \cdot s^{-1}$.

3.1.6 Contact angle

The wettability of a solid surface is an important parameter that strongly depends on the surface roughness. In general, the wettability is commonly evaluated by contact angle (CA), given by *Young*'s equation [16]. This equation is applicable only to flat surfaces and not to rough ones. However, most real solid surfaces are rough and heterogeneous. Thus, some contact angles on real surfaces may show hysteresis.

The control of surface wettability is important for many biological processes and industrial applications. Both superhydrophobicity (water contact angle (CA) >150°) and superhydrophilicity (water CA<5°) have attracted extensive attention [17,18]. TiO_2 exhibits both super-hydrophobicity and super-hydrophilicity behavior by UV illumination. Superhydrophobic surfaces are often prepared by hydrophobic modification of rough surfaces, for example by treating the surface with hydrophobic reagents, like fluorosilane [19], which have applications in microfluidic devices or in textile areas [20].

However, another aspect is the super-hydrophilicity with a water contact angle of 0°C [21,22], showing antifogging and self-cleaning properties [23]. When this surface is illuminated by UV irradiation, water starts to exhibit a decrease of contact angle, in certain cases even to near 0°C [21-24,25]. This photo-induced superhydrophilicity is useful for environmental applications

as self-cleaning materials [26]. The CA starts to spread up on the surface and, at this stage, it is termed "highly hydrophilic". The surface maintains a CA of a few degrees for a day without being exposed to UV light. Then, the CA increases, and the surface becomes less hydrophilic. At this point, the high hydrophilicity can be recovered simply by exposing the surface again to UV light. In this way, anti-fogging function can be achieved. The fogging of the surfaces of mirrors and glasses occurs when steam cools down on these surfaces forming water droplets. On a highly hydrophilic surface, the water droplets are not formed. Instead, a uniform thin film of water, which prevents the fogging, is formed. For this reason, in the last years many cars, fabricated in Japan, are equipped with antifogging highly hydrophilic side-view mirrors [27] in order to development new technological devices.

At the same way, self-cleaning effects are obtained with a hydrophilicity TiO_2 surface. An example is the deposition of oleic acid on the catalytic surface, in order to examine the combined effect of photo-oxidation and photo-induced hydrophilic efficiency. At first, a layer of oleic acid is deposited on the TiO_2 surface, and consequently the surface is converted to a hydrophobic state (with a contact angle of ~60°-70°) due to the hydrophobic property of oleic acid. When UV light is irradiated on TiO_2 surface, the water contact angle decreases slowly till to get ~10°C. Oleic acid adsorbed is, so, decomposed by the photocatalytic oxidation, meanwhile TiO_2 itself becomes a hydrophilic state. Moreover, when TiO_2 is illuminated by light, dirt and organic contaminants are decomposed and can easily be swept away by water (rain) (ISO/WD 27448-1).

In this PhD research self-cleaning action was checked through the simple irradiation of the gres tiles with the UV lamp (iron halogenide lamp,

Jelosil, model HG500), as reported in **Fig. 3.8**, and the measurements of the water CA before and after the irradiation.

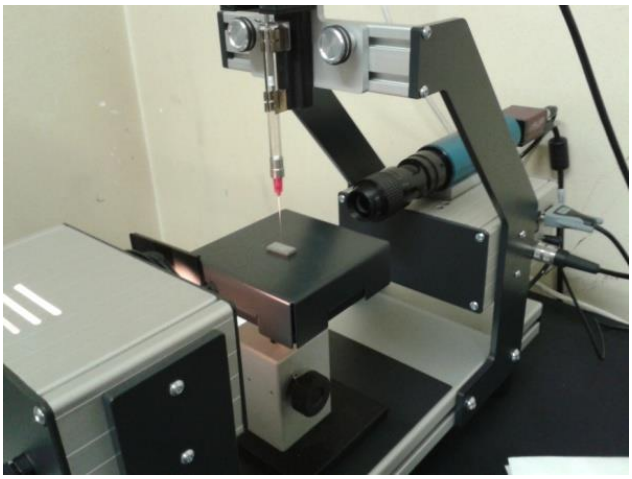

Fig. 3.8. Picture of water contact angle, model FM40Mk2 *EasyDrop*, KRUSS GmbH.

Experimental: self-cleaning action was followed through the measurement of the water contact angle (FM40Mk2 EasyDrop, KRUSS GmbH) before and after the irradiation for *n* hours. The oleic acid was used as contaminant pollutant. The contact angle was determined through a DSA1 program, which offers the possibility to evaluate mathematically the drop image. It is possible to calculate the exact baseline of a CA and further, the correct angle value with the evaluation method that changes depending on the relative shape. To calculate the angles highs it is suitable the use of *the Conic Section method*, which completes profile of a sessile drop, giving a general conic equation. On the other hand, for small angles it is possible to adopt the *the Young-Laplace* and *Circle Fitting methods* (CA inferior than 60° and 30°). The first one determines the CA fitting it to a polynomial function.

The second one is particularly suitable for small CA (<30°C). In that case, the drop shape is adapted mathematically to a circular segment shape, by evaluating the whole drop outline and not just the area of intersection with the baseline. All the results were collected and conveyed the drop volume, the area and the contact angle.

3.2 Experimental characterization results

The results reported in this paragraph concern both TiO_2 powders and porcelain gres tiles. All the characterization analyses of powders have been made on fresh samples, before their photocatalytic applications. For what concerns tile samples, the analyses have been made without any specific pretreatment. The characterization is able to highlight the difference between the various catalysts, supporting the peculiar photoresponse of every sample.

3.2.1 TiO_2 naked powders results

The present section reports an accurate characterization study among different kinds of catalysts. The main discrimination is the size of the relative samples. We analyzed both a series of commercial micro-sized TiO_2 samples, sold as not photocatalytic materials as already discussed in the **Chapter 2**, and a sequence of classical nano-crystallites commercial

materials. In **Table 3.2** the photocatalytic powders used in this PhD work is reported. The XRD patterns relative to the four selected samples, chosen as example, are reported in **Fig. 3.9**. Anatase is the unique polymorph present for all samples, except for the well-known P25, which exhibits the phase composition 75:25 in anatase/rutile ratio, and for the micro-sized Hombikat N.10 with 2% of rutile.

Table 3.2. Main features of the selected TiO_2 sample.

Sample	BET (m^2g^{-1})	Crystallites size (nm)	XPS Ti $2p_{3/2}$ (eV)	XPS OH/O_{tot}	Band Gap (eV)
P25	50	26	458.4	0.14	3.21
PC105	80	23	458.4	0.85	3.19
1077	12	130	458.3	0.32	3.15
1071	10	Mix (30-130)	458.3	0.18	3.25
1001	11	Mix (30-130)	458.3	0.27	3.28
1002	9	Mix (30-130)	458.3	0.35	3.25
Hombitam AZ	4	130	458.3	0.27	3.17
Hombitam AN	12	180	458.3	0.5	3.18
HombiKat N.10	13	90	458.3	0.13	3.15
AT-1	12	192	458.3	0.24	3.15
AH-R	12	130	458.3	0.19	3.15

The crystallographic reflexes (1 0 1), (2 0 0) and (2 1 1) have been employed to calculate the average crystallites size of the various titania particles (**Table 3.2**, third column). P25 and P105 have comparable crystallite size centered at around 25 nm, while the samples 1077, AT-1, AH-R, Hombitam AN, AZ and HombiKat N.10 have values at around 130-180 nm. These latters exhibit well-crystalized particles of rather roundish shape, closely packed. These structural properties are reflected in the BET

surface area of micro-sized samples (1077, AT-1, AH-R, Hombitam AZ, AN and HombiKat N.10) which is much lower compared to the nano-sized one (**Table 3.2**, second column) [28].

Commercial TiO_2 powders are investigated by UV-vis analysis with the aim to check the region where the adsorption of radiation can occur (**Fig. 3.10**). In fact, we can highlight interesting features: all samples adsorb in the region of $\nu > 400$ nm. This adsorption is not expected, except P25 because of the presence of the rutile (25%). In fact, for the Hombikat N10, which possess the 2% of rutile, the adsorption in that region is higher than the other ones. However, these feature states that all commercial TiO_2 samples, not sold as photocatalysts, have the adsorption even in the visible region. The obtained band-gap values do not exhibit large differences among the various samples and fall in the range expected for anatase [29] and it seems not to be influenced by the crystallites size.

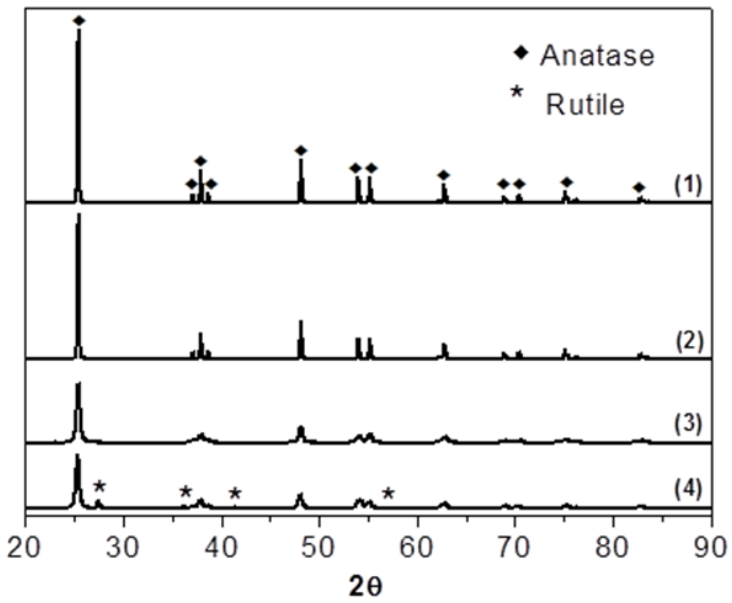

Fig. 3.9. XRD patterns of AT-1 (1), 1077 (2), PC105 (3) and P25 (4).

The morphological aspects of all samples was highlighted by HR-TEM (**Fig. 3.11**) and SEM (**Fig. 3.12**). TEM images (**Fig. 3.11**) confirm the above average crystallites size extrapolated by XRD analysis also excluding the presence of ultrafine particles as it is visible in 1077, AT-1 and AH-R samples. It can be also evidenced that the nano-sized materials perfectly fall within the "nano" definition: in fact, both samples are characterized by average particles size of 15–30 nm, closely packed features and roundish contours. In any case, the highly crystalline nature of the particles is witnessed by the incidence of fringe patterns, generated by the superimposition of crystals (mostly) belonging to the TiO_2 anatase polymorph. For both nano-sized samples, the most frequently observed planes (d = 0.357 nm) are due to the (1 0 1) family [30].

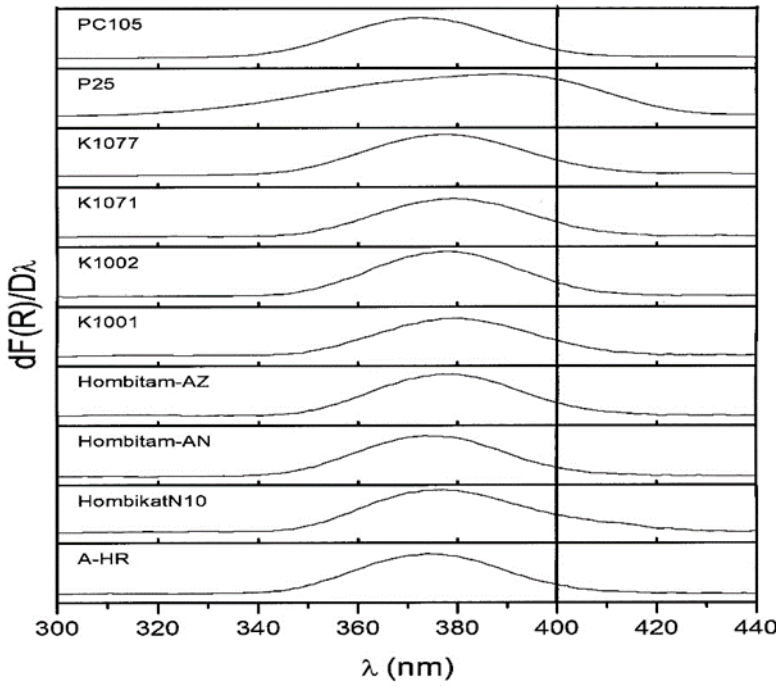

Fig. 3.10. UV-vis spectra for all commercial TiO_2 powders (nano- and micro-sized samples).

As for what concern the micro-sized materials, they are characterized by huge average dimensions of the particles: see the bottom sections of **Fig. 3.11**. This feature totally agrees again with the indications coming from XRD analysis, pointing out that both 1077, AT-1 and AH-R samples exhibit average dimensions in the 120–200 nm range. Moreover, the (1 0 1) crystal planes belonging to the TiO_2 anatase polymorph are also in these cases the most frequently observed, with a consequent less defective nature of the particles themselves. For 1001, 1002 and 1071, TEM investigations again confirm that they are composed by a mixture of both micro-sized crystallites and some ultrafine particles.

The surface state of the TiO_2 particles was analyzed by XPS. The survey shows traces of K and P for AT-1 (5.3 and 3.4 at%, respectively), K for 1077 (3.3 at%) and S for AT-1 (1.4 at%) surely due to the starting reactants of the industrial process. No significant differences can be appreciated in the Ti 2p region among all the present samples concerning the binding energies (BE) and the full width at half-maximum (FWHM) values. The peak Ti $2p_{3/2}$ is always regular and the BE (forth column in **Table 3.2**) compares well with the data for Ti(IV) in TiO_2 materials [31]. The analysis of the oxygen peaks exhibits the presence of more than one component, which can be attributed to lattice oxygen in TiO_2 (529.9 eV) and to surface OH species (>531.5 eV) respectively [32]. A particular O_{1s} shape was observed for PC105 (**Fig. 3.13**). In this case, the OH component is very intense probably due to a particular industrial synthesis in order to enhance the photocatalytic efficiency of the sample.

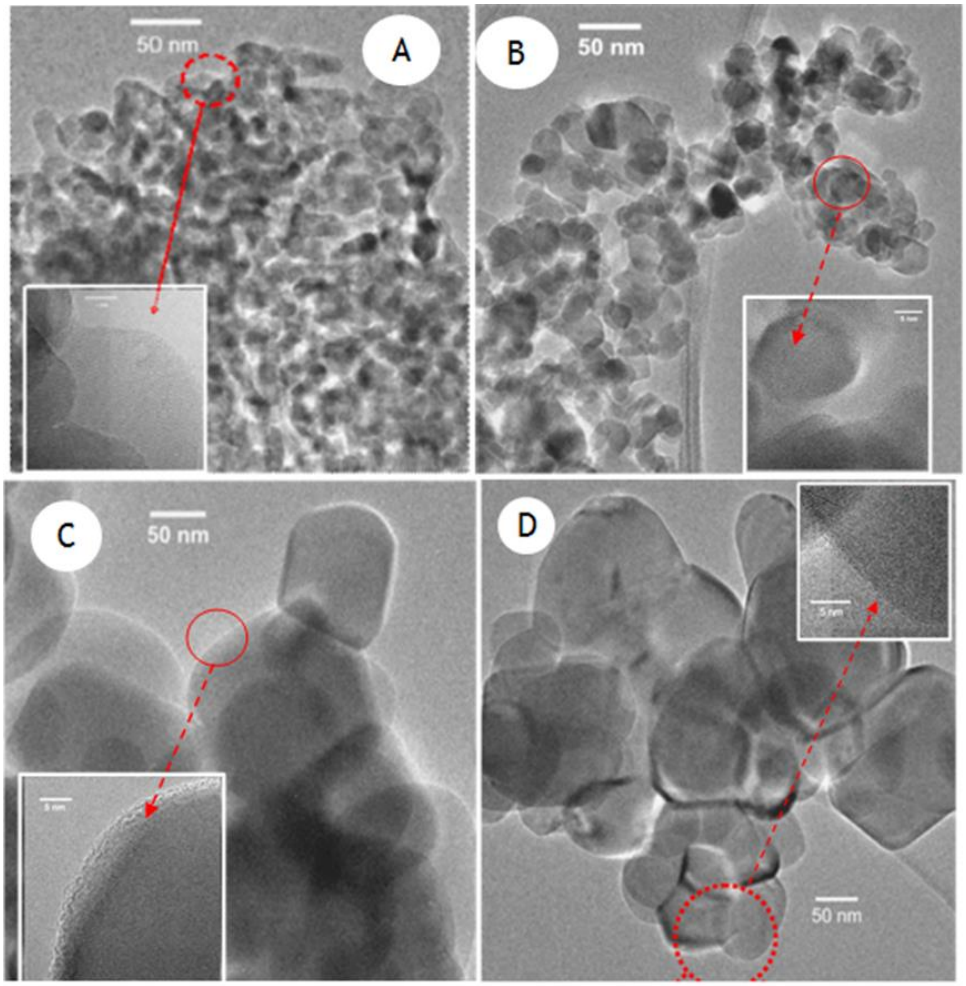

Fig. 3.11. HR-TEM images of nano-sized samples (P25 and PC105) and micro-sized sample (1077 and AT-1), respectively at the top and the bottom of the section, whose the section (a) has a magnitude of 50 nm, whereas the section (b) of 2 nm.

SEM analysis were performed by FEG-LEO 1525. Samples were metalized with chromium. High magnification SEM images (**Fig. 3.12**) contribute to highlight that P25 and PC105 are composed by the aggregation of titanium dioxide nanoparticles and also result to be more aggregated than micro-sized samples. The average particle size is in agreement with TEM

data that is 20-30 nm range. On the contrary, micro-sized samples are constituted of particles with a spherical shape, about the same diameter (ranging from 100 to 130 nm), and they are free of overlapping. The samples are constituted of regular TiO_2 crystallites all in the micro-sized range. This feature may be due to the different particle thickness that leads to such morphological position. In fact, it seems that the presence of particles much bigger than nano-dimensional ones leads to a configuration without agglomerations.

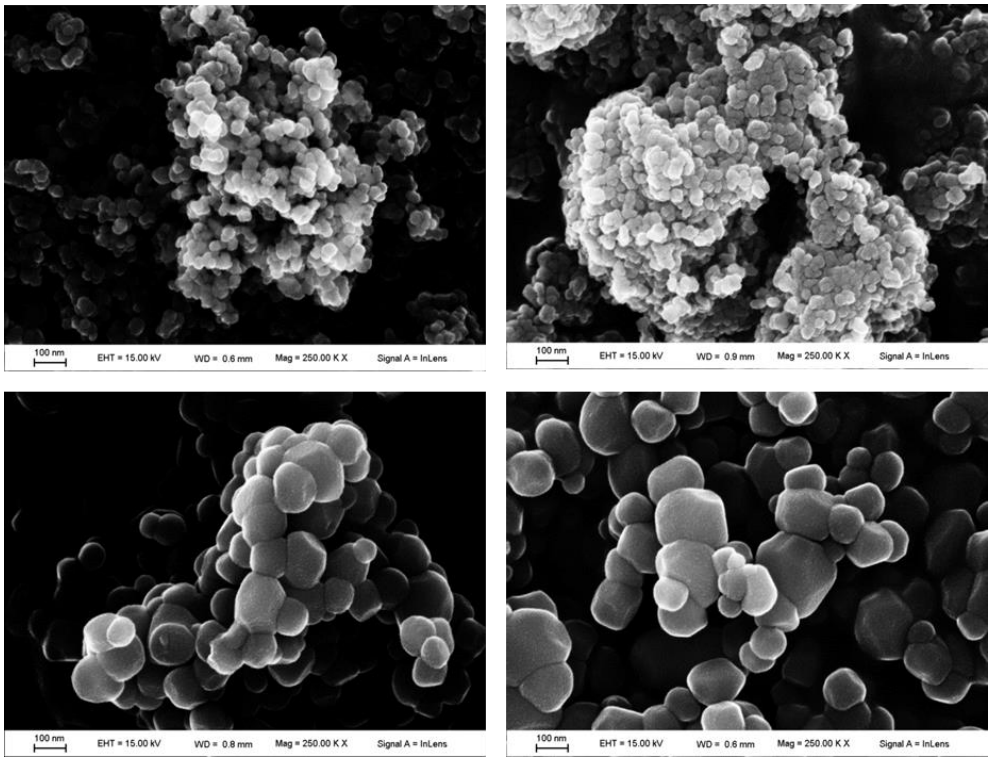

Fig. 3.12. Top sections: left-hand image refers to P25, right-hand image refers to PC105. Bottom sections: left-hand refers to 1077, right-hand image refers to AT-1. Magnification of 250000.

The hydrophilicity/hydrophobicity character of photocatalysts surface plays a crucial role in determining the adsorption step and thus the photocatalytic activity, at least in the degradation of pollutants [33,34]. The fifth column of **Table 3.2** reports the OH/O_{tot} surface ratio, a quantitative measure of the hydrophilicity/hydrophobicity of the TiO_2 surface, estimated using the XPS-determined surface OH atomic concentrations normalized by the total oxygen atomic concentrations (O_{tot}). PC105 exhibits the highest concentration of OH that represent the 85% of the oxygen at the surface. It is noteworthy that the micro-sized samples present a higher atomic concentration of OH groups in comparison with P25, pointing out the higher hydrophilic character of their surface.

In XPS, not only the information on the BE of a specific element can be obtained but also the total density of states (DOS) of the valence band (VB) [35]. This measurement is useful to unravel the effect of TiO_2 structural modifications on the electronic properties of the material. For example, the insertion of non-metal elements such as N, S, C has been reported to introduce additional electronic states above the valence band edge thus creating a band-gap narrowing and a consequent shift of TiO_2 absorption toward the visible region [36]. In addition, when comparing semiconductor nanoparticles/microparticles the quantum size effect could play also a role, giving band-gap narrowing in the bigger sized particles in respect to the smaller ones. The VB XPS spectra of both nano-sized (a, b) and micro-sized samples (c, d) are reported in **Fig. 3.14**. The VB maximum position was determined through linear extrapolation and the same values around −2.6 eV (±0.2 eV that is inside the instrumental error) were observed for all samples, which is a typical value for TiO_2. The absence of additional bands above the

VB in the AT-1 spectra suggests that the impurity (i.e., S) revealed by survey analysis are not inserted in the TiO_2 lattice.

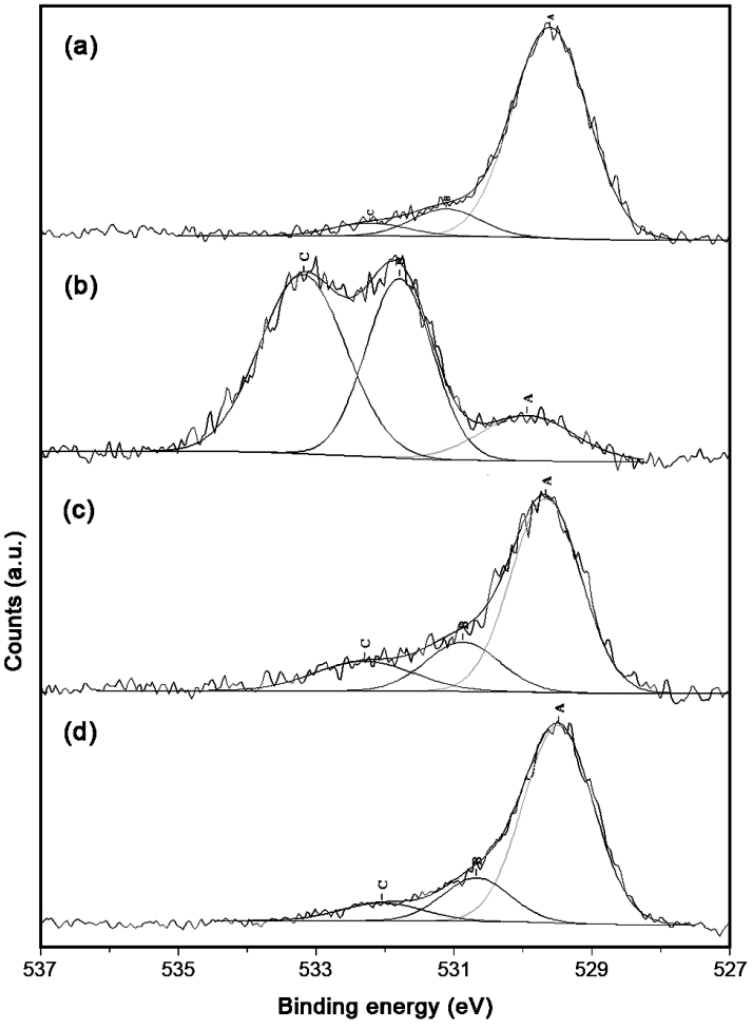

Fig. 3.13. O1s XPS spectra for (a) P25; (b) PC105; (c) 1077; (d) AT-1.

Experimental data of diffuse reflectance were elaborated to absorption coefficient values *F*(R) according to the Kubelka–Munk equation. The corresponding band-gap values obtained by this procedure for all samples

are reported in **Table 3.2** (sixth column). The obtained band-gap values do not exhibit large differences among the various samples and fall in the range expected for the TiO_2 material.

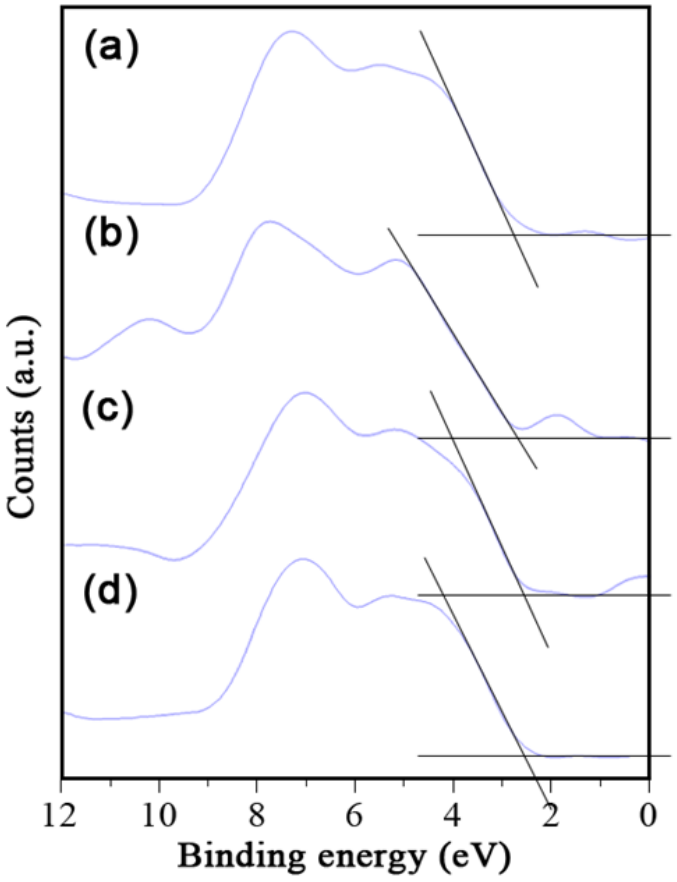

Fig. 3.14. VB XPS spectra along with VB maximum determining by the linear extrapolation method for (a) P25; (b) PC105; (c) 1077; (d) AT-1.

It's observable by XPS results a high OH concentration at the surface for nanocrystallites powders, such as PC105. This feature can favor the adsorption of pollutants (and intermediates of degradation) thus leading to a very active photocatalyst, able to show an efficient photocatalytic activity.

Alternatively, micro-sized powders have higher hydrophilicity/hydrophobicity ratio than P25, which will be taken into account for the photodegradation kinetics. FTIR spectra in the m(OH) spectral range of the four chosen samples (P25, in air are reported in **Fig. 3.15**. All the materials exhibit two complex absorption bands, respectively located in the 3000–3450 cm^{-1} range and at $\nu \geq 3600$ cm^{-1}. On the basis of the spectral behavior and of literature data [28], the former envelope can be ascribed to the stretching mode of all H-bonded OH groups present at the surface of the various solids, whereas the latter corresponds to the stretching mode of all Ti–OH species free from hydrogen bonding interactions [37,38]. Comparing the spectra of both P25 and pigmentary TiO_2 in the OH region, it is evident that P25 is characterized by a significant higher amount of hydroxyl species.

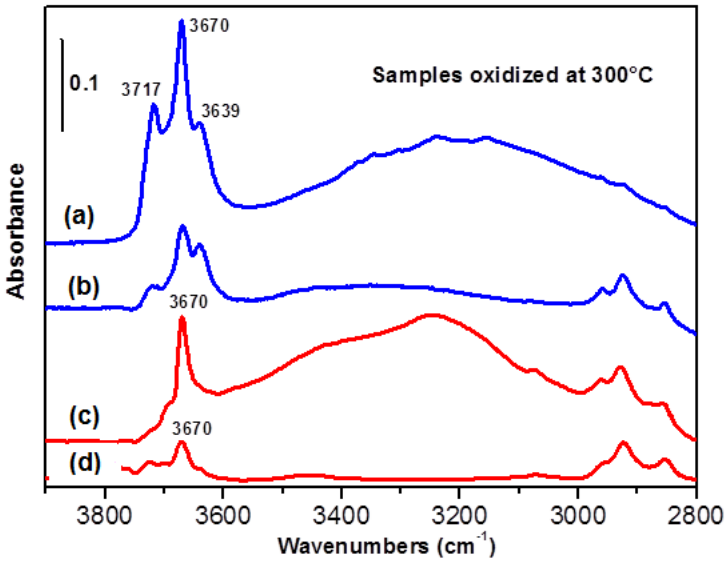

Fig. 3.15. FT-IR spectra of the samples (a) PC105, (b) PC25, (c) 1077 and (d) AT-1 outgassed at 300°C.

Two micro- (1077 and AH-R) and two nano-sized powders (P25 and PC105) were characterized through photoelctrochemical experiments (**conducted in the University of Alicante during the abroad period in the 3rd PhD year**); in particular, the investigation of the photoelectrochemical oxidation of acetone on TiO_2 as a model reaction. The electrochemical analysis were conducted in both saturated N_2 and O_2 solutions. In this way, it is possible to monitor properly the reduction and oxidation processes individually, revealing the exact photocurrent-onset of samples. In addition, photoelectrochemical analyses were also conducted under different acetone solution concentrations investigating the influence of the amount of pollutant on the photoefficiency. In photoelectrochemistry, two separated processes take place: the oxidation process based on the photogenerated holes transfer and the reduction with generated electrons [39], that can be separately studied, including their kinetics. For both kinds of TiO_2 catalysts (nano- and micro-sized particles) the oxidation photocurrent increases by adding acetone until 10 mM concentration, **Fig. 3.16**. For an acetone range of 10-100 mM it is assumed that the current reaches a maximum and decreases for higher concentrations of acetone until the near negligible photocurrent at 1 M of acetone. The values of the photocurrent depend on the TiO_2 type, but the characteristic trend is similar for all samples. The current registered using 10 mM acetone for the nano TiO_2 samples, P25 and PC105, reaches the range of 7-9 $mAcm^{-2}$, whereas for 1077 and AH-R those values are slightly lower (5.5-6 $mAcm^{-2}$). The adsorption of acetone on the surface of the TiO_2 film might be a reasonable cause of the trend of the photocurrent observed as the acetone concentration in the electrolyte solution is increased. The addition of acetone (<10 mM) increases the

photocurrent because the oxydril radicals ($OH^{\cdot}$) formed reacts easily with the adsorbed acetone on TiO_2 surface allowing to enhance the oxidative process. However, further increase of the concentration of acetone gradually decreased the photocurrent observed maybe according to a strong adsorption of the acetone that diminishes the formation of $OH^{\cdot}$.

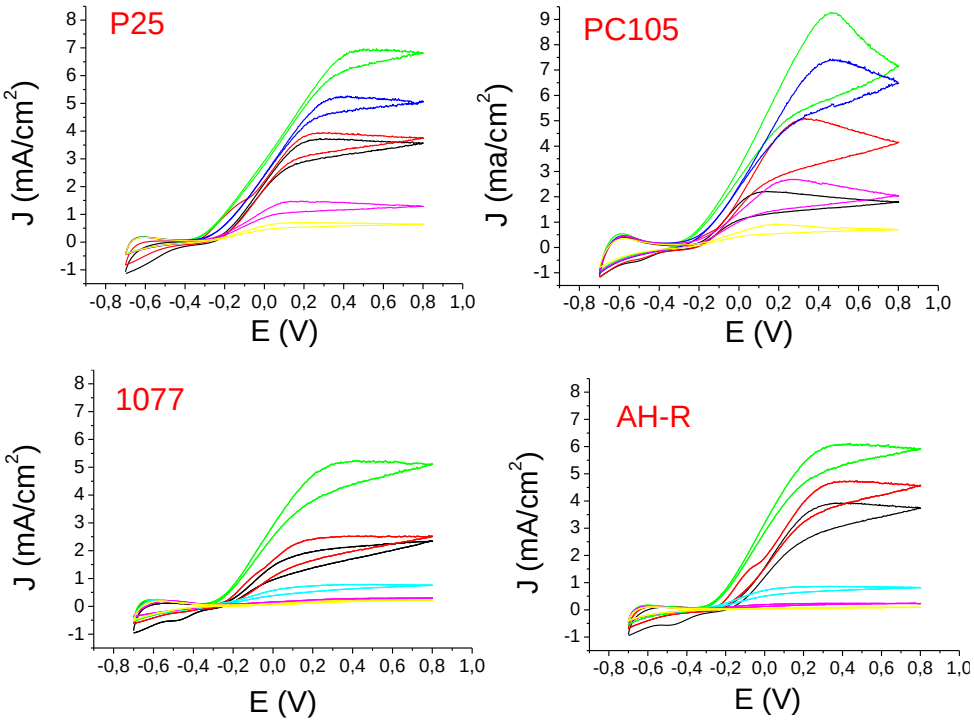

Fig. 3.16. Voltammograms using UV light of nano-sized sample (P25 and PC105) and micro-sized sample (1077 and AH-R) in 0.1M $HClO_4$ + acetone: 0 M (dark line), 1 mM (red line), 10 mM (green line), 100 mM (cyan line), 500 mM (pink line), 1 M (yellow line).

For acetone concentration higher than 1 M very low photocurrents can be recorded probably due to a complete inhibition of the anodic process by blocking the TiO_2 electrode surface. Therefore, the oxidative activity of the TiO_2 electrodes prepared reached a maximum when the acetone concentration turns around 10 mM.

On the other hand, it is deeply interesting to focus on the reduction of oxygen for a complete study of the photo-redox process. **Fig. 3.17** shows the voltammograms for nano- and micro-sized TiO_2 samples in 0.1 M $HClO_4$ aqueous solution saturated with oxygen in the dark. The reductive currents shown directly associated to the accumulation of electrons in the TiO_2 film. Nanometric samples P25 and PC105 show higher reductive currents according to the literature [40]. This is likely related to the higher internal surface area of these samples with respect to micro-sized ones. In order to explain all these differences in the photoelectrochemical behavior, it is necessary to consider features such as the particle size, the morphology, and the electronic states. The charge recombination is diminished, because of the distribution of TiO_2 particles, as noted in TEM images, **Fig. 3.11**. The connection of particles is less pronounced in nanometric powders than micrometric ones, and this feature can contribute to a retarded charge carrier recombination. Voltammograms in **Fig. 3.17** confirmed a diminished charge recombination in the case of the nano-sized electrodes, probably due to the morphology and the connection of particles diminished.

Recently, Berger et al. [39,41] experimentally established that the accumulation region onset reflects the conduction band properties and this photocurrent is correlated to the active surface area. For this theory, a high onset value in the accumulation potential region indicates an efficient photoactivity.

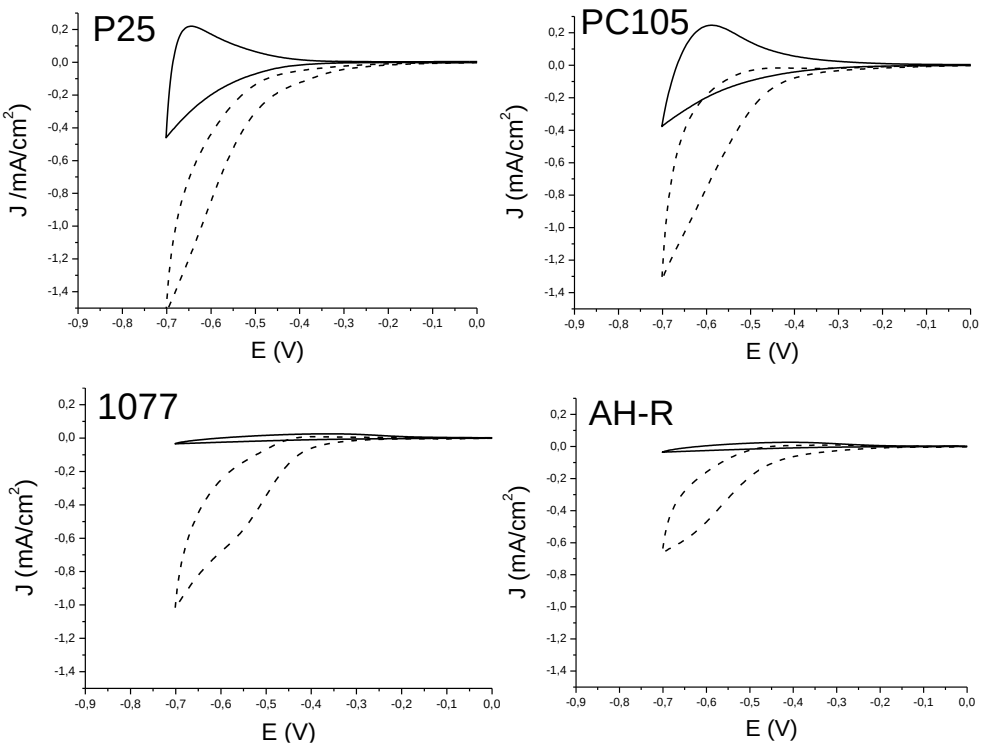

Fig. 3.17. Voltammograms of nano-sized (P25 and PC105) and micro-sized (1077 and AH-R) samples: tests conducted in the dark under O_2 flux (dashed line) and in the dark under N_2 flux (solid line).

To gain more information about oxidation and reduction processes, in **Fig. 3.18** are plotted the current density under illumination for the different TiO_2 electrodes corresponding to the photooxidation of acetone (dashed line) together with the current density in the dark corresponding to the reduction of oxygen (solid line). The intersection point gives the value of photocurrent (acetone oxidation) and dark current (oxygen reduction) under open circuit conditions (i.e. under the typical conditions of suspended photocatalysts). **Fig. 3.18** shows that P25 powder gives the fastest acetone oxidation of all the samples checked. PC105 and AH-R have very similar photoonset values

that are higher than the value for 1077, which shows the lowest photoefficiency.

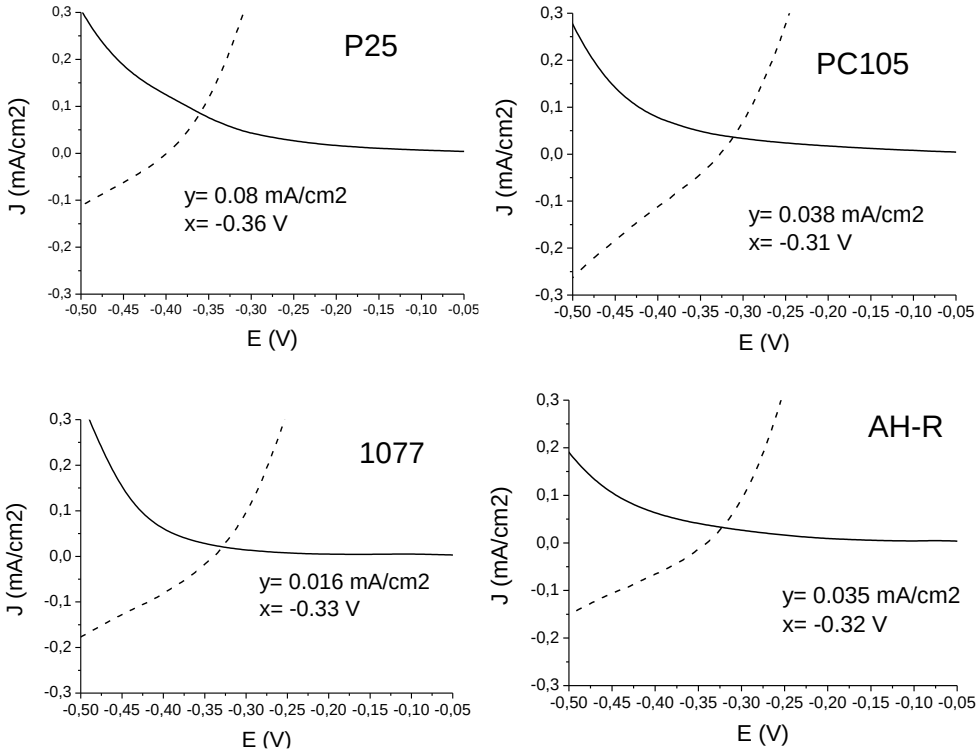

Fig. 3.18. Current density plots for the TiO_2 electrodes on 0.1M $HClO_4$ + 10mM acetone solution corresponding to the photooxidation of acetone (----) and the reduction of oxygen (—) in the dark.

The significant revealed differences in the TiO_2 powders highlighted that P25 thanks to its peculiar properties, like the high surface area, the presence of rutile and the morphology, brought to the best photoefficiency. But, in any cases, AH-R, though being micrometric with lower surface area, shows good catalytic response in photoelectrochemical experimentals. Despite the lower surface area of AH-R than PC105, others factors play a key role determining a good photoresponse that contributes to consider it a valuable

candidate for both oxidation and reduction processes. Band gap energy is a very important parameter depending on many factors such as the electronic structure. This parameter corresponds to the energy difference between the conduction band and the valence band redox levels (H_2O/H_2) and oxidation (O_2/H_2O). For TiO_2 the band gap is 3.0 eV for rutile and 3.2 eV for anatase phase [42]. Surely the relative contribution from kind of phase affects also the band gap energy. Probably, P25 efficiency is highly influenced from the presence of both phases, leading to the photooxidation improvement.

To summarize the photoelectrochemical results it is possible to state that nanometric and micrometric catalysts showed different behaviour. By the comparison of both kind of powders, nanometric samples exhibit a higher photoefficiency than micro-sized ones, even though it was evident that high concentration of pollutant (acetone in this case) inhibits the photodegradation process in all samples. Importantly, both nano-and micro-sized TiO_2 samples revealed that the optimal concentration for the oxidation of acetone was close to 10 mM. By the comparison between cyclic voltammograms in the dark under O_2 flux saturation and under UV illumination with 10 mM of acetone under N_2 flux, the best efficiency is the nanometric P25, which has the photocurrent higher (0.08 mA cm^{-2}) than the other ones. Otherwise, both nano-sized PC105 and micro-sized AH-R have the same value of photocurrent (0.03 mA cm^{-2}), resulting higly photoactive. The increased reactivity in nanometric powders could be caused, not only by the high surface area, but even by the connection between particles, that reflects in a retarded carrier recombination. In parallel with this, AH-R, even if it has low surface area (12 mg cm^{-2}), shows a reduced recombination between electrons and holes, as a probably consequence of the morphology

of particles and defects sites. Thus, in photoelectrochemical analysis even the morphology and the connection of particles strongly affect the capacity. Finally, micro-sized TiO_2 samples, although the low surface area, result valuable candidates for the photooxidation by the characterization of photoelectrochemical.

3.2.3 TiO_2 porcelain gres tiles results

A fundamental aspect of the new photoactive tiles is the preservation of the basic tiles features such as lack of porosity, hardness and durability. For this reason all these features were carefully checked. Lack of porosity was measured by water absorption. Water absorption rates are a measurement of how much moisture a specific type of porcelain tile may absorb on an ongoing basis. Some types of tile may crack if the moisture penetration is too high. In our case a porosity value of less than 0.5% was obtained for both WGA and Orosei samples allowing to classify both the tile as impervious (extremely dense) and categorized them as porcelain tiles. Tiles hardness was verified by the measure of the resistance to abrasion which involves the rotation of a defined abrasive powder load on the surface of a tile sample for a specific number of revolutions, and assigning the tile to a PEI class of abrasion resistance on the basis of a visual examination of the abraded test samples under well-defined conditions of observations, in agreement with the recommendations of the CEC (Federation Europenne des Fabricants de Carreaux Ceramiques) [43]. In our case both WGA and Orosei were classified as PEI IV that means that they are suitable for use in

areas subjected to considerable traffic with the presence of some abrasive dirt.

Tiles durability was checked verifying their resistance to frost. After impregnation with water, the tiles were subjected to temperature cycles between +5 and -5 °C, during a minimum of 100 freeze–thaw cycles. No evident cracks or damages were observed on our samples.

XPS measurements were performed in an M-Probe Instrument (SSI) equipped with a monochromatic Al Ka source (1486.6 eV) with a spot size of 200 x 750 lm and a pass energy of 25 eV, providing a resolution for 0.74 eV. The surface area was investigated by nitrogen adsorption studies using the Brunauer–Emmett–Teller (BET) method. TiO_2 + SiO_2-based compound after the calcination treatment at 680°C shows the decrease of the surface area (BET measurements) compared to the pure TiO_2 powder (see in the **Paragraph 3.2.1**, from 11.0 to 2.6 m^2g^{-1}). From the surface point of view, XPS analysis reveals the classical Ti2p doublet at 458.6 eV ($Ti2p_{3/2}$) attributed to Ti^{4+} with a Ti/Si ratio of 0.20.

The X-ray powder diffraction (XRPD) pattern at room temperature from the WGA powdered sample was collected at the high-resolution powder diffractometer at the ID31 beam line of the European Synchrotron Radiation Facility (ESRF), Grenoble, France [44]. A wavelength of k = 0.39620(9) Å was selected using a double-crystal Si(111) monochromator. The detector bank collected data in the $0 < 2\theta < 30°$ range. XRPD patterns were analyzed with the Rietveld method as implemented in the GSAS software suite of programs [45], which feature the graphical interface EXPGUI [46]. Line profiles were fitted using a modified pseudo-Voigt function [47] accounting for asymmetry correction [48].

As it can be observed in **Table 3.4**, the formulation with the SiO_2-based compounds and the following calcination step lead to a decrease of the surface area. For the same compounds the preservation of the pure anatase form was verified by both XRPD and XPS measurements. As reported by Anderson and Bard [49] the presence of SiO_2, together with TiO_2, enhances the formation of hydroxyl radical ·OH, which may be achieved via strong Brønsted acid sites at the TiO_2/SiO_2 interface region. Such incorporation inhibits the crystal growth of TiO_2 allowing the preservation of the anatase structure at high temperature [50].

Table 3.4. Physico-chemical features of both pure TiO_2 (Kronos 1077) and after its formulation and calcination at 680°C with the SiO_2-based compound.

Sample	BET surface area (m^2/g)	XRPD	XPS Ti $2p_{3/2}$ (eV)	UV-vis (eV)
Pure TiO_2	11.0	Pure anatase	458.5	3.22
TiO_2+SiO_2-based compound	2.6	Pure anatase	458.4	3.23

In **Fig. 3.19** the XRPD pattern of the sample is shown. The experimental (crosses) and calculated (continuous line) curves are reported together with the difference curve (bottom). The XRPD pattern of the sample is correctly interpreted using a single crystalline phase, which is the anatase TiO_2 polymorph: space group $I4_1/amd$ (N°141, origin choice 2) [51].

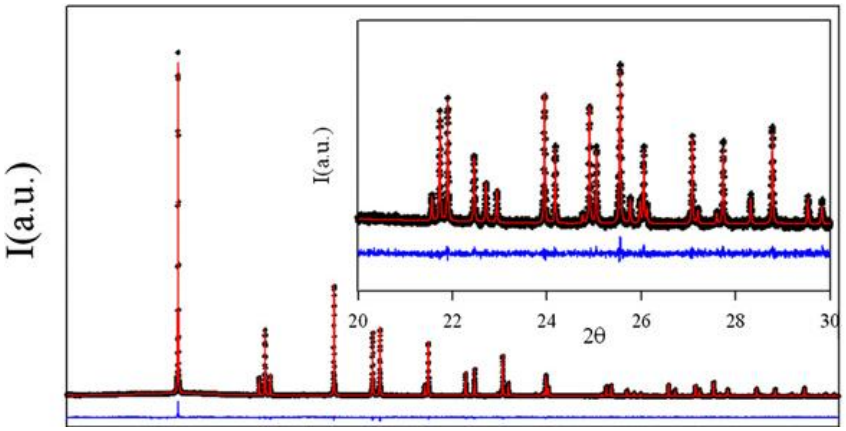

Fig. 3.19. XRPD pattern of WGA powdered sample. Measured (black crosses) and calculated (red line) profiles are shown as well as residuals (blue line). The inset highlights the high angle 2h region. (For interpretation of the references to color in this figure legend, the reader is referred to the web version of this article).

In this structure Ti ions lie in (0, 1/4, 3/8) site while O in (0, 1/4, z) [52]. The refined structural parameters are shown in **Table 3.5**. The nearest neighbors Ti–O distances are the following: *d*(Ti–O) x 4 → 1.9354(2) Å; *d*(Ti–O) x 2 → 1.9734(9) Å.

Table 3.5. Rietveld refinement results referring to TiO_2 sample.

Space group	$I4_1/amd$
a (Å)	3.78550
c (Å)	9.51000
V (Å^3)	136.278
z_0	0.1675
U_{TI} (Å^2)	0.0042
U_0 (Å^2)	0.0047
wRp	0.073
Rp	0.056
X^2	1.29
R(F^2)	0.038

Micro-TiO_2 gres tile**s** were investigated by HR-TEM technique in order to see the morphological features If we compare the images of gres-tiles with the pure micro commercial powder (see **Paragraph 3.2.1**), the main features of the TiO_2 particles are maintained when the presence of the SiO_2-based compound is considered. It's possible to see in **Fig. 3.20(a)** and **3.20(b)** the presence of the large dimensions of the particles (50-200 nm range), beside rather smooth edges. Nevertheless, some peculiarities have to be mentioned: in particular, the presence of the SiO_2-based compound is evident (see either the inset in **Fig. 3.20(a)** or **Fig. 3.20(b)**), in the form of either small protruding crystalline particles or an amorphous coating covering the TiO_2 particles. In any case, the very thin nature of these particles and/or coating allows to inspect the fringe patterns located below, confirming that the spacings among the fringes are still ascribable to the anatase TiO_2 polymorph [53].

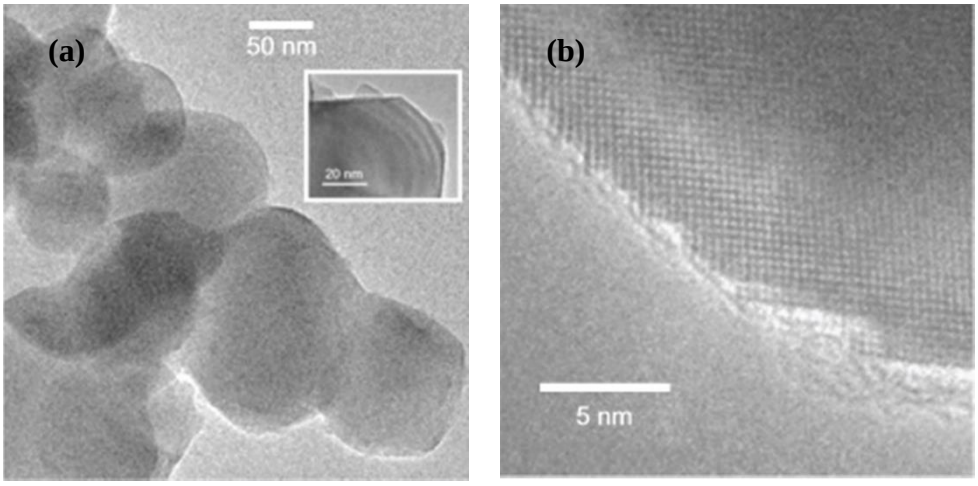

Fig. 3.20. HR-TEM images of the TiO_2 porcelain gres tiles materials. (a) refers to low magnification and (b) to high magnification.

The morphological features, obtained from HR-TEM measurements were even equipped with an Oxford INCA X-ray energy dispersive spectrometer (XEDS) with a Pentafet Si(Li) detector. Samples were "dry" dispersed on lacey carbon Cu grids. The image of the WGA photoactive tile (**Fig. 3.21b**) shows a quite homogeneous surface with a good distribution of both Si and Ti atoms, as revealed by EDX analysis. As expected, no Ti signals were observed on the non-photoactive tile (**Fig. 3.21a**).

The surface wettability was evaluated by static contact angle (CA) measurements performed with an OCA20 instrument (DataPhysics Co., Germany) equipped with a CCD camera and a 500 μL-Hamilton syringe to dispense liquid droplets. Measurements were made at room temperature (∼22◦C) by means of the sessile drop technique and were replicated at least 15 times on each sample [53]. Ultrapure water (HPLC grade, Sigma-Aldrich) was used as probe liquids and the volume of drop was fixed at 2 μL. The Young-Laplace fitting method was used in the calculation of static contact angles for all measurements giving an experimental error of ±5% due to the surface roughness of the samples [54,55] that was experimentally determined by a laser profilometry (3D laser profilometer, UBM Microfocus Compact, Nano Focus AG, Germany) with vertical and lateral resolution of 10 nm. The parameters used during measurements follow the standard DIN 4768 and were adopted a transverse line measurement of 17.5mm and a density of 150 dots per mm. Diffuse reflectance spectra of the powders were measured on UV–vis spectrophotometer (PerkinElmer, Lambda 35), which was equipped with a diffuse reflectance accessory, as reported previously.

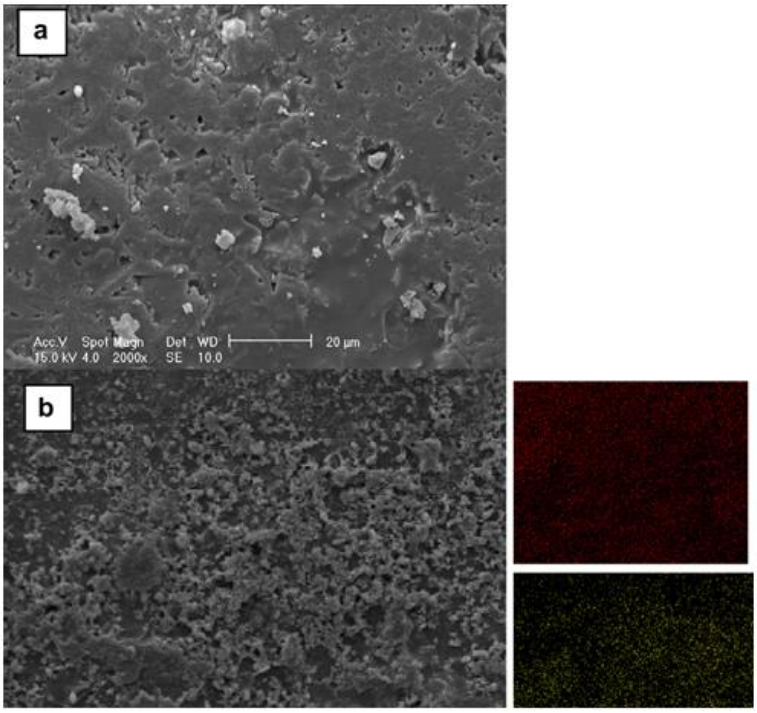

Fig. 3.21. SEM images (2000x) of WG tile (a) and photocatalytic WGA (b). Element mapping by EDX for WGA sample (red picture: Si; green picture: Ti).

Wettability measurements were performed on 15 different areas of both Orosei and Orosei Active (**Fig. 3.22(a)** and **3.22(b)**, resp.). Drop shapes are dramatically different enhancing a completely different surface [55]. Orosei sample shows a mean contact angle value of 78.2°, while Orosei Active shows very hydrophilic surface features with an average angle of 23.0°. This very low value can be explained by the super-hydrophilic property of TiO_2 photocatalyst as already observed by other authors [56]. In particular the copresence of TiO_2 and SiO_2 can lead to a modification of the angle value depending on the TiO_2/SiO_2 ratio [57] with values in the range of 20–25° with a SiO_2 content at 70–80% (molar basis), in agreement with the XPS Ti/Si ratio obtained on Orosei Active. The term hydrophilic is usually

referred to the ability of a material or a chemical species (such as molecules or particles) to interact with water. The term hydrophilic, in the widest sense, can also describe the ability of some materials to absorb and retain water on their surface or in their bulk. When the TiO_2 is exposed to light, it is able to attract and retain water (H_2O). By coating solid surfaces by TiO_2 particles it is possible to confer them self-cleaning features, in fact the dirt hardly adhere on such hydrophilic surfaces. As a consequence the surface cleaning is easier and the use of detergents (which are pollutant for the environment) is unnecessary. Samples roughness, measured as root mean squared (R_q), was 19.354 μm and 18.860 μm for Orosei Active and Orosei (Ti-free), respectively.

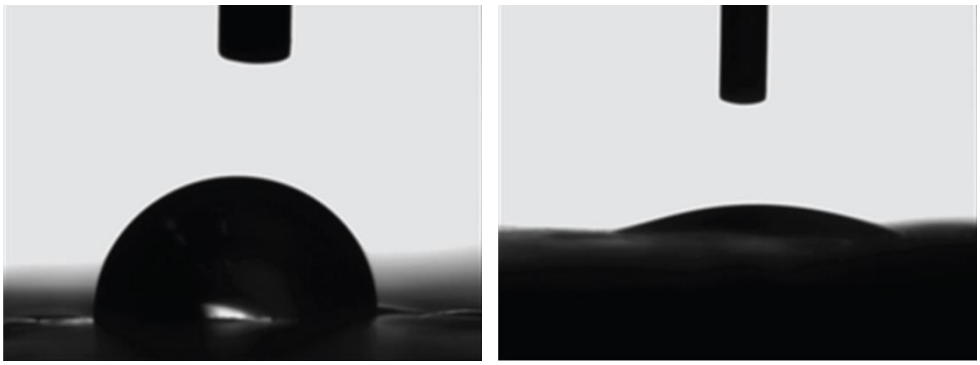

(a) (b)

Fig. 3.22. Contact angle: (a) Orosei; (b) Orosei Active tiles.

3.3 References

[1] Fadoni, M., Lucarelli L. Temperature programmed desorption, reduction, oxidation and flow chemisorption for the characterization of heterogeneous

catalysts. Theoretical aspects, instrumentation and applications. *Studies Surf. Sci. Catal*. **1999**.

[2] Nelsen F.M., Eggertsen F.F. Determination of surface area. Adsorption measurements by continuous flow method. *Analytic. Chem*. **1958**, *30*, 1387-1390.

[3] Haber J., Block J.H., Delmon B. Manual of methods and procedures for catalyst characterization. *Pure Appl. Chem*. **1995**, *67*, 1257-1306.

[4] Brunauer S., Emmett P.H., Teller E. Adsorption of gases in multimolecular layers. *J. Am. Chem. Soc*. **1938**, *60*, 309-319.

[5] Lemaitre, J.L., Menon, P.G., Delannay, F. In: Delannay, F., Eds., Characterization of Heterogeneous Catalysts. Marcel Dekker Inc., New York and Basel **1984**.

[6] Bartholomew C.H. In: Paal, Z. and Menon, P.G., Eds., Hydrogen Effects in Catalysis. Marcel Dekker Inc., New York and Basel **1988**.

[7] David W.I.F., Shankland K., Mc Cusker L.B., Baerlocher C. Structure Determination from Powder Diffraction Data. *Oxford Science Publications* **1992**.

[8] Bish D.L., Post J.E., Modern J.E. Powder Diffraction. *Mineral. Soc. Am*. **1989**.

[9] Azaroff L.V., Buerger M.J. The Powder Method in X-ray Crystallography. *McGraw Hill Book Company, Inc*, **1975**.

[10] Buerger M.J. X-ray Crystallography. *J. Wiley*, New York, **1942**, *20*.

[11] Smart L., Moore E.A. A Solid State Chemistry: an introduction. CRC Press: United States of America, **2005**.

[12] Gehrke C.W., Wixom R.L., Bayer E. Chromatography: A century of discovery. *Elsevier*, Amsterdam **2001**, *64*.

[12] Knox J.H., Done J.N. Fell A.F. et al. High-Performance Liquid Chromatography. Edinburgh University Press **1978**.

[13] Skoog D.A., Holler F.J., Crouch S.R. Principles of instrumental analysis. *Thomas Brooks/Cole* **2006**.

[14] Von Ardenne, M. Das Elektronen-Rastermikroskop. Theoretische Grundlagen. Zeitschrift fur Physik. *Techn. Phys*. **1938**, *108*, 407-553.

[15] Berger T., Monllor-Satoca D., Jankulovska M., Lana-Villarreal T., Gómez R. The electrochemistry of nanostructured titanium dioxide electrodes. *ChemPhysChem* **2012**, *13*, 2824-2875.

[16] Grundke K. Handbook of applied surface and colloid chemistry. Edited by Krister Holmberg, *John Wiley & Sons* **2001**, *2*.

[17] Gao L., McCarthy T.J. Contact angle hysteresis explained. *Langmuir* **2006**, *22*, 6234-6237.

[18] Zhang X., J in M., Liu Z., Tryk D.A., Nishimoto S., Murakami T., Fujishima A. Superhydrophobic TiO_2 surfaces: preparation, phototcatalytic wettability conversion, and superhydrophobic-superhycdrophilic patterning. *J. Phys. Chem*. **2007**, *111*, 14521-14529.

[19] Zhang F., Chen S., Dongb L., Lei Y., Liu T., Yin Y. Preparation of superhydrophobic films on titanium as effective corrosion barriers. *Appl. Surf. Sci.* **2011**, *257*, 2587−2591.

[20] Blossey R. Self-cleaning surfaces-virtual realities. *Nat. Mater.* **2003**, *2*, 301-306.

[21] Wang R., Hashimoto K., Fujishima A., Chikuni M., Kojima E., Kitamura A., Shimohigoshi M., Watanabe T. Light-induced amphiphilic surfaces. *Nature* **1997**, *388*, 431-432.

[22] Sakai N., Wang R., Fujishima A., Watanabe T., Hashimoto K. Effect of ultrasonic treatment on highly hydrophilic TiO_2 surfaces. *Langmuir* **1998**, *14*, 5918-5920.

[23] Chen X., Mao S.S. Titanium dioxide nanomaterials synthesis, properties, modifications and applications. *Chem. Rev*. **2007**, *107*, 2891-2959.

[24] Fujishima A., Rao T.N., Tryk D.A. Titanium dioxide photocatalysis. *J. Photoch. Photobio. C* **2000**, *1*(1), 1-21.

[25] Fujishima A., Zhang, X. Titanium dioxide photocatalysis: present situation and future approaches. *C.R. Chim*. **2006**, *9*(5-6), 750-760.

[26] Ochiai T., Fujishima, A. Photoelectrochemical properties of TiO_2 photocatalyst and its applications for environmental purification. *J. Photo. Photobio. C* **2012**, *13*(4), 247-262.

[27] Chaturvedi S., Dave P.N. Environmental application of photocatalysis. *Mater. Sci. Forum* **2013**, *734*, 273-294.

[28] Bianchi C.L., Gatto S., Pirola C., Naldoni A., Di Michele A., Cerrato G., Crocellà V., Capucci V. Photocatalytic degradation of acetone, acetaldehyde and toluene in gas-phase: comparison between nano and micro-sized TiO_2. *App. Catal. B: Environ*. **2014**, *146*, 123-130.

[29] Diebold U. The surface science of titanium dioxide. *Surf. Sci. Rep*. **2003**, *48*, 53–229.

[30] Zhang J.H., Wang S.Z., Liu J.B., Wang Z.L., Ming N.B. Preparation and adsorption properties of polystyrene/Ag/TiO_2 multiple coated colloids. *J. Mater. Res*. **2005**, *20*, 965-970.

[31] Cappelletti G., Bianchi C.L., Ardizzone S. XPS study of the surfactant film adsorbed onto growing titania nanoparticles. *App. Surf. Sci*. **2006**, *253*, 519–524.

[32] Ardizzone S., Bianchi C.L., Cappelletti G., Gialanella S., Pirola C., Ragaini V. Tailored anatase/brookite nanocrystalline TiO_2. The optimal particle features for liquid- and gas-phase photocatalytic reactions. *J. Phys. Chem. C* **2007**, *111*, 13222–13231.

[33] Ardizzone S., Bianchi C.L., Cappelletti G., Naldoni A., Pirola C. Photocatalytic degradation of toluene in the gas phase: relationship between surface species and catalyst features. *Environ. Sci. Technol*. **2008**, *42*, 6671–6676.

[34] Naldoni A., Bianchi C.L., Pirola C., Suslick K.S. Porous TiO_2 microspheres with tunable properties for photocatalytic air purification. *Ultras. Sonochem*. **2013**, *20*, 445–451.

[35] Naldoni A., Allieta M., Santangelo S., Marelli M., F. Fabbri, Cappelli S., Bianchi C.L., Psaro R., Dal Santo V. Effect of nature and location of defects on bandgap narrowing in black TiO_2 nanoparticles. *J. Am. Chem. Soc.* **2012**, *134*, 7600–7603.

[36] Chen X., Burda C. The electronic origin of the visible-light adsorption properties of C-, N- and S-doped TiO_2 nanomaterials. *J. Am. Chem. Soc*. **2008**, *130*, 5018–5019.

[37] Morterra C. An infrared spectroscopic study of anatase properties. Surface hydration and strong Lewis acidity of pure and sulphate-doped preparations. *Faraday Trans. 1* **1988**, *84*, 1617–1637.

[38] Morterra C., Bolis V., Fisicaro E. The hydrated layer and the adsorption of carbon monoxide at the surface of titania (anatase). *Colloids Surf*. **1989**, *41*, 177–188.

[39] Berger T., Monllor-Satoca D., Jankulovska M., Lana-Villarreal T., Gomez R. The electrochemistry of nanostructured titanium dioxide electrodes. *ChemPhysChem* **2013**, *13*, 2824-2875.

[40] Lyon L.A., Hupp J.T. J. Energetics of semiconductor electrode/solution interfaces: EQCM evidence for change-compensating cation adsorption and intercalation during accumulation layer formation in the titanium dioxide/acetonitrile system. *Phys. Chem*. **1995**, *99*, 15718-15720.

[41] Jankulovska M., Barcelò I., Lana-Villarreal T., Gomez R. Improving the photoelectrochemical response of TiO_2 nanotubes upon decoration with quantum-sized anatase nanowires. *J. Phys. Chem. C* **2013**, *117*, 4024-4031.

[42] Mo S.D., Ching W.Y. Electronic and optical properties of three phases of titanium dioxide: rutile, anatase and brookite. *Phys. Rev. B* **1995**, *51*, 13023-13031.

[43] ISO 10545-7. Ceramic tiles – Part 7: Determination of resistance to surface abrasion for glazed tiles; **1996**. www.iso.org.

[44] Fitch A.N. The high resolution powder diffraction beam line at ESFR. *J. Res Natl. Inst. Stand Technol.* **2004,** *109*, 133–142.
[45] Larson A.C., Von Dreele R.B. General structural analysis system (GSAS*). Los Alamos National Laboratory Report LAUR* **2004,** 86–748.
[46] Toby B.H. EXPGUI, a graphical user interface for GSAS. *J. Appl. Cryst*. **2001**, *34*, 210–214.
[47] Thompson P., Cox D.E., Hastings J.B. Rietveld refinement of Debye-Scherrer synchrotron X-ray data from alumina. *J. Appl. Crystallogr*. **1987**, *20*, 79–83.
[48] Finger L.W., Cox D.E., Jephcoat A.P. A correction for powder diffraction peak asymmetry due to axial divergence. *J. Appl. Crystallogr*. **1994**, *27*, 892–900.
[49] Anderson C, Bard A. Improved photocatalytic activity and characterization of mixed TiO_2/SiO_2 and TiO_2/Al_2O_3 materials. *J. Phys. Chem. B* **1997**, *101*, 2611–2616.
[50] Xie TH, Lin J. Origin of photocatalytic deactivation of TiO_2 film coated on ceramic substrates. *J. Phys. Chem. C* **2007**, *111*, 9968–9974.
[51] Bianchi C.L., Gatto S., Pirola C., Scavini M., Vitali S., Capucci V. Micro-TiO_2 as a starting material for new photocatalytic tiles. *Cem Conc. Compos*. **2013**, *36*, 116-120.
[52] Howards C.J., Sabine T.M., Dickson F. Structural and thermal parameters for rutile and anatase. *Acta Cryst. B* **1991**, *47*, 462–468.
[53] Bianchi C.L., Pirola C., Gatto S., Nucci S., Minguzzi A., Cerrato G., Biella S., Capucci V. New surface properties in porcelain gres tiles with a look to human and environmental safety. *Adv. Mater. Sci Engin*. **2012**, *2012*.
[54] Drelich J., Chibowski E. Superhydrophilic and superwetting surfaces: definition and mechanisms of control. *Langmuir* **2010**, *26*, 18621–18623.
[55] Watanabe T., Fukayama S., Miyauchi M., Fujishima A., Hashimoto K. Photocatalytic activity and photo-induced wettability conversion of TiO_2 thin film prepared by sol-gel process on a soda-lime glass. *J. Sol-Gel Sci. Technol*. **2000**, *19*, 71–76.
[56] Wang R., Hashimoto K., Fujishima A.et al. Light-induced amphiphilic surfaces. *Nature* **1997**, *388*, 431–432.
[57] Machida M., Norimoto K., Watanabe T., Hashimoto K., Fujishima A. Effect of SiO_2 addition in super-hydrophilic property of TiO_2 photocatalyst. *J. Mater. Sci*. **1999**, *34*, 2569–2574.

Chapter 4

Nano- and micro-sized TiO_2 in gas phase

Nitrogen oxides (NO_x) emitted from vehicles exhausts and volatile organic compounds (VOCs), not to be underestimated, are associated with adverse health effects on the plants and humans. Heterogeneous photocatalysis has a great potential to overcome with the increasing pollution in the air. The use of micro-sized TiO_2 as photocatalyst instead of nanometric particles, results in a greater environmental impact and higher production costs. Furthermore, the addition of a photocatalyst to ordinary building materials such as tiles, concrete, paints creates environmental friendly materials by which air pollution or pollution of the surface itself can be controlled and diminished. This work reports the results of the research for the evaluation of NO_x and VOCs abatement in gas-phase, employing both powder and gres-tiles constituted of TiO_2 microparticles.

4.1 NO_x photodegradation with TiO_2 powders

Air pollution due to nitrogen oxides (NO_x) is a dramatic issue that modern societies are facing. They are amongst the main responsible for photochemical smog [1] (mixture of hazardous chemicals formed in the atmosphere due to interaction of sunlight with already present pollutants); together with sulphur oxides (SO_x) they generate acid rains [2]. Direct exposures or acid vapours generated by reaction with atmospheric moisture can cause emphysemas and bronchitis due to their interaction with lung tissues and, not least, they seriously affect plant regular metabolism. In atmospheric chemistry NO_x refers to the sum of nitric oxide, NO, and nitrogen dioxide, NO_2. NO is considered a primary pollutant, because mainly introduced in the atmosphere directly from a source (high temperature combustions in transport and industrial activities [3]). NO_2, on the other hand, is considered as a secondary pollutant because mainly formed in the atmosphere by interaction of a primary pollutant (NO) with O_2 (or O_3) and/or sunlight. Further reactions in the atmosphere can transform NO and NO_2 in nitric acid, HNO_3, peroxyacyl nitrates (PANs), $RC(O)OONO_2$, peroxynitric acid, HNO_4, etc. The sum of all these species and NO_x is known as NO_y, total reactive nitrogen. NO_x emission has been and still is subject of intense environmental regulations. Therefore, their control and remediation have been the subject of intense research.

Amongst the most used technologies for NO_x remediation (combustions modifications, dry processes and wet processes [4,5]) advanced oxidation processes (AOP) of NO_x has become, over the past ten years, a valid alternative as confirmed by the large number of literature produced [6-9]. In

particular, TiO_2 is used as photoactive material with the aim of the depollution effect due to the oxidation of NO_x in the atmosphere to NO_3^-.

Although TiO_2 is chemically inert, TiO_2 nanoparticles can cause negative health effects, such as respiratory tract cancer in rats. Trouiller et al. [10] investigate TiO_2 nanoparticles-induced genotoxicity, oxidative DNA damage, and inflammation in a mice model. The increased use of nanomaterials in commercial products has raised a growing public debate on whether the environmental and social costs of nanotechnologies outweigh their numerous benefits [11]. Up to now, few studies have investigated the toxicological and environmental effects of direct and indirect exposure to nanomaterials and nanoparticulate and no clear guidelines exist to quantify these effects [12]. There are no specific regulations on nanoparticles, except existing regulations covering the same material in bulk form [13]. Difficulties abound in devising such regulations, beyond self-imposed regulations by responsible companies, because of the likelihood of different properties exhibited by any type of nanomaterial, which are tunable by changing their size, shape and surface characteristics [14].

The possibility to use micro-sized TiO_2 powders instead of nanometric ones, opens a new generation of materials intrinsically safer than the traditional photocatalytic products for both workers in the factories and public safety, even though, with such materials that are surface vitrified, the release of TiO_2 particles is extremely remote.

In this PhD work commercial micrometric TiO_2 powders are investigated: physical-chemical properties of the samples are correlated with photoactivity results, obtained in air for the NO_x abatement. The photodegradation tests are carried out by using two different irradiation

sources: UV light and LED (Light Emitting Diode) lamp (MW mean well, 350mA rated current, 9-48V DC voltage range, 16.8W rated power) with an emission between 400 and 700nm), as will be reported in **Chapter 7**. The last lamp is applied because it is UV components free and is actually widely used in indoor environments as illumination [15,16]. In the early 2010s, in fact, it was found that LED technology could vastly improve the brightness, colour and distribution of lighting in social housing communal areas: LED light bulbs save electricity and remain cool. Not only that, but it could deliver huge energy savings (up to 90%), and reduce long-term costs and maintenance, while making residents feel safer. It is issued that by 2015, LED technology dominates both the commercial and domestic lighting markets. The plan envisage the replacement of the entire "park lights" existing (mercury vapor lamps, incandescent pans, the old systems to low and high pressure sodium) in Milan with new systems LED, able to consume less and work better [17]. Moreover, certain studies [18,19] have reported that LEDs could be energy-efficiently utilized as alternative light sources for the photodegradation of VOCs, even if with lower photocatalytic degradation efficiencies compared to conventional UV lamp ones.

4.1.1 Materials and Methods

4.1.1.1 Powder samples preparation

Commercial samples of titanium dioxide, nanometrics and micrometrics, were used as photocatalysts without any treatment or activation. TiO_2

powders (0.05 g) were first suspended in 2-propanol (50 ml) so obtaining a homogeneous suspension and then deposited by drop casting onto one side of the laminas. The solvent was simply evaporated at room temperature without any further treatment. The samples consisted in a ticker layer, obtained by overlapping three TiO_2 coatings (labelled as T, standing for triple layers, followed by the substrate abbreviation), shown in previous works [20,21], as it is reported in **Fig. 4.1**.

Fig. 4.1. TiO_2 powders catalysts deposited on glass laminas.

This section has the objective to provide the description of the TiO_2 commercial catalysts employed, both nano- and micro-sized.

The two principal catalytic phases of TiO_2, anatase and rutile, have numerous structural and functional differences. Commercially available anatase particles have a band gap of 3.2 eV, corresponding to a UV wavelength of 385 nm. In **Table 4.1** it is reported the different typologies of TiO_2 commercial powders employed in this research work. For each powder it is indicated the crystalline phase.

The adsorptive affinity of anatase for organic compounds is higher than that of rutile [22], and anatase exhibits lower rates of recombination in comparison to rutile due to its 10-fold greater rate of hole trapping [23]. In

contrast, though some exceptions exist, the thermodynamically stable rutile phase generally exists as particles larger than 200 nm.

Table 4.1. TiO_2-based commercial powders, used in the photocatalytic tests, with the corresponding crystalline phase: nanometric and micrometric samples.

Commercial powder	**Crystalline phase**	**BET (m^2/g)**	**Micro/Nano**	**OH/O**
P25 (by Evonik)	75% anatase; 25% rutile	52	NANO	0.14
PC105 (by Crystal)	anatase	80	NANO	0.85
1077 (by Kronos)	anatase	11	MICRO	0.32
AH-R (by Hundsman)	anatase	12	MICRO	0.19
AT-1 (by Crystal)	anatase	12	MICRO	0.24
1001 (by Kronos)	anatase	11	MIXED PHASE (micro+nano)	0.27
1002 (by Kronos)	anatase	9	MIXED PHASE (micro+nano)	0.35
1071 (by Kronos)	anatase	10	MIXED PHASE (micro+nano)	0.18
A-Z (by Hombitam)	99% anatase	4	MICRO	0.27
AN (by Hombitam)	98,5% anatase	12	MICRO	0.5
N.10 (by HombiKat)	98% anatase; 2% rutile	13	MICRO	0.13

Rutile has a smaller band gap of 3.0 eV with excitation wavelengths that extend into the visible at 410 nm. Nevertheless, anatase is generally

regarded as the more photochemically active phase of titania, presumably due to the combined effect of lower rates of recombination and higher surface adsorptive capacity. Given the wide range of photoefficiencies observed among various TiO_2 phases and formulations, past research has been unable to explain comprehensively the high photoactivity observed in some mixed-phase TiO_2 preparations such as Degussa P25. A research group tried to explain the enhanced activity of P25 mixed-phase TiO_2 using EPR spectroscopic method [24].

4.1.1.2 Photocatalytic plant in gas phase

NO_x degradation was performed in a cylindrical reactor of 20 L with two opening valves: one is for the pollutant injection and the other one for the NO_x sample taking. The sample was placed inside on a glass support, where a magnetic stirrer was maintained to obtain an optimal homogenization. In **Fig. 4.2** it's reported a scheme of the NO_x reactor plant used for TiO_2 powders in gas phase.

In order to irradiate the photocatalytic sample it was used UV lamp with a power of 500 Watt and an emission maximum at 364 nm. In terms of UV irradiation, the distance between the light source and the reactor was properly adjusted so that the UV irradiance at the sample surface is 10 ± 0.5 W/m^2. The emission spectrum of UV-A is shown in **Fig. 4.3**.

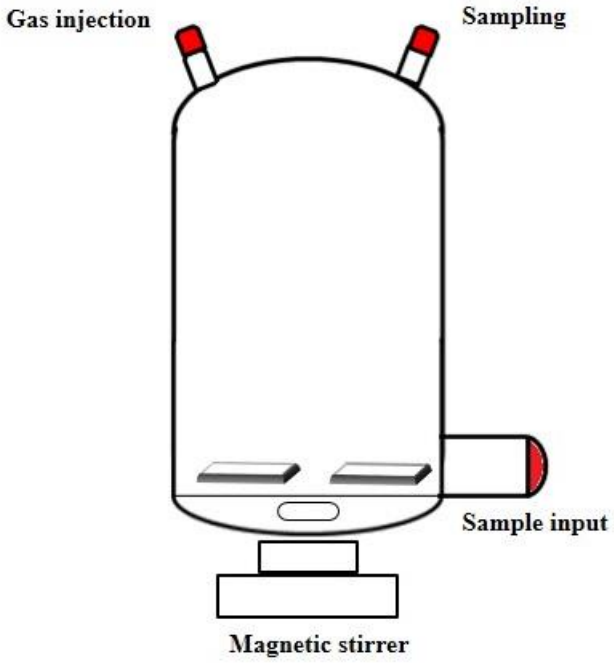

Fig. 4.2. Photocatalytic reactor in gas phase for NO_x degradation using TiO_2 powdered samples.

A chemiluminescence instrument was used to check the final conversion of the pollutant.

$$NO_x\ conversion = \frac{([NO_x]_{t=0} - [NO_x]_t)}{[NO_x]_{t=0}} x\ 100 \quad \textbf{(4.1)}$$

where $[NO_x]_{t=0}$ and $[NO_x]_t$ are the concentration at initial time and at a generic time t of reaction of NO_x, respectively.

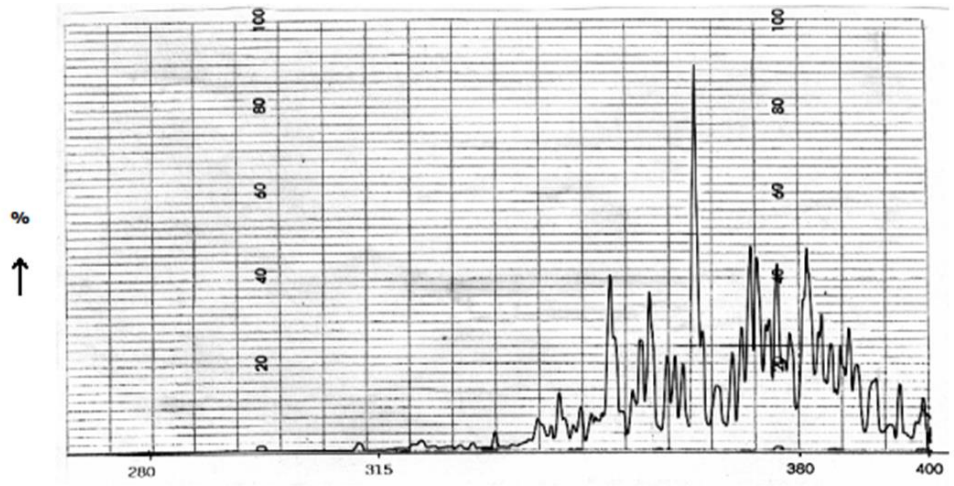

Fig. 4.3. Emission spectrum of a UV-A lamp (Jelosil, model HG500) in the ultraviolet region.

Two initial concentrations of NO_x in the reactor were tested: 1000 ppb in order to follow the same pollutant concentration requested by the ISO 22197-1 rules [26] and 200 ppb that is very close to the alert threshold set by EU Directive 2008/50/CE for NO_2 [27]. In addition to the kinetics tests of photocatalytic degradation, proper runs were carried out by irradiating the reactor without samples of titanium dioxide inside, to evaluate the effect of the simple photolysis action; after 6 h a maximum total conversion of 3% was obtained and then this contribute will be considered as negligible in this paper. Moreover, dark experiments (i.e. with the catalyst inside the reactor but without UV irradiation) were conducted in order to obtain a proper estimation of the NO_x adsorption on the different catalytic samples.

4.1.2 NO_x photodegradation results

In this section several commercial pigmentary powders were analyzed for NO_x degradation and were compared with the nanometric powders efficiency (P25 and PC105). As already mentioned, two initial concentrations of NO_x in the reactor were tested: 1000 ppb and 200 ppb. The results obtained with all the catalysts starting from 1000 ppb of NO_x are reported in **Fig. 4.4**. In all cases the abatement of NO_x is early completed at the end of 3 hours, except the 1071 (by Kronos) sample, which show lower photodegradation (61,5 %). The efficiency of the other samples is between 90 and 99%: this behavior leads to hypothesize a compete degradation of the pollutant within the chosen limited time of the run (3 h).

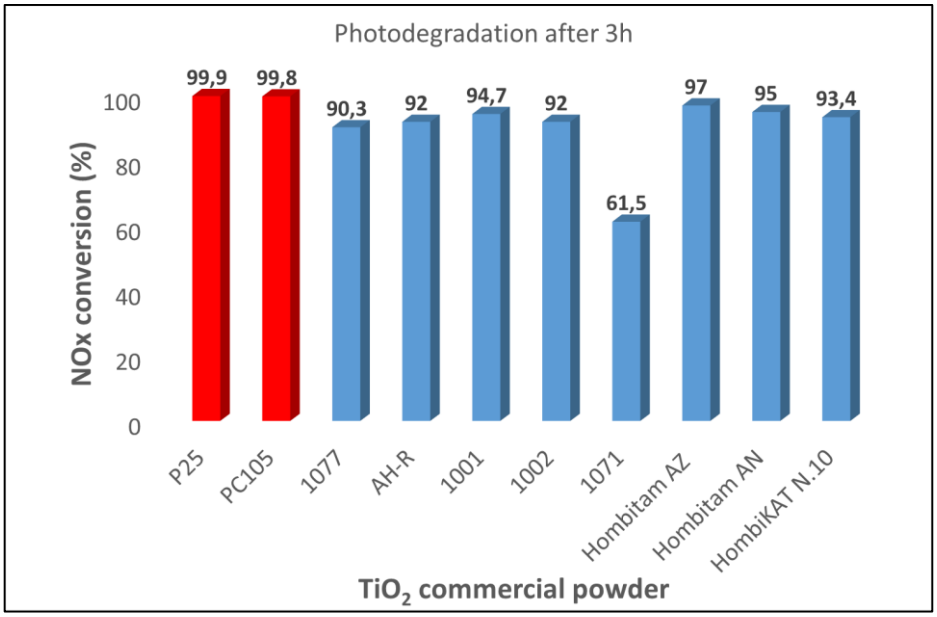

Fig. 4.4. NO_x photodegradation within 3h for TiO_2 micro-sized powders compared with nano-sized ones (P25 and PC105).

However, in order to understand the differences among the photocatalytic samples, it is useful to observe the photodegradation at 15min, 30min, 60min and 240 min, the most significantly times, for only micro-sized samples (1077, AH-R, Hombitam AZ, Hombitam AN and HombiKat N.10). In **Fig. 4.5** we can observe the peculiar differences, which arise in the initial period of the degradation. The samples with highest photoefficiency are 1077, Hombitam AZ and Hombitam AN, showing the best activity in the first times of reaction (15, 30 min). This behavior can be explained through the physico-chemical features and the amount of hydroxyl radicals that initiate the oxidation of NO. The ratio of OH/O_{tot}, obtained by XPS analysis, resulted to be, in fact, higher than the other micrometric ones; 0.32, 0.25 and 0.35, respectively for the 1077, Hombitam AZ and Hombitam AN samples, as it is reported in **Table 4.1.**

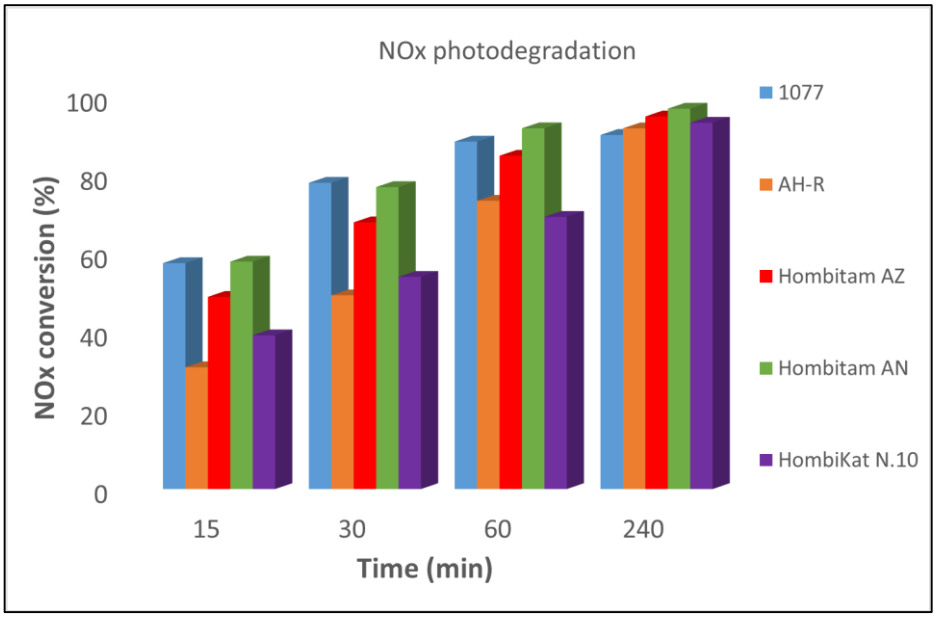

Fig. 4.5. Graph of TiO_2 commercial micro-sized powders for NO_x abatement at 15, 30, 60, 240 min.

In particular, after 30 min of reaction the NO_x conversion of 1077, Hombitam AZ and Hombitam AN is in the range 50-70%. After 1 h, the NO_x conversion of these samples is higher than 80%, very close to that of P25 (90%). Thus, even if the nano-sized materials (P25 and PC105) show the best performances, as expected also on the basis of XPS spectrum in the OH region (see **Paragraph 3.2.1**), the photocatalytic activities of the pigmentary samples are very good, in agreement with the presence of appreciable amount of surface hydroxyls. From the trend in the **Fig. 4.5** it is immediately apparent that the micrometric samples showing the best photocatalytic performances are the ones showing the largest OH component. This result indicates that the interactions with humidity play a relevant role in affecting the final performance. For what concerns the morphological feature and the particles size, any significant differences were observed.

The results obtained using 200 ppb (**Fig. 4.6**) are even more interesting. As a matter of fact, nano-sized and micro-sized powders show quite the same photocatalytic activity, reaching the complete NO_x degradation within 50 min. Working in more diluted initial concentrations, the difference between micro and nano-samples is highly limited and this means that the amount of surface OH species on the pigmentary TiO_2 is enough to guarantee performances similar to that of P25.

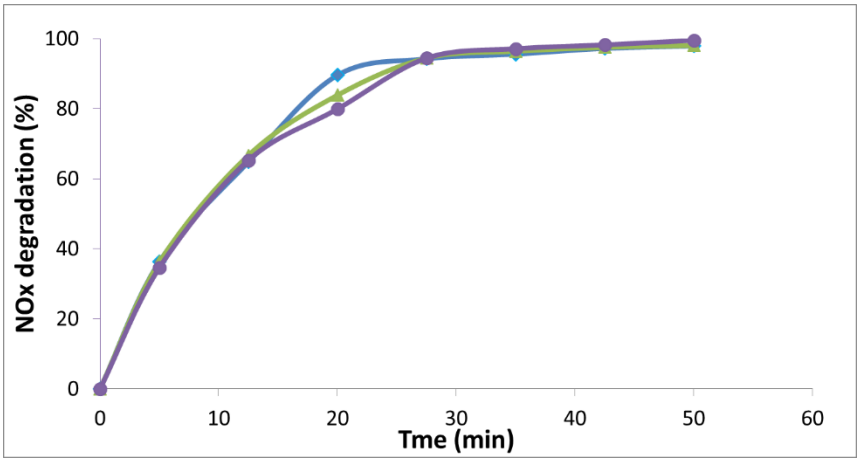

Fig. 4.6. NO_x photodegradation starting from 200 ppb, RT, RH: 40%, UV-A irradiation with the samples: 1077 (♦), AH-R (▲), P25 (●).

4.1.3 Conclusions

Commercial pigmentary micro-sized TiO_2 powders were tested for the photodegradation of NO_x in gas-phase and their photocatlytic performances were compared to that of P25 and PC105, nanometric samples sold as photocatalytic materials. Band gap values fall in the classical range (3.15–3.28 eV) of the anatase polymorph and without any particular difference due to the different crystallites size.

The photocatalytic activity in NOx degradation was tested with a concentration of 1000 ppb (to follow the 22197-1 ISO rules) and 200 ppb (2008/50/CE threshold alert). As expected, at 1000 ppb P25 and PC105 show the highest efficiency, reaching the complete pollutant degradation only after 120 min; however, pigmentary powders exhibit very good

efficiency, reaching conversion percentages higher than 90%. At 200 ppb of NO_x nano-sized and micro-sized powders show quite the same photocatalytic activity. The presence of surface OH groups, which are well known to play a key role in leading to a good photocatalytic activity, was assessed by FTIR spectroscopy. It was evident that P25 and PC105 is characterized by a significant higher amount of hydroxyl species, in agreement with the best performances in NO_x abatement at 1000 ppb. However, also the pigmentary TiO_2 samples show appreciable amounts of OH groups and this justifies their good catalytic performances at 1000 ppb and the same activity of P25 at 200 ppb. All samples reveal good photoactivity in the photodegradation of NO_x in gas phase with an evident superiority of the nano-sized samples. However, the gap of activity between nano and micro-sized samples tends to be avoided when the starting NO_x concentration was reduced and fixed from 1000 to 200 ppb, closer to the real pollution level in our cities.

4.2 NO_x photodegradation with TiO_2 tiles

Titanium dioxide nanoparticles are manufactured worldwide in large quantities for use in a wide range of photocatalytic applications including pigment and cement manufacturing. These products are essentially paints or cements containing photoactive TiO_2 [28-30], photocatalytic pavement blocks [31], filters and membranes for indoor/outdoor air purifications. Although TiO_2 is chemically inert, TiO_2 nanoparticles can cause negative health effects, such as respiratory tract cancer in rats. Trouiller et al. [10]

investigate TiO_2 nanoparticles-induced genotoxicity, oxidative DNA damage, and inflammation in a mice model. However, incorporation of nanophotocatalysts into cementitious materials has been an important achievement in the field of photocatalytic pollution mitigation [32]. In the field of construction materials, nano-sized TiO_2 is particularly common since it has been traditionally used as a white pigment. Nowadays TiO_2 is being used in air purification devices and as a surface treatment and additive in ceramics, cement, transportation infrastructure and glass. These products, such as porcelain gres tiles, are being used or evaluated for their depollution, self-cleaning, antifungal, and environmental improvement attributes [33].

The increased presence of nanomaterials in commercial products has raised a growing public debate on whether the environmental and social costs of nanotechnologies outweigh their numerous benefits [11]. Difficulties abound in devising such regulations, beyond self-imposed regulations by responsible companies, because of the likelihood of different properties exhibited by any type of nanomaterial, which are tunable by changing their size, shape and surface characteristics [34].

The possibility to use micro-sized TiO_2 powders instead of nanometric ones, opens a new generation of materials intrinsically safer than the traditional photocatalytic products for both workers in the factories and public safety, even though, with such materials that are surface vitrified, the release of TiO_2 particles is extremely remote.

In this work, commercial micrometric a new generation of photocatalytic tiles, prepared starting from the relative commercial micro-sized TiO_2 powder in the anatase form, are investigated for the NO_x abatement. Two series of photoactive porcelain gres tiles by GranitiFiandre

S.p.A were subsequently covered at the surface with a mixture of pure anatase micro-TiO_2 (1077 by Kronos) and a commercial SiO_2-based compound. To ensure the requested product stability, at the end of the preparation procedure tiles were treated at high temperature (min 680°C) for 80min and then brushed to remove the powder present at the sample surface and not completely stuck (samples name: White Ground Active® (WGA) and Orosei Active).

For the sake of comparison, samples were also prepared with the same procedure but without adding the photoactive oxide into the SiO_2-based compound (sample name: White Ground (WG) and Orosei).

4.2.1 Experimental section of TiO_2 gres tiles

4.2.1.1 Preparation of vetrified tiles

Commercially available white tiles by GranitiFiandre SpA (sample name White Ground Active® (WGA) or Orosei Active) were covered at the surface with a mixture of micro-TiO_2 and a commercial SiO_2-based compound prepared via ball–mill [35,36]. To achieve the desired product stability, at the end of the preparation procedure tiles were treated at high temperature (680 °C) for 80 min and then brushed to remove the powder present at the surface and not completely stuck. Temperature was precisely chosen to maintain the anatase form of the semiconductor and allow the vitrification of the tiles surface. Tiles were also prepared with the same procedure but without adding the photoactive oxide into the SiO_2-based

compound for the sake of comparison (sample name White Ground (WG) or Orosei).

4.2.1.2 Tiles physical properties

Porcelain gres tiles are characterized by a very low water absorption rate (less than 0.5%) and are manufactured under high pressure by dry-pressing fine processed ceramic raw materials with large proportions of quartz, feldspar, and other fluxes. Afterwards, the body of these materials is fired at very high temperatures (1200–1300°C) in kilns [37]. The final material is thus characterized by lack of porosity, complete water-proofing, durability, hardness, wear resistance properties, and a complete frost resistance.

In the past decades porcelain gres tiles underwent significant transformations in terms of appearance and size. At the beginning of the industrial productions, porcelain gres tiles were considered as just a technical material characterized by strong resistance to both abrasion and acid attack, almost lack of porosity, but aesthetically not very beautiful. Today thanks to new industrial production methods, both properties and beauty of these materials completely fit the market requests. In particular, the possibility to prepare slabs of large sizes is the new frontier of building materials. Previously Marcos et al. [38] reported the deposition of TiO_2 layers on common ceramic glazed tiles using the screen-printing process, which is a low cost and common technique used for decoration in the ceramic industry. Labrincha et al. [39] deposited several commercial titania powders by jet spray on ceramic tiles, then fired to stabilize the layers. In both cases, a good activity of nano-sized TiO_2 photocatalytic layers on ceramic tiles was demonstrated in the degradation of Orange II dye.

In the present paper, the industrial preparation of a new generation of photocatalytic tiles is reported. The porcelain gres slabs are prepared with a commercially available photoactive TiO_2 with crystallites larger than the classical nanoparticles usually used in photocatalysis. The final heat treatment at 680°C assures a perfect and stable fixation of the TiO_2 particles.

4.2.1.3 Tiles testing procedures

Basic tiles features were verified after the coverage with the photocatalytic SiO_2-based mixture. Lack of porosity, resistance to surface abrasion and durability were measured by water absorption [40], rotation of an abrasive load on the tile surface [41] and determination of frost resistance (that is an intrinsic measurement of the product durability) [42], respectively.

NO_x degradation was performed in three plants working in two different experimental conditions: the first set-up, shown in **Fig. 4.8**, works in static conditions, using a fixed-bed reactor at atmospheric pressure and room temperature with a volume of 20 L and irradiated with a halogen lamp (Jelosil, model HG500) emitting in the 340-400 nm wavelength range, photon flux 2.4 x 10^{-5} E dm^{-3} s^{-1}, checked by actinometry [43]. The degradation was performed at different NO_x concentrations ranging from 40 ppb to 1000 ppb, room temperature, RH: 50%. The chosen values include the limit values reported on the Directive 2008/50/EC, in particular, 106.43 ppb (value not to be exceeded more than 18 times in a calendar year) and 212.96 ppb (alert threshold).

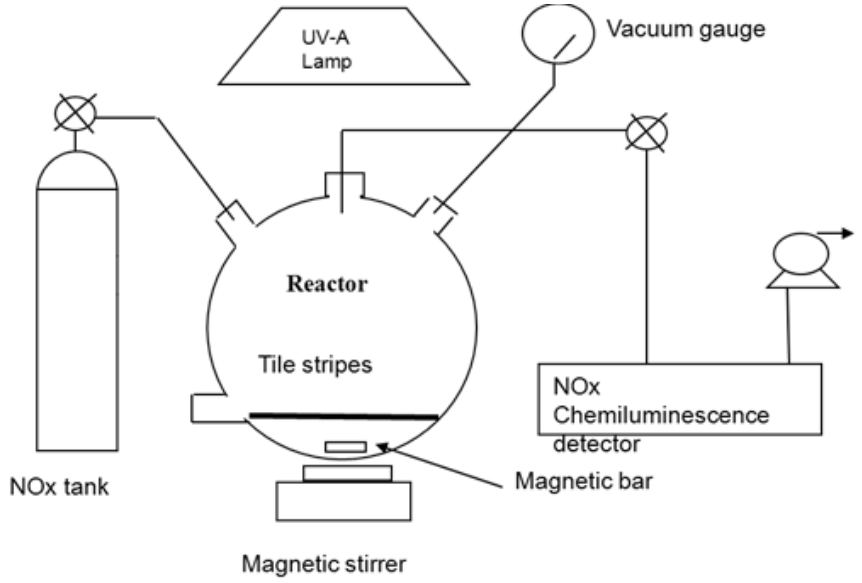

Fig. 4.8. Experimental apparatus for photocatalytic NO_x reaction in static conditions.

The distance between the light source and the reactor was properly adjusted so that the UV irradiance at the sample surface is 20 ± 0.5 W/m^2 for TiO_2 gres-tiles.

A second and third set-up were used towards the same reaction, but in flowing conditions. One reactor was built following the scheme ISO 22197-1 [44], with an effective volume of 0.025 L. The other one was of 3.3 L, known as TCNA. Experimental conditions were maintained as follows: RH (Relative Humidity): 40 %, lamp power: 10 W/m^2, total gas flow: 180, 32.4 and 4.2 L/h. The photoreactor system is shown in **Fig. 4.9**.

In both the experimental setups, the same chemiluminescence instrument, used for NO_x degradation with TiO_2 powders, was used to check the final conversion of the pollutant.

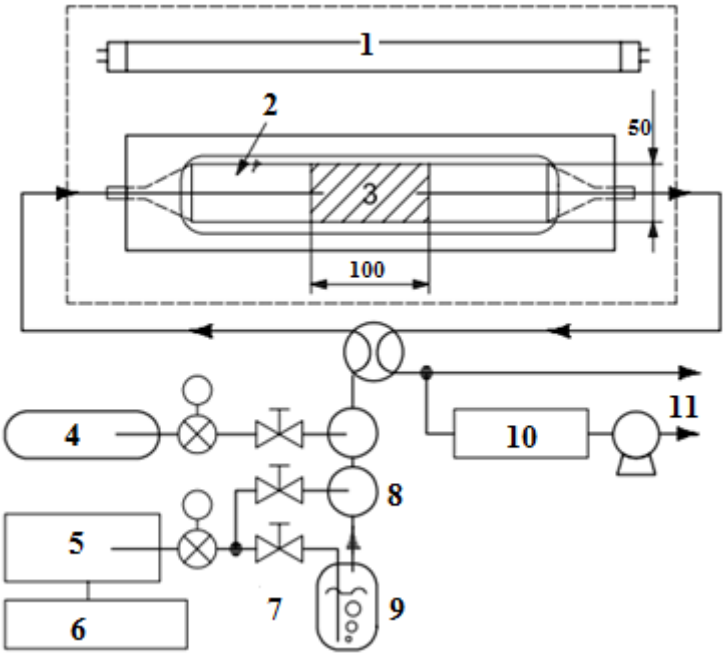

Fig. 4.9. Irradiation set-up for the air purification ISO 22197-1 procedure, comprising: (1) UV light source, (2) glass cover, (3) sample under test, (4) standard gas (i.e. test pollutant), (5) purified air source, (6) air compressor, (7) mass-flow controllers, (8) gas mixers, (9) humidifier, (10) analyser and (11) vent.

4.2.2 Results and Discussions

4.2.2.1 Photocatalytic Tests

One of the most important properties of a photocatalytic material is the possibility to degrade pollutants in the gas phase: in particular, NO_x is often chosen as reference pollutant to monitor the level of air pollution [45]. **Fig. 4.10** reports the NO_x degradation profiles relative to WGA tiles. The NO_x concentration is the sum of the NO and NO_2 concentrations as the general mechanism for NO_x degradation by photocatalysis implies the oxidation of the nitric monoxide to nitric or nitrous acid induced by oxygen species produced at the TiO_2 surface [46]. The reaction path for NO_x conversion is generally mediated by OH radicals [47]:

$$NO_2 + \cdot OH \rightarrow HNO_3$$

$$NO + \cdot OH \rightarrow HNO_2$$

It's possible to determine the photocatalytic efficiency in two different experimental condition: in static and in continuous.

4.2.2.1a Batch reactor

In static conditions good results were obtained testing WGA in the gas phase. In this case, using 1000 ppb of NO_2, i.e. the same amount required by the ISO 22197-1 specifications, the 65% of degradation was measured after 6 h (**Fig. 4.10**). A very interesting trend (**Fig. 4.11b**) was observed following the NO_2 degradation at different pollutant concentration. More in detail, the tests were carried out the material with 106 ppb (value not to be exceeded more than 18 times in a calendar year), and 212 ppb (alert threshold), according to the Directive 2008/50/EC of the European

Parliament and stating the guidelines for the protection of the human health [48]. NO_2 was chosen as specific reference pollutant instead of the more generic NO_x, because of its higher hazardousness. NO_2 is in fact an irritant agent affecting the mucosa of the eyes, nose, throat, and respiratory tract and the continued exposure to high NO_2 levels can contribute to the development of acute or chronic bronchitis [48].

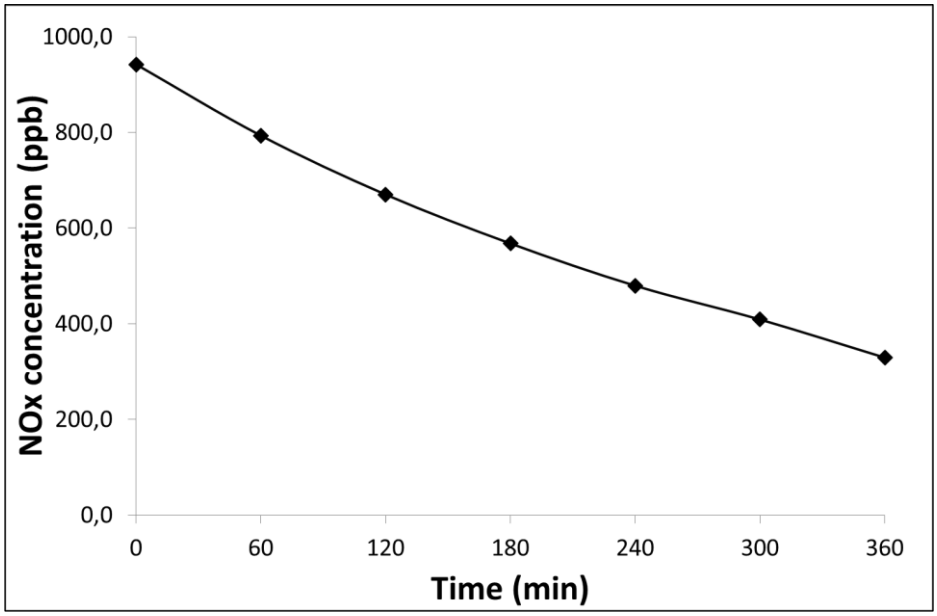

Fig. 4.10. Photocatalytic efficiency with WG Active tile starting from 1000 ppb of NO_2: 65% degradation after 6 hours.

It is possible to observe (**Fig. 4.11b**) that, as the amount of starting pollutant is decreased, the time necessary to bring its concentration under the limit required by the European Directive (21 ppb) also decreases. In the **Fig. 4.11a** the degradation trend can be observed in the case of an initial pollutant concentration close to the alert threshold.

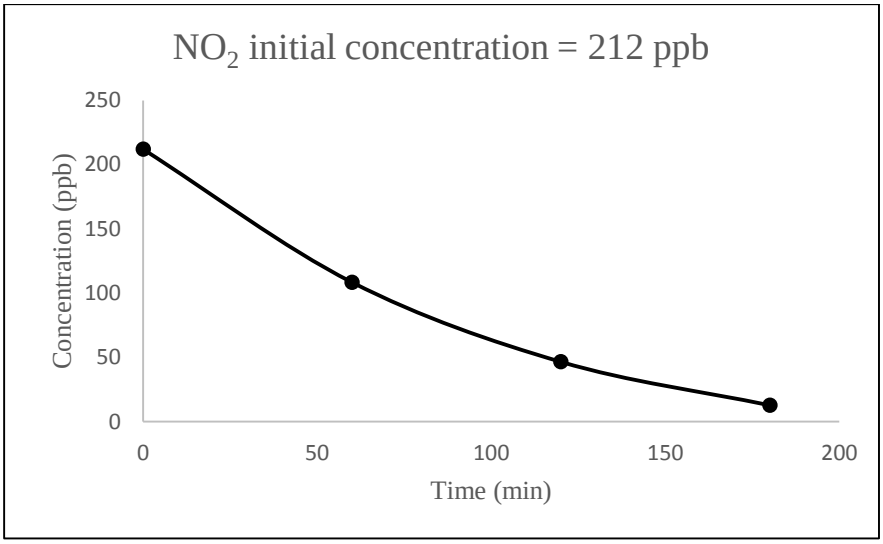

(a)

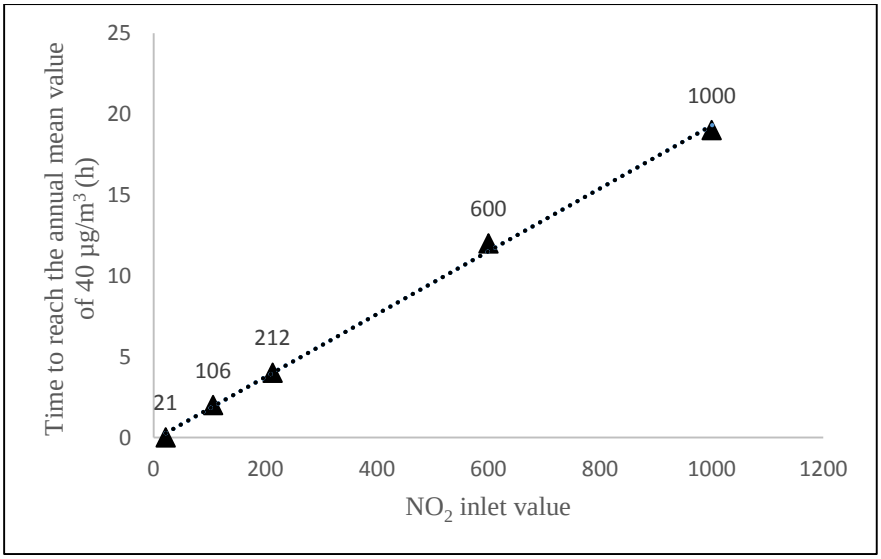

(b)

Fig. 4.11. Degradation trend starting from the NO_2 concentration close to alert threshold (a) and time necessary to degrade the pollutant and decrease its amount under the limit value required by the Directive 2008/50/EC of the European Parliament and of the council on ambient air quality and cleaner air for Europe (21 ppb) (b); 20 W/m^2, RH 50%, static conditions.

Therefore under real pollution conditions, simulating a day in the absence of wind (static conditions) WGA is able to degrade NO_2 in a very efficient way bringing the pollutant concentration down to the required limit (21 ppb) in a matter of hours [49]. **Fig. 4.12** reports the NO_2 degradation profiles relative to WGA tiles under different NO_x starting concentrations. As discussed above, it's clear that the lower is the starting pollution amount, the faster is the NO_2 removal. In all cases, the acid moieties produced by the degradation of NO_2 remains on the tiles surfaces without any alteration of the tile properties, being them vitrified on top, and simply washed with water to restore the original surface [36].

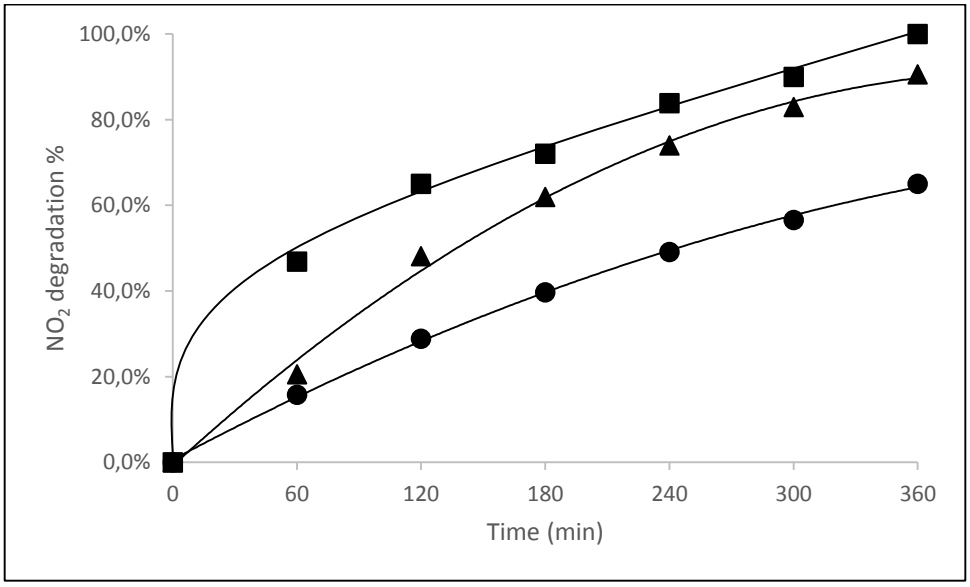

Fig. 4.12. NO_2 degradation profiles for WGA tiles: tests performed at three different NO_2 concentrations in a batch reactor, 10 W/m^2, RH: 40%; ■100 ppb, ▲400 ppb, ●1000 ppb.

It has been also conducted a proper study with the aim to investigate the influence of the relative humidity (RH) on the photodegradation efficiency. We chose three different amounts of RH (4, 40, 75%) and, subsequently, it was followed the NO_2 photoabatement irradiating with a UV lamp power of

20 W/m^2. The same experimental analysis were tested with both Orosei Active and WGA tiles.

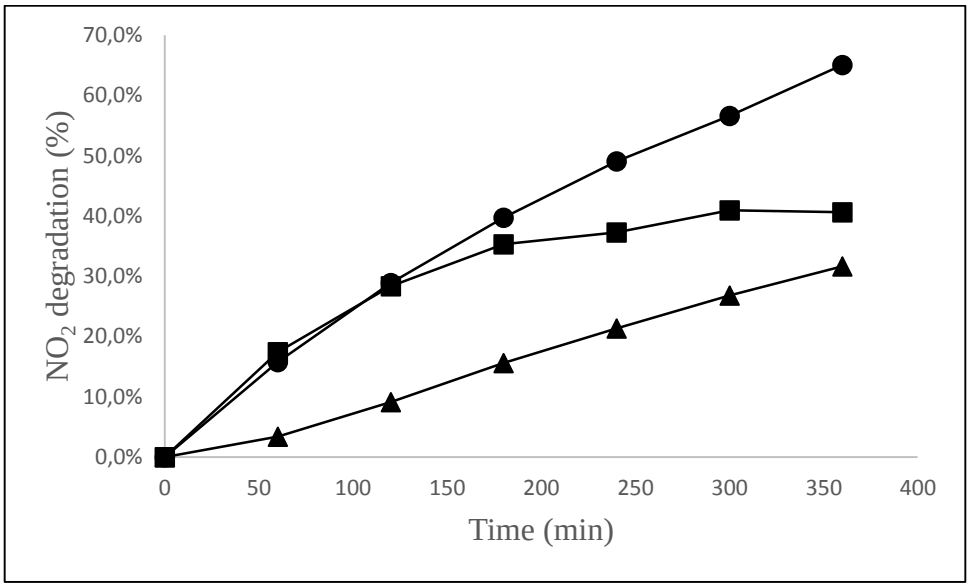

Fig. 4.13. Degradation 1000 ppb, WGA (● 40%, ■ 75%, ▲ 4% RH).

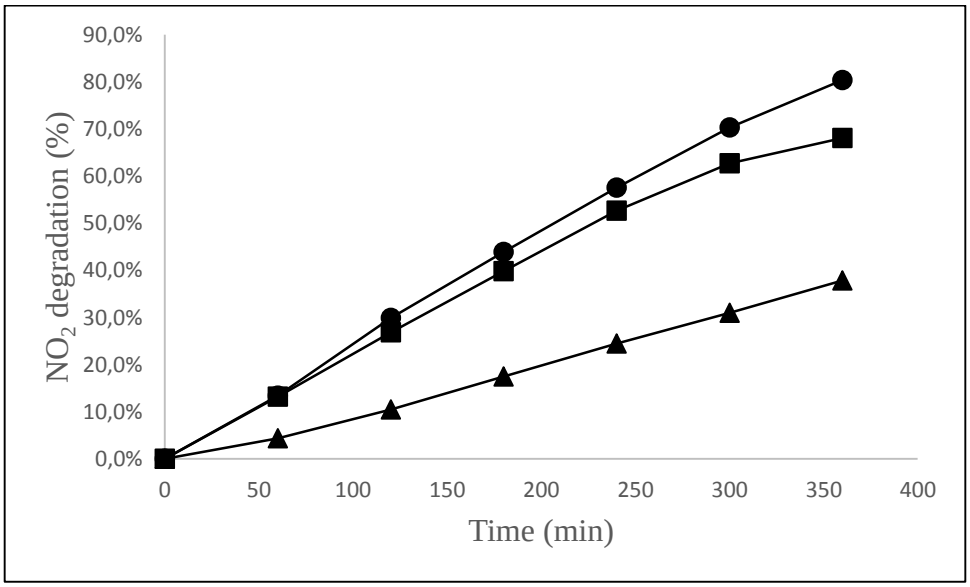

Fig. 4.14. Degradation 1000 ppb, Orosei Active (● 40%, ■ 75%, ▲ 4% RH).

As we can observe by **Fig. 4.13** and **4.14**, the highest degradation efficiency was obtained with the 40% of humidity. In fact, the presence of humidity is greatly necessary, because the increasing humidity facilitates reaction between the conduction band molecules and hydroxyl radicals formed from water molecules at the interfaces [50]. The hydroxyl groups (OH^-) of the TiO_2 surface can trap photogenerated positively charged holes (h^+) to yield hydroxyl radicals ($OH^{\cdot}$). These species are generally considered to initiate the attack on the pollutant molecules. Moreover, photocatalytic reactions require hydroxylation of the TiO_2 surface; so, the vapour-phase water molecules must also be consumed on the catalytic surface to promote the further generation of radicals. Hence, the small amount of humidity in the reaction environment greatly reduces the probability to guarantee a proper formation of hydroxyradicals that can come into contact with the catalyst surface [51]. On the other hand, several authors [52,53] have proposed that water adsorption favors electron-hole recombination and reduces the photocatalytic oxidation rate. Competition for the adsorptive sites between water and oxygen molecules could justify the decrease in the photoactivity with increasing the humidity. However, the presence of humidity is a fundamental requirement, as demonstrated in our case where the optimal amount of relative humidity resulted 40%. In detail, the degradation % for WGA tiles with 40% were 65%, whereas for Orosei Active were 80%. These latters showed the best photoactivity performance pointing out the real possibility to use them for environmental and industrial applications. In **Table 4.2** it is reported a summary of the NO_2 degradation in different experimental conditions for both WGA and Orosei Active tiles.

Table 4.2. NO_2 degradation with 4, 40, 75% RH for WGA and Orosei Active.

	Reactor (20 L, 20 W/m^2)			
% RH	**OROSEI ACTIVE**		**WGA**	
	% after 3h	% after 6h	% after 3h	% after 6h
4	17	38	16	32
40	44	80	40	65
75	40	68	35	41

4.2.2.1b Plug-flow reactor

Micro-sized TiO_2 tiles were tested towards the same reaction but in flowing conditions using a plug-flow reactor built following strictly the ISO 22197-1 rule [54] with an effective volume of 0.025 L. Experimental conditions were maintained as follows: RH: 40%, 20 W/m^2, $[NO_x]_{inlet}$: 500 ppb, and 180, 32.4 and 4.2 L h^{-1} total flow, respectively. The same chemiluminescent analyzer (Teledyne Instruments M200E) was employed to check the final conversion of the pollutant.

The reactor configuration under flowing conditions was also modeled by digital simulations carried out using COMSOL Multiphysics 4.0a coupling the laminar flow (experimentally verified) with the transport of diluted species physics in a 3D space with each geometry resembling the relevant reactor dimensions and considering steady-state conditions. Each simulation was carried out using the following values: $C_0in = 2.04 \times 10^{-5}$ mol m^{-3} (equivalent to 500 ppb of NO_x); $\rho = 1.165$ kg m^{-3} (air density at 30°C); $\mu =$

1.86 × 10−5 Pa s (air dynamic viscosity at 30°C); D = 1.9 × 10^{-5} m^2 s^{-1} (diffusion coefficient of NO_2 in air [55]).

Simulations were performed considering six different inlet fluxes: V_{in} (4.2, 9, 20, 32.4, 100, and 180 L h^{-1}) and two different apparent reaction rate values, calculated on the basis of the experimental results obtained using micro-sized TiO_2 gres tiles (Orosei Active) at 32.4 L h^{-1} and at 180 L h^{-1}. A first-order kinetic was considered for the reaction, as usual in photocatalysis with reactants such as NO_x at sub-ppm level [56,57]. The apparent kinetic constant was determined by performing simulations varying k_{app} until the NO_x conversion resembled the experimental one. After this, k_{app} was used for the remaining V_{in} values.

ISO 22197-1 rule provides for very sharp experimental conditions such as an inlet NO_x concentration of 1000 ppb coupled with a low irradiation power (10 Wm^{-2}) and mainly with a very strong flow at 180 L h^{-1}. These conditions are too extreme for our samples being vitrified at their surface and having no porosity. For these reasons, the operating conditions have been softened cutting the inlet concentration by half (500 ppb), doubling the power irradiation (20 Wm^{-2}), and investigating the role of the flow per hour on the final NO_x conversion. To check to have maintained the correct fluid dynamic conditions, the Reynolds number was calculated:

$$R_e = \frac{\rho U D_e}{\mu} \quad \textbf{(4.2)}$$

where U is the is the velocity of the fluid (m s^{-1}), μ is the dynamic viscosity of the fluid (kg m^{-1} s^{-1}), ρ is the density of the fluid (kg m^{-3}), and D_e is the hydraulic diameter of the pipe (m), defined as 4 times the cross-sectional area

(of the fluid), divided by the wetted perimeter. The wetted perimeter for a channel is the total perimeter of all channel walls that are in contact with the flow. In all chosen flows of the present paper, the laminar flow is confirmed (**Table 4.3**, second column).

Table 4.3. Data from continuous reactor (0.025 L) and Comsol simulations (NO_x 500 ppb, 20Wm^{-2}, sample size 0.005 cm^2, RH: 40%, run time: 3h. For the Comsol simulation: laminar flow).

Flow (L h^{-1})	Reynold's number	Space velocity (h^{-1})	Contact time (s)	Orosei Active NO_x Experimental data	Conversion (%) COMSOL
180.0	112	7200	0.5	1.3	25.6
32.4	20	1296	2.8	74.2	74.9
9.0	5.6	360	10.0	72.6	98.8
4.2	2.5	168	21.4	82.0	100.0

On the contrary, the modification of the flow per hour leads to an evident change of the contact times that is the time the pollutant can stay "in contact" with the catalyst surface. As expected, increasing the contact time, the final conversion proportionally increases. This result is very evident, as it is shown in **Table 4.3**, fifth column; NO_x conversion on Orosei Active varies from 1.3% to 82.0% at 180 L h^{-1} and 4.2 L h^{-1}, respectively.

The same procedure was carried out too for 1077 sample, in order to compare the different behavior in the case of porcelain tile or pure powder application as already reported by the authors Bianchi et al. [35]. In the case of a micro-sized powder such as 1077, prepared on purpose on a glass sheet following the same procedure used for the batch setup (**Paragraph 4.1.1**), higher NO_x conversion was reported, but it was flattened towards the same value (ca. 90%) (**Table 4.4**, column fifth). This fact is very interesting and

was observed also performing the test on a three-layer of P25. In this case a value of ca. 90% was observed at both 32.4 and 9 L h^{-1} too, and a complete degradation (100%) was never present in our operative conditions as some fluid dynamics problems could exist inside the reactor configuration and part of the gas stream could pass undisturbed through the reactor. Moreover, the difference in the photocatalytic efficiency between P25 and 1077 evidenced by the tests performed in the batch reactor seems to be completely invalidated with this kind of reactor configuration.

Pure 1077 showed higher NO_x conversion than Orosei Active; this fact was fully expected as the number of surface of active sites on the tile surface is not comparable to a film of pure TiO_2 on a glass sheet. For this reason, the obtained 82% conversion at 4.2 L h^{-1} flow can be considered a very good value.

Table 4.4. Data from continuous reactor (0.025 L) and Comsol simulations (NO_x 500 ppb, 20Wm^{-2}, sample size 0.005 cm^2, RH: 40%, run time: 3h. For the Comsol simulation: laminar flow).

Flow (L h^{-1})	Reynold's number	Space velocity (h^{-1})	Contact time (s)	1077 NO_x Experimental data	Conversion (%) COMSOL
180.0	112	7200	0.5	5.0	36.8
32.4	20	1296	2.8	89.1	87.5
9.0	5.6	360	10.0	90.0	99.8
4.2	2.5	168	21.4	90.1	100.0

In regards to digital simulations, **Fig. 4.15** reports a *xz* cross-section of the gas stream 3D fluid dynamics digital simulation in the two extreme flow rates: 180 and 4.2 L h^{-1}. In more detail, the figure reports the local gas linear speed in the inlet side of the photoreactor. It is evident that the linear

velocity of the gas stream is strongly influenced by the inlet flow rate: at 4.2 L h^{-1} the gas stream follows a natural path from the inlet to the channel containing the photoactive material, while at 180 L h^{-1} the inlet speed makes the gas to hit the wall in front of the inlet.

Notwithstanding that this effect might generate some turbulence in the inlet chamber (not included in the present simulation), the fluid speed profile inside the channel containing the photoactive material remains homogeneous through the channel length. In both cases, in the channel containing the photoactive material, the gas follows speed profile typical of laminar flows.

Fig. 4.16 represents the *xz* cross-section of the simulated NO_x concentration profiles in the reactor volume under steady-state conditions. Note that the inlet is on the left side of the reactor (i.e., the same side considered in **Fig. 4.15**), while the outlet is on the right. The color code represents in this case the concentration of NO_x in the air stream, expressed in mol m^{-3} (500 ppb corresponds to 2.04×10^{-5} mol m^{-3}). It is evident that, as expected, the concentration gradient is located at the reactor center, in correspondence to the photoactive tile. This is better represented in the two insets, a (in which the 3D space is transparent) and b (*xz* cross-section). In particular, inset b suggests the formation of a concentration gradient generated by the consumption of NO_x at the photoactive surface. The gradient is at the origin of mass transport, that, at the lowest flow rate values, might become the rate determining step of the whole process, just before the maximum conversion (100%) is reached; see the simulated points (**Fig. 4.17**) and values in Table 4 and 5, sixth column.

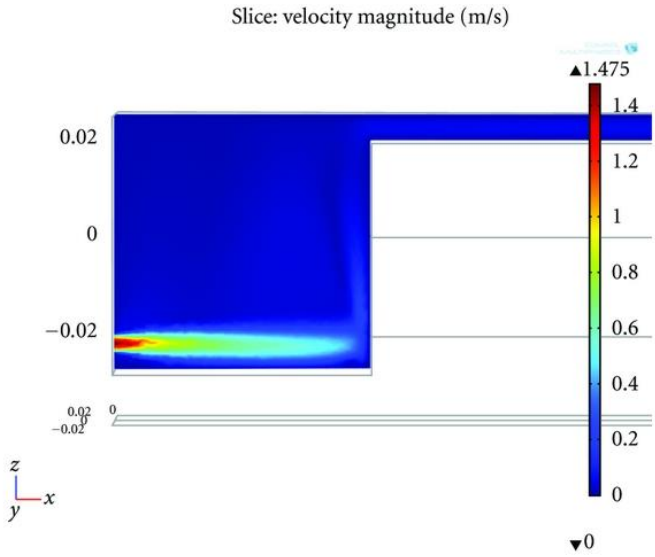

(a) V_{in} = 32.4 L h^{-1}

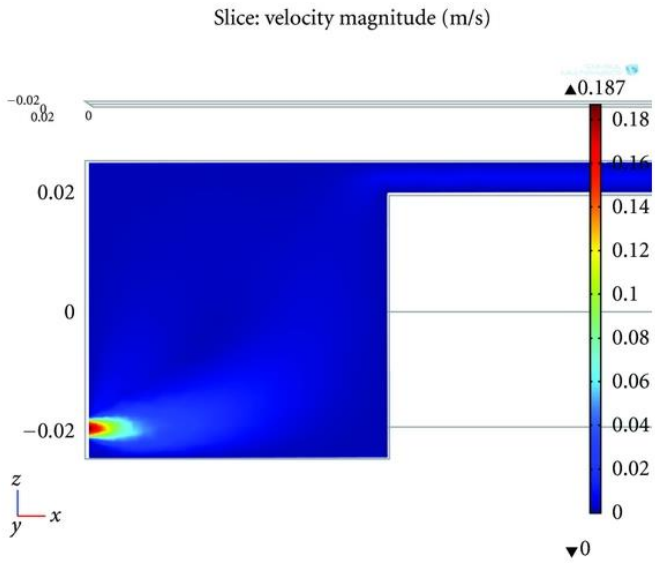

(b) V_{in} = 4.2 L h^{-1}

Fig. 4.15. *xy* cross-sections of simulated fluid dynamic under steady-state conditions of the reactor used for the photocatalytic test (flowing conditions). (a) V_{in} = 32.4 L h^{-1}, (b) V_{in} = 4.2 L h^{-1}. The cross-section follows the longitudinal symmetry and is focused on the inlet gas chamber and a portion of the channel containing the photoactive tile.

This is even more evident considering the experimental and simulated percentage NO_x conversion values in dependence on the flow rate, reported in **Fig. 4.17**. In the case of simulated results, which include the data at 20 L h^{-1} and 100 L h^{-1} as well as a set of data corresponding to $k_{app} = 1 \times 10^{-4}$ s^{-1} it is evident that the trend follows the expected exponential decay predicted by a first-order kinetics:

$$\mathbf{NO_x\ conversion} = \frac{([\mathbf{NO_x}]_{\mathbf{inlet}} - [\mathbf{NO_x}]_{\mathbf{outlet}})}{[\mathbf{NO_x}]_{\mathbf{inlet}}} \bullet \mathbf{100} = \mathbf{100} \bullet (\mathbf{1} - e^{-kt}) \qquad \mathbf{(4.2)}$$

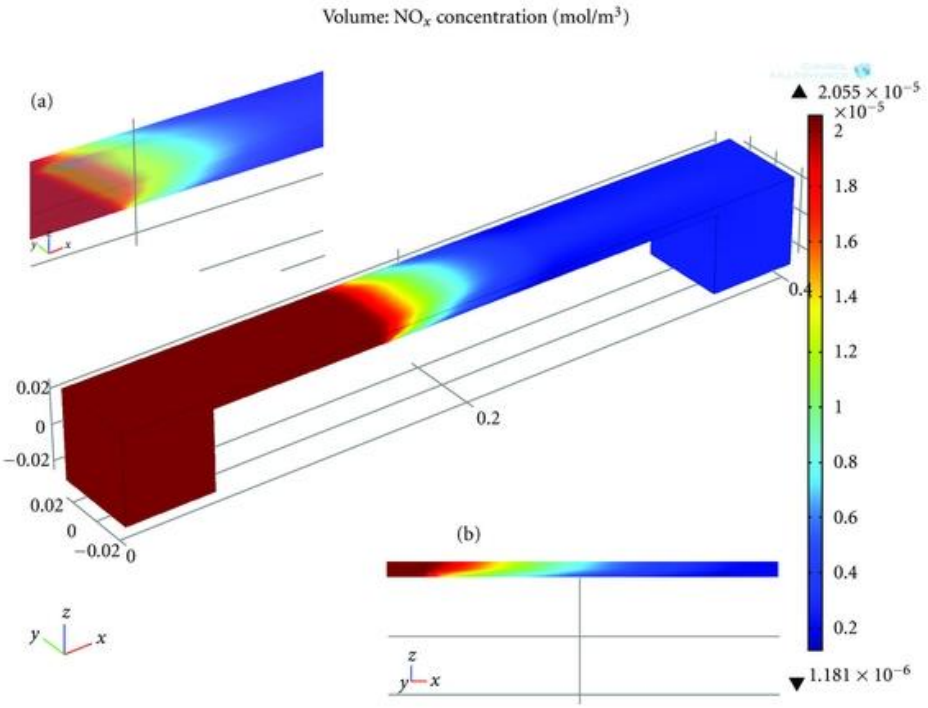

Fig. 4.16. NO_x local concentration in the reactor volume, expressed in mol m^{-3} (k_{app} = 4 x 10^{-3} m s^{-1}, 32.4 L h^{-1}). Inset (a), zoom on the photoactive tile; inset (b), *xz* cross-section of the photoactive tile.

In fact, the flow rate is inversely proportional to the contact time and thus to the reaction time, t. At the lowest flow rates (highest reaction times) a limiting-value results are reached, as indicated in **Fig. 4.17** by the colored ovals.

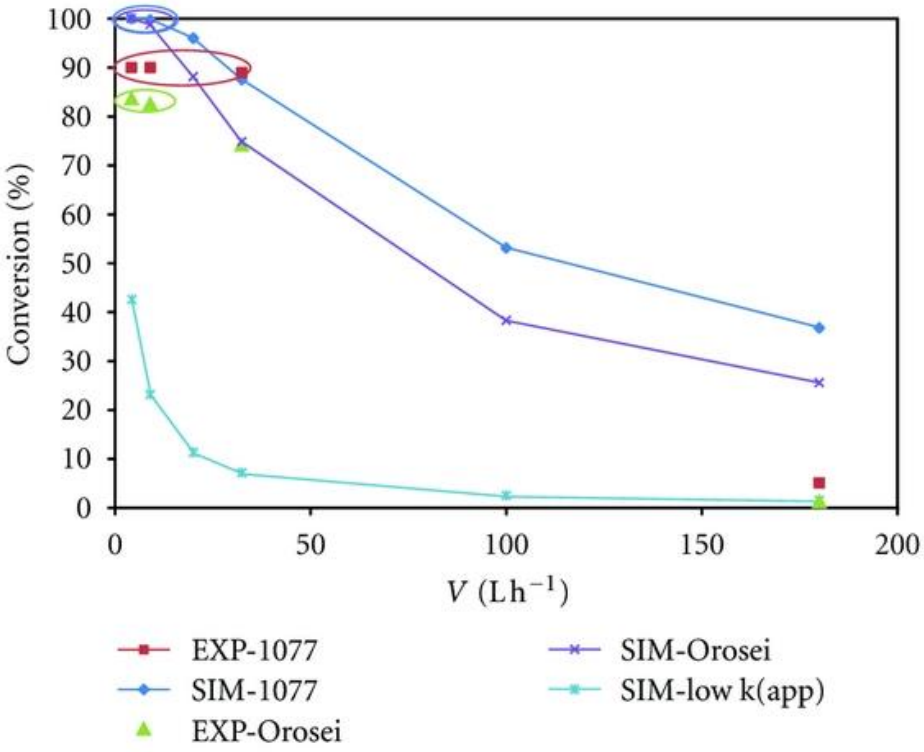

Fig. 4.17. Experimental (EXP) and simulated (SIM) percentage conversion in dependence on the flow rate, as reported in Table 4 and 5, relevant to the two samples considered in the flowing condition experiments (1077 and Orosei active) or the relevant simulated apparent kinetic constants (4×10^{-3} and 2.3×10^{-3} m s^{-1}, respectively. The light blue curve corresponds to the simulated data adopting a lower apparent kinetic constant, 1×10^{-4} m s^{-1}.

These limiting values are 100% for the simulated data and about 90% for the experimental. This unexpected discrepancy can be explained considering the existence of preferential gas paths on the tiles sides (uncovered by the catalyst) that lead to the presence of unreacted NO_x at the reactor outlet. The figures also evidence that the only common points between simulated and experimental data are those obtained 32.4 L h^{-1}, that is, the conditions at which the kinetic constants used in the simulations have been determined. In other words, this means that also the experimental results obtained at high flow rates do not find any correspondence with the simulated data. This aspect might be explained by the formation, in the real reactor, of turbulence (likely in the inlet chamber) that can actually change the fluid dynamics of the whole system due to the reactor geometry.

Table 4.5. Data from continuous TCNA (3.3 L) reactor (NO_x 500 ppb, 20Wm^{-2}, sample size 0.005 cm^2, RH: 40%, run time: 3h).

Flow (L h^{-1})	**Reynold's number**	**Space velocity (h^{-1})**	**Contact time (s)**	**Orosei Active NO_x Experimental data**
32.4	20	1296	367	74.3
9.0	5.6	360	1320	79.7
4.2	2.5	168	2200	89.2

The experiments in flow conditions were conducted also in a reactor of 3.3 L, known as TCNA, using three different fluxes: 32.4, 21, 9 and 4.2 L/h. In the Table 6 we note that the time contact values are much higher than the other ones, because of the size of the reactor (3.3 L). The degradation % resulted to be improved, especially when the pollutant gas flows slowly at

4.2 L h^{-1}; in this case the contact time is high, around 2200 s. As confirmed from the analysis conducted on the previous reactor, the time contact and, consequently, the flow of the gas pollutant on tile is an important parameter to take into account.

4.2.3 Conclusions

In the present paper, the photocatalytic activity of vitrified tiles is discussed. To avoid possible future drawbacks due to the nanometric size of the photocatalytic active powder, the samples were prepared using a commercial micro-sized TiO_2. The final tile couples the classical requested features typical for a tile (hardness, lack of porosity, vitrified surface, durability) with good performance as photocatalytic material both in water and in air. White Ground Active tiles (WGA) show good photocatalytic performances especially in the pollution ranges indicated by the Directive 2008/50/EC of the European Parliament and of the Council on ambient air quality and cleaner air for Europe (NO_2 concentration lower than 200 µg/m^3, corresponding to 106.43 ppb). A final remark is devoted to the inadequacy of the ISO 22197-1 specifications as standard test on vitrified, non-porous materials. Employed NO_x photoreactor was built following the ISO 22197-1 rule but the requested ISO experimental conditions, such as inlet NO_x concentration, low irradiation power, and high flow, are too extreme for our tiles samples being vitrified at their surface and having no porosity. For these reasons, the operating conditions have been softened and the role of the flow per hour on the final NO_x conversion was fully investigated. The discrepancies between the experimental data and the

simulated ones might be related to the presence of preferential gas paths in the test reactor and to the formation of turbulence (due to the reactor geometry) in the case of the highest flow rate values.

In fact, due to the lack of porosity of the tested tiles together with the velocity of the gas (contact time 0.4 s), the adsorption of the pollutant molecules at the sample surface cannot occur, so preventing the photocatalytic process.

Micro-sized TiO_2 can be really used as a valid choice for antipollutant photocatalytic processes avoiding the intrinsic risk due to the nanometric dimension. TiO_2 larger size compared to more traditional nano-sized crystallites allows to reach fully comparable results in the photodegradation of NO_x, reference molecule for outdoor air pollution. Good photocatalytic efficiency was achieved by the pure commercial micro-sized powder in comparison to P25. Porcelain gres tiles prepared entrapping micro-TiO_2 at the SiO_2 surface also show a stable and reproducible photocatalytic activity towards the degradation of NO_x in air as expected by the surface feature results (surface wettability and Ti content). This result opens a new generation of material intrinsically safer than the traditional photocatalytic products prepared starting from nano-sized semiconductors.

4.3 VOCs photodegradation with TiO_2 powders

VOCs are well-known indoor pollutants. These latters are emitted from different sources such as combustion by-products, cooking, construction

materials, office equipment, and consumer products. Many VOCs are known to be toxic and considered to be carcinogenic and mutagenic [58]. TiO_2 have been used as photocatalyst, in order to achieve their complete abatement.

In the present PhD's thesis, TiO_2 catalysts have been tested to degrade three different VOCs: acetone, acetaldehyde and toluene, chosen as they are specific molecules for indoor pollution. The aim is to degrade these pollutants through micro-sized TiO_2 photocatalysts, because of the possible health risks, as previous reported. Furthermore, a great attention is focus on both the application of commercial TiO_2 micropowders and the improvement their photoefficiency by doping them. Nano-sized powders were tested too, as reference materials.

4.3.1 Materials and Methods

Both nanometric and micrometric commercial TiO_2 powders are applied and compared on the photoefficiency of VOCs degradation. The powders were applied with the same procedure described in **Paragraph 4.1.1**. The commercial samples tested are reported in **Table 4.1**:
All samples are mostly characterized by anatase phase, with the exception of P25, which has both rutile and anatase phases.

4.3.1.1 VOCs photocatalytic plant

Photocatalytic degradations of VOCs, such as acetone, toluene, acetaldehyde, were conducted in a Pyrex glass cylindrical reactor with diameter of 200 mm and effective volume of 5 L, as reported in **Fig. 4.18**.

The gaseous mixture in the reactor was obtained by mixing hot chromatographic air, humidified at 4, 40 or 75%, and a fixed amount of volatilized (250 °C) organic compound, in order to avoid condensation, as already reported in previous works of Bianchi at al. [20,59].

The role of water in photodegradation is controversial. Some reports have indicated that high humidity favours certain photodegradation processes [60]. The molecular water adsorbed on the photocatalyst will react with the hole and generate some hydroxyl groups, such as OH, which, in turn, oxidizes pollutants. It has been found that an oxidation photocatalytic reaction is typically governed by the generation of the hydroxyl radical [61,62], although reactions that generate other radicals (e.g., chlorine [63]) can display higher reaction rates. In the absence of water vapor, the photocatalytic degradation of some chemical compounds (e.g., formaldehyde [64], acetone [65], toluene [66]) is seriously retarded. However, excessive water vapor on the catalyst surface will inhibit the reaction rate because the presence of water vapor competes with pollutants for adsorption sites on the photocatalyst, thus reducing the pollutant removal rate. Some studies summarized the experimental data with empirical equations. For instance, Peral and Ollis [67] found the rate of acetone oxidation decreased with increasing water vapor.

In this PhD research it has been taken into account a further photocatalytic study performing tests by using both very low values of RH (4%) and high amount of water humidity in the reactor (75%). It will be shown in the next Paragraph the specific role of humidity on the photoefficiency of the catalyst.

The actual concentration of VOC in the reactor is determined directly by micro-GC sampling (Agilent Technologies 3000A). Photon sources were provided by a 500 W iron halogenide lamp (Jelosil, model HG 500) emitting in the 315-400 nm wavelength range (UV-A). The power of the UV lamp at the sample surface is 30 ± 0.5 W/m^2 [20]. The experimental apparatus of VOCs setup is reported in **Fig. 4.19**.

Fig. 4.18.VOCs reactor irradiated by UV light with TiO_2 glass sheets.

The term "micro" is relative to the miniaturization of the instrument. It provides fast, accurate, reliable analysis of the gas sample on-line at the sampling point. It is ideal for the rapid analysis of gas streams (3 minutes), by using minimal amounts of sample and gas-carrier (in our case He), with a detector that is 10 times more sensitive than traditional thermal conductivity detectors. Multiple channels make, also, analyzing complex samples quick and easy. Each channel or module is a self-contained GC comprised of a micro injector and micro thermal conductivity detector and a high-resolution

capillary column. As a result, you can simultaneously analyze the sample on three different columns working simultaneously.

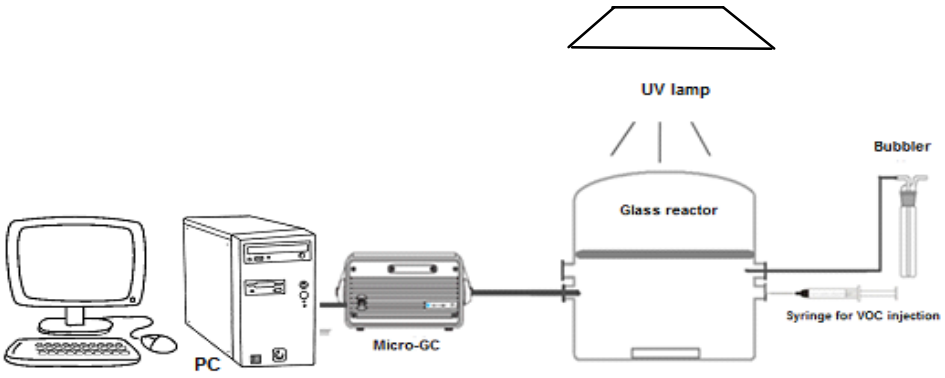

Fig. 4.19. Experimental apparatus for VOCs degradation.

The main steps that take place during an analysis can be summarized into:

1. Injection
2. Separation
3. Detection.

The heart of the instrument is the GC module. It includes a heated injector, sample column, reference column, thermal conductivity detector (TCD), electronic pressure control (EPC) hardware, gas flow solenoids, and control board. The gaseous sample enters the micro-GC through a pump. The system regulates the pressure, so the sampling occurs at atmospheric pressure, whatever is the flux and the pressure outbound from the system. An amount of sample is discharged outside through a "switch" valve, while another amount is injected inside the column. After passing through the injector, the sample gas enters the column, which separates it into its component gases in typically less than 180 seconds. After separation on the

column, the sample gas flows through a thermal conductivity detector (TCD). Carrier and sample gases separately feed this detector, each passing over different hot filaments. The varying thermal conductivity of sample molecules causes a change in the electrical resistance of the sample filaments when compared to the reference filament (He). The signal, or rather, the imbalance Weathstone bridge (in mV), is transduced in electric signal and registered by computer system. Thus, the detector reveals any compound with an intensity proportional to the conductivity difference between the compound and gas carrier (He).

The assembled columns are "RT PLOT-Q", "STABILWAX" and "Molecularsieves". The "RT PLOT-Q" column is able to separate hydrocarbons and oxygen compounds C1-C4. For this reason, it is used for the detection of CO_2 peak. The "STABILWAX" column is ideal to separate alcohols, aldehydes, ketones and aromatic isomers (benzene, toluene, xylene). In fine, the Molecularsieves column separates compound in bases to their sizes. In general, it is used for gases like He, H_2, Ar, O_2, N_2, CH_4, CO.

The gaseous mixture in the reactor was obtained by mixing hot chromatographic air (f.i. 250 ◦C for toluene) humidified at 40%, and a fixed amount of volatilized pollutant, in order to avoid condensation. The initial concentration of VOCs in the reactor was 400 ppmv. The degradation was conducted using different percentages of relative humidity (RH): 4, 40, 75%. The values of RH were checked and measured by a hygrometer instrument. At first the air cylinder was loaded inside, then the CO_2 concentration in the reactor was measured through micro-GC analysis. Successively, the VOC pollutant, with the desired concentration, was

introduced inside through the injection with a syringe in a rubber septum. The pollutant quantity was measured volumetrically through a GC syringe, as follows:

$$ppm_{inquinante} = (mol_{inquinante}/mol_{aria}) * 10\text{^}6 \quad \textbf{(4.3)}$$

$$mol_{aria} = (P * V)/(R * T) \quad \textbf{(4.4)}$$

$$V_{inquinante} = (mol_{inquinante} * PM_{inquinante}) * d_{inquinante} \quad \textbf{(4.5)}$$

where P is the pressure in atm, T is the temperature in Kelvin, V is the volume in ml, d is the density in g/ml and R is 0.082 (l*atm)/(K*mol).

Once the equilibrium is achieved, the pollutant concentration was determined through GC analysis, linking the relative area of the pollutant peak to its concentration in ppm through the angle coefficient of the calibration curve. Acetone and acetaldehyde tests lasted for 2 h; 6 h for toluene due to the difficulty in degrading a molecule with an aromatic ring. The actual concentration of pollutant in the reactor was determined directly by micro-GC sampling.

Toluene and all its intermediate oxidation products were determined directly investigating the sample surface after the kinetic run by FTIR spectroscopy: the reactor was opened and the catalytic powder was removed from the glass sheets and put back in a test tube. The powder was successively analyzed through HPLC and FT-IR analysis to verify the adsorbed by-products nature and consequently their possible presence on the catalytic surface. The determination of CO_2 by gas chromatography was also performed.

4.3.2 VOCs photodegradation results

In this PhD's section some significantly different aspects with respect to the major part of literature data. The first aspect concerns the use of micro-sized TiO_2 samples as already discussed in the previous Paragraph, and the comparison between their photoactivity with respect to the classical nano-crystallites materials. For this reason, both nano- and micro-sized TiO_2 powders were considered and compared. Furthermore, a second aspect regards the pollutant level in the reacting chamber. The major part of the literature results pertain to several hundred parts per billion (ppb) levels or to a few parts per million (ppm) [68-71]. In this work, significantly higher VOCs levels (400 ppm) were adopted in order to bring to light catalyst deactivation processes on a short time scale, to precisely identify the nature of the reaction intermediates and also to evaluate the possible feasibility of a photocatalytic degradation process even in several pollution conditions on sample of different crystallite sizes.

The VOC concentration was calculated through the following equation:

$$(([VOC]_0 - [VOC]_t)/[VOC]_0) * 100 \quad \textbf{(4.6)}$$

and the formed CO_2 concentration was calculated by the mass balance:

$$(([CO_2]_t - [CO_2]_0)/(7([VOC]_f - [VOC]_0))) * 100 \quad \textbf{(4.7)}$$

The degradation of three different VOCs: acetone, acetaldehyde and toluene has been performed.

When the photocatalyst is irradiated with energy equal to or greater than the band gap, an electron is excited from the valence band (VB) to the conduction band (CB) leaving a hole in the former. The formation of these

photogenerated charges starts the photocatalytic process that then proceeds through a series of complex reactions that induce the degradation of pollutants adsorbed onto the TiO_2 surface [72].

4.3.2a Acetone and acetaldehyde photodegradation

Photodegradation of both acetone and acetaldehyde, two hydrophilic and polar pollutants that usually are present in high concentration in indoor environment, was firstly investigated. They were used two nano- and two-micro-sized commercial TiO_2 powders: two well-known photocatalytic TiO_2 materials (P25 and PC105) and two large-size, high purity, commercial anatase samples, sold as not photocatalytic materials (1077 and AT-1).

Their main features are reported in **Table 4.6**, where it is notable that P25 and P105 have comparable crystallite size centered at around 25 nm, while the samples 1077 and AT-1 have values of 130 and 192 nm, respectively. These structural properties are reflected in the BET surface area of micro-sized samples (1077 and AT-1) which is much lower compared to the nano-sized one (**Table 4.6**, second column).

At first the photolysis test of both acetone and acetaldehyde was performed to verify the eventual presence of abatement in absence of catalyst. As shown below there was not happened any phenomena of pollutant degradation (**Fig. 4.20**).

Table 4.6. Main features of the selected TiO_2 powders.

Sample	BET ($m^2 g^{-1}$)	Crystallites size (nm)	XPS Ti $2p_{3/2}$ (eV)	XPS OH/O_{tot}	Band Gap (eV)
P25	52	26	458.4	0.14	3.21
PC105	80	23	458.4	0.85	3.19
1077	11	130	458.3	0.32	3.15
AT-1	12	192	458.3	0.24	3.15

As we can observe by the **Fig. 4.20**, the photolysis process do not lead to the degradation of VOC and, consequently, not to take form the carbon dioxide.

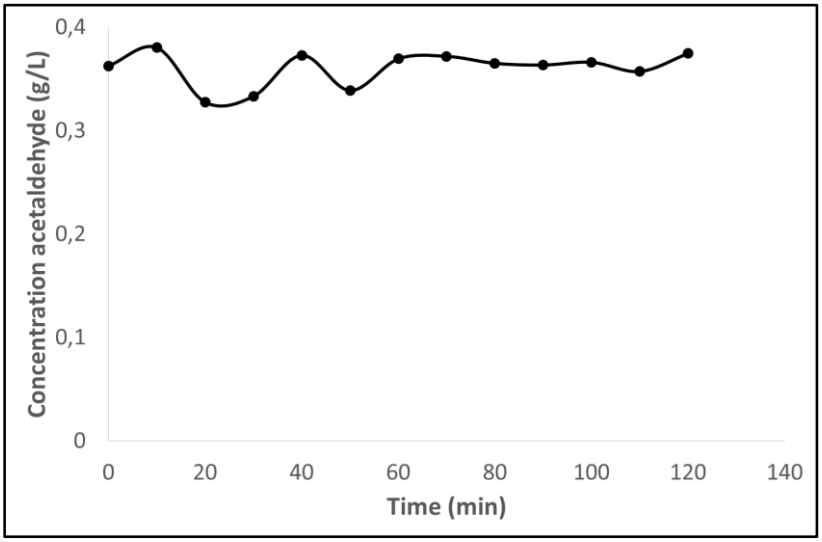

Fig. 4.20. Kinetic trend of acetaldehyde photolysis.

The acetone and acetaldehyde photocatalysis were tested using different values of RH: 4, 40, 75%. In the following figures the photocatalytic results of both micro- and nano-sized TiO_2 were reported. In particular in **Fig. 4.21** it is reported the photodegradation of acetaldehyde of P25 nanopowder and 1077 micropowder comparing the influence of 4 and 40% RH. As can be

seen in the **Fig. 4.21**, 1077 catalyst has an improvement with 40% of humidity in acetaldehyde degradation, while it shows minor acetaldehyde degradation with 4% of RH.

(a)

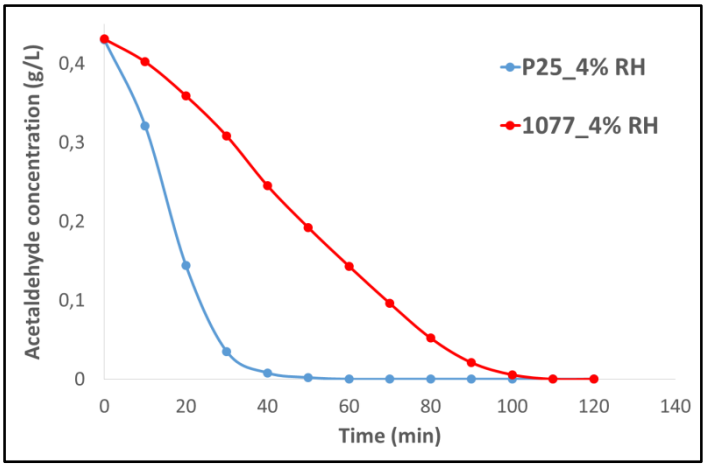

(b)

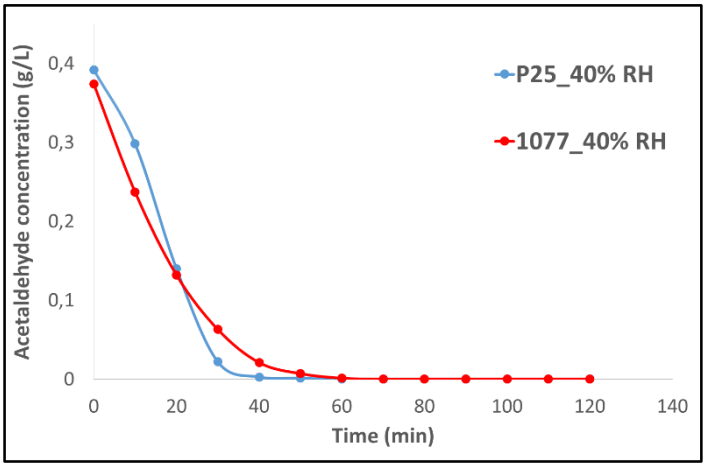

Fig. 4.21. Comparison between P25 and 1077 catalysts in conditions of 4% (a) and 40% (b) of RH for acetaldehyde degradation.

On the contrary, for the acetone degradation there are not significantly differences if we test 1007 in both RH conditions (4 and 40%). The complete photoabatement of acetone is complete within 80 minutes (**Fig. 4.22**).

(a)

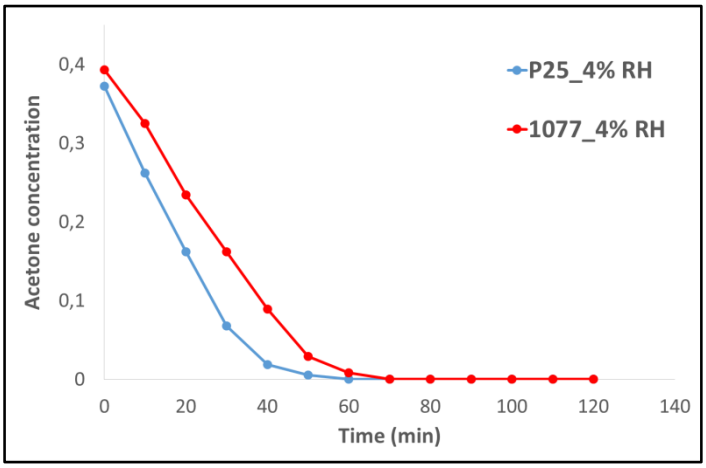

(b)

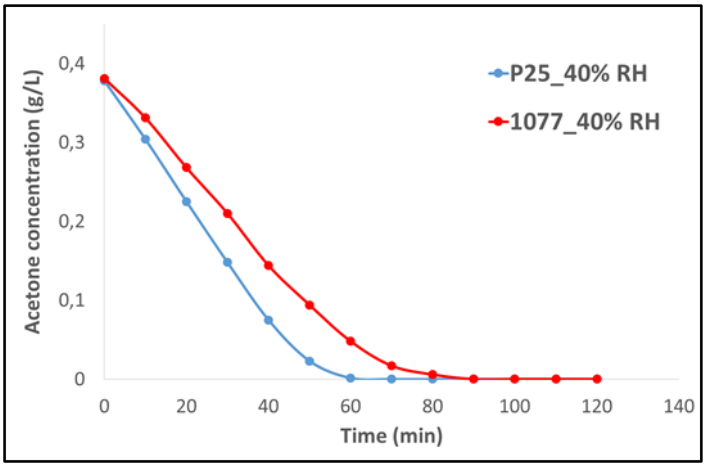

Fig. 4.22. Comparison between P25 and 1077 catalysts in conditions of 4% (a) and 40% (b) of humidity for acetone degradation.

A similar aspect was obtained under 75% RH: the photoefficiency was not improved with higher amount of humidity. This is probably due to the increase in water vapour competing with the adsorption site on the TiO_2 surface [73]. Although the increase in water vapour increased the hydroxyl radicals formed on the TiO_2 surface due to water dissociation using TiO_2 as photocatalyst, a high amount of RH can avoid the adsorption of pollutant on the catalytic surface. Moreover, after these preliminary tests we decided to carry out the following experiments using other catalysts at 40% of humidity, because it's the standard value.

For what concerns photocatalytic results under 40% RH, degradation percentages for different VOCs are reported in **Table 4.7**.

Table 4.7. Photocatalytic degradation percentages of VOCs.

Sample	**Degradation acetone (2h)**	**Degradation acetaldehyde (2h)**
P25	100% in 70 min	100% in 60 min
PC105	100% in 60 min	100% in 50 min
1077	100% in 90 min	100% in 70 min
AT-1	40% after 120 min	46% after 120 min

Acetone is a very interesting molecule from the degradative point of view because its reaction pathway passes through the formation of acetaldehyde as byproduct (**Fig. 4.22**) as reported by Stengl et al. [74]. This hypothesis is confirmed also in our case as acetaldehyde reaction time is always lower than the acetone time for all samples (see **Table 4.7**, second and third column). In both cases, the nano-sized samples exhibit high photocatalytic efficiency, leading to the complete pollutants degradation

within shorter reaction time compared to the micro-sized 1077 material. Despite the high starting pollutants concentration, for both pollutants, PC105 exhibits the best photocatalytic results with their complete disappearance in 60 min in the case of acetone and 50 min for acetaldehyde. For P25, PC105, and 1077, CO_2 is the only byproduct of the reaction confirming the complete degradation of both acetone and acetaldehyde (depending on the reaction test) without formation of adsorbed byproducts on the samples surface (verified by FTIR measurements on the sample surface after the kinetic runs), as already shown by Bianchi et al. [20]. A different behavior was achieved by AT-1 sample, which exhibits an incomplete degradation of both acetone and acetaldehyde.

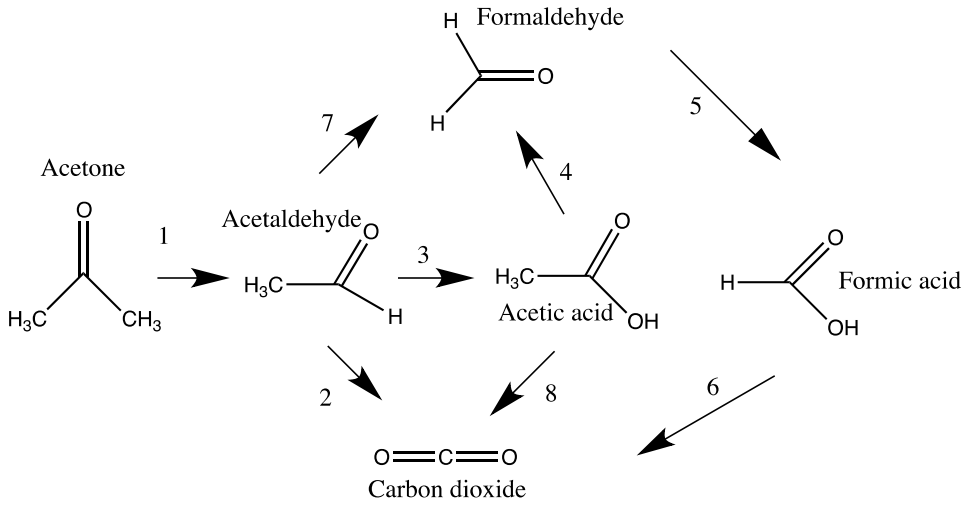

Fig. 4.22. Reaction pathway of photocatalytic acetone oxidation.

In both cases, the nano-sized samples and the micro-sized 1077 materials exhibit a very good photocatalytic efficiency, leading to the complete pollutants degradation within the reaction time (2 h). These preliminary

results allow us to demonstrate that one of the micro-sized material (1077) exhibits almost the same photocatlytic performances of the nano-sized materials as reported in the correspondent curves for acetone (**Fig 4.23**). Probably, in spite of their morphological differences, 1077 possess the same "type" of active sites.

However, in order to investigated the main causes of the highest activity of nano-sized powders (PC105 and P25), it's highly interesting to analyze the catalysts's chimico-physical characteristics.

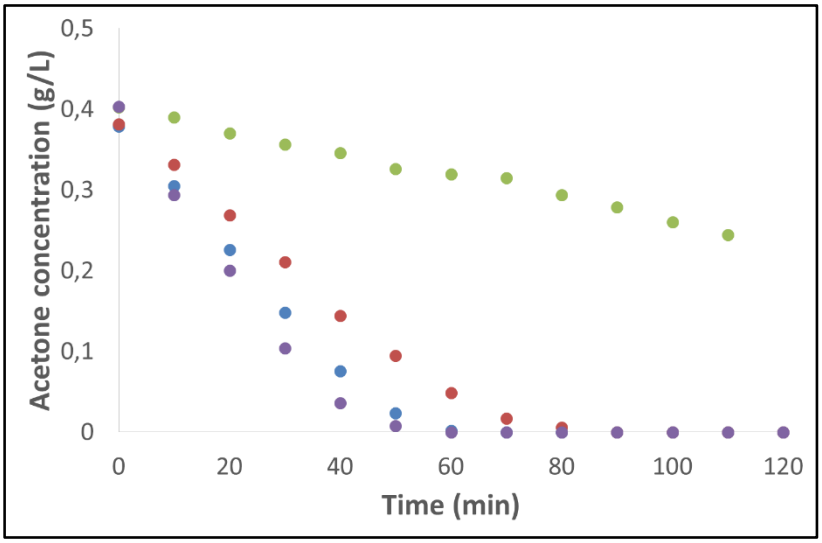

Fig. 4.23. U.V. photodegradation of acetone with nanometric and micrometric samples respectively: P25 (●) and PC105 (●), 1077 (●) and AT-1 (●).

A reason for the high photocatalytic activity of PC105 could be the high OH concentration at the surface revealed by XPS that can favor the adsorption of pollutants (and intermediates of degradation) thus leading to a very active photocatalyst. However, considering only OH/O_{tot} ratio, the catalytic results presents some discrepancies. For example, micro-sized samples have higher hydrophilicity/hydrophobicity ratio than P25 but lower catalytic efficiency.

On the other hand, considering surface area and particle size (see **Table 4.6**), acetone and acetaldehyde photodegradation follows the trend: the smaller is the crystallite size the faster is the photocatalytic kinetic. The growth of metal oxide (i.e., TiO_2) crystallites influence the degree of reconstruction, stoichiometry, and reactive sites (e.g., terrace, vacancies) at its surface thus driving also the catalytic behavior. Nanocrystals should have a higher number of coordinately defects sites (i.e., steps and corner) compared to micro-sized crystals. Therefore, we think that the surface reactivity of our photocatalysts depends on the OH/O_{tot} ratio and that the importance of OH groups might be determined by the TiO_2 crystallite size, which in turn is induced for the different type of exposed OH reactive sites onto the surface of nano- and micro-sized TiO_2 samples.

In order to find a correlation between the samples reactivity and the type of OH reactive sites exposed at the surface of the material, a thorough study of the surface OH species by means of in situ FTIR spectroscopy has been carried out. Section (a) of **Fig. 4.24** reports, in the ν_{OH} spectral range (3900–2800 cm^{-1}), the spectra of the various samples after prolonged outgassing at room temperature (RT). All the materials exhibit two complex absorption bands, respectively located in the 3000–3450 cm^{-1} range and at $\nu \geq 3600$ cm^{-1}. On the basis of the spectral behavior and of literature data, the first envelope can be ascribed to the ν_{OH} of all H-bonded OH groups present at the surface of the solid, whereas the second one corresponds to the stretching mode (ν_{OH}) of all Ti-OH species free from hydrogen bonding interactions [75-77]. This is not surprising, as an activation in vacuo at RT can only get rid of the physisorbed fraction of

(associated/undissociated) water molecules present at the surface of the various TiO_2 systems. The comparison between the OH profile of the different samples allows then to state that:

(i) The total amount of OH species (both free and H-bonded) present at the surface of PC105 is definitely higher than for all other TiO_2 (see **Fig. 4.24**, curve 1), confirming the results reported in the XPS section.

(ii) The signals relative to the free OH species appear more complex in the case of the two nano-sized samples (see **Fig. 4.24**, curve 1 and 2).

To better identify the different spectral components present at higher ν, i.e. the OH species free from hydrogen bonding interactions and thus active in the photocatalytic process, all samples have been activated in vacuo at 300°C. This thermal treatment is able to remove the interference between the ν_{OH} signals of adsorbed water and the surface OH groups, as it should only remove the signals of adsorbed water leaving virtually unchanged the distribution of surface "free" OH species [78].

The spectra collected after such thermal treatment are reported in the blown-up section (b) of **Fig. 4.24**. It is well known from the literature [79-81] that the variety of components present in this spectral range can be related to the presence of OH groups located on sites with a different "local" structure i.e. exposed on either reactive facets and/or borders. The bands observed at $\nu \geq 3680$ cm^{-1} can be ascribed to linear (terminal) Ti-OH species, whereas the bands at lower frequencies can be related to Ti-OH-Ti bridged species.

For all samples, a specific family of bridged OH groups, located at ~3670 cm^{-1}, is predominant with respect to all the other free OH species (both linear and bridged). Still, the presence of the signal at around 3640 cm^{-1},

evident only for nano-sized TiO_2 (**Fig. 4.24b**, curve 1 and 2), except for AT-1 sample for which a very weak band is also present, highlights that the Ti-OH-Ti bridged species are located in different coordination environments. At the same way, comparing nano- (**Fig. 4.24b**, curve 1 and 2) and micro-sized (**Fig. 4.24b**, curve 3 and 4) spectra in the region at $\nu \geq 3680$ cm^{-1}, it is evident that the former are characterized by a significant higher amount of terminal Ti-OH species (see signals located at ~3717 cm^{-1}). Moreover, the direct comparison of the two micro-sized TiO_2 highlights that there is a different ratio between the family of bridged-OH species at 3670 cm^{-1} and the families of terminal OH groups located at 3723 and 3700 cm^{-1} and that this ratio is definitely higher for the 1077 sample. The detailed FTIR analysis of the ν_{OH} stretching region demonstrates that the Ti-OH-Ti bridged species play a key role in driving the photocatalytic activity of both nano- and micro-sized TiO_2. Indeed, the higher is the amount of Ti-OH-Ti bridged groups, the higher is the photocatalytic efficiency toward the degradation of acetone and acetaldehyde [20]. On the contrary, linear Ti-OH species seems to have a less relevant impact on the samples activity. Still, the peculiar photocatalytic behavior exhibited by AT-1 sample could be explain considering that it possesses a different amount of bridged-OH species with respect to the other micro-sized sample (1077).

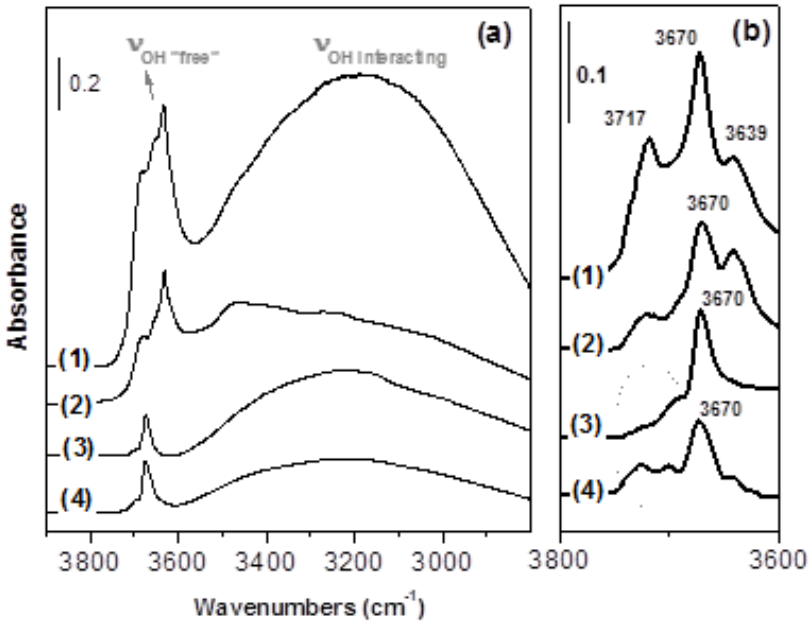

Fig. 4.24. Absorbance IR spectra, mass-normalized to the weight of the heaviest sample, relative to the OH stretching spectral region of samples outgassed at RT for 60 min (section (a)) and activated (in presence of O_2) at 300 ◦C for 60 min (section (b)): PC105 (1), P25 (2), 1077 (3), AT-1 (4).

4.3.2b Toluene photodegradation

In order to compare the photocatalytic efficiency of nano- and micro-sized TiO_2 toward a less polar and less hydrophilic (if compared with acetone and acetaldehyde) VOC, the photodegradation of toluene has been performed. Additional commercial nanometric and micrometric powders were tested; the corresponding chimico-physical characterizations were reported in **Table 4.1**.

A series of commercial micro-sized TiO_2 catalysts (1077, AT-1, AH-R, Hombitam AN, Hombitam AZ, HombiKat N.10) were analyzed for the

toluene photoabatement and their efficiency was compared with nano-sized P25 and PC105 one with the intent that micrometric powders could substitute for the traditional smaller size ones. The photocatalytic results for all samples are shown in **Fig. 4.25**.

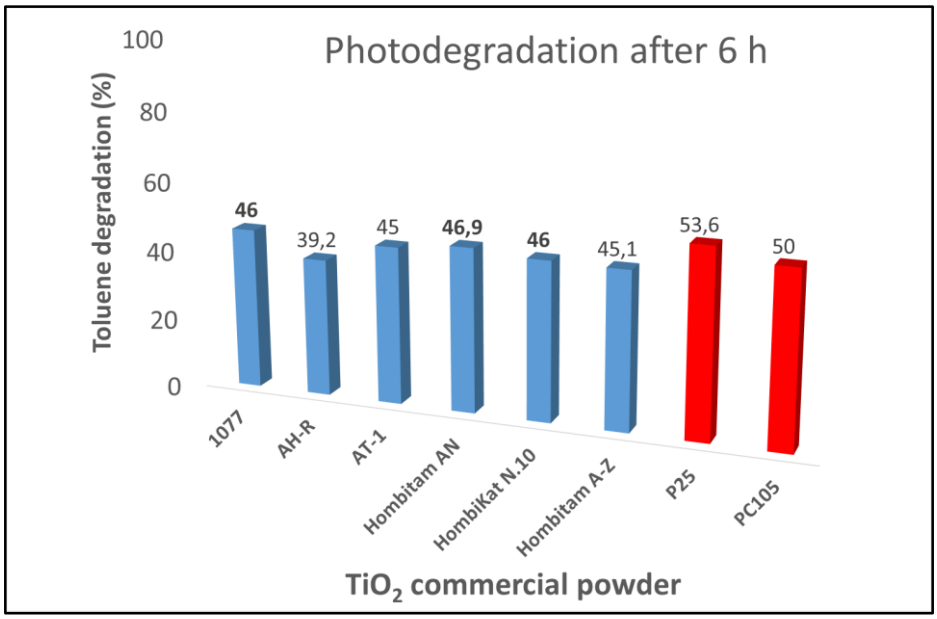

Fig. 4.25. Toluene degradation histogram: photoefficiency achieved with commercial micro-sized TiO_2 and compared to the P25 and PC105 ones (nanometric).

Toluene degradation results more difficult, mainly due to the presence of the aromatic ring. In fact, for all tested samples, the pollutant is not completely degraded even after 6 h of reaction. Moreover, it is noteworthy that the degradation percentages for all catalysts fall more or less in the same range (46–52%) with a slightly higher value for the P25 system. The different catalysts show similar behaviour toward the toluene degradation, irrespective of their physico-chemical characteristics. On the contrary, the pollutant mineralization is rather different for almost all samples, as it is observable in **Table 4.7**.

The main aspect of the toluene degradation is that, being a complex molecule, the analysis of mineralization and the by-products formation result to be helpful for a valuable comparison between nano- and micro-sized TiO_2 catalysts efficiency.

Table 4.7. Percentage of toluene degradation and CO_2 formation.

Sample	Toluene degradation (6h)	CO_2 formation (6h)
P25 (nano)	53	43
PC105 (nano)	50	35
1077 (micro)	46	31
AH-R (micro)	39	31
AT-1 (micro)	45	10
AN (micro)	47	36
AZ (micro)	45	27
N.10 (micro)	46	5

In fact, the photodegradation of micro-sized powders is, in fact, comparable to the P25 and PC105 one, differently from what expected, whereas the amount of CO_2 formation is slightly different among all powders; in particular, it is observable a low amount of CO_2 with respect to the degradation reactions of the other two VOCs, confirms the incompleteness of the degradation reaction (**Fig. 4.26A** for 1077 and **Fig. 4.26B** for P25, reported as example). Ardizzone et al. [59] report a possible degradation scheme for toluene (**Fig. 4.27**) in which the formation of various byproducts is evident and monitored by FTIR and HPLC measurements. The authors highlighted that these species remain irreversibly adsorbed at the catalyst surface avoiding the photo-degradation

reaction to continue, probably because the photoactive sites are completely covered and thus deactivated.

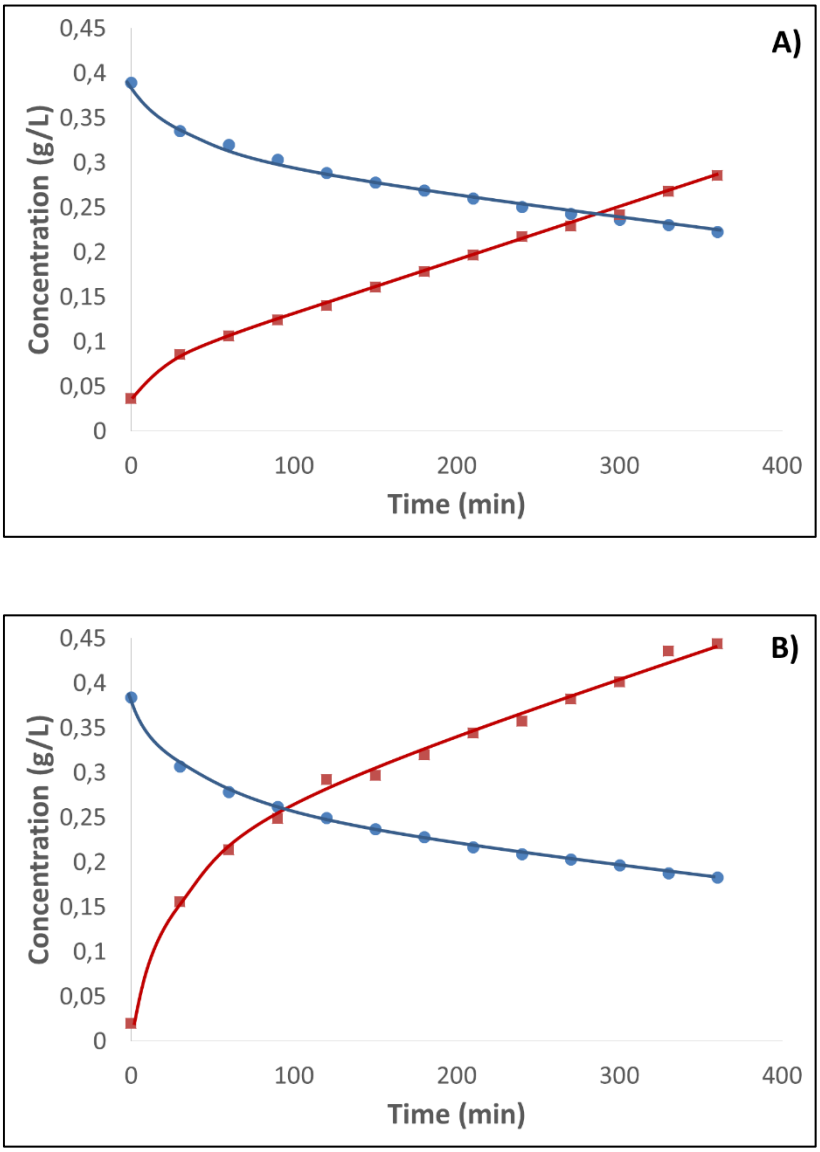

Fig. 4.26 Toluene degradation (■) and CO_2 conversion (●) for A) 1077 and B) P25 samples.

This aspect was investigated by means of FTIR measurements performed analyzing the samples surface after the kinetic run with toluene (see full

curves in **Fig. 4.28**). The spectra collected on both fresh (dotted lines) and used (full lines) samples are reported in **Fig. 4.28** in the 3900–2800 cm^{-1} (section (a)) and 1800–1200 cm^{-1} (section (b)) spectral ranges. Only the spectra of one nano-sized (spectral set I) and one micro-sized (spectral set II) TiO_2 have been reported for reason of space, being the behavior of the other two materials substantially coincident.

After the employment in toluene degradation, the spectra of the materials undergo deep changes. In particular, in the 3900–2800 cm^{-1} region (see section (a) of **Fig. 4.28**), it is possible to observe:

- the total disappearance of the signals due to the stretching mode (ν_{OH}) of Ti-OH species free from hydrogen bonding interactions with the parallel increase of the broad envelope generated by H-bonded OH groups;
- the formation of a new complex of bands located in the 3150–2850 cm^{-1} range (somehow superimposed to the envelope of interacting OH species) ascribable to the ν_{CH} stretching modes of CH-containing species of either aliphatic or aromatic nature [82].

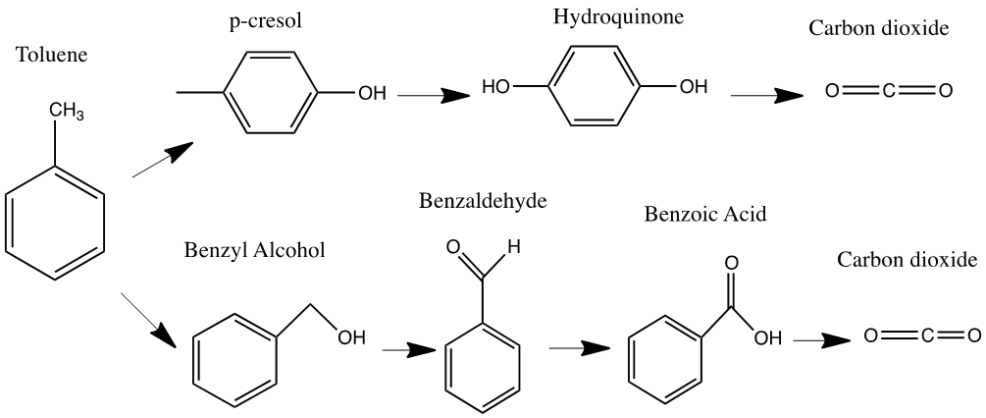

Fig. 4.27. Reaction pathway of photocatalytic toluene oxidation.

For what concerns the low frequency region (1800–1200 cm^{-1} range, see section (b) of **Fig. 4.28**), new intense and well defined components appear in the spectrum. These bands can be ascribed to the formation of new adsorbed surface species generated during toluene degradation, as reported in the reaction profile of **Fig. 4.27**.

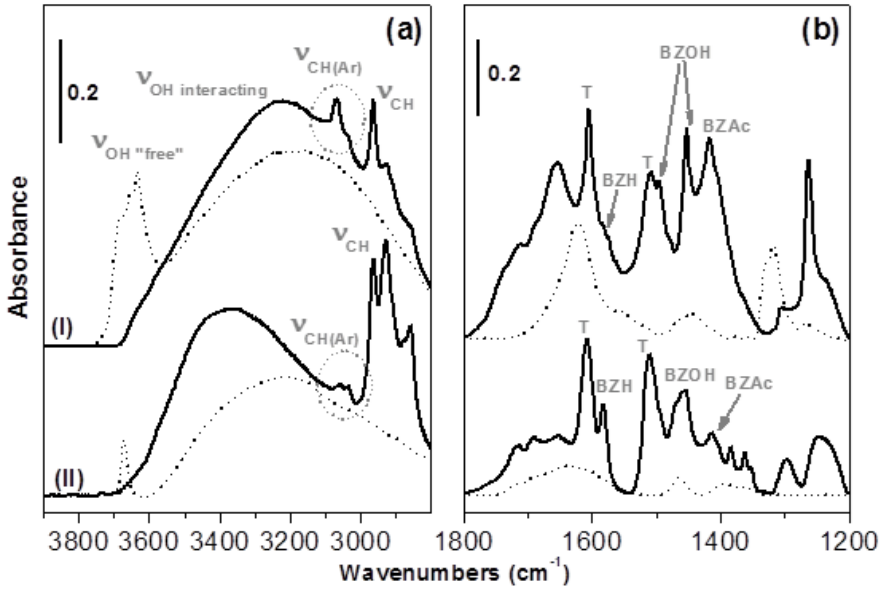

Fig. 4.28. Absorbance IR spectra in the 3900–2800 cm^{-1} (section (a)) and 1800–1200 cm^{-1} (section (b)) spectral regions of fresh (dotted lines) and used in toluene degradation reaction (full lines) samples. Spectral set I: nano-sized P25. Spectral set II: micro-sized 1077. The abbreviations T, BZH, BZOH and BZAc are explained in the text.

In particular, it is possible to recognize signals of unreacted toluene (T) and of several by-products deriving from its degradation, among which benzyl alcohol (BZOH), benzoic acid (BZAc) and benzaldehyde (BZH). It is possible to state that the catalysts surface undergoes irreversible changes after the employment in the photodegradation reaction of toluene: the

photoactive "free" Ti-OH sites are completely absent, as a result of their participation to the reaction. Their disappearance is a clear evidence of why toluene degradation appears incomplete even after 6 h of reaction for all the samples, regardless of the morphological features of the materials, as follows in a previous work [20]. Therefore, in the case of toluene and in general for all less hydrophilic VOCs, it is well evident that both micro-sized materials and nano-sized ones possess almost the same photocatalytic behavior. The OH/O_{tot} ratio, as obtained to be 0.14, 0.85, 0.32, 0.24, respectively for P25, PC105, 1077, AT-1 by elaboration of the O 1s XPS peak, is generally considered to be a measure of the hydrophilicity/hydrophobicity of an oxide [83] and seems to be a key factor to explain the nanomaterials behavior. In the present case, the nano-sized samples seem to be very different, as the OH/O_{tot} values for the PC105 material is much higher than that reported for P25 and this difference is due to the presence of a very intense OH peak for PC105. An efficient adsorption of the pollutant molecule at the semiconductor surface may promote the photocatalytic reaction: as a consequence, the adsorption of toluene or any VOC molecule on TiO_2 surface has been demonstrated to be a crucial point in affecting the subsequent photocatalytic efficiency.

In order to identify the adsorbed species on catalyst and, consequently, to recognize the possible reaction path, HPLC measurements were conducted after kinetic. In this way it is possible also to recognize potential differences among catalysts. At first, the eluition times of various by-products were studied, by using an eluent of water/acetonitrile/acetic acid, glacial 1:1:1. The results, as shown in **Fig. 4.29** for 1077 powder, confirmed the presence of hydroquinone in all samples, whereas the phenol was only in

the 1077 and AH-R samples, differently from the other ones where it was in very low amounts. The remainder peaks were due to the presence of cresols (ortho, meta and para), which were taken form during reaction kinetic. In this case, the presence of benzoic acid, benzaldehyde or benzoic alcohol was not noticed: this means that there is not possible to establish an only pathway. Thus, both reaction paths can occur, by leading to the formation of hydroquinone and cresols as intermediated, or, on the contrary, benzoic acid, benzaldehyde and benzoic alcohol.

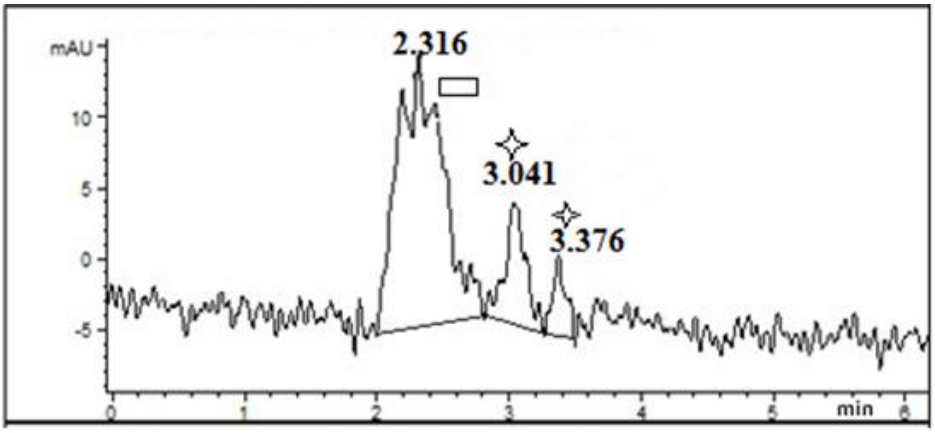

Fig. 4.29. HPLC spectra of 1077 samples post-kinetic: □ hydroquinone, ◊ cresols.

4.3.3 Conclusions

The present paragraph compares the photocatalytic performance of various commercial TiO_2 powders in the degradation of three important VOCs, representative of the indoor pollution. An efficient adsorption of the pollutant molecule at the semiconductor surface promotes the photocatalytic reaction. As a consequence, the adsorption of acetone/acetaldehyde or

toluene on TiO_2 surface has been demonstrated to be a crucial point in affecting the subsequent photocatalytic activity. In particular, FTIR analysis of the OH stretching region demonstrated that the Ti-OH-Ti bridged species play a key role in driving the photocatalytic acivity of both nano- and micro-sized TiO_2. Indeed, the higher is the amount of Ti-OH-Ti bridged groups, the higher is the photocatalytic efficiency toward the degradation of acetone and acetaldehyde. Among the different TiO_2, PC105 sample exhibits the best results for both acetone and acetaldehyde photodegradation. On the contrary, in the case of less hydrophilic VOCs like toluene in this case, it is well evident that both micro- and nano-sized materials possess almost the same photocatlytic behavior. In fact, the catalysts surface seems to undergo irreversible changes after the employment in the photodegradation reaction of toluene. In particular, after the contact with toluene, the photoactive "free" Ti-OH sites totally disappear, as result of their participation to the reaction, explaining why toluene degradation appears incomplete even after 6 h of the reaction for all the samples, regardless of the morphological features of the materials. The catalyst, more importantly, acts in different way on the by-products formation. The most interesting results of catalysts, analyzed for toluene abatement, are reported in **Table 4.8**.

Table 4.8. Results of catalysts with the best performance for toluene degradation.

Catalyst	**Toluene degradation**	**CO_2 formation**	**OH/O**	**BET (m^2/g)**
1077 (micro)	46	31	0.32	11
Hombitam AN (micro)	47	36	0.5	12
Hombitam A-Z (micro)	45	27	0.27	4
P25 (nano)	53	43	0.14	52

The photoactivity depends on both surface area and OH groups amount on the catalytic surface: the best catalysts have high surface area (P25 and

PC105, nanometric) or high OH groups amount (1077 and Hombitan AN). Moreover, it can be assumed that the OH effect is highly important, as it can be clear by comparison of P25 and micrometric Hombitam A-Z (**Table 5.8**): in spite of the lower surface area of micro-sized TiO_2, the presence of more OH groups leads it to the photoefficiency comparable to the nanometric one. Finally, it is important to highlight that the present study allowed to demonstrate that micro-sized TiO_2 are very promising materials to be employed in the photocatlytic degradation of VOCs, so limiting the possible risks for the human health deriving by the use of nanoparticles.

4.4 References

[1] Harrison R.M. Pollution: causes, effects and control (2 ed.) The Royal Society of Chemistry, Cambridge, **1992**.
[2] Seinfeld J.H. Atmospheric chemistry and physics: from air pollution to climate change (1 ed.) Wiley, New York **1998**.
[3] Cotton F.A., Wilkinson G. Adv. Inorg. Chem. (5 ed.) Wiley-Interscience, USA, **1988**.
[4] Latta C.A. Methods for reducing NO_x emissions. *Plant Eng*. **1998**, *52*, 105–112.
[5] Gangwal S.K., Howe G.B., Spivey J.J., Silveston P.L., Hudgins R.R., Metzinger J.G. Low-temperature carbon-based process for flue-gas cleanup. *Environ. Prog*. **1993**, *12*, 128-132.
[6] Mills A., Le Hunte S. An overview of semiconductor photocatalysis. *J. Photochem. Photobiol. A* **1997**, *108*, 1–35.
[7] Chen D.H., Li K. Photocatalytic Coating on Road Pavements/Structures for NO_x Abatement. *Lamar University Report* **2007**, 1-17.
[8] Chen S., Cao G. Study on the photocatalytic oxidation of NO_2– ions using TiO_2 beads as a photocatalyst. *Desalination* **2006**, *194*, 127–134.

[9] Kawakami M., Furumura T., Tokushige H. NO_x removal effects and physical properties of cement mortar incorporating titanium dioxide powder L. Cassar, P. Baglioni (Eds.), International RILEM Symposium on Photocatalysis, *Environment and Construction Materials*, RILEM, Florence **2007**, 163–170.
[10] Trouiller B., Reliene R., Westbrook A., Solaimani P., Schiestl R.H. Titanium dioxide nanoparticles induce DNA damage and genetic instability in vivo in mice. *Cancer Res*. **2009**, *69*, 8784–8789.
[11] Colvin VL. The potential environmental impact of engineered nanomaterials. *Nat. Biotechnol*. **2003**, *21*(10), 1166–1170.
[12] Hye Won K., Eun-Kyung A., Bo Keun J., Hyoung-Kyu Y., Kweon Haeng L., Young L. Nanoparticulate-induced toxicityand related mechanism in vitro and in vivo. *J. Nanoparticle Res*. **2009**, *11*, 55–65.
[13] Bowman D.M., Hodge G.A. A small matter of regulation: an international review of nanotechnology regulation. *Columbia Sci. Technol. Law Rev*. **2007**, *8*(1).
[14] Albrecht M.A., Cameron W.E., Raston C.L. Green chemistry and the health implications of nanoparticles. *Green Chem*. **2006**, *8*, 417–432.
[15] Tsai M.-D., Chen J.-J., Huang K.-L. A design of LED panel for indoor illumination. *Intell. Technol. Engin. Syst*. **2013**, *234*, 487-493.
[16] Aman M.M., Jasmon G.B., Mokhlis H., Bakar A.H.A. Analysis of the performance of domestic lighting lamps. *En. Pol*. **2013**, *52*, 482-500.
[17] http://www.expo2015.org
[18] Ghosh J.P., Sui R., Langford C.H., Achari G., Berlinguette C.P. A comparison of several nanoscale photocatalysts in the degradation of a common pollutant using LEDs and conventional UV light. *Water Res*. **2009**, *43*, 4499-4506.
[19] Jo W.K., Eun S.S., Shin S.H. Feasibility of light-emitting diode uses for annular reactor inner-coated with TiO_2 or nitrogen-doped TiO_2 for control of dimethyl sulfide. *Photochem. Photobiol.* **2011**, *87*, 1016-1023.
[20] Bianchi C.L., Gatto S., Pirola C.,.Naldoni A, Di Michele A., Cerrato G., Crocellà V., Capucci V. Photocatalytic degradation of acetone, acetaldehyde and toluene in gas-phase: comparison between nano and micro-sized TiO_2. *App. Catal. B: Environ*. **2014**, *146*, 123-130.
[21] Bianchi C.L., Pirola C., Selli E., Biella S. Photocatalytic NO_x abatement: the role of the material supporting the TiO_2 active layer. *J. Hazard. Mater*. **2012**, *211-212*, 203-207.
[22] Stafford U., Gray K.A., Kamat P.V., Varma A. An in situ diffuse reflectance FTIR investigation of photocatalytic degradation of 4-chlorophenol on a TiO_2 powder surface. *Chem. Phys. Lett*. **1993**, *205*, 55-61.
[23] Riegel G., Bolton J.R.J. Photocatalytic efficiency variability in TiO_2 particles. *Phys. Chem*. **1995**, *99*, 4215-4224.

[24] Hrum D.C., Agrios A.G., Gray K.A. Explaining the enhanced photocatalytic activity of Degussa P25 mixed-phase TiO_2 using EPR. *J. Phys. Chem. B* **2003**, *107*, 4545-4549.
[25] Han H.J., Jeon Y.I., Lim S.H., Kim W.W., Chen K. New developments in illumination, heating and cooling technologies for energy-efficient buildings. *Energy* **2010**, *35(6*), 2647–2653.
[26] www.iso.org
[27] http://eur-lex.europa.eu/LexUriServ/LexUriServ.do?uri=OJ:L:2008:152:0001:0044:EN:PDF
[28] Guo S., Wu Z.B., Zhao W.R. TiO_2-based building materials: above and beyond traditional applications. *Chinese Sci. Bulletin* **2009**, *54*, 1137-1142.
[29] Periyat P., Divya A.S., Warrier K.G.K. Photocatalytic cement by TiO_2 addition. *Mater. Sci. Forum* **2012**, *712*, 65-72.
[30] Diamanti M.V., Del Curto B., Ormellese M., Pedeferri M.P. Photocatalytic and self-cleaning activity of colored mortars containing TiO_2. *Construct. Build. Mater.* **2013**, *46*, 167-174.
[31] De Marco T., Fava G., Guerrini G.L., Manganelli G., Moriconi G., Riderelli L. Use of photocatalytic products for sustainable construction development. *Third international conference on sustainable construction materials and technologies*, Japan, August **2013**.
[32] Chen J, Poon C.S. Hydration and properties of nano-TiO_2 blended cement composites. *Environ. Sci. Technol*. **2009**, *43*(23), 8948–8952.
[33] Maltby J.E., Geninazza E. Photocatalytic products for the construction industry. In: *Proceedings of 30th FATIPEC congress* **2010**, *2*, 798–807.
[34] Albrecht M.A., Cameron W.E., Raston C.L. Green chemistry and the health implications of nanoparticles. *Green Chem.* **2006**, *8*, 417–432.
[35] Bianchi C.L., Pirola C., Gatto S., Nucci S., Minguzzi A., Cerrato G., Biella S., Capucci V. New surface properties in porcelain gres tiles with a look to human and environmental safety. *Adv. Mater. Sci. Engin.* **2012**, *2012*, 1-8.
[36] C.L.Bianchi, S. Gatto, S. Nucci, G. Cerrato and V. Capucci, Self-cleaning measurements on tiles manufactured with micro-sized photoactive TiO_2. *Adv. Environ. Res.* **2013**, *2*.
[37] Casasola R., Rincón J.M., Romero M. Glass-ceramic glazes for ceramic tiles: a review. *J. Mater. Sci.* **2012**, *47*, 553–582.
[38] Marcos P.S., Marto J., Trinidade T., Labrincha J.A. Screen-printing of TiO_2 photocatalytic layers on glazed ceramic tiles. *J. Photochem. Photobiol. A* **2008**, *197*, 125–131.
[39] Seabra M.P., Pires R.R., Labrincha J.A. Ceramic tiles for photodegradation of Orange II solutions. *CEJ* **2011**, *171*, 692–702.
[40] ASTM C373-88(2006). Standard test method for water absorption, bulk density, apparent porosity, and apparent specific gravity of fired whiteware products. *West*

Conshohocken (PA): ASTM International; **2003**. http://dx.doi.org/10.1520/C0033-03, www.astm.org.
[41] ISO 10545-7. Ceramic tiles – Part 7: Determination of resistance to surface abrasion for glazed tiles; **1996**. www.iso.org.
[42] ISO 10545-12. Determination of frost resistance. www.iso.org.
[43] Naldoni A., Bianchi C.L., Pirola C., Suslick K.S. Porous TiO_2 microspheres with tunable properties for photocatalytic air purification. *Ultras. Sonochem*. **2013**, *20*, 445-451.
[44] "ISO 22197-1—test method for air-purification performance of semiconducting photocatalytic materials. Part1: removal of nitric oxide," http://www.iso.org/iso/home.html.
[45] Air Quality Guidelines, WHO (World Health Organization) **2005**.
[46] Ardizzone S., Bianchi C.L., Cappelletti G., Gialanella S., Pirola C., Ragaini V. Tailored anatase/brookite nanocristalline TiO_2. The optimal particle features for liquid-and-gas-phase photocatalytic reactions. *J. Phys. Chem. C* **2007**, *111*, 13222-13231.
[47] Cappelletti G., Ardizzone S., Bianchi C.L., Gialanella S., Naldoni A., Pirola C., Ragaini V. Photodegradation of pollutants in air: Enhanced properties of nano-TiO_2 prepared by ultrasound. *Nanoscale Res. Lett*. **2009**, *4*, 97-105.
[48] http://www.epa.gov/iaq/no2.html.
[49] Bianchi C.L., Gatto S., Pirola C., Scavini M., Vitali S., Capucci V. Micro-TiO_2 as a starting material for new photocatalytic tiles. *Cem. Concr. Compos*. **2013**, *36*, 116-120.
[50] Zhang L., Anderson W.A., Sawell S., Moralejo C. Mechanistic analysis on the influence of humidity on photocatalytic decomposition of gas-phase chlorobenzene. *Chemosphere* **2007**, *68*, 546-553.
[51] Raillard C., Héquet V., Le Cloirec P., Legrand J. TiO_2 coating types influencing the role of water vapor on the photocatalytic oxidation of methyl ethyl ketone in the gas phase. *App. Catal. B: Environm*. **2005**, *59*, 213-220.
[52] Park D.R., Zhang J., Ikeue K., Yamashita H., Anpo M. Photocatalytic oxidation of ethylene to CO_2 and H_2O on ultrafine powdered TiO_2 photocatalysts in the presence of O_2 and H_2O. *J. Catal*. **1999**, *185*, 114-119.
[53] Coronado J.M., Zorn M.E., Tejedor-Tejedor I., Anderson M.A. Photocatalytic oxidation of ketones in the gas phase over TiO_2 thin films: a kinetic study on the influence of water vapor. *App. Catal B: Environm*. **2003**, *43*, 329-344.
[54] "ISO 22197-1—test method for air-purification performance of semiconducting photocatalytic materials. Part1: removal of nitric oxide," http://www.iso.org/iso/home.html.
[55] Chen N. H., Othmer D. F. New generalized equation for gas diffusion coefficient. *J. Chem. Engin. Data* **1962**, *7*, 37–41.

[56] Obee T. N., Brown R. T. TiO_2 photocatalysis for indoor air applications: effects of humidity and trace contaminant levels on the oxidation rates of formaldehyde, toluene, and 1,3-butadiene. *Environ. Sci. Technol.* **1995**, *29*, 1223–1231.
[57] Tomkins D. T., Zeltner W. A., Lawnicki B. J., Anderson M. A. Eval. Photocat. Gas-Phase Air Clean. Part 1: Proc., Technical, and Sizing Conside. *ASHRAE Transactions*, **2005**, *111*, 64.
[58] Alberici R.M., Jardim W.E. Photocatalytic destruction of VOCs in the gas-phase using titanium dioxide *Appl Catal B Environ*. **1997**, *14*, 55–68.
[59] Ardizzone S., Bianchi C.L., Cappelletti G., Naldoni A. Pirola C. Photocatalytic degradation of toluene in gas phase: relationship between surface species and catalyst features. *Environ. Sci. Technol*. **2008**, *42*, 6671-6676.
[60] G.F. Tjandraatmadjaa, L.S. Burna, M.C. Jollandsb, Evaluation of commercial polycarbonate optical properties after UV-A radiation—the role of humidity in photodegradation. *Pol. Degrad. Stab.* **2002**, *78*, 435-448.
[61] Park, D.R., Zhang, J.L., Ikeue, K., Yamashita, H., Anpo, M. Photocatalytic oxidation of ethylene to CO_2 and H_2O on ultrafine powdered TiO_2 photocatalysts in the presence of O_2 and H_2O. *J. Catal*. **1999**, *185*, 114-119.
[62] Tompkins, D.T. Evaluation of photocatalytic air cleaning capability: a literature review and engineering analysis. *ASHARE Research Project RP-1134* **2001**.
[63] Yamazaki, S., Fu, X.Z., Anderson, M.A., Hori, K. Chlorinated byproducts from the photoassisted catalytic oxidation of trichloroethylene and tetrachloroethylene in the gas phase using porous TiO_2 pellets. *J. Photochem. Photobiol. A – Chem.* **1996**, *97*, 175–179.
[64] Ao, C.H., Lee, S.C., Yu, J.Z., Xu, J.H. Photodegradation of formaldehyde by photocatalyst TiO_2: effects on the presences of NO, SO_2 and VOCs. *App. Catal. B: Environm*. **2004**, *54*, 41-50.
[65] Chang, C.P., Chen, J.N., Lu, M.C. Heterogeneous photocatalytic oxidation of acetone for air purification by near UV-irradiated titanium dioxide. *J. Environm. Sci. Health Part A – Toxic/Hazard. Sub. Environm. Engin.* **2003**, *38*, 1131-1143.
[66] Kim, S.B., Hong, S.C. Kinetic study for photocatalytic degradation of volatile organic compounds in air using thin film TiO_2 photocatalyst. *App. Catal. B – Environm*. **2002**, *35*, 305–315.
[67] Peral, J., Ollis, D.F. Heterogeneous photocatalytic oxidation of gas-phase organics for air purification: acetone, 1-butanol, butyraldehyde, formaldehyde and m-xylene oxidation. *J. Cat*. **1992**, *136*, 554–565.
[68] Ao C.H., Lee S.C., Mak C.L., Chan L.Y. Photodegradation of volatile organic compounds (VOCs) and NO for indoor air purification using TiO_2: promotion versus inhibition effect of NO. *Appl. Cat. B* **2003**, *42*, 119–129.

[69] Jeong J., Sekiguchi K., Sakamoto K. Photochemical and photocatalytic degradation of gaseous toluene using short-wavelength UV irradiation with TiO_2 catalyst: comparison of three UV sources. *Chemosphere* **2004**, *57*, 663–671.
[70] Addamo M., Augugliaro V., Coluccia S., Di Paola A., Garcia-Lopez E., Loddo V., Marcì G., Martra G., Palmisano L. The role of water in the photocatalytic degradation of acetonitrile and toluene in gas-solid and liquid-solid regimes. *Int. J. Photoen.* **2006**, 1–12.
[71] Marcì G., Addamo M., Agugliaro V., Coluccia S., Garcia-Lopez E., Loddo V., Martra G., Palmisano L., Schiavello M. Photocatalytic oxidation of toluene on irradiated TiO_2: comparison of degradation performance in humidified air, in water and in water containing a zwitterionic surfactant. *J. Photochem. Photobiol. A* **2003**, *160*, 105–114.
[72] Kwon S., Fan M., Cooper A.T., Yang H. Photocatalytic applications of micro- and nano-TiO_2 in environmental engineering. Crit. Rev. Environm. Sci. Technol. **2008**, *38*, 197–226.
[73] Ao C.H., Lee S.C., Mak C.L., Chan L.Y. Photodegradation of volatile organic compounds (VOCs) and NO for indoor air purification using TiO_2: promotion versus inhibition effect of NO. *App. Catal. B: Environ.* **2003**, *42*, 119-129.
[74] Stengl V., Houskova V., Bakardjieva S., Murafa N. Photocatalytic degradation of acetone and butane on mesoporous titania layers. *New J. Chem.* **2010**, *34*, 1999–2005.
[75] Little L.H. Infrared Spectra of Adsorbed Species. *Academic Press*, London, **1966.**
[76] Morterra C. An infrared spectroscopic study of anatase properties. Part 6.—Surface hydration and strong Lewis acidity of pure and sulphate-doped preparations. *Faraday Transactions 1* **1988**, *84* (5), 1617–1637.
[77] Morterra C., Bolis V., Fisicaro E. The hydrated layer and the adsorption of CO at the surface of TiO_2(anatase). *Colloids Surf.* **1989**, *41*, 177–188.
[78] Minella M., Faga M.G., Maurino V., Minero C., Pelizzeti E., Coluccia S., Martra G. Effect of fluorination on the surface properties of titania P25 powder: an FTIR study. *Langmuir* **2010**, *26*, 2521–2527.
[79] Primet M., Pichat P.P., Mathieu M.V. Infrared study of the surface of titanium dioxides. I. Hydroxyl groups. *J. Phys. Chem.* **1971**, *75*, 1216–1220.
[80] Tsyganenko A.A., Filimonov V.N. Infrared spectra of surface hydroxyl groups and crystalline structure of oxides. *J. Molec. Struct.* **1973**, *19*, 579–589.
[81] Deiana C., Fois E., Coluccia S., Martra G. Surface structure of TiO_2 P25 nanoparticles: infrared study of hydroxy groups on coordinative defect sites. *J. Phys. Chem. C* **2010**, *114*, 21531–21538.
[82] Colthup N.B., Daly L.H., Wiberley S.E. Introduction to Infrared and Raman Spectroscopy, 2nd ed., *Academic Press*, New York, **1975**.

[83] Inaba R., Fukahori T., Hamamoto M., Ohno T. Synthesis of nanosized TiO_2 particles in reverse micelle systems and their photocatalytic activity for degradation of toluene in gas phase. *J. Molec. Catal. A: Chem.* **2006**, *260*, 247–254.

Chapter 5

Nano- and micro-sized TiO_2 in aqueous-phase

The water pollution deriving from organic compounds is a problem that is currently important for the contemporary society. In particular, the use of textile dyes and surfactants are increasing. Consequently, their stability during the time leads them to persist and remain in the rivers and sea waters. In this paragraph it is considered the photoabatement of various types of textile dyes and PFOA (perfluooroctanoic acid), as a reference surfactant. As photocatalyst it is applied TiO_2 powder in both forms, nanometric and micrometric size. The photoefficiency is then evaluated by studying the sub-products formation during degradation path. A further study has been conducted with micro-sized TiO_2 gres-tiles for the study of dyes degradation, using a different reactor specific for the porcelain tiles.

5.1 Perfluorooctanoic acid degradation with P25 powder

Perfluorooctanoic acid (PFOA), $C_8HF_{15}O_2$ (AMW = 414.07 g/mol), a representative of perfluorinated chemicals (PFCs), is largely used as surfactant in the fluoropolymers synthesis with the aim to obtain chemical compounds with specific properties for a wide range of industrial applications, such as manufacturing, aerospace, automotive, electronics, semiconductors and textile [1,2]. Moreover, PFOA is applied for the production of breathable membranes for clothing, *e.g.* Gore-Tex® [3]. Its strong stability and high surface-active effects are due to the presence of C–F bonds (about 130 kcal/mol) in its molecular structure [4,5]. The production of surfactants is nowadays estimated at around 15 Mton/y, about half of which are soaps like linear alkyl-benzene sulfonates, lignin sulfonates, fatty alcohol ethoxylates and alkylphenol ethoxylates [6].

However, many studies indicate that PFOA is environmentally persistent and bioaccumulative [7,8]. For these reasons, in the last years many research groups have devoted efforts to develop methods able to eliminate PFOA from the environment [9,10]. Actually, the US-EPA (Environmental Protection Agency) and EEA (European Environmental Agency) launched an industrial program aimed to reduce global emissions and product content of PFOA and related chemicals. In particular, the eight major producers of fluoropolymers and fluorotelomers have pledged to reduce global facility emissions and product content of PFOA and its related chemicals by 95% in 2010 as well as to completely eliminate emissions and product content of PFOA by 2015 [11,12].

Advanced oxidation processes (AOPs) are usually more effective in the degradation of surfactants. However, the photomineralization of PFOA by a

commercial titanium dioxide showed a deactivation of the photocatalyst. Thus, in this PhD work, the chemical modification of the catalyst and its deactivation were studied by different approaches. The present paragraph is focused on PFOA photodegradation promoted by commercial TiO_2 powder (P25 by Evonik®). The mineralization was monitored by Total Organic Carbon (TOC) analysis and Ionic Chromatography (IC) and the intermediate degradation products were determined by High-Performance Liquid Chromatography combined with Mass Spectrometry (HPLC-MS) analysis. The presence of the fluorinated surfactant in solution was also monitored by ^{19}F-NMR. HPLC-MS and ^{19}F-NMR analyses were performed on samples of PFOA solution collected from the photoreactor after different reaction times. The subject of this article can be of interest to a wide range of readers in the fields of the applied catalysis for AOPs and of the environmental protection.

5.1.1 Materials and Methods

5.1.1.1 Materials

Perfluorooctanoic acid (purity 96% - from Sigma Aldrich®) was used as received. PFOA is soluble in water (9.5 g/L) and its critical micelle concentration (CMC) is $7.80 \cdot 10^{-3}$ mol/L at 25°C. Titanium dioxide P25 (75% Anatase, 25% Rutile [13]) was supplied by Evonik® and it was tested

as titanium-based photocatalyst. Water was purified using an Elga Option 3 deionizer and was used to prepare all solutions. Milli-Q water was employed for ion chromatography. HPLC-MS analyses were carried out using as eluting phase a mixture of methanol (CHROMASOLV®, for HPLC, ≥99.9% - from Sigma Aldrich®) and 2 mM aqueous ammonium acetate solution.

5.1.1.2 Photocatalytic reactor

The photocatalytic apparatus was a 1 L glass stirred reactor equipped with an iron halogenide UV lamp (500 W, Jelosil® HG500) emitting light at wavelengths of 315-400 nm and able to irradiate the reactor with a specific power of 95 W/m^2. The scheme of the reactor is shown in **Fig. 5.1**. The reactor is constituted from two parts: one upper and the other one lower, held together by a steel flange. The lower part is constituted by a cylinder of diameter of 10 cm and height of 10 cm, where the aqueous solution is introduced. The upper part is instead composed of a shell with five holes of different diameters, where are inserted a thermocouple, septa for ultrasound, a heat exchanger coil in glass for the cooling. The UV lamp was placed beside the reactor, which was cooled with water at a temperature of 30±0.5°C [14]. Titanium dioxide was introduced in the reactor at the beginning of each test (0.66 g/l). As previously reported, the variation of the surfactant concentration ([PFOA]$_0$ = 4 mM) in solution was monitored by Total Organic Carbon (TOC) analysis and Ionic Chromatography. Samples (10 ml) of the reaction mixture were collected at different reaction times: typically at 0 min (before the start of the reaction), 30 min, 60 min, 120 min,

180 min, 240 min, 360 min and 540 min. Each kinetic test was repeated three times in order to evaluate the error extent. Each sample was centrifuged and filtered through a 0.45 μm polycarbonate membrane in order to separate the TiO_2 powder from the solution, as shown by Gatto et al. [14]. The residual photocatalytic performances of exhaust TiO_2 after 9 hours of PFOA photodegradation were also evaluated by reusing it in an additional test performed on a standard 4 mM PFOA solution.

Photocatalysis follows the Langmuir-Hinshelwood model [15]. When the PFOA adsorption onto the photocatalyst surface is negligible, the reaction mechanism can be approximated to a pseudo-first order kinetic (6.1):

$$r = -\frac{dC}{dt} = k_{app}C \qquad \textbf{(5.1)}$$

In Eq. 6.1, *r* is the reaction rate, *C* is the surfactant concentration in solution, *t* is the time and k_{app} is the apparent first order rate constant. The reactions were conducted without a constant feed of oxygen as reported by Li, *et al.* [10], but using just the naturally dissolved O_2 (DO), in order to simulate conditions of non-enriched water, as industrially feasible.

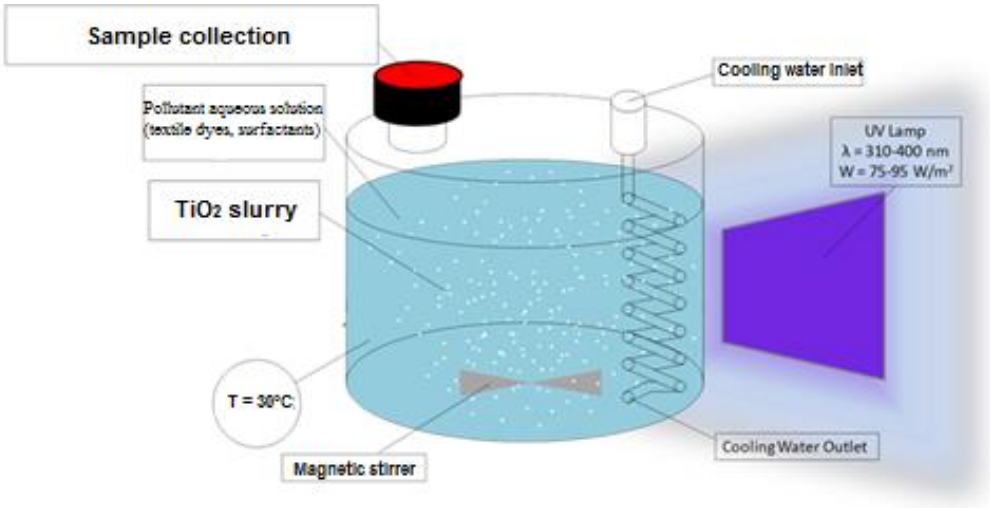

Fig. 5.1. Experimental apparatus for aqueous solutions degradation equipped with a UV lamp located on the side of the reactor.

5.1.2 PFOA photodegradation results

PFOA total degradation reaction in water can be summarized as follows:

$$CF_3(CF_2)_6COOH + 7/2\ O_2 + 7\ H_2O \rightarrow 8\ CO_2 + 15\ HF \qquad (\mathbf{5.2})$$

The photocatalytic mechanism is still not totally explained, particularly with regard to the role played by oxygen. It has been verified that the reduction of O_2 is a determining step of the photodegradation process [16].

The whole mechanism of PFOA decomposition in presence of TiO_2, comprehensive of both photo-redox (**Fig. 5.2-A**) and β-scission (**Fig. 5.2-**B) pathways, is presented in **Fig. 5.2**. The commonly accepted mechanism of PFOA decomposition starts with the excitation of titanium dioxide caused

by the irradiation of UV light (**Fig. 6.5** - reaction a) [17,18]; excited TiO_2 accepts one electron from carboxylate of PFOA ($CF_3(CF_2)_6COO^-$) and a PFOA radical (**Fig. 5.2** - reaction b) is generated [19]. The so formed species undergoes a Kolbe decarboxylation reaction (**Fig. 5.2** - reaction c) [20,21]. In presence of oxygen, the C_7 radical reacts with molecular oxygen in the reaction environment and peroxyradicals are generated (**Fig. 5.2** - reaction d) [22]. The coupling of two peroxyradicals allows the formation of O_2 and two oxyradicals (**Fig. 5.2** - reaction e) that, in the presence of the surface excited electrons of TiO_2 and water, generate an unstable primary perfluorinated alcohol (**Fig. 5.2** - reaction f) [23]. This unstable compound originates acyl fluoride and hydrogen fluoride (**Fig. 5.2** - reaction g); in presence of water, the acyl fluoride is hydrolyzed to the corresponding carboxylic acid C_{n-1}, $CF_3(CF_2)_5COOH$ (**Fig. 5.2** - reaction h) [24,25]. This photo-redox mechanism explains a step-by-step $C_n \rightarrow C_{n-1}$ chain length decrease of PFOA [26] and the formed carboxylic acid C_{n-1}, $CF_3(CF_2)_5COOH$, should compete with the PFOA on the catalytic sites of TiO_2 particles (**Fig. 5.2** - reaction b). Therefore, in the decomposition reaction the concentration of shorter chain perfluorinated acids should increase proportionally to fluoride formation.

Another possible reaction pathway can be hypothesized assuming that the oxyradical formed in reaction (e) evolves eliminating COF_2 by mono molecular β-scission and consequent generation of a C_{n-1} radical (**Fig. 5.2** - reaction i) [27-29]. The so formed carbon-centered perfluorinated radical takes part to reaction (d), while fluorophosgene is quenched in aqueous environment generating hydrogen fluoride and carbon dioxide. Assuming that this pathway is active, it is remarkable that this mechanism can promote

an almost complete PFOA decomposition without the formation of perfluorinated acids as intermediates. The key steps of the complete oxidation mechanism are represented by the two competing reactions: the bimolecular reduction of the oxyradical activated by TiO_2 surface (reaction f) and the monomolecular β-scission generating COF_2 and C_{n-1} radical (reaction i).

During the first 4 hours of PFOA photoabatement, the major release of fluoride ions was recorded as a consequence of PFOA mineralization (**Fig. 5.3-A**). This phenomenon might be promoted by a predominant β-scission mechanism, able to directly mineralize PFOA and to generate fluoride ions with negligible formation of shorter chain perfluorinated acids as degradation intermediates. The presence of fluoride ions in concentrations up to around 17 mM is reasonably related to the surface fluorination of TiO_2-catalyst. For the entire duration of the photoabatement process, it was possible to observe a decrease in the PFOA content in solution (**Fig. 5.3-B**).

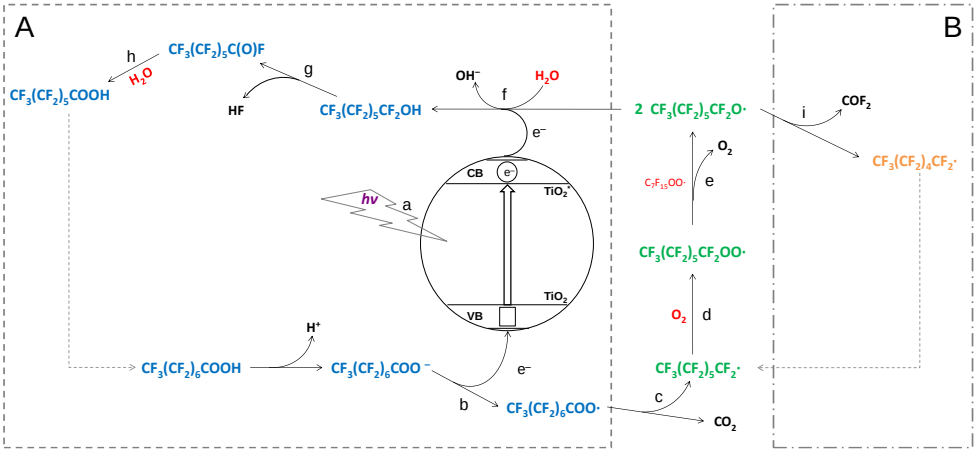

Fig. 5.2. Reaction mechanism of PFOA degradation in the presence of TiO_2 photocatalyst, comprehensive of both photo-redox (A) and β-scission (B) pathways.

Mineralization data obtained by TOC and IC determined that after 4 hours the mineralization ratio was 32% and the yield in fluoride ions (calculated as the ratio of the concentration of fluoride ions over the initial concentration of PFOA multiplied by 15 due to the stoichiometric ratio) resulted to be 29%. The adsorption of fluoride ions on the surface of TiO_2 particles might be a reason of the fluoride ions loss (3%) in the aqueous phase. The presence of an evident limit condition for the photomineralization (*plateau*) can be noticed in the kinetic curve after 4 hours (**Fig. 5.3-A**, **5.3-B**). In fact, the fluoride content and the percentage mineralization after 6 and 9 hours remained equal to 29% and 32%, respectively. The lack of photoactivity of exhaust TiO_2 after 9 hours of PFOA photodegradation was confirmed by evaluating its photocatalytic performances in a reusing test on a standard 4 mM PFOA solution, as already reported by Gatto et al. [14]: TOC data revealed that after other additional 6 hours PFOA mineralization was only 10%.

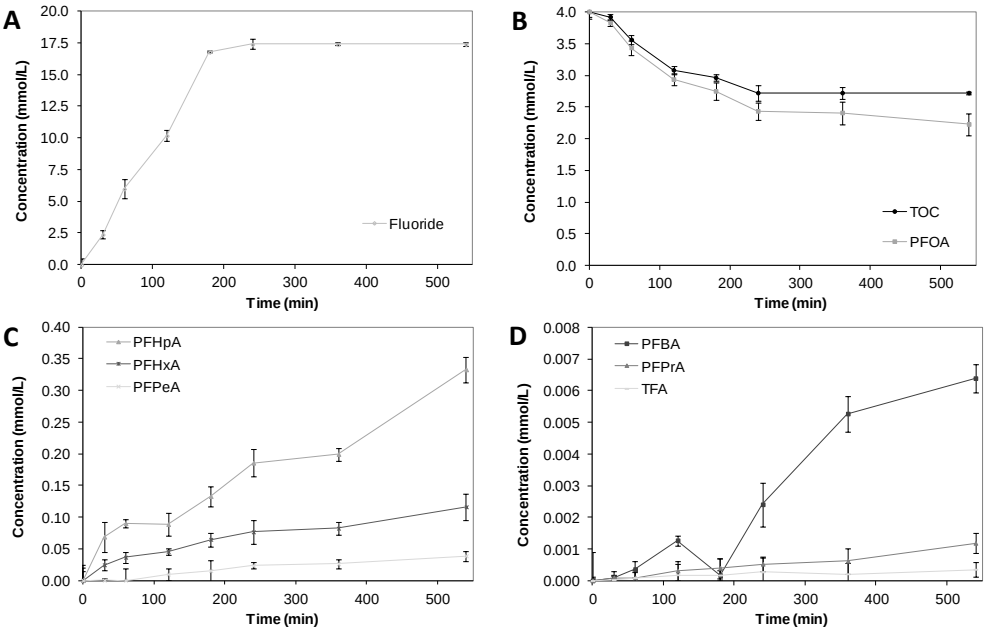

Fig. 5.3. Trends of fluoride ions release (A), total organic carbon content and PFOA concentration in solution (B), and degradation intermediates concentrations in solution (C, D).

In order to evaluate PFOA degradation intermediates content, samples of the solution from the photoabatement reactor were collected at different reaction times and analyzed by HPLC-MS. Firstly, an increasing difference between the trends of TOC content and PFOA concentration was overall present and after 4 hours it became particularly evident (**Fig. 5.3-B**). However, even if the photoabatement rate of PFOA after 4 hours was significantly reduced, an increase in the degradation intermediates concentrations was observed (**Fig. 5.3-C** and **5.3-D**). The concentration trends of the degradation intermediates in solution followed a well-defined order: the higher the molecular weight of the intermediate, the higher its presence in solution (PFHpA > PFHxA > PFPeA > PFBA > PFPrA > TFA).

However, all the expected degradation intermediates were already detected in the sample collected after 30 minutes, even if their presence in solution was negligible if compared to PFOA concentration. In particular, the presence in solution of TFA and PFPrA after 30 minutes of treatment (**Fig. 5.3-D**) could not be ascribed to photo-redox $C_n \rightarrow C_{n-1}$ chain length decrease mechanism, but it could be justified by a competitive direct chain length decomposition mechanism based on the elimination of COF_2 as decomposition product induced by β-scission reactions of the oxyradical formed in reaction (e) (**Fig. 5.2**). The photo-redox $C_n \rightarrow C_{n-1}$ chain length decrease mechanism appeared to be significant after 4 hours of photoabatement, when the mineralization rate of PFOA was evidently lowered. Kinetic data of photodegradation of a 4 mM PFOA solution revealed that, under an UV irradiation of 95 W/m^2 and with a TiO_2 content of 0.66 g/L, the degradation fitted with a pseudo-first order kinetic during the first 4 hours (**Fig. 5.4**). The kinetic apparent constant (k_{app}) referring to the rate of PFOA disappearance was equal to 0.1296 h^{-1} (R^2 = 0.9956).

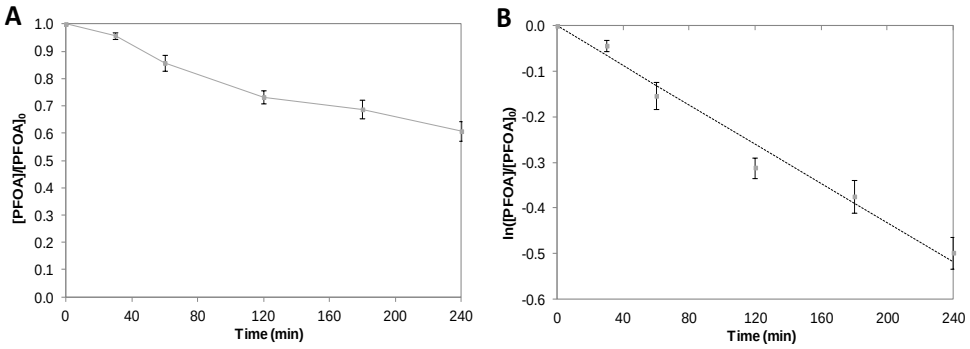

Fig. 5.4. PFOA photodegradation kinetic data plotted against time as [PFOA]/[PFOA]$_0$ (A) and its corresponding linearization (B).

As reported in the literature, no PFOA abatement was observed working in the presence of TiO_2 as photocatalyst without UV irradiation as well as under UV irradiation in the absence of photocatalyst (photolysis). As already shown by Sansotera et al. [30].

In order to understand the chemical modification induced on TiO_2 photocatalyst during the degradation process, the high-resolution XPS spectra in the F *1s* region were recorded on TiO_2 samples collected at different reaction times. After 2 and 4 hours of photodegradation (**Fig. 5.5-A** and **5.5-B**), XPS analysis revealed two peaks at around 684 and 688 eV which can be attributed to molecules of hydrofluoric acid and PFOA, respectively, adsorbed on the TiO_2 surface. After 9 hours the XPS spectrum in the F *1s* region showed three peaks which could be assigned to different fluorinated species (**Fig. 5.5-C**): the first peak at around 684 was still related to adsorbed hydrofluoric acid; the signal at around 687 eV was due to the formation of fluorinated $TiO_{(2-x/2)}F_x$ species induced by fluoride ions generated during the photoabatement of PFOA [31]; the third peak at around 690 eV can be assigned to fluorinated organic derivatives generated during the PFOA photodegradation and adsorbed on the photocatalyst surface.

Further evidences of fluoride adsorption on the surface of TiO_2 particles were derived from the differences between the mineralization ratio and the yield in fluoride ions (3% after 4h) as well as from a mass balance of fluorine atoms. Mass balance of fluorine atoms at different reaction times have been evaluated on the basis of the concentrations of initial PFOA, residual PFOA, degradation intermediates (PFHpA, PFHxA, PFPeA, PFBA, PFPrA, TFA) and fluoride ions (see **Table 5.1**).

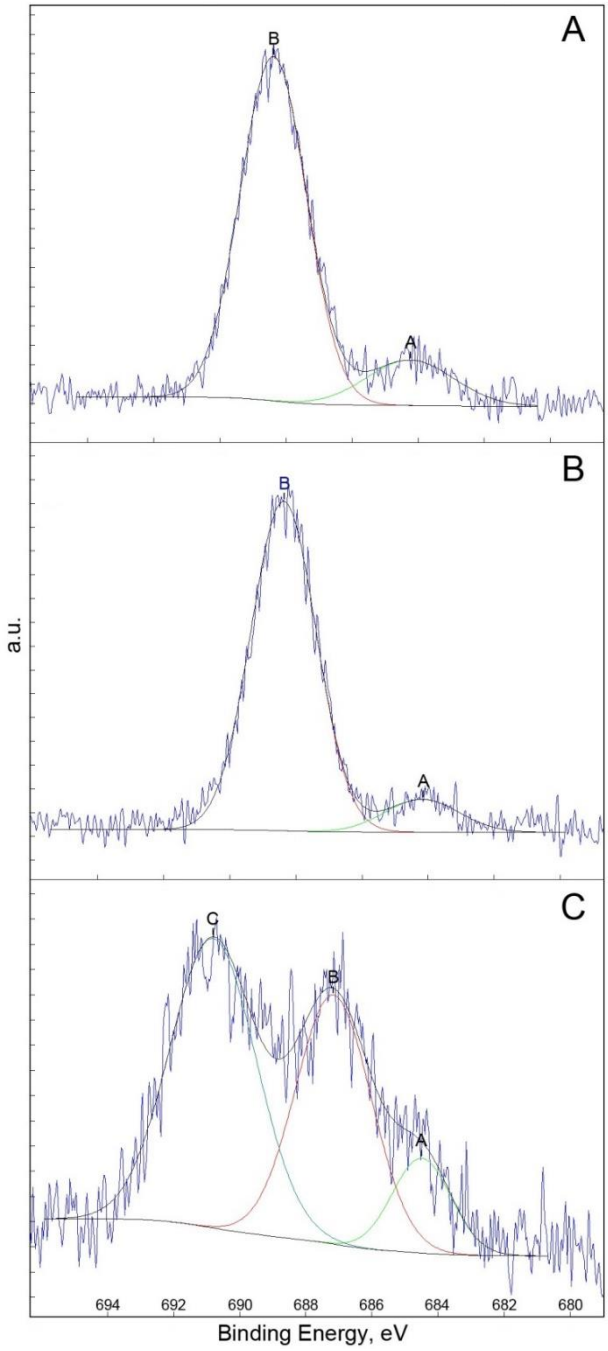

Fig. 5.5. XPS results - F 1s region XPS spectra of titanium dioxide catalyst: after 2 h (A); after 4 h (B); after 9 h reaction (C).

The results of mass balance calculation revealed an increasing loss of fluorine, till about 5% of fluorine after 9 h. The incorporation of a moderate amount of fluoride ions as dopant onto TiO_2 nanoparticles generally enhances effectively their photocatalytic activity due to the formation of Ti-F species on the facets [32-41].

Table 5.1. HPLC-MS data of PFOA and its degradation intermediates monitored during a photoabatement (UV lamp specific power 95 W/m^2) with TiO_2 slurry as photocatalyst (catalyst content 0.66 g/L).

Compound	**Time (min)**	**HPLC-MS Area (counts)**	**Relative Area (-)**	**C[a] (mmol/l)**
Perfluorooctanoic acid	0	-	-	4.00
(PFOA)	30	691806266	0.97611	3.83
	60	713933137	0.96436	3.43
	120	700640410	0.95265	2.93
	180	563212039	0.92791	2.75
	240	446126561	0.89380	2.43
	360	543928439	0.88458	2.41
	540	440233201	0.81782	2.22
Perfluoroheptanoic acid	0	0	0	0
(PFHpA)	30	12437567	0.01755	0.069
	60	18694212	0.02525	0.090
	120	21176190	0.02879	0.089
	180	27230746	0.04486	0.133
	240	34061273	0.06824	0.186
	360	45074843	0.07331	0.199
	540	65888153	0.12240	0.333
Perfluorohexanoic acid	0	0	0	0
(PFHxA)	30	4427872	0.00625	0.024
	60	7568624	0.01022	0.036
	120	10889019	0.01481	0.046
	180	13252458	0.02183	0.065
	240	14028651	0.02811	0.076
	360	18589489	0.03023	0.082
	540	22961222	0.04266	0.116

However, variations of reaction operative conditions, especially pH, and use of an excessive F:Ti molar ratio can cause an opposite behavior: the stabilization of F^- ions in the vicinity of Ti^{4+} cations and the limitation of charge carriers mobility hinder the photocatalytic activity of TiO_2. These results were in agreement with the XPS analyses in the Ti-2p region recorded on catalyst samples collected at different reaction times: in the first 4 h of photoabatement, no variations were observed on the TiO_2 surface and both binding energy values and peaks distribution remained almost identical to that of the pristine P25: conversely, considerable variations were noticed after 9 h of PFOA photodegradation.

The assignments of 19F-NMR spectra of PFOA, referring to the labeled formula $CF_{3(m)}CF_{2(n)}CF_{2(o)}CF_{2(p)}CF_{2(q)}CF_{2(r)}CF_{2(s)}COOH$, were in agreement with literature: δ = -81.4 (3 F, F_m), -126.7 (2 F, F_n), -123.7 (2 F, F_o), -123.4 (2 F, F_p), -122.6 (2 F, F_q), -122.4 (2 F, F_r), -117.9 (2 F, F_s) ppm [42]. The presence of the same set of 7 signals in both the starting and the final solutions suggested that a significant portion of undecomposed PFOA remained [14]. Only at the end of the considered decomposition time (9 hours), the amount of shorter acids in solution was enough to be clearly detected and a peak due to a CF_2 near a CF_3 not ascribable to PFOA appeared at -131 ppm [43]. Peaks of shorter perfluorinated acids have almost the same chemical shifts of the corresponding signals of PFOA [44]. The integrals of the signals in the ^{19}F-NMR spectra recorded at 0 min, 3 and 9 hours were also calculated. The $CF_{3(m)}$ integral was used as reference, with an imposed value of 3. The PFOA mineralization results in less concentrated solutions of the starting acid and, consequently, the ratio

between ^{19}F-NMR integrals of $CF_{3(m)}$ and of all the CF_2 should remain constant. If PFOA decomposition stops before the complete mineralization, shorter perfluorinated acids should be generated. In this situation, the elimination of COF_2 in pathway B (**Fig. 5.2** - reaction i) as well as the decarboxylation in pathway A (**Fig. 5.2** - reaction c) reduce the number of CF_2 groups in the chains and, consequently, the number of peaks in ^{19}F-NMR spectra. In the starting solution (0 min), the ratio between CF_3 and CF_2 integrals was 3:2 (**Fig. 5.6**).

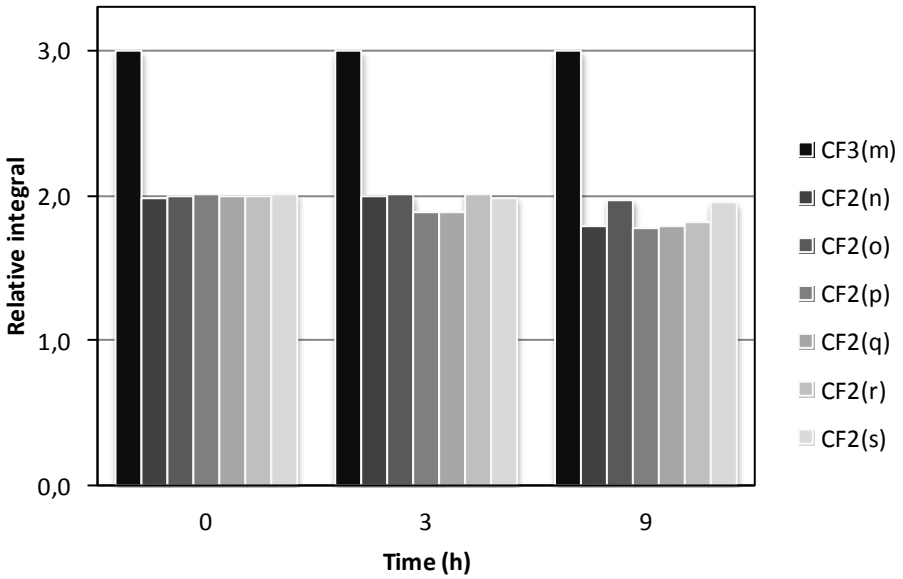

Fig. 5.6. ^{19}F-NMR spectra integrals values at different decomposition time. All the CF_2 integral values are relative to their ratio with CF_3 ones and the assignments are referred to the labeled formula of PFOA: $CF_{3(m)}CF_{2(n)}CF_{2(o)}CF_{2(p)}CF_{2(q)}CF_{2(r)}CF_{2(s)}COOH$.

After 3 hours, the integrals of two inner CF_2 signals, $CF_{2(p)}$ and $CF_{2(q)}$, slightly decreased, because of the formation of perfluorinated acids with shorter chains. In fact, these acids have progressively a lower number of

CF_2 groups than PFOA and a CF_3 as carbon-chain end-group. Therefore, a diminishing number of CF_2 signals can contribute to the ^{19}F-NMR spectra even if the CF_3 signal is present until the complete mineralization of PFOA. After 9 hours, the relative integral of four CF_2 signals, $CF_{2(n)}$, $CF_{2(p)}$, $CF_{2(q)}$ and $CF_{2(r)}$, decreased and this can be due to the formation of perfluorinated acids with even shorter chains.

5.1.3 Conclusions

The influence of fluoride ions on the surface of titanium dioxide, during the perfluorooctanoic acid degradation, was studied. The photocatalytic reaction was carried out working under optimal conditions, using a 4 mM PFOA solution and a TiO_2 content of 0.66 g/L under an UV irradiation of 95 W/m^2. The degradation mechanism was investigated by HPLC-MS analysis, confirming the presence of the intermediates through two possible degradation pathways: the photo-redox and the β-scission pathway. The mechanism based on β-scission reactions resulted dominant during the first 4 hours of photoabatement, when the complete mineralization with the fastest rate of fluoride release is more significant; afterwards, the photo-redox mechanism prevailed and noticeable concentrations of shorter chain perfluorinated acids as degradation intermediates were observed. The PFOA concentration was monitored during the reaction and a kinetic apparent constant (k_{app}) referring to the rate of PFOA disappearance was measured as equal to 0.1296 h^{-1}. The surface of TiO_2 was analyzed by XPS technique, revealing the modification of TiO_2 catalyst after 9 hours of reaction. The

surface modification was induced by fluoride ions due to hydrofluoric acid generated by PFOA degradation and it might influence the catalyst reducing the photocatalytic efficiency of TiO_2. ^{19}F-NMR analysis revealed the signals due to PFOA in both the starting and the final solutions, proving that the surfactant was not completely decomposed. Thus, the chemical modification of the catalyst surface induced by fluoride anions can be at the basis of the limited performances of titanium dioxide photocatalyst for PFOA degradation.

5.2 Textile dyes photodegradation

Many industries use dyes in order to colour their products. The presence of these dyes in water, even at very low concentrations, is highly visible and undesirable. Colour is the first contaminant to be recognized, and environmental regulations in most of the countries (EU directive 91/271) have made it mandatory to decolourise the dye wastewater prior to discharge [45]. Many dyes are difficult to degrade due to their complex structure and xenobiotic properties.

Since the formation of the Ecological and Toxicological Association of the Dyestuffs Manufacturing Industry (ETAD), in 1974, measures have been taken to minimise environmental damage [46]. In Great Britain, government legislation is becoming more and more stringent regarding dye removal and effluent toxicity: in the UKs 1997 environmental policy, stating that zero synthetic chemicals should be released into the marine environment [47].

Many treatments have been investigated regarding their effectiveness in either removing the dyes from dye-containing effluent, or decolourizing dyes through liquid fermentations [48]. Dyes may also be problematic if broken down anaerobically in the sediment, leading to the production of toxic amines. Lethal levels may be reached affecting aquatic systems and associated flora and fauna. Azo dyes account for 70% of synthetic dyes used worldwide [49] and at least 10% of the applied dyestuff is released into the process water during textile dyeing with azo dyes.

Main target of the present work is to investigate the performance of a commercial micro-sized TiO_2 (1077 by Kronos) used as photocatalyst in the degradation of three different dyes (rhodamine B, crystal violet and methylene blue) in water. Micro-sized sample was used as received, so to compare the obtained results with the classical nano-sized commercial P25 by Evonik, always used as photocatalyst reference material. Previously Marcos et al. [50] reported the deposition of TiO_2 layers on common ceramic glazed tiles using the screen-printing process, which is a low cost and common technique used for decoration in the ceramic industry. Labrincha et al. [51] deposited several commercial titania powders by jet spray on ceramic tiles, then fired to stabilize the layers. In both cases a good activity of nano-sized TiO_2 photocatalytic layers on ceramic tiles was demonstrated in the degradation of Orange II dye. In the present case, micro-sized 1077 was industrially hot coated at the surface of a porcelain grès tile (Orosei ActiveTM). Tests using photoactive tiles were carried out to verify the efficacy of the coated catalyst to degrade dyes in water media to obtain a stable and very easy way to separate the solution at the end of the reaction from the photoactive catalyst.

5.2.1 Materials and Methods

5.2.1.1 TiO_2 powders and porcelain gres tiles

TiO_2 1077 by Kronos was chosen as micro-sized photocatalyst, commercially classified as pigment. 1077 is also used in commercially available photoactive porcelain grès tiles (named Orosei Active™). The industrial procedure for the preparation is described in **Paragraph 4.2.1**. Rhodamine B (RhB, dye content ~95%, $C_{25}N_3H_{30}Cl$, PM 409 g/mol), Methylene Blue (MB, dye content ≥97%, $C_{28}H_{31}ClN_2O_3$, PM 479 g/mol) and Crystal Violet (CV, dye content ≥90%, $C_{28}H_{31}ClN_2O_3$, PM 479 g/mol) were chosen as organic pollutant. Each dye (Sigma–Aldrich) was used without further purification. Two different dye concentrations were used in the present paper: 1×10^{-4} M and 1×10^{-5} M, depending on the reaction set-up. The most concentrated solution was used to verify the efficiency in the photodegradation of organic molecules in water of powdered micro-sized TiO_2 as stressing conditions. These results were compared to the results already obtained by P25 by several authors in the past [52,53] and reconfirmed in this text. The less concentrated solution, higher than the one reported by Marcos et al. [50], were used to test the performance of Orosei Active™ tiles. The solutions were prepared by dissolving the dye in distilled water and without any pH adjustment, but leaving them at their spontaneous values.

5.2.1.2 Photocatalytic tests with powdered TiO_2 catalysts

Dyes degradation in water media was performed in a slurry reactor, described in the **Paragraph 5.1.1.2** and already reported by Djellaby et al. [54]. Irradiation was allowed by the use of an external UV lamp (500 W, Jelosil®, HG500, halide lamp), emitting in the range 315–400 nm and with a emitting power evaluated in the middle of the reactor by a radiometer instrument (DeltaOHM, model HD2102.2) of 75 W/m^2. Dye adsorption tests have been carried out in the dark using a catalyst amount of 1 g/L at four different dyes solution (concentration ranged between 10^{-6} and 10^{-4} M) for six hours. Photolysis tests have been performed for six hours; the same for photocatalysis performed using fresh 0.1 g/L TiO_2 in powder form. Dyes degradation was checked every 60 min. Analytic determination of the dyes concentrations in water solution was performed by a UV–vis spectrophotometer analyzer (T60 UV–vis PG LTD instruments), using water as the reference. Pure CV has an absorbance maximum at 590 nm, RhB at 555 nm and MB at around 670 nm. It has been conducted also mass spectrometry analysis for the investigation of dyes by-products forming during the degradation.

5.2.1.3 Photocatalytic tests with photoactive TiO_2 tiles

A cylindrical batch reactor of 1 L volume was used for dye degradation tests in presence of ten photoactive tiles (0.03 m^2 total surface photoactive area) immersed into the liquid solution, as schematically shown in **Fig. 5.7**. Refrigeration was allowed by a cooling jacket.

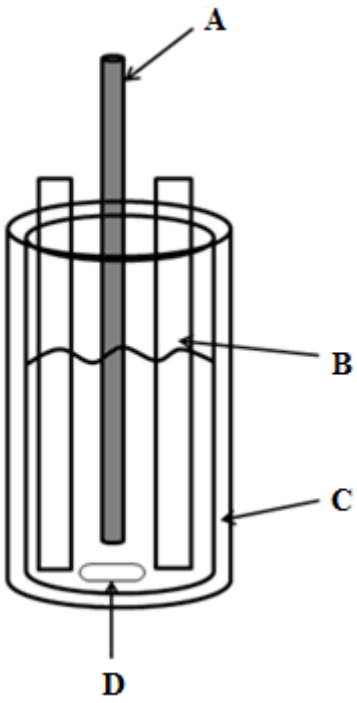

Fig. 5.7. Cylindrical batch reactor used for photocatalytic experiments: A: UV lamp; B: Orosei Active™ tiles; C: cooling jacket; D: magnetic stirrer.

Two different lamps directly immersed into the dye solution were used with this setup: a typical germicidal 9 W UV-C lamp (Philips TUV BL-S, model AEPL-7913 mercury vapor low pressure), with a UV-A illuminance at the tiles surface of 1 W/m^2 and a 125 W UV-A lamp (Jelosil, mercury vapor low pressure), with an illuminance of 65 W/m^2, as reported in a previous work by Bianchi et al. [55]. The same batch of Orosei Active™ tiles was used for all the tests reported in the present paper; after each test the tiles were simply washed using deionized water and acetone and then left in deionized water all night long.

Adsorption tests were carried out by dipping the tiles into the dyes solutions in dark conditions for six hours. To avoid any alteration of both irradiating

conditions and fluid dynamic of the system, photolysis was performed with the tiles still inside the reactor but with the active faces turned towards the dark side of the reactor, thus preventing the photoactivation of the TiO_2 catalyst. During photocatalytic tests the TiO_2 active faces of the tiles were turned towards the UV light. The same dyes solution described in the **Paragraph 5.2.1.1** were used in the present setup at a concentration of 1×10^{-5} M. Kinetics were monitored by UV–vis spectrophotometric analysis.

5.2.2 Results and Discussions

5.2.2.1 Dyes photodegradation in presence of TiO_2 powders

Experimental dark tests have shown a very low adsorption of all the dyes on both P25 and 1077 catalyst at the spontaneous pH we have in our working conditions. Notwithstanding P25 has specific surface area double than 1077 (25 m^2/g and 12 m^2/g, respectively) photolysis of CV and MB are almost negligible for both the catalysts (6% for both dyes for P25, 9% and 4% for CV and MB, respectively, for 1077). 12% of dye degradation for simple photolysis (10% for P25) was achieved for RhB. The dye molecules here considered are all cationic organic-based ones with a several benzene rings and high molecular weight, being thus quite complex systems to be degraded. Photocatalytic tests show good results in dyes abatement. Nano-sized powder shows the best results for all the considered dyes achieving the complete decolorizing of the water solution (see **Fig. 5.8**), but also micro-

sized sample are able to degrade the pollutants with a good efficiency (ranging from 48 to 58% depending on the dye in six hours) (**Fig. 5.9**).

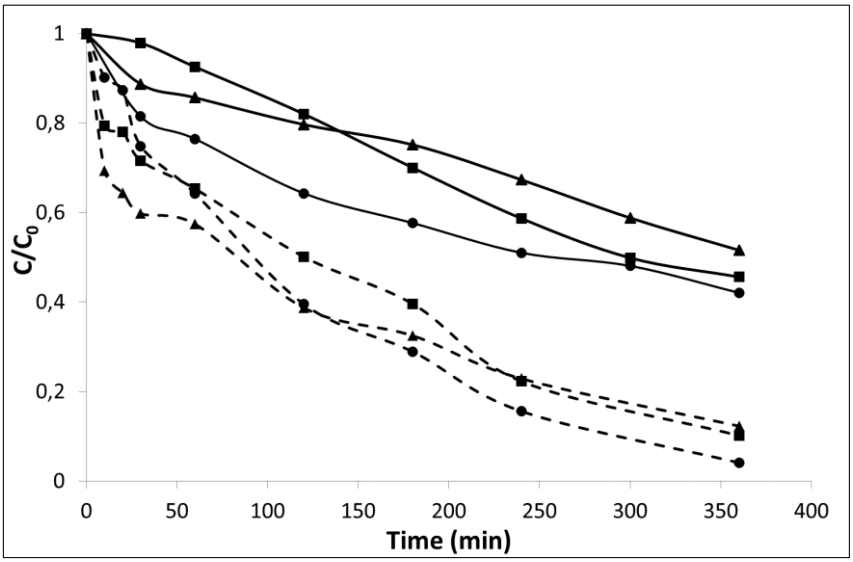

Fig. 5.8. Photocatalysis of MhB (▲), RhB (■) and CV (●) with 1077 (solid line) and P25 (dashed line).

In **Table 5.2** there are reported the photodegradation results for both micro- and nano-sized TiO_2 powders.

A study on the reaction rate has been done by elaborating the kinetic constants for both 1077 and P25 samples. Photocatalysis generally follows a Langmuir-Hinshelwood mechanism, whose equation can be approximated to a pseudo-first order kinetic with respect to the negligible adsorption of the dyes by the micrometer catalyst used:

$$r = -\frac{dC}{dt} = k_{app}C \qquad \textbf{(5.3)}$$

The integral form in function of time of the Eq. 6.1 can be withdrawn and the slope of the straight line interpolated represents the k_{app}. The rate constants were consequently calculated for both samples and for all the

tested dyes and are all in the 10^{-3} magnitude order (RhB = 1.78 or 5.0 $*10^{-3}$, MB = 1.78 or 5.1 $*10^{-3}$, CV = 2.64 or 8.2 $*10^{-3}$, respectively the first value corresponds to 1077 and the second one to P25). It is worth noting that both nano- and micro-powders exhibit k values in the same order of magnitude, most likely because the photocatalytic process follows a similar pathway despite the dimensions of the TiO_2 powder.

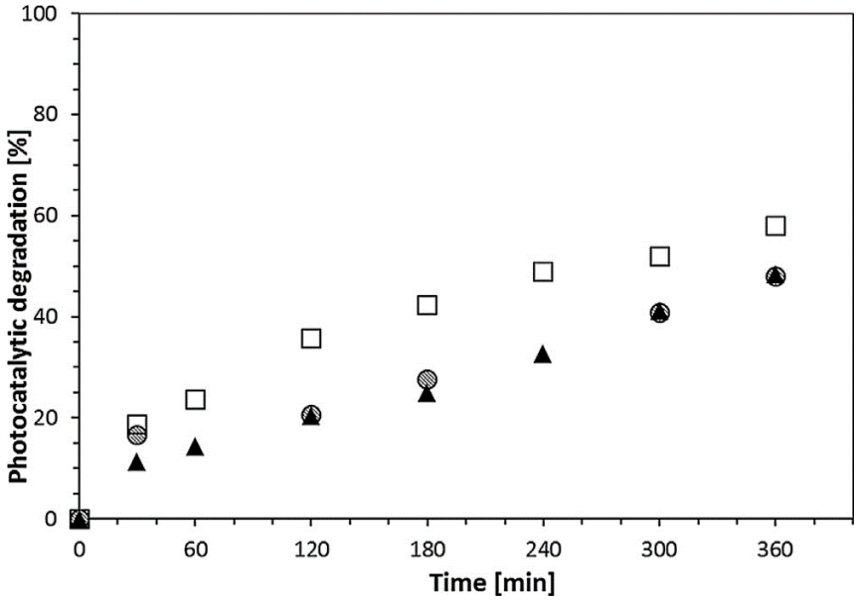

Fig. 5.9. Photocatalysis of dyes performed with powdered micro-TiO_2 catalyst (1077): crystal violet □; methylene blue ▲; rhodamine B ○.

Table 5.2. Photocatalytic results of micro- and nano-sized powders concerning MB, RhB and CV degradation.

TiO_2 powder	**MB degradation (%)**	**RhB degradation (%)**	**CV degradation (%)**
1077	48	48	58
P25	88	81	96

The possibility to recover the powdered catalyst was checked by simply filtering the final degraded solution in a standard Bückner funnel equipped with a filter paper or directly centrifuging it in a laboratory scale equipment working at 10,000 rpm. For 1077 sample, the simple centrifugation was sufficient to recover all the used photocatalyst. The powder was washed several times in deionized water and reused in the same dye degradation test (CV discoloration) with no loss of photoactivity. On the other hand, no recovery of P25 was possible neither filtering or centrifuging the solution. The nano-powder passed completely through the filter paper and it was not separated by the solution by centrifugation remaining very well-dispersed in water. The lower efficiency of 1077 micro-sized TiO_2 in the degradation of dyes in water than nano-sized photocatalyst is fully rewarded by the facility to recover the photoactive powder from the solution at the end of the purification reaction and reuse it eventually after a simple washing in water, as shown by Bianchi et al. [55].

It is interesting to highlight that during the photodegradation, the dye is not completely degraded, but it happens the formation of by-products. This fact is attributable to the products forming during photoabatement that could gloss over the dye concentration. It is confirmed by mass spectrometry analyses that reveal just after 30 minutes the existence of species without one or more ethyl groups on nitrogen atoms, being them the first to be attached by oxydril radicals, formed by photocatalyst. In this way, it is possible to verify, at least partly, the degradation paths present in the literature. The peak area of the main adsorption centered on 541.5 nm is indicative of the concentration of the RhB dye molecule and it can be observed that under illumination, the area reduces as a function of time. The

adsorption band relative to by-products of RhB photoabatement is clear in the region under 500 nm, as we can note in **Fig. 5.10**, where there is an increase of absorbance. As it is confirmed by UV-vis results, the dye molecule is not just visible after 30 minutes.

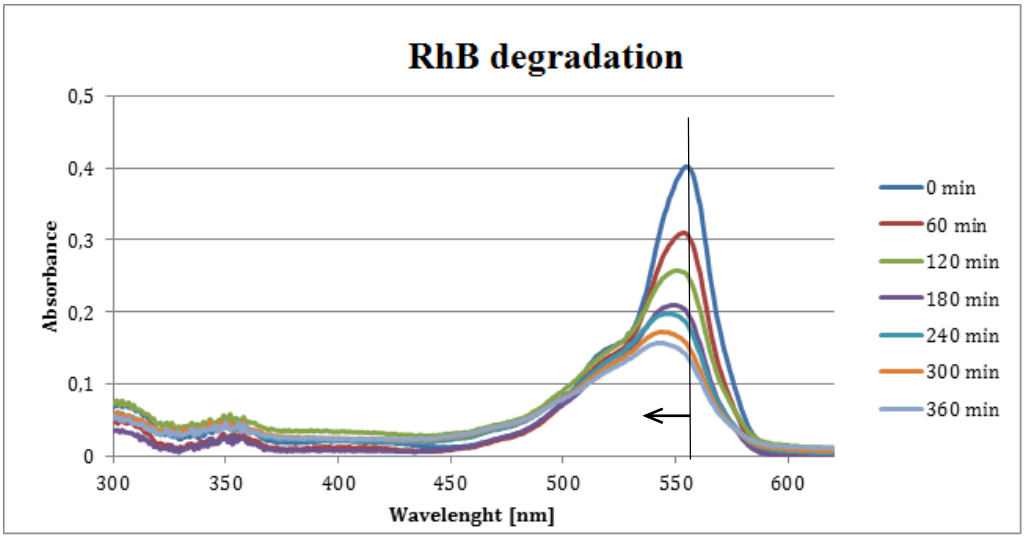

Fig. 5.10. UV-vis spectra at different times of RhD degradation.

This fact is due to the first degradation paths, which don't modify or destroy the molecule, but they only change the conjugation of dye, modifying the absorption spectra, confirming the blue-shift: the adsorption shifts toward lower wavelength, as just demonstrated in the past literature by He et al. [56]. In the **Fig. 5.11** it is shown the degradation path of RhB. A similarity is noticed by degrading also MB and CV: the degradation path is verified through mass spectrometry analysis. They can be recognizable the by-products for each dye, taking form during photoreaction, even though diagnosis of reaction pathways is complicated by the dye sensitization mechanism and the influence of resulting products.

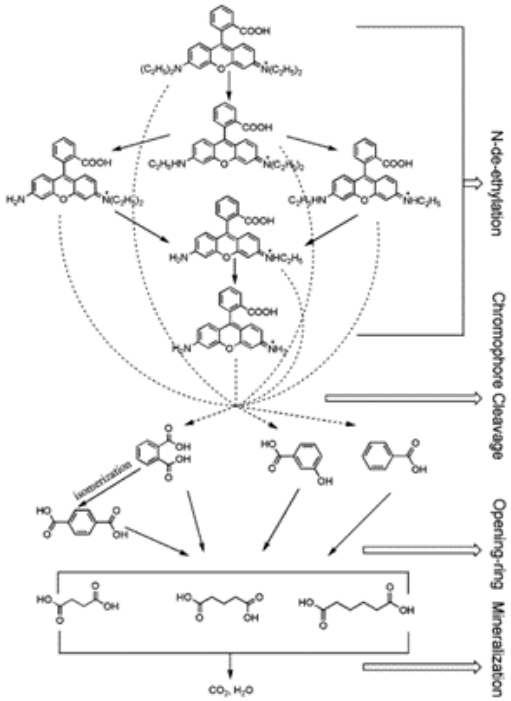

Fig. 5.11. Degradation path of Rhodamine B during photocatalytic reaction.

5.2.2.2 Dyes photodegradation in presence of TiO_2 activated tiles

According to the previous results obtained by the use of micro-sized TiO_2 catalyst [55] the activity of 1077 industrially hot-coated onto porcelain grès tiles was evaluated in another experimental setup verifying the material efficiency with two different UV lamps immersed inside the dyes solution. Control experiments of photolysis and adsorption of dyes on the tiles were carried out. Dark tests shown a 25% adsorption of CV and MB, while RhB adsorption is on the contrary almost negligible. However, dyes were

exclusively fixed in the backside and lateral sides of the ceramic pieces, i.e. in the surfaces uncovered by the photocatalytic layer. Direct photolysis highlights different results depending on the used lamp: a percentage degradation of 64% for CV, 70% for MB and 14% for RhB was achieved for 9 W immersion lamp, a very high result in comparison to the photolysis tests conducted with catalytic powders. It is worth to note that there is also degradation of colour when there is not photocatalyst and this creates difficulties to understand very well the efficiency deriving by catalyst. The loss of colour by photolytic degradation of the dye is quite common, in fact this effect is observed as buildings are discoloured under sunlight. In addition, in this case this was a germicidal lamp and therefore an emission in the UV-C region is present and is probably enhancing the photolysis process. Lower results, as shown in **Fig. 5.12**, were instead obtained using the 125 W UV-A (illuminance of 65 Wm^{-2}) immersion lamp.

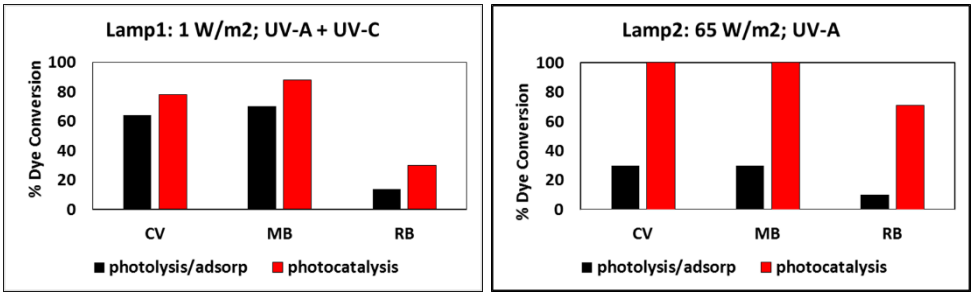

Fig. 5.12. Photocatalytic degradation of dyes performed with the two different immersion lamps (1 Wm^{-2} and 65 Wm^{-2}).

The absence of UV-C allows to have dyes degradation due to pure photolysis within 30% for CV and MB, 10% for RhB (we have not to forget that tiles are already immersed not to alter the reactor flow dynamic and therefore adsorption process is still present). However, results obtained by photocatalytic tests and carried out by using the coated micro-TiO_2 catalyst

onto the tiles surface, showed that there is an enhanced degradation of colour in the presence of photocatalyst. The kinetic results are showed in **Fig. 5.13** for 9 W lamp.

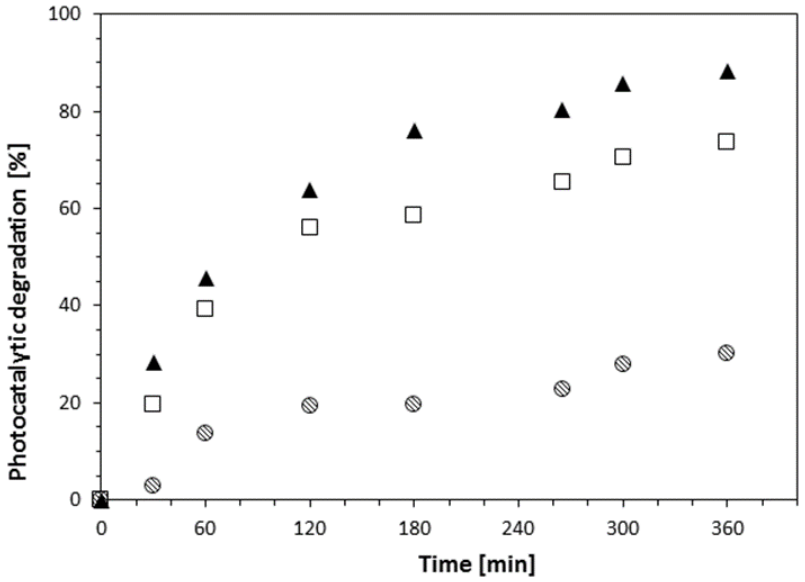

Fig. 5.13. Photocatalysis with TiO_2 activated tiles and UV light irradiation (1 W immersion UV lamp); crystal violet □; methylene blue ▲; rhodamine B ◌.

Degradation of dyes is improved by the use of the photoactive tiles; in fact after a six hours reaction, the percentage degradation value obtained is 78% for CV, 88% for MB, and the 30% for RhB, revealing an increase of about 15% of degradation on all dyes in comparison to the simply photolysis tests. Tests with the 125 W UV-A lamp lead to the complete degradation of CV and MB in less than three hours and the disappearance of 71% RhB in 6 h. This proves the self-cleaning effect of gres tiles if TiO_2 is present.

5.2.3 Conclusions

The obtained results for dyes degradation are very interesting: micro-sized TiO_2 powders have shown good photocatalytic efficiency, reinforcing the interest for further photodegradation reactions. The degradation steps highlights that, even though the dye absorbance peak decrease during the time, several by-products take form a lead to the modifications in the UV-vis spectra. In fact, for all dyes there is a blue-shift in the spectra due to the formation of products during photodegradation. Through the comparison of the kinetic results with nano-sized powders ones, only a small difference is observed respect to micro-sized ones; k values are in the same order of magnitude for both kinds of powders. The dyes photodegradation results confirms the possibility to apply micro-sized TiO_2 powders improving upon the applications: they can easily filtered and recovered, in order to be immediately reused for further photodegradation reactions, opening the way of a fully industrial use of photocatalysis in environmental remediation.

A further improvement can be achieved coating micro-TiO_2 on porcelain grès tiles surfaces. The photocatalytic materials described here can be reused, just after mere rinsing of the tiles in distilled water, and without affecting the photocatalytic activity. In fact, all the tests performed in the present work were done using the same batch of ten samples obtained from industrially prepared tiles (Orosei Active^{TM}), and no loss in their photoactivity was monitored. This indicates that the TiO_2 deposited layers are not deactivated during the reaction either by loss or poisoning of the catalyst, and can be reutilized in subsequent runs. These new industrial ceramic materials are surely an interesting alternative to TiO_2 suspensions,

for example in photocatalytic applications avoiding the removal of the particles at the end of the process.

5.4 References

[1] Schultz M.M., Barofsky D.F., Field J.A. Fluorinated alkyl surfactants. *Environ. Eng. Sci*. **2003**, *20*, 487-501.

[2] Cousins I.T., Buck R.C., Korzeniowski S.H. Surface, fate and transport of perfluorocarboxylates. *Environ. Sci. Technol*. **2006**, *40*, 32-44.

[3] Ylinen M, Hanhijärvi H., Peura P., Rämö O. Quantitative gas chromatographic determination of perfluorooctanoic acid as the benzyl ester in plasma and urine. *Arch. Environ. Contam. Toxicol*. **1985**, *14*, 713-717.

[4] Persico F., Sansotera M., Diamanti M.V, Magagnin L., Venturini F., Navarrini W. Effect of amorphous fluorinated coatings on photocatalytic properties of anodized titanium surfaces. *Thin Solid Films* **2014**, *545*, 210-216.

[5] Lemal D.M., Org J. Perspective on fluorocarbon chemistry. *Chem*. **2004**, *69*, 1-11.

[6] Smulders E., von Rybinski W., Nordskog A. Laundry Detergents, in: Ullmann's Encyclopedia of Industrial Chemistry, seventh ed., *Wiley-VCH*, Weinheim **2011**.

[7] Hori H., Hayakawa E., Einaga H., Kutsuna S., Koike K., Ibusuki T., Kiatagawa H., Arakawa R. Decomposition of environmentally persistent perfluorooctanoic acid I water by photochemical approaches. *Environ. Sci. Technol*. **2004**, *38*, 6118-6124.

[8] Zaggia A., Ameduri B. Recent advances on synthesis of potentially non-bioaccumulable fluorinated surfactants. *Curr. Opin. Colloid Interface Sci*. **2012**, *17*, 188-195.

[9] Lin H., Niu J., Ding S., Zhang L. Electrochemical mineralization of perfluorocarboxylic acids (PFCAs) by Ce-doped modified porous nanocrystalline PbO_2 film electrode. *Wat. Res*. **2012**, *46*, 2281-2289.

[10] Li X., Zhang P., Jin L., Shao T., Li Z., Cao J. Efficient photocatalytic decomposition of perfluorooctanoic acid by indium oxide and its mechanism. *Environ. Sci. Technol*. **2012**, *46*, 5528-5534.

[11] US EPA (2002), Revised draft – Hazard assessment of Perfluorooctanoic Acid and its salts, Office of Pollution Prevention and Toxics, *Risk Assessment Division*, (November 4, **2002**).

[12] Järnberg U., Holmström K., van Bavel B., Kärrman A. Perfluoroalkylated acids and related compounds (PFAS) in the Swedish environment- Chemistry, Sources & Exposure. *Report to Swedish Environment Protection Agency* **2006**.

[13] Ohno T., Sarukawa K., Tokieda K., Matsumura M. Morphology of a TiO_2 photocatalyst (Degussa, P25) consisting of anatase and rutile crystalline phase. *J. Catal*. **2001**, *203*, 82-86.

[14] Gatto S., Sansotera M., Persico F., Gola M., Pirola C., Panzer W., Navarrini W., Bianchi C.L. Surface fluorination on TiO_2 catalyst induced by photodegradation of perfluooroctanoi acid. *Catal. Today* **2014**.

[15] Selli E., Bianchi C.L., Pirola C., Cappelletti G. Efficiency of 1,4-dichlorobenzene degradation in water under photolysis, photocatalysis on TiO_2 and sonolysis. *J. Hazard. Mater*. **2008**, *153*, 1136-1141.

[16] Carp O., Huisman C.L., Reller A. Photoinduced reactivity of titanium dioxide. *Prog. Solid State Chem*. **2004**, *32*, 33-177.

[17] Munter R. Advanced oxidation processes – current status and prospects. *Proc. Estonian Acad. Sci. Chem*. **2001**, *50*, 59-80.

[18] Carp O., Huisman C.L., Reller A. Photoinduced reactivity of titanium dioxide. *Prog. Solid State Chem*. **2004**, *32*, 33-177.

[19] Zaggia A., Ameduri B. Recent advances on synthesis of potentially non-bioaccumulable fluorinated surfactants. *Curr. Opin. Colloid Interface Sci*. **2012**, *17*, 188-195.

[20] Panchangam S.C., Lin A.Y.C., Tsai J.H., Lin C.F. Sonication-assisted photocatalytic decomposition of perfluooroctanoic acid. *Chemosphere* **2009**, *75*, 654-660.

[21] Wang Y., Zhang P. Photocatalytic decomposition of perfluooroctanoic acid (PFOA) by TiO_2 in the presence of oxalic acid. *J. Hazard. Mater*. **2011**, *192*, 1869-1875.

[22] Lin H., Niu J., Ding S., Zhang L. Electrochemical mineralization of perfluorocarboxylic acids (PFCAs) by Ce-doped modified porous nanocrystalline PbO_2 film electrode. *Wat. Res*. **2012**, *46*, 2281-2289.

[23] Kutsuna S., Hori H. Rate constants for aqueous-phase reactions of SO_4^- with $C_2F_5C(O)O^-$ and $C_3F_7C(O)O^-$ at 298 K. *Int. J. Chem. Kinet*. **2007**, *39*, 276-288.

[24] Kormann C., Bahnemann D.W., Hoffmann M.R. Photolysis of chloroform and other organic molecules in aqueous titanium dioxide suspensions. *Environ. Sci. Technol*. **1991**, *25*, 494-500.
[25] Talaeemashhadi S., Sansotera M., Gambarotti C., Famulari A., Bianchi C.L., Guarda P.A., Navarrini W. Functionalization of multi-walled carbon nanotubes with perfluoropolyether peroxide to produce superhydrophobic properties. *Carbon* **2013**, *59*, 150-159.
[26] De Bruyn W.J., Shorter J.A., Davidovits P., Worsnop D.R., Zahniser M.S., Kolb C.E. Uptake of haloacetyl and carbonyl halides by water surfaces. *Environ. Sci. Technol*. **1995**, *29*, 1179-1185.
[27] Sansotera M., Navarrini W., Gola M., Bianchi C.L., Wormald P., Famulari A., Avataneo M. Peroxidic perfluoropolyether for the covalent binding of perfluoropolyether chains on carbon black surface. *J. Fluorine Chem.* **2011**, *132*, 1254-1261.
[28] Giessing A.M.B., Feilberg A., Mögelberg T.E., Sehested J., Bilde M., Wallington T.J., Nielsen O.J. Atmospheric chemistry of HFC-227ca: spectrokinetic investigation of the $CF_3CF_2CF_2O_2$ radical, its reactions with NO and NO_2, and the atmospheric fate of the $CF_3CF_2CF_2O$ radical. *J. Phys. Chem*. **1996**, *100*, 6572-6579.
[29] Sansotera M., Navarrini W., Magagnin L., Bianchi C.L., Sanguineti A., Metrangolo, Resnati G. Hydrophobic carbonaceous materials obtained by covalent bonding of perfluorocarbon and perfluoropolyether chains. *J. Mater. Chem.* **2010**, *20*, 8607-8616.
[30] Sansotera M., Persico F., Pirola C., Navarrini W., Di Michele A., Bianchi C.L. Decomposition of perfluorooctanoic acid photocatalyzed by titanium dioxide: chemical modification of the catalyst surface induced by fluoride ions. *App. Catal. B: Environ*. **2014**, *148*, 29-35.
[31] Demourgues A., Penin N., Durand E., Weill F., Dambournet D., Viadere N., Tressaud A. New titanium hydroxyfluoride $Ti_{0.75}(OH)_{1.5}F_{1.5}$ as a UV. *Absorber Chem. Mater*. **2009**, *21*, 1275-1283.
[32] Wang Q., Chen C., Zhao D., Ma W., Zhao J. Change of adsorption modes of dyes on fluorinated TiO_2 and its effect on photocatalytic degradation of dyes under visible irradiation. *Langmuir* **2008**, *24*, 7338-7345.
[33] Liu S., Yu J., Cheng B., Jaroniec M. Fluorinated semiconductor photocatalysts: tunable synthesis and unique properties. *Adv. Colloid Interface Sci*. **2012**, *173*, 35-53.

[34] Liu G., Sun C., Yang H.G., Smith S.C., Wang L., Lu G.Q.M., Cheng H.-M. Nanosized anatase TiO_2 single crystals for enhanced photocatalytic activity. *Chem. Commun*. **2010**, *46*, 755-757.
[35] Ho W., Yu J.C., Lee S. Synthesis of hierarchical nanoporous F-doped TiO_2 spheres with visible light photocatalytic activity. *Chem. Commun*. **2006**, *10*, 1115-1117.
[36] Zhang H., Liu P., Li F., Liu H., Wang Y., Zhang S., Guo M., Cheng H., Zhao H. Facile fabrication of anatase TiO_2 microspheres on solid substrates and surface crystal facet transformation from {001} to {101}. *Chem. A Europ. J.* **2011**, *17*, 5949-5957.
[37] Wu G., Wang J., Thomas D.F., Chen A. Synthesis of F-doped flower-like TiO_2 nanostructures with high photoelectrochemical activity. *Langmuir* **2008**, *24*, 3503-3509.
[38] Liu M., Piao L., Zhao L., Ju S., Yan Z., He T., Zhou C., Wang W. Anatase TiO_2 single crystals with exposed {001} and {110} facets: Facile synthesis and enhanced photocatalysis. *Chem. Commun*. **2010**, *46*, 1664-1666.
[39] Han X., Kuang Q., Jin M., Xie Z., Zheng L. Synthesis of titania nanosheets with a high percentage of exposed (001) facets and related photocatalytic properties. *J. Am. Chem. Soc*. **2009**, *131*, 3152-3153.
[40] Yang H.G., Liu G., Qiao S.Z., Sun C.H., Jin Y.G., Smith S.C., Zou J., Cheng H.M., Lu G.Q.M. Solvothermal synthesis and photoreactivity of anatase TiO_2 nanosheets with dominant {001} facets. *J. Am. Chem. Soc*. **200**9, *131*, 4078-4083.
[41] Li D., Haneda H., Labhsetwar N.K., Hishita S., Ohashi N. Visible-light-driven photocatalysis on fluorine-doped TiO_2 powders by the creation of surface oxygen vacancies. *Chem. Phys. Lett*. **2005**, *401*, 579-584.
[42] Karoyo A.H., Borisov A.S., Wilson L.D., Hazendonk P. Formation of host-guest complexes of β-cyclodextrin and perfluorooctanoic. *Acid J. Phys. Chem. B* **2011**, *115*, 9511-9527.
[43] Ribeiro A.A. ^{19}F, ^{13}C single-and two-bond 2D NMR correlations in perfluoroheptanoic acid. *J. Fluorine Chem*. **1997**, *83*, 61-66.
[44] Dolbier W.R. Guide to Fluorine NMR for Organic Chemists. *Wiley Hoboken* **2009**.
[45] O'Neill C., Hawkes F.R., Lourenco N.D., Pinheiro H.M., Delee W. Colour in textile effluents—sources. Measurement, discharge consents and simulation: a review. *J. Chem. Technol. Biotechnol*. **1999**, *74*, 1009–1018.
[46] Anliker R. Ecotoxicology of dyestuffs - a joint effort by industry. *Ecotox. Environ. Saf*. **1979**, *3*, 59–74.

[47] Robinson T., McMullan G., Marchant R., Nigam P. Remediation of dyes in textile effluent: a critical review on current treatment technologies with a proposed alternative. *Bioresour. Technol*. **2001**, *77*, 247–255.
[48] Banat I.M., Nigam P., Singh D., Marchant R. Microbial decolourisation of textile-dye-containing effluents: a review. *Bioresour. Technol*. **1996**, *58*, 217–227.
[49] Vandevivere P.C., Bianchi R., Verstraete W. Treatment and reuse of wastewater from the textile wet-processing industry: review of emerging technologies. *J. Chem. Technol. Biotechnol*. **1998**, *72*, 289–302.
[50] Marcos P.S., Marto J., Trinidade T., Labrincha J.A. Screen-printing of TiO_2 photocatalytic layers on glazed ceramic tiles. *J. Photochem. Photobiol. A* **2008**, *197*, 125–131.
[51] Seabra M.P., Pires R.R., Labrincha J.A. Ceramic tiles for photodegradation of Orange II solutions. *CEJ* **2011**, *171*, 692–702.
[52] Nagaveni K., Sivalingam G., Hegde M.S., Madras G. Photocatlytic degradation of organic compounds over combustion synthesized nano-TiO_2. *Environ. Sci. Technol*. **2004**, *38*, 1600–1604.
[53] Turchi C.S., Ollis D.F. Photocatalytic degradation of organic water contaminants: mechanisms involving hydroxyl radical attack. *J. Catal*. **1990**, *122*, 178–192.
[54] Djellabi R., Ghorab M.F., Cerrato P., Morandi S., Gatto S., Oldani V., Di Michele A., Bianchi C.L. Photoactive TiO_2-montmorillonite composite for degradation of organic dyes in water. *J. Photochem. Photobiol. A: Chem*. **2014**.
[55] Bianchi C.L., Colombo E., Gatto S., Stucchi M., Cerrato G., Morandi S., Capucci V. Photocatalytic degradation of dyes in water with micro-sized TiO_2 as powder or coated on porcelain tiles. *J. Photochem. Photobiol. A: Chem*. **2014**, *280*, 27-31.
[56] He Z., Sun C., Yang S., Ding Y., H. He, Wang Z. Photocatalytic degradation of rhodamine B by Bi_2WO_6 with electron accepting agent under microwave irradiation: Mechanism and pathway. *J. Hazard. Mater*. **2009**, *162*, 1477–1486.

Chapter 6

Self-cleaning effect of micro-sized TiO_2

In this section it is reported the results, carried out towards self-cleaning measurements. In particular, the research is focused on the study of the self-cleaning properties of industrially prepared tiles starting from commercial micro-sized TiO_2. The degradation of oleic acid at the surface, also called self-cleaning action, is verified by measurements of contact angle. The method consists on the evaluation of water contact angle under illumination with ultraviolet light, which is one of the indices influencing the self-cleaning performances of photocatalytic materials. Furtermore, two different organic dyes were put on the tiles surfaces, as contaminants, and the dyes degradation was checked by Vis-spectrometer with an integrated sphere to analyze the color changes.

6.1 Introduction

An interesting possibility to cause low contact angles (<5°) is the use of active thin films on the material surface. Such coatings are already commercialized for antifogging mirrors, glasses and outwards walls of buildings. For the preparation of this thin layers, in the last years TiO_2 coated materials are of increasing interest [1-3]. If TiO_2 is exposed to UV light and very low contact angles are obtained, these materials have the unique property of "attracting" rather than repelling water (super-hydrophilicity). The water lies flat on the surface in sheets instead of forming droplets. Furthermore, UV illumination of titanium dioxide leads to the formation of powerful agents with the ability to oxidize and decompose many types of bacteria, organic and inorganic materials. The photoinduced hydrophilicities of these films were evaluated by measuring the change of the water contact angle on the surfaces, as reported in **Paragraph 3.2.3**. When the TiO_2 film surface is irradiated under UV irradiation, it becomes very hydrophilic with a contact angle very low and this confirms the self-cleaning properties.

In order to evaluate the self-cleaning effect of micro-sized TiO_2, oleic acid was applied onto the gres tiles surface [4]. The test method evaluated the self-cleaning performance of micro-sized TiO_2 ceramic samples by obtaining the final contact angle of a test piece, on which organic substances, i.e. oleic acid, are applied. The organic substance was first applied to attest piece (pretreatment), which was then irradiated by UV at a constant intensity. The water contact angle after n hours can be measured in the process. This test simultaneously evaluated the decomposition of the organic substance and change of water affiliation. The concerning test was

based on ISO standard proposal. ISO (International Organization for Standardization) is a worldwide federation of national standard bodies, whose work of preparing International Standards is normally carried out through ISO technical committees. ISO 27448-1 was prepared by Technical Committee ISO/TC 206, *Fine Ceramics*.

In addition, the self-cleaning properties of these tiles were verified by monitoring the degradation of two different organic dyes directly put at tiles surfaces (Rhodamine B and Metanil Yellow).

6.2 Measurement procedures

The self-cleaning action was followed in two different ways: (1) through the measurement of the water contact angle (CA) (KRUSS GmbH, see **Paragraph 3.1.6**) of a tile after oleic acid deposition during the UV irradiation (Jelosil, model HG 500) for 76 h and (2) through the discoloration of dyes directly put at the tiles surfaces, and exposed to the sunlight (Milan – Italy, May 2012). The sunlight power was continuously checked from 9 am to 5 pm every day by a radiometer DeltaOhm HD2012,2. A mean power irradiation value of 7.28 W/m^2 was measured.

For water CA measurements, a test piece of gres tile of 100 ± 2mm square was used as the standard-size test pieces. At first, the sample was pretreated, irradiating it under ultraviolet irradiation of 20 W/m^2 for at least 24 hours. Then, oleic acid (Fluka, >80%) was applied onto the TiO_2 active surface by dipping: it was prepared a 0.5vol% oleic acid solution by diluting with n-heptane and dip the test piece in the solution. After lifting the test

piece from the solution, dried it at 70°C for 15 minutes. After that, it was measured the CA at 5 points on each test piece and averaged the values. These averaged values are defined as the CA before UV irradiation of each test piece.

After starting UV irradiation, it was measured the CA at five places on each test piece at an appropriate irradiation time interval. The mathematical average value of the five measurements is set as the "contact angle after 76 hours of UV irradiation". The CA was determined by fitting the profile of the drop on each image. The self-cleaning performance was evaluated from the CA development: determination of the final contact angle as the average of the last 3 values of specific irradiation, if the relative standard deviation (RSTD) is less than 10 %. The measurement can be considered concluded when the value of CA reappears to the same initial value of the sample, before the oleic acid deposition.

For comparison, the measurement was repeated on a sample similarly coated with oleic acid, but left in the dark for 76 hours. Furthermore, it was taken a sample of porcelain gres tile, not containing TiO_2, and it was immersed into oleic acid solution and irradiated, with the aim to evaluate the pure contribute of UV irradiation. In this way, it occurs that the change in the value of the contact angle was due merely to the photodegradation of the oleic acid due to the both action of UV radiation and the photocatalytic efficiency of the material under test and not by spontaneous degradation of oleic acid, induced by non photocatalytic factors.

Dyes degradation instead was monitored by Vis-spectrometer equipped with an integrated sphere (OceanOptics, USB400-VIS-NIR-ES). Calibration: 100% reflectance: $BaSO_4$ (x=0.3105; y=0.3238; z=0.3658). 0%

reflectance: black carbon (x=0.2175; y=0.166; z=0.6035). 1 μL of dyes (Rhodamine B and Metanil Yellow), dissolved in water, were put at the tiles surfaces. The color analysis was performed using the CIEXYZ and CIELAB models.

6.3 Results and Discussions

The obtained contact angle results for micro-sized TiO_2 commercial gres tiles (Orosei Active), treated with oleic acid and irradiated by UV lamp, are reported in **Tab. 6.1**. Another sample, always Orosei Active, was kept under dark and analyzed through contact angle at the end of 76 hours.

Table 6.1. Orosei Active contact angle for the evaluation of self-cleaning performance.

Sample	UV	Sample CA pre-deposition	CA t_0	CA t_{48}	CA t_{76}
Orosei Active™	Yes	31°± 0.9°	69°±1.0°	41°±2.9°	30°±2.8°
Orosei Active™	No	31°± 0.9°	68°± 0.9°	-	68°±1.1°

We can note that the contact angle of Orosei Active progressively decreases during the time, when it is irradiated: from time t_0 to t_{76}, reaching to the starting value before the oleic acid application. **Fig. 6.1** shows the contact angel measurements of a Orosei Active tile before and after the irradiation under UV light. This CA modification is due to the photocatalytic efficiency of gres tile; under UV irradiation, in fact, it is able to degrade oleic acid [5].

After 76 hours, oleic acid can be considered degraded and CA comes to the starting value. The CA value at 72, 74 and 76 remains more or less unchanged: this fact confirms that the completely degradation of oleic acid by photoactive gres tile. On the contrary, the same kind of gres tile (Orosei Active), treated with oleic acid, but maintained in the dark, does not show modifications about contact angle in the range t_0 and t_{76}: it is necessary, so, the photocatalytic process to activate the photoabatement of organic pollutant [4]. The same procedure, consisting in the deposition of oleic acid solution and irradiation under UV light for 76 h, was performed for a porcelain gres tiles, not containing TiO_2. Even in this case the CA measurement during the UV irradiation remained the same, i.e., the initial CA measured on the oleic acid film. It is justified that the change in the value of the contact angle is due merely to the photodegradation of the oleic acid due to both the action of UV radiation and the photocatalytic efficiency of the used material and not by spontaneous degradation of oleic acid, induced by non photocatalytic factors. Moreover, when TiO_2 is illuminated by light, grease, dirt and organic contaminants are decomposed and can warily swept away by water (rain) (ISO/WD 27448-1).

Fig. 6.1. Contact angle measurements for (left) before and (right) after irradiation with the UV lamp for 8h.

Contact angles data and the results obtained by process as required by the ISO standard are listed in **Table 6.2**.

Table 6.2. Contact angles data (ISO standard).

Kreo White Active		5 (five) contact angle misurements at each time (°)					θ_n	s	$\bar{x}$	$s/\bar{x}$
		1	2	3	4	5	degree	degree	degree	%
Ultraviolet radiation time (hour)	0	67,8	70,1	68,4	67,6	68,8	68,54	-	-	-
	2	68,9	71,0	64,7	66,0	67,2	67,56	-	-	-
	4	67,2	59,1	57,6	67,8	60,2	62,38	3,3	66,2	5,0
	6	64,4	68,0	64,2	68,0	59,6	64,84	2,6	64,9	4,0
	24	52,0	52,9	44,8	53,8	46,6	50,02	7,9	59,1	13,4
	28	51,5	53,6	45,9	51,0	48,6	50,12	8,5	55,0	15,5
	48	41,3	42,3	44,3	36,3	41,0	41,0	5,2	47,1	11,1
	72	29,4	31,9	24,7	33,5	32,8	30,5	9,8	40,5	24,3
	74	31,9	26,9	32,0	26,8	31,4	29,8	6,3	33,8	18,7
	76	27,7	31,4	27,2	34,2	30,0	30,1	0,3	30,1	1,1
	Starting slab	32,3	31,8	31,6	29,9	30,9	31,3			

θ_n = mean of the contact angle value measured on 5 (five) measurements made on 5 points chosen randomly on the surface of the material
s = standard deviation
$\bar{x}$= mean of the values of θn obtained at three consecutive time

In order to verify once more the photocatalytic properties, these tiles were dirtied with two selected chemical dyes: Rhodamine B, often used as a tracer dye within water, and Metanil Yellow, a stuff dye once used also as food color [4]. **Fig. 6.2** shows the colors disappearance after 5 days of exposure to the sunlight at an UV-A mean power of 7.28 W/m^2). The color disappearance was also monitored by a spectrophotometer equipped with an integrated sphere following the dye degradation and the return to the starting color of the substrate. Physiological studies over the years have shown that human eye contains three different types of receptors that respond to short-, mid- and long length light waves. These responses correspond to colors blue, green and red. In the study of color perception, one of the first

mathematically defined color spaces is the CIE 1931 XYZ color space, created by the International Commission on Illumination (CIE) in 1931(CIE 1932) [6]. The CIE XYZ color space was derived from a series of experiments done in the late 1920s [7,8].

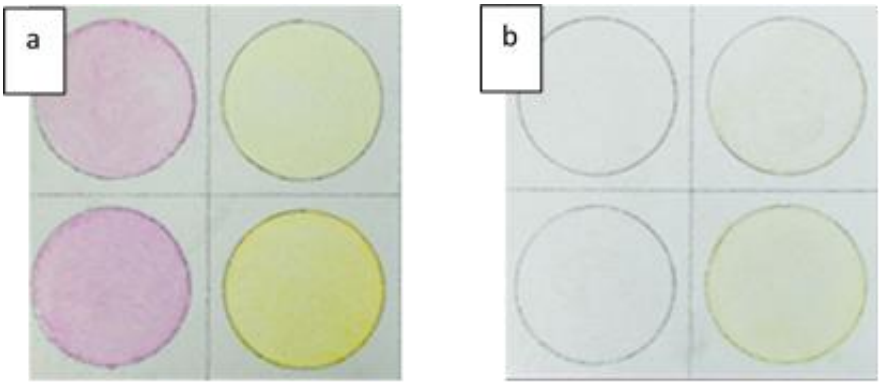

Fig. 6.2. Photoactive tiles dirtied by Rhodamine B and Metanil yellow: a) t = 0; b) t = 10 days; solar irradiation (May 2012, UV-A mean irradiation power: 7.28 W/m^2).

These experimental results were combined into the specification of the CIE RGB color space, from which the CIE XYZ color space was obtained. As the human eye possesses three different types of color sensors that are sensitive to different ranges of wavelengths, a full plot of all visible colors is a three-dimensional figure. The CIE XYZ color space was deliberately designed so that the Y parameter was a measure of the brightness or luminance of a color. The chromaticity of a color was then specified by the two derived parameters x and y, two of the three normalized values which are functions of all three tristimulus values X, Y and Z. Detailed values are reported in **Table 6.3** at both starting time (t=0) and at complete disappearance of the color. Rhodamine B is a less resistant dye than Metanil Yellow and, notwithstanding it was put on the photocatalytic materials tenfold more concentrated than the yellow dye, its degradation is faster.

Metanil Yellow follows a slower degradation process, even if all the substrates exhibit a net self-cleaning action.

Table 6.3. XYZ values for Rhodamine B and Metanil Yellow at the beginning and at the end of the self-cleaning process under the sunlight.

Dye	Time (h)	x	y	z
Rhodamine B	0	0,3248	0,2968	0,3784
	33	0,3218	0,3344	0,3438
Metanil Yellow	0	0,3464	0,3657	0,2879
	107	0,3427	0,3374	0,3012

In particular, WGA shows an efficient self-cleaning action considering that the tiles were irradiated by the sunlight and the UV-A mean value was only 7.28 W/m^2 (corresponding to the sun "power" in May 2012 in the Northern Italy).

6.4 Conclusions

In summary, we highlighted newly industrially prepared materials coated of micro-sized TiO_2 with self-cleaning properties for various applications, such as the removal of organic molecule pollutants. The removal of oleic acid, deposited on porcelain TiO_2 gres slabs, during UV irradiation demonstrates the photocatalytic activity of the concerning material, opening a new way for the application of gres tiles towards the pollution reducing. The pollution degradation of two different organic dyes, directly put at tiles surfaces (Rhodamine B and Metanil Yellow), also

exhibits excellent results confirming the photocatalytic activity of this material.

6.5 References

[1] Fateh R., Ismail A.A., Dillert R., Bahnemann D.W. Highly active crystalline mesoporous TiO_2 films coated onto polycarbonate substrates for self-cleaning applications. *J. Phys. Chem. C* **2011**, *115*, 10405-10411.

[2] Ramirez A.M., De Belie N. Applications of TiO_2 photocatalysis to cementitious materials for self-cleaning purposes. *RILEM State of the Art Reports* **2011**, *5*, 11-15.

[3] Wang Y., Lu L., Yang H., Che Q. Development of high dispersed TiO_2 paste for transparent screen-printable self-cleaning coatings on glass. *J. Nnaopart. Res*. **2013**, *15*, 1384.

[4] Bianchi C.L., Gatto S., Nucci S., Cerrato G., Capucci V. Self-cleaning measurements on tiles manufactured with micro-sized photoactive TiO_2. *Adv. Environm. Res*. **2013**, *2*.

[5] Wanatabe T., Fukayama S., Miyauchi M., Fujishima A., Hashimoto K. Photocatalytic activity and photo-induced wettability conversion of TiO_2 thin film prepared by sol-gel process on a soda-lime glass. *J. Sol-Gel Sci & Tech.* **2000**, *19*, 71-76.

[6] Smith T., Guild J. The C.I.E. colorimetric standards and their use. *Transact. Opt. Soc*. **1931**, *33*(3), 73-134.

[7] Wright W.D. A re-determination of the trichromatic coefficients of the spectral colours. *Transact. Opt. Soc*. **1928,** *30*(4), 141-164.

[8] Guild J. The colorimetric properties of the spectrum. *Philos. Trans. Royal Soc. London, A* **1931**, *230*, 149-187.

Chapter 7

Doping of commercial micro-sized TiO_2

In order to enhance the photoactivity of commercial micro-sized TiO_2, catalysts have been surface doped by both anionic and cationic species. The fluorination of commercial powders perturbs and modifies the surface OH population on the photocatalyst, improving the catalytic efficiency. At the same time surface cation-doping is carried out on the TiO_2 samples with the aim to enhance the photoactivity and to shift the light absorption towards the visible region. Cations like rhenium, tin and tungsten have been used as dopants.

7.1 Introduction

As already mentioned, TiO_2 can still be envisaged as the most active and most suitable semiconductor photocatalyst [1], because it is biologically and chemically inert, photostable and cheap, and has a high oxidation ability, its holes being photogenerated at E_0 = 2.9 V *vs.* NHE at pH 0. However, two major factors limit the photocatalytic efficiency of TiO_2: *i)* its band gap is larger than 3 eV, *i.e.* it mainly absorbs light in the UV region and only a small portion (less than 5%) of the sunlight can be exploited for photocatalytic processes; *ii)* as in all photoexcited semiconductors, photogenerated electron-hole pairs undergo fast recombination in competition with charge transfer to adsorbed species yielding redox reactions. These problems become harder when one thinks about TiO_2 used in the indoor areas where the lighting system is moving towards the total use of LED lamps, which are UV-radiation free. Therefore, several modification methods were developed in order to accelerate the photoconversion and enable the adsorption of the visible light.

Surface fluorination is widely considered as a useful approach for the increase of the photocatalytic performance of nano-sized TiO_2, as suggested by many authors [2-5]. They reported that the photooxidation of VOCs like phenol can be enhanced with F-TiO_2 and proposed that the fluorinated surface favors the generation of free OH radicals (not surface-bound $^{\cdot}OH$), which are responsible for the enhanced oxidation. In the following studies, Choi and co-workers [4] not only confirmed this claim but also showed that hole mediated photocatalytic reactions are inhibited on the contrary because of the hindered adsorption of substrates on F-TiO_2.

In addition, it has been found that F-TiO_2 enhances the remote photocatalytic oxidation at the air/catalyst interface by facilitating the desorption of OH radicals under UV irradiation [6]. In parallel with this, cationic species were used to dope the TiO_2 surface. There has been some research [7,8] that suggests the surface deposition of metal, such as Re, can enhance the electron transfer or the change separation and improve the formation of the free hydroxyl radicals. It was shown that also metal oxides particles can have a positive effect because they support the charge separation and prevent their recombination. Metal oxides, in fact, have been applied to dope TiO_2, among which SnO_2, [9] and WO_3 [10,11], as known by the literature. It has been shown that the photo-oxidation of 1,4-dichlorobenzene was improved by adding WO_3 to the surface of TiO_2 powders. The band-gap energy of WO_3 is 2.8 eV, which falls within the solar spectrum. This combined with its physicochemical properties makes it attractive for photocatalysis research.

In the present research work, different fluorine precursors, among which elemental F_2 and several inorganic salts (NaF, NH_4F and CaF_2), were applied for the surface fluorination of a pure anatase commercial sample (1077 by Kronos) characterized by the complete absence of ultrafine particles. The photocatalytic performances of fluorinated micro-sized TiO_2 were investigated in the photodegradation of both NO_x and VOC in gas phase, as already reported by Bianchi et al. [12]. In parallel with this, catalytic activity was studied by metals doping like rhenium (Re), tin (Sn), and tungsten (W) with the aim to improve even the photooxidation induced by visible light. Therefore, the main target of doping is to reduce band-gap

level and consequently increase the photoactivity of micro-sized TiO_2 catalysts, making them comparable with nanometric samples.

7.2 Experimental section

7.2.1 Deposition method of TiO_2 powders

1077 powder has been doped with cations like rhenium (Re), tin (Sn) and tungsten (W), and fluoride anions (F^-). Nanometric commercial sample P25 by Evonik was used as photocatalytic material. The classical impregnation method was applied to dope the catalyst surface. The W, Sn and Re doped TiO_2 samples were obtained by different deposition procedures. For Sn doping the wet-impregnation was used starting from SnO_2 as precursor. At the end of the impregnation procedure (24 h, room temperature), powder was calcined at 400°C for 4 h and rinsed in distilled water three times. For Re and W surface deposition it was used decoration method using ultra-sounds (US) in aqueous or organic solutions where ceramic or polymer substrate powders are dispersed. In a 100 ml glass flask 0.25 g of $W(CO)_6$ or $Re_2(CO)_{10}$ and 2 g (1 g for the decoration with Re) of TiO_2 1077 are weighted; 100 ml of diphenylmethane are then added and the solution obtained is sonicated at a constant temperature of 80°C for 3 h, with 33.0% amplitude and a 50 Wcm^{-2} intensity. The $W(CO)_6$ solution changed colour from white to brownish. At the end the solution is centrifuged many times to remove all the solvent; the final powder is washed three times with n-pentane and centrifuged again, and one time with pentane and also in this case is centrifuged after washing. The residual

solvent is evaporated and the sample is finally calcined at 480°C for 40 h to completely remove the organic scents. For all the powders the amount of Re, Sn, and W was 1% wt.

NaF, NH_4F and CaF_2 are Fluka Products (purity > 99.9%). Chemicals were used as received without any further purification. Elemental fluorine, F_2, was supplied by Solvay Fluor GmbH in a pre-passivated high pressure cylinder (50 L, at 8 bar). F_2, (Solvay Fluor und Derivate, stored in 50 L cylinder) was expanded in a trap of a metal vacuum line meanwhile the reactor containing the TiO_2 was set under vacuum. The pressure gradient between the trap and the reactor forced F_2 into the reactor. The fluorine reacted 15 min for every addition and after that time, the unreacted portion was pumped away in a soda lime trap. The reactor was maintained at room temperature by a water bath during the additions of F_2 (final sample 3% F_2 on molar basis) [13]. Inorganic fluoride salts were simply dissolved in water and impregnated onto the TiO_2 powder by wet-impregnation: for all the samples the amount of F species was 1% wt. At the end of the impregnation procedure (24 h, room temperature), powders were calcined at 400°C for 4 h and rinsed in distilled water three times.

Fluorinated samples were labelled as reported in the following:

- 1077: blank micro-sized TiO_2 1077 by Kronos;
- 1077_F: micro-sized TiO_2 treated with elemental fluorine, F_2;
- 1077_Na: micro-sized TiO_2 treated with NaF solution;
- 1077_NH_4: micro-sized TiO_2 treated with NH_4F solution;
- 1077_Ca: micro-sized TiO_2 treated with CaF_2 solution;
- P25: blank nano-sized TiO_2 P25 by Degussa.

7.2.2 Photocatalysts characterization

7.2.2.1 Anion-doped TiO_2 powders characterization

The enhancement in photoactivity of a micro-sized TiO_2 was induced by two different surface fluorination techniques: fluorination with elemental fluorine in mild conditions and wet-impregnation of inorganic fluorides followed by calcination.

The physico-chemical characterization of all the fluorinated powders employed (either plain of fluorinated) in the photocatalytic tests was performed (**Table 7.1**).

Table 7.1. Sample features of fluorinated and naked TiO_2 samples.

Samples features.					
Sample	**S.S.A. (m^2 g^{-1})**	**Crystallite Size (nm) (XRD)**	**OH/O_{TOT} (XPS)**	**F/Ti (XPS)**	**M^a/Ti (XPS)**
P25	50	26	0.14	-	-
1077	12	105	0.32	-	-
1077_Na	11	104	0.07	0.18	0.09
1077_NH_4	14	101	0.04	0.21	n.d.[b]
1077_Ca	9	105	0.29	0.74	0.40
1077_F	12	105	0.15	0.32	-

a. counter-ion of the fluoride source; b. not detectable.

Both specific surface area and average crystallites size are very similar (within the experimental error typical of the measurements) to those of the parent TiO_2 matrices employed to obtain all the fluorinated materials, as reported in **Table 7.1** (first and second columns).

The surface chemical composition of the TiO_2 particles was analyzed by XPS. The survey analysis revealed traces of K and P in the 1077 sample

(2.3 at% and 1.8%at, respectively), certainly deriving from the starting reactants of the industrial process. All the dopants, as well as elemental fluorine, introduced F atoms on the surface of the TiO_2 particles (ratio F/Ti in the fifth column of **Table 7.1**). The fluoride precursors also leave small amounts of the counter ions at the samples surfaces (M/Ti ratio in the sixth column of **Table 7.1**). The OH/O_{TOT} surface ratio was also affected by the doping with fluoride precursors: in particular, NaF and NH_4F significantly reduced the OH content, elemental F_2 approximately halved it and CaF_2 let it almost unchanged. The OH/O_{TOT} surface ratio measures TiO_2 wettability and it allows predicting how the TiO_2 photocatalytic surface can perform towards hydrophilic/hydrophobic molecular targets. HR-XPS analysis in the Ti 2p region clarified the different behaviors of dopants on 1077 (see **Fig. 7.1**): NaF generated titanium(IV)-based partially fluorinated species (Ti(IV)–F) as revealed by the comparison of the intense signal at approximately 460 eV. On the contrary, the doping with CaF_2 did not influence the signals in the Ti 2p region, which remained the same of 1077. Thus, it can be assumed that CaF_2 was simply intercalated in the TiO_2 particles without any evident bonding between F and Ti, probably because of the strength of $Ca^{2+}(F^-)_2$ ionic bond, avoiding the stabilization of F ions in the vicinity of Ti^{4+} cations and the limitation of charge carriers in such ionic compounds as reported by Tressaud et al. [14]. The treatment with elemental F_2 altered the TiO_2 particles and two signals due to fluorinated and highly fluorinated species, such as TiF_4 and $TiF_6^{=}$, appeared at 461 and 462 eV, respectively. If we focus our attention on the structure of the various plain and fluorinated materials, few comments are necessary.

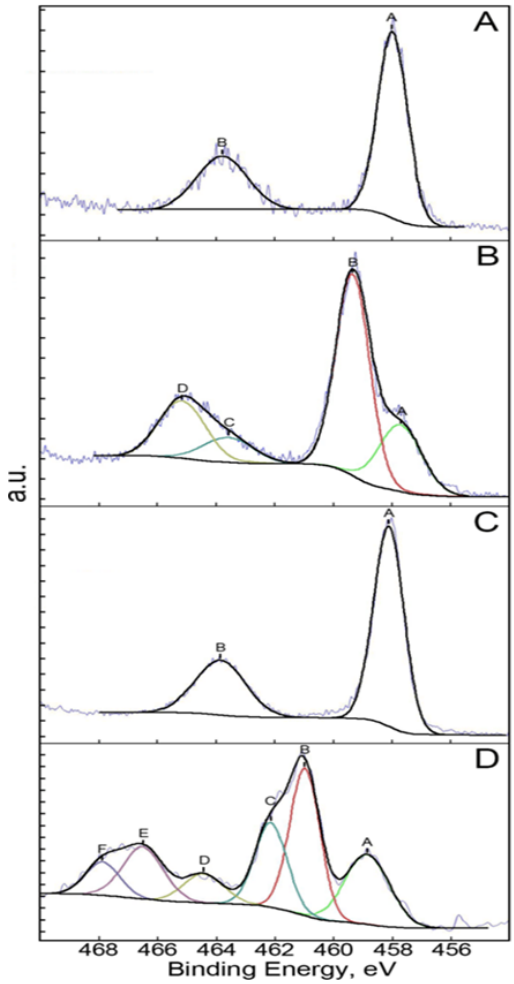

Fig. 7.1. Ti 2p XPS spectra of Kronos samples: (A) plain 1077; (B) 1077_Na; (C) 1077_Ca; (D) 1077_F.

Fig. 7.2 reports the XRD patterns relative to all TiO_2-based samples. In the case of the P25 matrix, the parent oxide exhibits the typical "anatase and rutile" XRD peaks, marked with either + or ▲ symbols, respectively, in section a of **Fig. 7.2**, whereas after the treatment with NaF, the presence of new peaks is evident in the diffractogram (see the ● symbols). The analysis

of these newly formed peaks indicate a specific NaF crystalline phase, known as villiaumite [ICDD card: 00-001-1184].

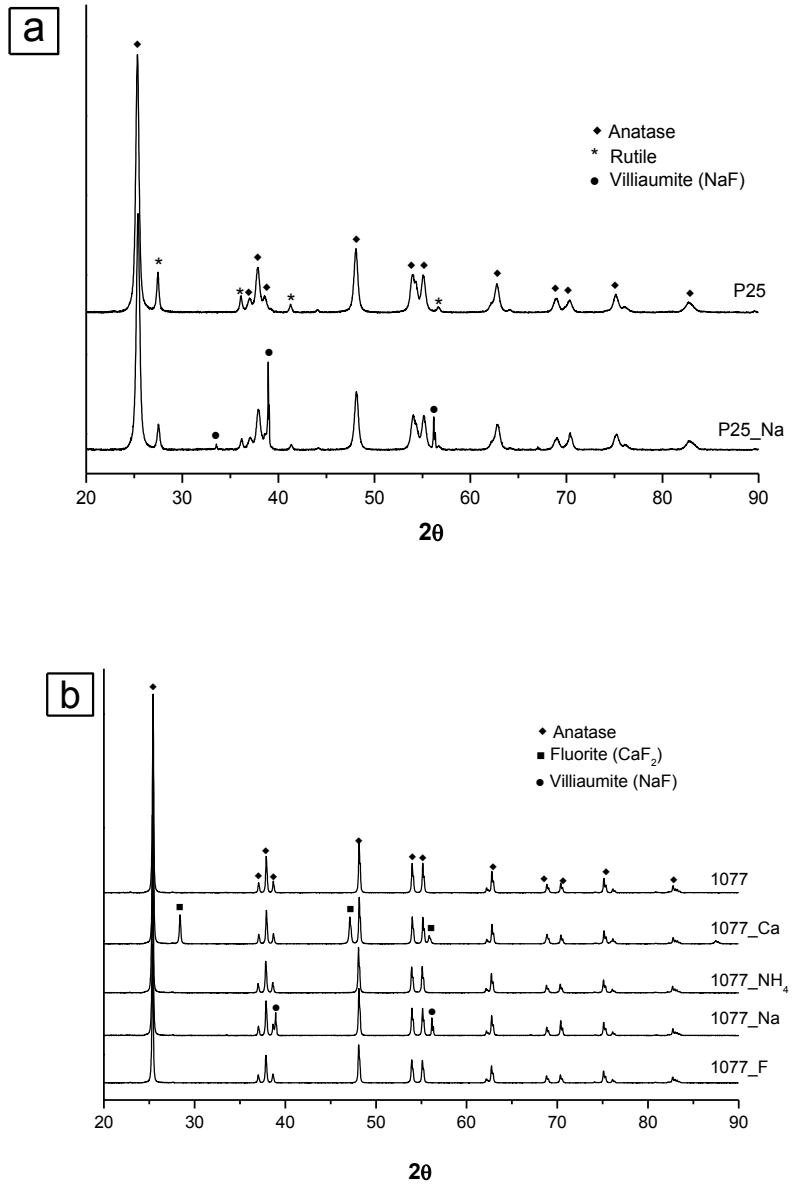

7.2. XRD patterns of the various TiO_2-based samples. Section a: P25-based materials; section b: 1077-based materials.

In the case of the 1077-based family (see section b in **Fig. 7.2**), for the parent TiO_2 only the anatase phase is observed: on the other hand, when the fluorination procedure has been carried out with CaF_2, the typical peaks relative to fluorite CaF_2 (see the ■ symbols; ICDD card: 00-002-1305] are observable, whereas no extra peaks are evident when the treatment has been carried out with NH_4F. When the fluorinating agent is NaF, a new NaF phase (villiaumite) is again evident (see the ● symbols).

As for what it may concern the morphology of the various materials investigated by means of HR-TEM microscopy, interesting results are obtained by fluorine doping of either P25 (**Fig. 7.3**) or 1077 (**Fig. 7.3**) samples.

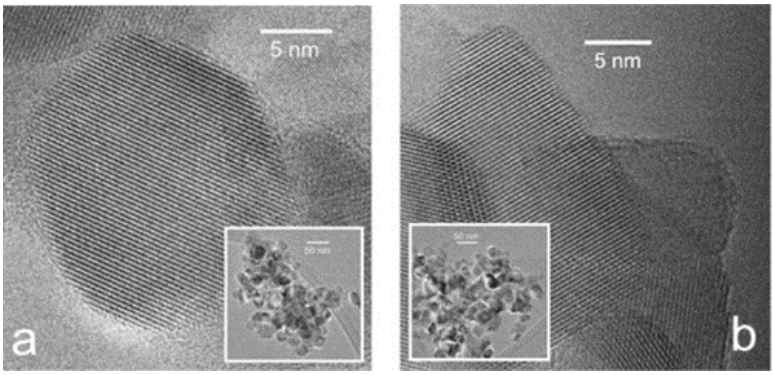

Fig. 7.3. HR-TEM images of P25 samples: (a) plain P25; (b) P25_Na.

The general features of the materials are retained (i.e., crystallites dimensions and crystalline phase) on both anatase and rutile samples, but the external habit of the various TiO_2 particles has somewhat changed: in particular, as for the P25 systems, the most effective doping agent seems to be NaF, whereas a few changes are evident for the corresponding 1077 powder for which the most relevant effects are obtained using NH_4F. In particular, it can be evidenced that for P25 the doping by fluorine results in

a general loss of the smoothed character of the external part of the crystallites, remaining unaltered the dimensions of the particles (see section b in **Fig. 7.3**) [12].

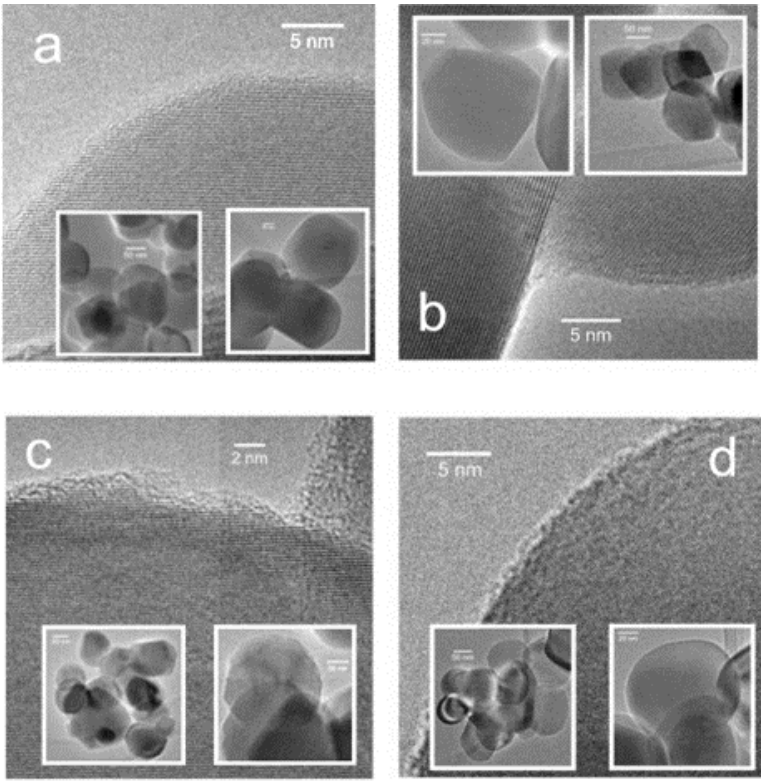

Fig. 7.4. HR-TEM images of 1077 samples: (a) plain 1077 Kronos; (b) 1077_Na; (c) 1077_NH4; (d) 1077_Ca.

On the other hand, in the case of 1077, this effect is less pronounced, being observable only in the case of doping by NH_4F (see section c in **Fig. 7.4**). The morphological features evidenced in the HR-TEM images are paralleled by the FT-IR spectral patterns relative to the various samples (ν_{OH} region). For both P25 and 1077 systems, important changes are evident after the

fluorination doping procedure (see **Fig. 7.5**, sections a and b). In particular, it can be observed that:

• in the case of P25, at least two families of surface OH groups, among those typical of this TiO_2 system, are almost completely "leached out", leaving free only the high ν component, with the parallel formation of a huge amount of OH groups interacting by H-bonding (broad tail in the 3500-3000 cm^{-1} range): this is in line of what reported in the literature for this reference samples [15];

• in the case of 1077, different trends are evident: (i) an almost total "leaching" of the OH groups in the case of both NaF and NH_4F agents; (ii) an increasing of the OH groups interacting by H-bonding in the case of F_2 fluorination; (iii) the formation of different families of free OH groups involving Ca^{2+} ions, with ν ~ 3740 cm^{-1} and also in the envelope at ν ~ 3600-3620 cm^{-1} (this is consistent with what reported in the literature for different oxidic systems containing Ca species [16] with a parallel huge increasing of OH groups interacting by H-bonding in the case of CaF_2.

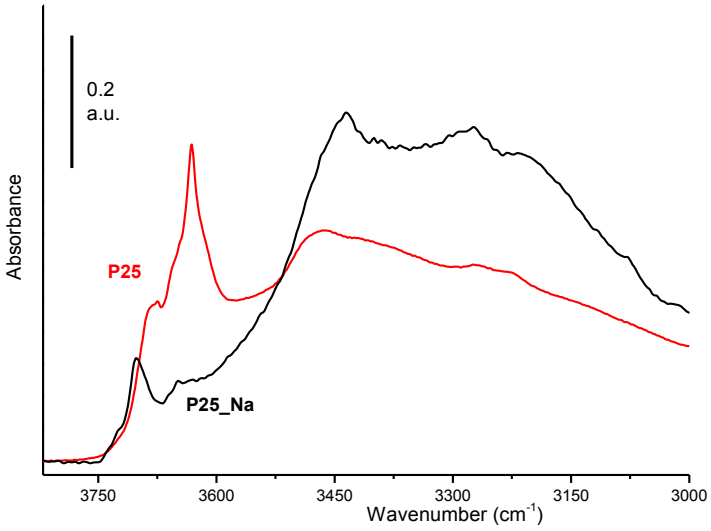

Fig. 7.5a. Spectral patterns relative to plain P25 and P25_Na.

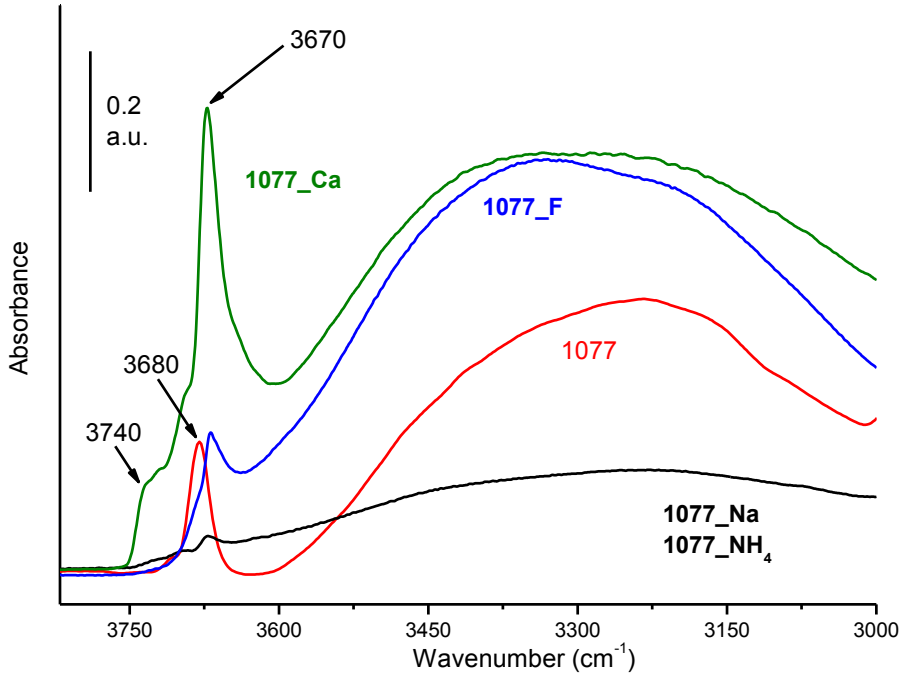

Fig. 7.5b. Spectral patterns relative to either plain or fluorinated 1077 samples.

7.2.2.2 Cation-doped TiO_2 powders characterization

The doping with noble metal cations (Re, Sn, and W) were prepared starting from the following precursors without further purification; they are SnO_2 (≥99.9 Sigma Aldrich), $Re_2(CO)_{10}$ (≥99.9 Sigma Aldrich) and $W(CO)_6$ (≥99.9 Sigma Aldrich). The doping effect was obtained in mild conditions and wet-impregnation followed by calcination.

XRD patterns relative to all TiO_2-doped samples (Re, Sn and W) show the only anatase phase, typical for 1077 sample. The impregnation method does not affect the structural properties of 1007. All the XRD patterns exhibit the presence of the peaks characteristic of the anatase phase.

As for what concerns the morphological aspect, there are not significant differences in the crystallites size. The dimensions remain unchanged and it is not visible noble metal particles, as it is reported in **Fig. 7.6**, as illustrative example.

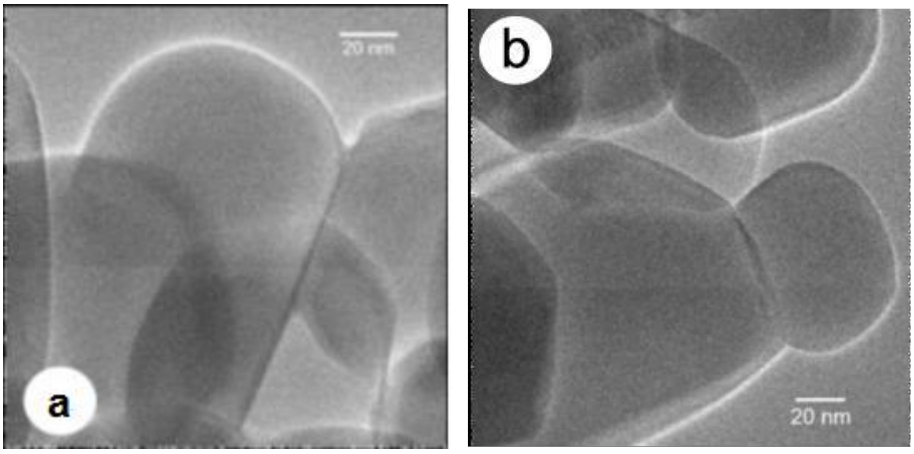

Fig. 7.6. Low magnification TEM images of 1077_W (a) and 1077_Re (b).

It is evident the only micrometric anatase TiO_2, maintaining the external habit of the 1077 powder: all doped samples exhibit the main morphological

features typical of the parent 1077 sample, i.e. well ordered TiO_2 crystallites with almost unchanged average dimensions, in agreement with XRD results. It was possible to evaluate the OH/O ratio for each decorated sample by means of the oxygen high-resolution spectra. The analysis of the surface hydroxyl groups was performed by collecting FT-IR spectra after prolonged outgassing at room temperature in order to remove physisorbed molecular water. The spectra of samples prepared with Re and W showed the typical peak related to the stretching mode of free hydroxyl groups of 1077 at 3670 cm^{-1}. The values measured by XPS analysis were 0.51 for 1077_W and 0.26 for 1077_Re. It was highlighted the presence of the metal species on the 1077 surface. In particular, their oxidation state was in form of oxide.

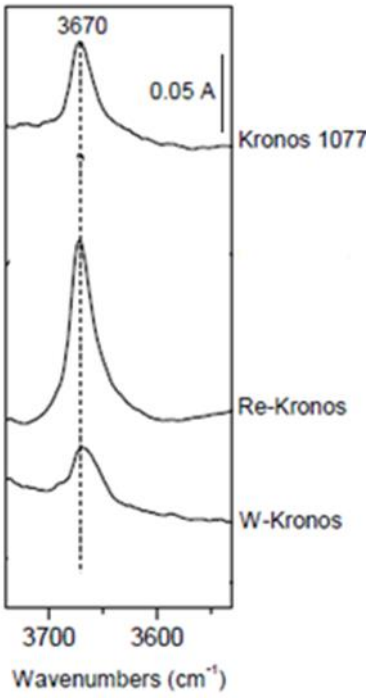

Fig. 7.7. FT.IR spectra of 1077, 1077_Re and 1077_W collected at room temperature (RT) after prolonged outgassing at RT.

7.3 Results and discussions

7.3.1 Fluorinated TiO_2

As expected, we have to state that nano-sized materials are definitively more active if compared to micro-sized TiO_2 (see **Table 7.2** for a comparison between nano-sized commercial P25 by Evonik and micro-sized commercial 1077 by Kronos in the photodegradation of NO_x, acetone and toluene).

Table 7.2. Photocatalytic degradation results of fluorinated TiO_2 powders.

Sample	NOx (% after 1h)	Acetone (% after 1h)	Toluene (% after 6h)
P25	90	99	52
P25_Na	94	54	99
1077	88	87	46
1077_Na	91	51	67
1077_NH_4	93	44	44
1077_Ca	94	96	49
1077_F	94	89	45

If we inspect in more detail these results, it is possible to observe that, depending on the pollutant to degrade, the various samples exhibit different behaviors. As for NO_x, the surface doping always leads to an increase of the photoactivity of the samples, bringing the micro-sized sample at the same level of P25. On the other hand, conflicting results are exhibited in the case of VOCs, acetone or toluene, as shown in a previous work [12]. In the **Fig.**

7.8 it is reported a comparison between P25 and 1077 samples, in both cases, naked and fluorinated with NaF. The photocatalytic activity resulted to be considerably increased in both cases; it is achieved, in fact, the almost complete degradation of toluene for P25_NaF, leading to an improvement respect to the naked one. In addition, the photoefficiency of 1077_NaF was 70% after 6 hours of kinetic, resulting to be more photoactive than the naked P25 one, which was only 51% at the end of the photoirradiation. For what concerns the pollutant mineralization into carbon dioxide and water, the photoactivity resulted increased. The 1077_NaF led to the 48% of final CO_2 production, whereas the P25_NaF even to the 88%. Therefore, it has to be assert that the doping with fluoride ions increase meaning fully the pollutant photoabatement and the mineralization.

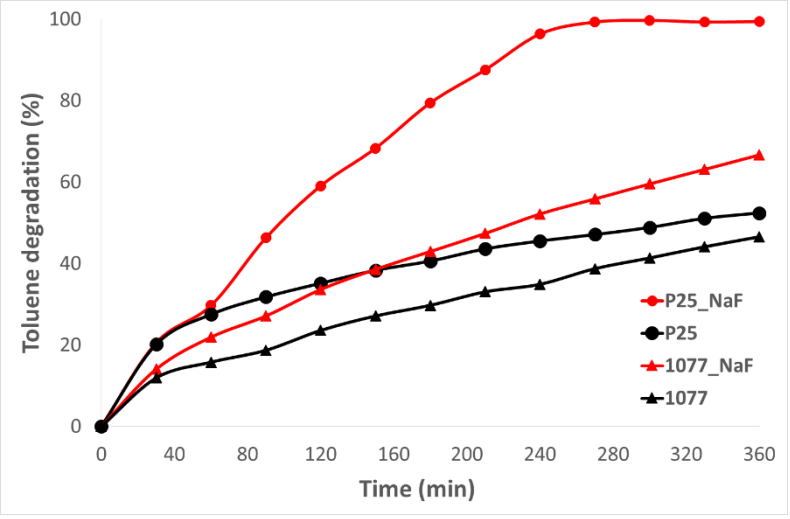

Fig. 7.8. Toluene degradation for both micro- (1077) and nano-sized (P25) TiO_2 samples, naked and fluorinated (NaF precursor).

The simple surface fluorination seems to be a good method to increase photoactivity in commercial TiO_2 samples, even with large crystallites. However, the choice of the dopant agent has a fundamental role to enhance

or to limit the photoactivity towards a particular kind of pollutant molecule. Physico-chemical characterization demonstrates that the surface fluorination seems to have an active role in making a sort of selection among all the surface OH groups, leaving free only some particular OH "families", probably the more active in the photocatalytic process.

Thus, the driving force of the process is both the presence of active OH population and the efficient adsorption of the pollutant molecule at the semi-conductor surface that promotes the photocatalytic reaction. In fact, the adsorption of NO_x, acetone/acetaldehyde or toluene on TiO_2 surface has been demonstrated to be a crucial point in affecting the subsequent photocatalytic activity. Moreover, the surface fluorination seems to perturb much more the surface OH population and, as a consequence, the final performance of the material. The precise choice of the fluorination precursors together with the physico-chemical properties of the molecules to degrade bring to have a very efficient photocatalytic process, apart from the TiO_2 crystallites size.

7.3.2 Noble metals particles doped TiO_2

To investigate the influence of the noble metals particles on the photocatalytic activity of commercial micro-sized TiO_2, the photocatalytic degradation of both VOCs and NO_x was analyzed. The photocatalytic performances of doped TiO_2 with Re, Sn and W particles was compared with naked 1077 powders, chosen as the reference micrometric catalyst.

Fig. 7.9 shows the photocatalytic degradation curves of NO_x on Sn- and W-TiO_2 (1077) under UV light irradiation. The degradation rate of NO_x on noble metals doped TiO_2 was higher than 1077 without doping effect.

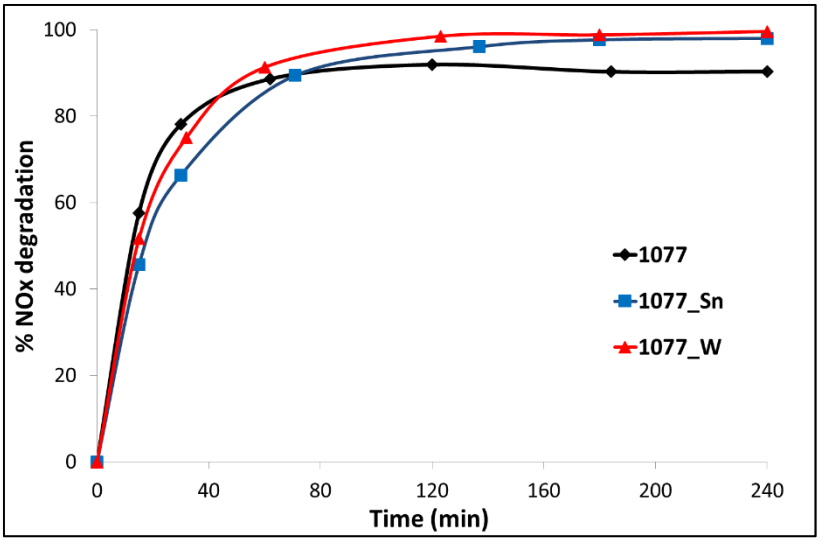

Fig. 7.9. NO_x photodegradation of 1077 and noble metals (Sn, W) doped 1077 powders under UV irradiation.

As we can observe, all doped TiO_2 samples exhibited the higher photocatalytic activity compared with naked micro-sized TiO_2. The presence of the metals gives good improvement for the NO_x abatement: more interesting study is to investigate the effect on the VOCs molecules of more complex structure. Thus, the same study was conducted for toluene and acetone degradation. As shown in **Fig. 7.10**, in case of the toluene degradation, apparently, the species put on the surface by the impregnation method did not increase the photocatalytic activity of the material; but they affected the byoproducts conversion into CO_2, so the doped surface acted on the byoproducts, showing its concrete help in the degradation of the

pollutant (**Fig. 7.11**). In particular, Re-doped 1077 sample showed the highest CO_2 formation.

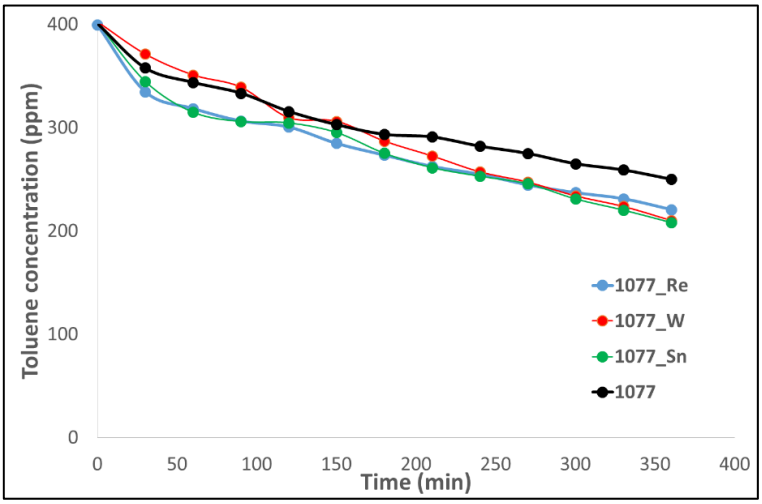

Fig. 7.10. Toluene photodegradation of 1077 and noble metals (Re, Sn, W) doped 1077 powders under UV irradiation.

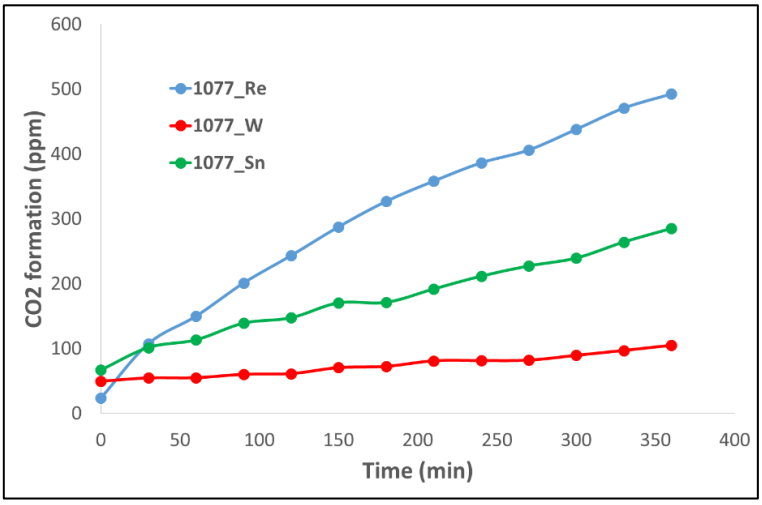

Fig. 7.11. CO_2 formation during the toluene photodegradation using 1077-doped under UV irradiation.

The tests on the acetone photodegradation were performed both with the UV lamp (**Fig. 7.12**) and the LED lamp (**Fig. 7.13**).

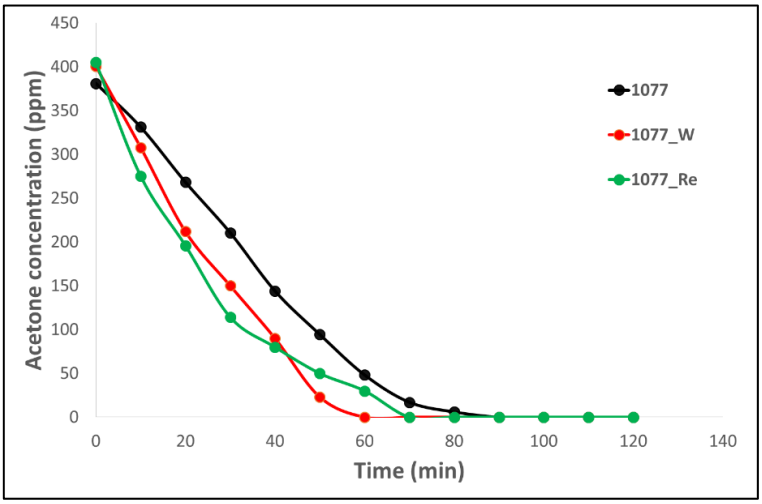

Fig. 7.12. Acetone photodegradation in gas-phase under UV light.

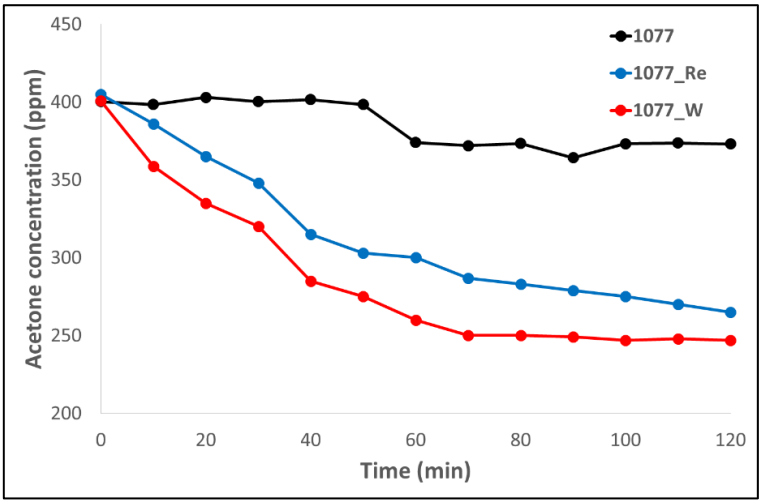

Fig. 7.13. Acetone photodegradation in gas-phase under visible light (performed with a LED lamp).

In case of acetone degradation, the effects of the surface doping can already be seen directly on the degradation kinetic of the molecule, where the

performances had definitely improved compared to Kronos 1077 results, in particular for W-containing sample. The presence of the tungsten oxide (WO_3) was confirmed in particular by the XPS analysis; moreover, in the TEM images it is possible to see that a thin film covers the 1077 surface, and it is tungsten oxide. Also the IR spectrum complied with this last information because the lower OH peak compared to 1077 is maybe due to the coating effect of tungsten oxide. All these concepts supported the good results in the photodegradation tests because WO_3 is a semiconductor with known photocatalytic activity [17,18] and in this case it plays an important role in the degradation of the pollutant, justifying its effects. At least, using the LED lamp, without any UV radiation, it is clear that W and Re addition onto the TiO_2 surface plays a crucial role in the activation of the catalyst under the visible light. In fact, the bare TiO_2 is not able to work under visible light, because of the band gap of the TiO_2, which needs higher energy as delivered by the UV light. The most apparent characteristic that could be related to the good activity of 1077_Re is the presence of a significant amount of free hydroxyl radicals, confirmed by the peak in the IR spectrum. If we take into consideration the chemical activity of the metal oxides themselves, the main concepts useful to explain the decorated TiO_2 behavior are the following: firstly, the presence of the metal oxides increases the "antenna effect"; the species on the TiO_2 surface are able to capture the electrons of the visible light, making them usable in the redox reactions that occur upon the surface. Secondly, it was shown that species like metal or metal oxides are able to act as an electron trap, reducing the electron-hole recombination rate [19]. The particle on the semiconductor

surface can act as much as electrons trap as holes trap, and the immediate effect is a better electron-hole separation.

Thus, the visible-light activity of the samples prepared with tungsten or rhenium gave good results: regarding the WO_3, with a band gap of 2.8 eV, it is able to absorb some portion of the visible light and it can be considered an optimal sensitizer [20].

7.4 Conclusions

In this Chapter it is observable that F-TiO_2 can enhances photooxidation activities because the generation of OH radicals is favored on the fluorinated surface. Such enhanced photooxidation activities were previously observed in aqueous environment [21-23], but not in the gaseous photocatalytic reaction systems. This study is conducted in gas phase with NO_x and VOCs pollutants, demonstrating that the surface fluorination of TiO_2 also enhances the photodegradation kinetics at the solid/air interface by investigating and comparing the photoefficiency of pollutants on naked micro-sized 1077 TiO_2 and F-1077 catalysts. The photodegradation kinetics are faster with fluorination doping. Thus, micro-sized 1077_F have the improved photocatalytic activity respect to the bare micrometric TiO_2, becoming highly competitive with nanometric TiO_2 catalyst.

On the other hand, the study conducted with cationic metals highlight that the doping with metals such as Re, Sn and W can increase the photoactivity in gas phase of TiO_2. Therefore, after UV light irradiation, the organic pollutants are decomposed. Parallel with this study, the LED

irradiation is used to investigate their photoefficiency using only the visible light. The most interesting species loaded on the TiO_2 surface are the Re and W because they have the best performances in terms of degradation of VOCs. They play a favorable role in the enhancement of photocatalytic activity by attracting electrons, thus helping electron–hole pair separation and preventing electron–hole recombination. Consequently, it is highly advantageous to add Re or W to titania photocatalysts, especially for the use of visible irradiation, because of their light absorption property.

7.5 References

[1] Chen X., Mao S.S. Titanium dioxide nanomaterials: synthesis, properties, modifications, and applications. *Chem. Rev*. **2007**, *107*, 2891-2959.

[2] Maurino V., Minero C., Pelizetti E., Serpone N. in: Phototransformations of Atrazine Over Different Metal Oxide Particles, in E. Pelizetti (Ed.); Fine particles science and technology - From micro to nanoparticles, NATO ASI Series, *Kluwer Academic Publishers*, Dordrecht, **1996**, *12*, 707-718.

[3] Park J.S., Choi W. Enhanced remote photocatalytic oxidation on surface-fluorinated TiO_2. *Langmuir* 2004, *20*, 11523-11527.

[4] Kim H., Choi W. Effects of surface fluorination of TiO_2 on photocatalytic oxidation of gaseous acetaldehyde. *Appl. Catal. B: Environ.* **2007**, *69*, 127-132.

[5] Dozzi M.V., Selli E. Effects of phase composition and surface area on the photocatalytic paths on fluorinated titania. *Catal. Today* **2013**, *206*, 26-31.

[6] Park J.S., Choi W. Remote photocatalytic oxidation mediated by active oxygen species penetrating and diffusing through polymer membrane over surface fluorinated TiO_2. *Chem. Lett*. **2005**, *34*, 1630-1631.

[7] Sobana N., Muruganadham M., Swaminathan M. Nano-Ag particles doped TiO_2 for efficient photodegradation of direct azo dyes. *J. Molec. Catal. A: Chem*. **2006**, *258*, 124-132.

[8] Choi J., Park H., Hoffmann M.R. Effects of single metal-ion doping on the visible-light photoreactivity of TiO_2. *J. Phys. Chem. C*. **2010**, *114*, 783-792.
[9] Umebayashi T., Yamaki T. Itoh H., Assai K. Band gap narrowing of titanium dioxide by sulfur doping. *App. Phys. Lett*. **2009**, *81*, 454-456.
[10] Couselo N., Einschlag F.S.G., Candal R.J., Jobbagy M. Tungsten-doped TiO_2 vs pure TiO_2 photocatalysts: effects on photobleaching kinetics and mechanism. *J. Phys. Chem. C*. **2008**, *112*, 1094-1100.
[11] Zhao D., Chen C., Yu C., Ma W., Zhao J. Photoinduced electron storage in WO_3/TiO_2 nanohybrid material in the presence of oxygen and postirradiated reduction of heavy metal ions. *J. Phys. Chem. C* **2009**, *113*, 13160-13165.
[12] Bianchi C.L., Cerrato G., Crocellà V., Gatto S., Pirola C., Stucchi M., Sansotera M., Capucci V. Photoactivity enhancement of commercial micro-sized TiO_2 induced by surface fluorinations. submitted to *J. Photochem. Photobiol. A: Chem*. **2014**.
[13] Venturini F., Sansotera M., Navarrini W. Recent developments in the chemistry of organic perfluoro hypofluorite. *J. Fluorine Chem*. **2013**, *155*, 2-20.
[14] Demourgues A., Penin N., Durand E., Weill F., Dam-bournet D., Viadere N., Tressaud A. *Chem. Mater*. **2009**, *21*, 1275-1283.
[15] Minero C., Bedini A., Maurino V. Glycerol as a probe molecule to uncover oxidation mechanism in photocatalysis. *Appl. Cat. B: Env*. **2012**, *128*, 135-143.
[16] Liu Y., Xie C., Li H., Chen H., Zou T., Zeng D. Improvement of gaseous pollutant photocatalysis with WO_3/TiO_2 heterojunctional-electrical layered system. *J. Hazard. Mater*. **2011**, *196*, 52–58.
[17] Carcel R.A., Andronic L., Duta A. Photocatalytic activity and stability of TiO_2 and WO_3 thin films. *Mater. Character*. **2012** *70*, 68-73.
[18] Pulido Meliána E., González Díaza O., Do˜na Rodrígueza J.M., Colónb G., Navíob J.A., Macíasb M., Pérez Pe˜naa J. Effect of deposition of silver on structural characteristics and photoactivity of TiO_2-based photocatalysts. *App. Catal. B: Environm*. **2012**, *127*, 112-120.
[19] Kubacka A., Mun oz-Batista M.J., Ferrer M., Fernández-García M. *Appl. Catal. B:Environm.* **2013**, *140*, 680–690.
[20] Shamaila S., Sajjad A.K.L., Chen F., Zhang J. WO_3/BiOCl, a novel heterojunction as visible light photocatalyst. *J. Colloid Int. Sci*. **2011**, *356*, 465–472.
[21] Minero C., Mariella G., Maurino V., Vione D., Pelizzetti E. Photocatalytic transformation of organic compounds in the presence of inorganic ions. 2.

Competitive reactions of phenol and alcohols on a titanium dioxide−fluoride system. *Langmuir* **2000**, *16*, 8964-8972.

[22] Park H., Choi W. Effects of TiO_2 surface fluorination on photocatalytic reactions and photoelectrochemical behaviors. *J. Phys. Chem. B* **2004**, *108*, 4086-4093.

[23] Ryu J., Choi W. Effects of TiO_2 surface modifications on photocatalytic oxidation of arsenite: The role of superoxides. *Environ. Sci. Technol*. **2004**, *38*, 2928-2933.

Chapter 8

Conclusions

The application of heterogeneous semiconductor titanium dioxide (TiO_2) photocatalysis for environmental applications, especially in the photodegradation of organic pollutants in air and aqueous suspensions, is a well-defined and proven technology. TiO_2 nanoparticles are even manufactured in large quantities for the use of commercial applications including pigment and cosmetic products. However, one of the key technical problems is the difficult in post-separation of the fine TiO_2 nanopowders, like P25 (i.e. 20-40 nm), widely used in this advanced technology. Ultrafine particles size presents various operational issues associated to recover them after the kinetic treatment. In the last period, in fact, a growing attention is directed to the possible risks towards the human safety as our tissues are not able to recognize crystallites of so small, which can penetrate into the human body either from skin or directly by breathing.

This PhD study focused on the using micro-sized TiO_2 powders for the photodegradation of pollutants molecules in both gas- and liquid-phases. The chosen molecules were nitrogen oxides (NO_x) and Volatile Organic Compounds (VOC_s) as the major contributors of indoor and outdoor pollution. Together to these, it has been evaluated the photodegradation of textile dyes and surfactants, like PFOA, for the water waste treatment. Parallel to the micrometric powders, the performances of building materials constituted of larger size TiO_2 were tested, opening a new generation of materials intrinsically safer than the traditional photocatalytic products. Because of the lower surface area of the micrometric powders and, consequently of the reduced photoefficiency in respect to the nanopowders one, finally it was performed the adding of anionic or cationic species on the

powders surface by the impregnation method with the aim to improve the photocatalytic activity.

Photocatalytic activity of micro-sized TiO_2: effects of the particles size and morphology

The crystallites size of commercial pigmentary micrometric TiO_2 powders, chosen for the photodegradation kinetics, possess smooth edges and average diameter size in the 95-180 nm range, with fringe patterns belonging to the anatase polymorph. The crystallites size confirms their micro-sized nature reflected in the surface area that are about 11-12 $m^2\ g^{-1}$. The pigmentary powders of micrometric powders studied for the evaluation of their photoactivity were 1007 (by Kronos), AH-R (by Hundsman), AT-1 (by Crystal), AZ and AN (Hombitam) and N.10 (by HombiKat). On the contrary, nanometric powders, which are P25 and PC105, have crystallites size lower than 30 nm and high surface area (50-80 $m^2\ g^{-1}$). These features agree very well with the indication coming from TEM and SEM investigations, confirming the presence of ultrafine particles.

As mentioned above, NO_x and VOCs were tested with both micrometric and nanometric TiO_2 powders. In a first phase of the study two different concentrations of NO_x were used (1000 and 200 ppb) with the aim to evaluate the influence of the amount of pollutant on the kinetic run. In a second moment the concentration of NO_x, on which the comparison was made among all pigmentary TiO_2 powders, was 1000 ppb in order to follow the same pollutant concentration requested by the ISO 22197-1 rules. All micrometric powders, even though they are sold as not photocatalytic

materials, showed good results, compared with the nanometric powders. The photodegradation tests lasted 3 hours and, at the end of the kinetic, the NO_x degradation was fully completed. In particular, the best micro-sized catalysts were identified during the first hour of the degradation. Through the analysis in the first 30 and 60 min of photo-reaction, 1077, AZ and AN powders showed the best photocatalytic performance, resulting in to the fastest photodegradation. This is confirmed by the high presence of OH groups, responsible for the good photoactivity, as evidenced by the XPS analysis (OH/O ratio). The micrometric samples with the best photocatalytic performances were the ones showing the largest OH components, the following 1007, Hombitam AZ and Hombitam AN.

Regarding VOCs degradation, acetone, acetaldehyde and toluene, chosen as reference molecules, were abated in the same way using both nano- and micro-sized TiO_2 catalysts. The initial acetone and acetaldehyde concentrations (1000 ppb) were fully converted into CO_2 within two hours for all kinds of powders. The mineralization for toluene was instead not complete, because of the complexity of the molecule. However, the main feature resulted the comparison between nano and micro-sized TiO_2 performances: both showed almost the same photoefficiency.

Photocatalytic activity of porcelain gres tiles based on micro-sized TiO_2

The second aspect of this PhD thesis is focused on the application of TiO_2 to the building materials in order to obtain various properties: self-cleaning effects, retardation of natural surface ageing as well as air pollution mitigation. The building materials, which are taken into account, are

porcelain gras tiles containing micrometric TiO_2 powder mixed with SiO_2. The presence of TiO_2 was confirmed by TEM images that evidenced the large dimensions of the particles beside rather smooth edges. This aspect was evidenced even by XPS analysis revealing the classical Ti2p doublet attributed to Ti^{4+} with a Ti/Si ratio of 0.20.

The NO_x photodegradation using porcelain gres tiles was performed in two different conditions: static and continuous flow. In both cases micro-sized TiO_2 tiles showed good catalytic response. The optimal concentration for a complete degradation of NO_x within 3 hours resulted 200 ppb, which corresponds to the alert threshold, as established by the Directive 2008/50/EC of the European Parliament, stating the guidelines for the protection of the human health. However, these porcelain gres tiles showed good photoactivity also starting from higher pollutant concentration, such as 600, 1000 ppb. The required time to a complete abatement was longer; the nitrogen oxides were photodegraded in the range 80-60 % within 6 hours. The pollutant concentration influenced the kinetic run; nevertheless, the photocatalytic process occured on the porcelain gres tiles containing micro-sized TiO_2, confirming their photoafficiency. In continuous flow condition it was calculated the contact time (reciprocal to spatial velocity) for each flow rate tested, allowing the assessment of the time for which the pollutant remained in contact with the sample. The results revealed that the micrometric TiO_2 tile is always photocatalytically active in the NO_x degradation. The best pollutant gas flow was 4.2 L h^{-1}, i.e. its efficiency was increased by reducing the flow rate. In fact, it was clear that it's important a quite long contact time between the photoactive part of the material and the pollutant (NO_x). The higher NO_x abatement was due to the surface of active

sites on the tile surface: if the velocity of the gas (contact time) is too fast (180 L h^{-1}), the adsoprption of the pollutant molecules at the sample surface cannot occur, so preventing the photocatalytic process. For this reason, the highest degradation was obtained at 4.2 L h^{-1} flow.

Another studied property typical of photoactive building materials was the self-cleaning effect. The test, performed depositing a molecule (oleic acid) on the tile surface, confirmed the phocatalytic performance of the building sample. Water contact angle (CA) formed on pure oleic acid was quite high (65°): during the test (it lasts an average of 76 hours) the CA continued decreasing until it stabilized at the value that the material presented at the beginning of the test (about 30°), before the deposition of the molecule on its surface. It is worth to note that in the case of materials without any photocatalytic properties, i.e. not containing TiO_2, the contact angle of pure oleic acid did not change during the entire length of the test confirming the non-decomposition of the polluting molecule.

Photocatalytic activity of micro-sized doped powders: effects of the anions and cations on the TiO_2 surface

In the last part of the thesis, the effect of anionic species, like fluoride ions, and of metals, such as Re, W and Sn, on the commercial micro-sized 1077 powder was investigated in both NO_x and VOCs photodegradation.

The photoactivity results obtained in NO_x and toluene degradation with fluorinated samples demonstrated that the photoefficiency depends on both the fluorinated precursor and the kind of pollutant (NO_x, VOCs).

Nevertheless, the fluorination seems to be a good method to the improvement of the photoefficiency of the micro-sized doped-TiO_2 samples. This feature was validated also by the I.R. analysis, which highlighted the different distribution of OH groups depending on the fluorinated precursors. The surface fluorination seems to have an active role in making a sort of selection among all the surface OH groups, probably leaving free the more active in the photocatalytic process. Thus, the driving force of the process is both the presence of active OH population and the efficient adsorption of the pollutant molecule at the semiconductor surface that promotes the photocatalytic reaction.

Very interesting effect was shown by the metals surface deposition. The best results were obtained by the W and Re doped TiO_2. The photodegradation resulted clearly improved when the LED irradiation was used. Through the innovations introduced by sonochemistry, it was possible to obtain this new type of surface decoration of a pigmentary micro-TiO_2, proving that this modification method can improve the photocatalytic activity of the material, in particular under the visible light, where pure TiO_2 is not an effective photocatalyst. The presence of different metal (oxide) nanoparticles on the micro-sized TiO_2 surface leads to the activation of the catalyst under visible light irradiation (LED lamp). This result get a very interesting product useful for the pollutants abatement and the consequent improvement of the air quality.

Final remarks

Heterogeneous photocatalysis is a potential solution that has been the object of intense research efforts since the early 1970s, when Fujishima and Honda discovered the photocatalytic splitting of water on TiO_2 electrodes. This technique can be envisaged as one of the most promising Advanced Oxidation Process (AOPs) because of its specific advantages, such as photooxidation of organic pollutants and their mineralization. Nanopowders of TiO_2 were always considered and used as high efficient photocatalysts, since many years. However, in the recent years the papers publication about the effects, which nanoparticles may have on the human health, is increased. The research and the work made for the environmental depollution are enormous, due to the increased contamination associated to the vehicles traffic, industry emissions, waste water. For this reason, the attention is focused on the use of micrometric TiO_2 powders with the aim to reduce health problems associated to the difficult recovery and consequently to the inhalation typical of nanoparticles. The results concern the micrometric commercial powders, evaluating them in photocatalytic reactions. In parallel with this, porcelain gres tiles containing micrometric TiO_2 were tested for the pollutants photodegradation, changing different parameters and experimental conditions, on the strength of urban conditions, to whom they are exposed.

Publications and Communications

List of Publications

- Bianchi C.L., Pirola C., **Gatto S.**, Nucci S., Minguzzi A., Cerrato G., New surface properties in porcelain gres tiles with a look to human and environmental safety. *Avd. Mat. Science Engin*., **2012**, *2012*, 1-8.
- Bianchi C.L., **Gatto S.**, Pirola C., Scavini M., Vitali S., Capucci V., Micro-TiO_2 as a starting material for new photocatalytic tiles. *Cem. Conc. Compos*. **2013**, *36*, 116-120.
- Pirola C., Bianchi C.L., **Gatto S.**, Ardizzone S., Cappelletti G., Pressurized photo-reactor for the degradation of the scarcely biodegradable DPC cationic surfactant in water. *Chem. Engin. J.* **2013**, *225*, 416-422.
- Bianchi C.L., **Gatto S**., Nucci S., Cerrato G., Capucci V. Self-cleaning measurements on tiles manufactured with micro-sized photoactive TiO_2. *Adv. Environ. Res.* **2013**, *2*.
- Bianchi C.L., **Gatto S.**, Pirola C., Naldoni A., Di Michele A., Cerrato G., Crocellà V., Capucci V. Photocatalytic degradation of acetone, acetaldehyde and toluene in gas-phase: comparison between nano and micro-sized TiO_2. *Appl. Cat. B: Environm*. **2014**, *146*, 123-130.
- Bianchi C.L., Colombo E., **Gatto S**., Stucchi M., Cerrato G., Morandi S., Capucci V. Photocatalytic degradation of dyes in water with micro-sized TiO_2 as powder or coated on porcelain tiles. J. *Photochem. Photob. A: Chem*. **2014**, *280*, 27-31.

- **Gatto S.**, Sansotera M., Persico F., Gola M., Pirola C., Panzer W., Navarrini W., Bianchi C.L. Surface fluorination on TiO_2 catalyst induced by photodegradation of perfluooroctanoi acid. *Catal. Today* **2014.**
- Djellabi R., Ghorab M.F., Cerrato P., Morandi S., **Gatto S.**, Oldani V., Di Michele A., Bianchi C.L. Photoactive TiO_2-montmorillonite composite for degradation of organic dyes in water. *J. Photochem. Photob. A: Chem*. **2014**, *295*, 5763.
- Bianchi C.L., Cerrato G., Crocellà V., **Gatto S.**, Pirola C., Stucchi M., Sansotera M., Capucci V. Photoactivity enhancement of commercial micro-sized TiO_2 induced by surface fluorinations. submitted to *J. Photochem. Photob. A: Chem.* **2014**.

Communications at Congress

- **Gatto S.**, Bianchi C.L. "Micro-sized TiO_2 photocatalyst for air purification from acetone and acetaldehyde", XVIII Congresso Nazionale della Divisione di Chimica industriale della Società Chimica italiana (SCI), Firenze, 11-14 June 2012 (*Poster presentation*).
- **Gatto S.**, Bianchi C.L. US-assisted preparation of photoactive TiO_2: role of the solvent on the final material features and photocatalytic efficiency", European Society of Sonochemistry Meeting, Lviv, Ucraina, 2-5 July 2012 (*Poster presentation*).
- Bianchi C.L., **Gatto S.**, Pirola C., Scavini M., Vitali S., Capucci V. "Micro TiO_2 as starting material for stable photocatalytic tiles",

NICOM4: 4th International Symposium on Nanotechnology in Construction, Crete, May 2012 (*Oral presentation*).

- Bianchi C.L., **Gatto S.**, Nucci S., Cerrato G., Capucci V. "Self-cleaning measurements on tiles manufactured with micro-sized photoactive TiO_2, ACEM 12, The 2012 World Congress on Advanced in Civil, Environmental, and Material Research, Seoul, Korea, 26-29 August 2012 (*Oral presentation*).
- **Gatto S.**, Bianchi C.L. "Photocatalytic degradation of acetone (acetaldehyde and toluene) in gas phase: comparison between nano and micro-sized TiO_2, 7th International Conference on Environmental Catalysis, Lyon, France, 2-6 September 2012 (*Oral presentation*).
- **Gatto S.**, Bianchi C.L. "Photocatalytic VOC degradation: comparison between commercial nano and micro-sized TiO_2", V International Workshop on Oxide Based Materials: OXIDE 2012, Torino, 23-26 September 2012 (*Poster presentation*).
- **Gatto S.**, Bianchi C.L. "Effect of the surface fluorination on both nano and micro-sized TiO_2 for the toluene photodegradation in gas-phase", XIth European Congress on Catalysis, Lyon, France, 1-6 September 2013 (*Poster presentation*).
- **Gatto S.**, Bianchi C.L. "Decomposition of perfluooroctanoic acid photocatalyzed by TiO_2: chemical modification of the catalyst surface induced by fluoride ions", XIth European Congress on Catalysis, Lyon, France, 1-6 September 2013 (*Oral presentation*).
- **Gatto S.**, Bianchi C.L., Gomez R., Bonete P. "Photoelectrochemical and photocatalytic characterization: comparison between nanometric and micrometric TiO_2 powders", ISE International Society of

Electrochemistry, Lausanne, Switzerland, 1-5 September 2014 (*Poster presentation*).